Microstructure of binary mixtures in bulk and nanoconfined phases

Ilham Essafri

UNIVERSITE MATIERE BRETAGNE MOLECULES LOIRE ET MATERIAUX

UNIVERSITÉ DE RENNES 1

THESE DE DOCTORAT DE

L'UNIVERSITE DE RENNES 1
COMUE UNIVERSITE BRETAGNE LOIRE

ECOLE DOCTORALE N° 596
Matière Molécules et Matériaux
Spécialité : « *Physique* »

Par

« Ilham Essafri »

« Microstructure of binary mixtures in bulk and nanoconfined phases »

Thèse présentée et soutenue à « Rennes », le « 13/12/2019 »
Unité de recherche : Institut physique de Rennes
Thèse N° :

Rapporteurs avant soutenance :

Frédéric Affouard — Pr à l'université de Lille
Jean-Marc Simon — MCF à l'université de Bourgogne

Composition du Jury :

Frédéric Affouard
Professeur à l'université de Lille
Rapporteur
Janine Emile
Professeur à l'université de Rennes 1
Examinatrice
Sean Mcnamara
Maitre de conférence à l'université de Rennes 1
Examinateur
Patrice Malfreyt
Professeur à l'université à l'Université Blaise Pascal
Examinateur
Jean-Marc Simon
Maitre de conférence à l'université de Bourgogne
Rapporteur

Directeur de thèse
Aziz Ghoufi
Maitre de conférence à l'université de Rennes 1

Contents

List of Tables

List of Figures

Chapter 1

Introduction

"*The discovery of the Hydrogen Bond could have won someone the noble prize, but it didn't.*" [1]

1.1 Literature review

Nanotechnologies and nanosciences have been accompanied by new challenge requiring the revision of condensed matter physics [2–6]. There are enormous scale differences in our universe, and at different scales, different forces dominate and different mechanisms better explain phenomena. At the nanometric scale, the physical properties of confined liquids such as the dielectric permittivity [7, 8], the surface tension [9, 10], and the melting point [11] drastically differ from the bulk counterpart. These behavioral changes occur when the length scale of the confined liquid is similar to the range of their molecular interactions. As a result, these systems appeared to have a strong surface-to-volume ratio. That is an important point because it influences how well a components will interact with other materials around it. Under confinement, the interactions of liquid with the confining walls clearly begin to have important effects and can impact the structure, dynamics, and thermodynamics of the liquids in comparison with the bulk state [12–14]. Among the so-studied fluids, the hydrophilic liquids (water, alcohol, amine, etc) are important given their manipulation at the nanoscale such as nanofluidic [15]. Additionally, the impact of the confinement on the behavior of fluids is important in diverse phenomena, from the creation of micro-emulsions to drug delivery [16–18], to the assembly of proteins into the functional

complexes, and to engineering processes [19–21].

Recently, a series of studies have been conducted to clarify the properties of fluids in nanometric confinement [22–28]. Gubbins et al. have essentially focused on study the adsorption of different gas [29, 30], water [31–33] and other mixtures [34, 35] systems confined to different nanopores using molecular dynamics. Other studies have also been conducted to understand the behaviour of confined fluids by characterizing the fluid-fluid and fluid-wall interaction [27,36–38]. Interestingly, they were able to demonstrate that the change in interaction in a given system can induce several significant changes in the behaviour of confined fluids. This is explained in particular by the fact that alcohol molecules composed of a hydrophobic part (non-polar part and otherwise it is the alkyl carbon chain) and a hydrophilic part (polar part or hydroxyl group) can make fluid-fluid and fluid-wall interactions increasingly anisotropic in a confined medium. While Zhang et al [39]., by studying the transport of water with methanol in hydrophilic and hydrophobic nanopores, using molecular dynamics, have shown that methanol diffuses more rapidly than water in hydrophobic nanopores, from which a phase separation has been proposed for this type of mixture (alcohol/water). Kaneko and his group are interested in studying the structure of the different alcohols included (ethanol, methanol and 1-propanol) confined in carbon nanopores by X-ray diffraction [40–42], they have shown that all alcohol molecules can form ordered structures in the nanopore, except ethanol which has a preferential orientation in this nanopore. In addition to these studies, Kumar et al. highlighted that water can freeze at 105-151 °C and 87-117 °C when confined in 1.05 nm and 1.06 nm single-walled nanotubes, respectively [11]. Morineau et al. also studied alcohol molecules confined in silica nanopores by X-ray diffraction [43], their results show that the creation of a hydrogen bonding interaction between the methanol and the confined surface affects the local structure of the methanol at the interface. While Ghoufi et al. were able to show a super-permittivity of the water confined in carbon nanotubes, they also highlighted remarkable dielectric properties of the confined electrolyte solutions [7, 8]. Muthulakshmi and coworkers reported an experimental evidence of a partial phase separation of an ethanol-water mixture confined in mesoporous silica using positron annihilation lifetime spectroscopy. They showed that a small fraction of the ethanol molecules seemed to be anchored at the silica surface [44]. A similar results was also established by Guo et al. who have studied confinement of

an ethanol-water mixture between two planar silica walls [45]. A partial and local separation between water and ethanol close to the silica surface were thus evidenced [45]. In the same time Schmitz et al. have exhibited that the glycol-water mixture could undergo an interfacial separation [46]. This phenomenon was also numerically observed by You et al. who exhibited a local demixing of binary hard-core Yukawa mixtures in a slitlike pore [47]. More recently, Krycka et al. displayed a separation between two confined apolar liquids [48]. Whereas these works only suggest a partial separation of two hydrogen bonds forming liquids or two apolar liquids near the solid surface,

More recently, Hamid et al. have provided a direct experimental structural evidence of the microphase separation of macroscopically miscible liquids consisting of hydrogen bonds forming liquid and an apolar one. Indeed, the structure of a mixture comprising toluene (TOL) and *tert*-butanol (TBA) molecules confined in a cylindrical silica nanopore (MCM-41) of radius 24 Å was explored by neutron scattering and compared with the miscible bulk one [49]. Using a core-shell (CS) model, the authors established, for the first time, a molecular-scale phase-separated tubular structure with the TBA molecules forming a layer at the pore surface (shell), surrounding a TOL-rich phase at the center of the pore (core). This observation was later extended down to low temperature in the glassy states and to the larger pores sizes of SBA-15 [50, 51]. A consistent picture, showing the highly selective segregation of polar molecules at the pore surface, was deduced from binary gas adsorption experiments [52]. Up to now, the physical mechanism ruling this phase separation at the nanometric scale stays unknown. In this context, we suggest that this peculiar structure is due to the hydrogen bond network. In order to better understand this behavior at the nanoscale. It is essential to provide a good description of the hydrogen bond network under these conditions. This work aims characterizing the connection between the hydrogen bonding (HB) network and phase separations at the nanoscale. On the other hand, these properties imply especially to study how the HB network evolves under nanoconfinement, its interaction with the confining surface and its impact on the physical properties.

1.2 Motivation and aim

The objective of this thesis is to capture and understand the structural behavior of the HB network at the nanoscale. We would also attempt to examine whether the hydrogen bonding network initially observed in bulk phase will survive in nanometric confinement or will change. Among HB forming liquids, alcohols are considered as good models to investigate the characteristics of the HB structure. Indeed, alcohols are capable of forming 1D, 2D, and 3D networks according to their hydrophobicity (alcohol tertiary, secondary and primary). In this work, Alcohols such as methanol, ethanol, propanol, butanol, and pentanol will be considered as well as their mixtures with other molecules toluene, and cyclohexane. The objective here is to investigate the dilution of HB network by using a non HB former liquid and the relation between two hydrogen bonding networks. For the cluster type structure, the *tert*-butanol will be considered. Finally, our goal will be to investigate the confinement through hydrophilic (silica nanopore [53, 54] and water nanotube) and hydrophobic nanopore as (carbon nanotube [55]). For that, molecular dynamics simulations of alcohols are performed to include linear, branched and tertiary alcohols within cylindrical nanopores (hydrophilic and hydrophobic pores) with the purpose of understanding how the surface effect can impact the hydrogen-bonding network.

As stated previously, in this work molecular dynamics simulation is used. This choice is based on the issue addressed in this work. This involves studying the dynamics and structure of binary liquids confined to the nanoscale. Since our study on confined binary liquids involves the use of models that can contain several thousand of atoms with dynamics that must be monitored for several hundred picoseconds (or even several nanoseconds), we chose an approach using classical mechanics. The selection of the numerical simulation method is based on both temporal and spatial scales. The quantum computation methods (ab initio, semi-empirical, DFT) concern both the atomic radius length-scales and the femtosecond time scale. These quantum techniques take an official interest in the field of chemistry such as modeling the making and/or breaking of chemical bonds. However, molecular dynamic methods handling interactions at molecular level combine space scales in the range of nanometers with time scales ranging from picoseconds to nanoseconds. Indeed, molecular dynamics refers to the physical motion of a collection of atoms or molecules interacting with each other. So depending on the physical problem, the length-scale

and the time scale we could choose our suitable simulation tool.

1.3 Structure of the thesis

Our work will be presented in this manuscript by five chapters, the first chapter discuss the state of the art of the confined liquids and our objectives related to that. The second chapter focuses on the methods used. The third chapter aims to study binary liquids in the bulk phase. Chapter four focused on the study of liquids in confined phases. As a final conclusion, the thesis presents the scope of the results obtained and their consequences in the scientific field of nanopores, and, more generally, materials at the nanometric scale.

Bibliography

[1] George A. Jeffrey and Wolfram Saenger. *The Importance of Hydrogen Bonds*, pages 3–14. Springer Berlin Heidelberg, 1991.

[2] J. Klein and E. Kumacheva. Confinement-induced phase transitions in simple liquids. *Science*, 269(5225):816–819, 1995.

[3] M. Alcoutlabi and Gregory B. McKenna. Effects of confinement on material behaviour at the nanometre size scale. *Journal of Physics: Condensed Matter*, 17(15):R461–R524, 2005.

[4] B. Coasne, S. K. Jain, and K. E. Gubbins. Freezing of fluids confined in a disordered nanoporous structure. *Phys. Rev. Lett.*, 97(10):105702, 2006.

[5] C. Alba-Simionesco, B. Coasne, G. Dosseh, G. Dudziak, K. E. Gubbins, R. Radhakrishnan, and M. Sliwinska-Bartkowiak. Effects of confinement on freezing and melting. *Journal of Physics: Condensed Matter*, 18(6):R15–R68, 2006.

[6] Steve Granick. Motions and relaxations of confined liquids. *Science*, 253(5026):1374–1379, 1991.

[7] A. Ghoufi, A. Szymczyk, R. Renou, and M. Ding. Calculation of local dielectric permittivity of confined liquids from spatial dipolar correlations. *EPL (Europhysics Letters)*, 99(3):37008, 2012.

[8] H. Zhu, A. Ghoufi, A. Szymczyk, B. Balannec, and D. Morineau. Anomalous dielectric behavior of nanoconfined electrolytic solutions. *Phys. Rev. Lett.*, 109(10):107801, 2012.

[9] A. Ghoufi and P. Malfreyt. Importance of the tail corrections on surface tension of curved liquid-vapor interfaces. *The Journal of Chemical Physics*, 146(8):084703, 2017.

[10] I. Essafri, J-C. Le breton, A. Saint-Jalmes, A. Soldera, A. Szymczyk, P. Malfreyt, and A. Ghoufi. Contact angle and surface tension of water on a hexagonal boron nitride monolayer: a methodological investigation. *Molecular Simulation*, 45(4-5):454–461, 2019.

[11] Kumar Varoon Agrawal, Steven Shimizu, Lee W. Drahushuk, Daniel Kilcoyne, and Michael S. Strano. Observation of extreme phase transition temperatures of water confined inside isolated carbon nanotubes. *Nature Nanotechnology*, 12:267, 2016.

[12] Song Hi Lee and Peter J. Rossky. A comparison of the structure and dynamics of liquid water at hydrophobic and hydrophilic surfaces: Äîa molecular dynamics simulation study. *The Journal of Chemical Physics*, 100(4):3334–3345, 1994.

[13] S. Han, M. Y. Choi, P. Kumar, and H. Eugene Stanley. Phase transitions in confined water nanofilms. *Nature Physics*, 6(9):685–689, 2010.

[14] Alexander I. Kolesnikov, Jean-Marc Zanotti, Chun-Keung Loong, Pappannan Thiyagarajan, Alexander P. Moravsky, Raouf O. Loutfy, and Christian J. Burnham. Anomalously soft dynamics of water in a nanotube: A revelation of nanoscale confinement. *Phys. Rev. Lett.*, 93(3):035503, 2004.

[15] W. Sparreboom, A. van den Berg, and J. C. T. Eijkel. Principles and applications of nanofluidic transport. *Nature Nanotechnology*, 4(11):713–720, 2009.

[16] Surya Singh. Nanomedicine nanoscale drugs and delivery systems. *Journal of Nanoscience and Nanotechnology*, 10(12):7906–7918, 2010.

[17] Vitaly V. Chaban, Timur I. Savchenko, Sergiy M. Kovalenko, and Oleg V. Prezhdo. Heat-driven release of a drug molecule from carbon nanotubes: A molecular dynamics study. *The Journal of Physical Chemistry B*, 114(42):13481–13486, 2010.

[18] Tamsyn A. Hilder and James M. Hill. Modeling the loading and unloading of drugs into nanotubes. *Small*, 5(3):300–308, 2009.

[19] Morineau D. Does molecular self-association survive in nanochannels? *J Phys Chem Lett*, 1:1155, 2010.

[20] Ghoufi A. Hydrogen-bond-induced supermolecular assemblies in a nanoconfined tertiary alcohol. *J Phys Chem C*, 115:17761, 2011.

[21] Chandler D. Interfaces and the driving force of hydrophobic assembly. *Nature*, 437:640, 2005.

[22] Niharendu Choudhury. Effect of surface hydrophobicity on the dynamics of water at the nanoscale confinement: A molecular dynamics simulation study. *Chemical Physics*, 421:68–76, 2013.

[23] Wolfram Saenger. Structure and dynamics of water surrounding biomolecules. *Annual Review of Biophysics and Biophysical Chemistry*, 16(1):93–114, 1987.

[24] Biman Bagchi. Water dynamics in the hydration layer around proteins and micelles. *Chemical Reviews*, 105(9):3197–3219, 2005.

[25] Jan Swenson, Helen Jansson, and Rikard Bergman. Relaxation processes in supercooled confined water and implications for protein dynamics. *Phys. Rev. Lett.*, 96:247802, 2006.

[26] G. Garberoglio, M. Sega, and R. Vallauri. Inhomogeneity effects on the structure and dynamics of water at the surface of a membrane: A computer simulation study. *The Journal of Chemical Physics*, 126(12):125103, 2007.

[27] Niharendu Choudhury. Orientational dynamics of water trapped between two nanoscopic hydrophobic solutes: A molecular dynamics simulation study. *The Journal of Chemical Physics*, 133(15):154515, 2010.

[28] Winarto, Eiji Yamamoto, and Kenji Yasuoka. Separation of water-alcohol mixtures using carbon nanotubes under an electric field. *Phys. Chem. Chem. Phys.*, 21(28):15431–15438, 2019.

[29] Shaoyi Jiang, Charles L. Rhykerd, and Keith E. Gubbins. Layering, freezing transitions, capillary condensation and diffusion of methane in slit carbon pores. *Molecular Physics*, 79(2):373–391, 1993.

[30] M. W. Maddox and K. E. Gubbins. Molecular simulation of fluid adsorption in buckytubes. *Langmuir*, 11(10):3988–3996, 1995.

[31] Erich A. Muller, Luis F. Rull, Lourdes F. Vega, and Keith E. Gubbins. Adsorption of water on activated carbons:,Äâ a molecular simulation study. *The Journal of Physical Chemistry*, 100(4):1189–1196, 1996.

[32] Alberto Striolo, Ariel A. Chialvo, Peter T. Cummings, and Keith E. Gubbins. Water adsorption in carbon-slit nanopores. *Langmuir*, 19(20):8583–8591, 2003.

[33] A. Striolo, A. A. Chialvo, K. E. Gubbins, and P. T. Cummings. Water in carbon nanotubes: Adsorption isotherms and thermodynamic properties from molecular simulation. *The Journal of Chemical Physics*, 122(23):234712, 2005.

[34] Abhijit V. Shevade, Shaoyi Jiang, and Keith E. Gubbins. Adsorption of water-Äîmethanol mixtures in carbon and aluminosilicate pores: a molecular simulation study. *Molecular Physics*, 97(10):1139–1148, 1999.

[35] Abhijit V. Shevade, Shaoyi Jiang, and Keith E. Gubbins. Molecular simulation study of water-Äìmethanol mixtures in activated carbon pores. *The Journal of Chemical Physics*, 113(16):6933–6942, 2000.

[36] Santiago Romero-Vargas Castrillon, Nicolas Giovambattista, Ilhan A. Aksay, and Pablo G. Debenedetti. Effect of surface polarity on the structure and dynamics of water in nanoscale confinement. *The Journal of Physical Chemistry B*, 113(5):1438–1446, 2009.

[37] G. Hummer, J. C. Rasaiah, and J. P. Noworyta. Water conduction through the hydrophobic channel of a carbon nanotube. *Nature*, 414(6860):188–190, 2001.

[38] L. D. Gelb, K. E. Gubbins, R. Radhakrishnan, and M. Sliwinska-Bartkowiak. Phase separation in confined systems. *Reports on Progress in Physics*, 63(4):727–727, 2000.

[39] Q. Zhang, Jie Zheng, A. Shevade, L. Zhang, Stevin H. Gehrke, Grant S. Heffelfinger, and Shaoyi Jiang. Transport diffusion of liquid water and methanol through membranes. *The Journal of Chemical Physics*, 117(2):808–818, 2002.

[40] T. Ohkubo, T. Iiyama, and K. Kaneko. Organized structures of methanol in carbon nanospaces at 303 k studies with in situ x-ray diffraction. *Chemical Physics Letters*, 312(2):191–195, 1999.

[41] T. Ohkubo, T. Iiyama, K. Nishikawa, T. Suzuki, and K. Kaneko. Pore-width-dependent ordering of c2h5oh molecules confined in graphitic slit nanospaces. *The Journal of Physical Chemistry B*, 103(11):1859–1863, 1999.

[42] T. Ohkubo and K. Kaneko. Oriented structures of alcohol hidden in carbon micropores with erdf analysis. *Colloids and Surfaces A: Physicochemical and Engineering Aspects*, 187-188:177–185, 2001.

[43] Regis Guegan, Denis Morineau, and Christiane Alba-Simionesco. Interfacial structure of an h-bonding liquid confined into silica nanopore with surface silanols. *Chemical Physics*, 317(2):236 – 244, 2005.

[44] Michael F. Harrach, B. Drossel, W. Winschel, T. Gutmann, and G. Buntkowsky. Mixtures of isobutyric acid and water confined in cylindrical silica nanopores revisited: A combined solid-state nmr and molecular dynamics simulation study. *The Journal of Physical Chemistry C*, 119(52):28961–28969, 2015.

[45] X-Y. Guo, T. Watermann, and D. Sebastiani. Local microphase separation of a binary liquid under nanoscale confinement. *The Journal of Physical Chemistry B*, 118(34):10207–10213, 2014.

[46] T. Muthulakshmi, D. Dutta, Priya Maheshwari, and P. K. Pujari. Evidence for confinement induced phase separation in ethanol–water mixture: a positron annihilation study. *Journal of Physics: Condensed Matter*, 30(2):025001, 2017.

[47] R. Schmitz, N. Muller, S. Ullmann, and M. Vogel. A molecular dynamics simulations study on ethylene glycol-water mixtures in mesoporous silica. *The Journal of Chemical Physics*, 145(10):104703, 2016.

[48] Kathryn L. Krycka, Joseph A. Dura, Luther J. Langston, and Christopher M. Burba. Nanoconfinement-induced phase segregation of binary benzene-Äìcyclohexane solutions

within a chemically inert matrix. *The Journal of Physical Chemistry C*, 122(14):7676–7684, 2018.

[49] Hamid ARA. Microphase separation of binary liquids confined in cylindrical pores. *J Phys Chem C*, 120:9245, 2016.

[50] A. Abdel Hamid, R. Mhanna, P. Catrou, Y. Bulteau, R. Lefort, and D. Morineau. Multiple glass transitions of microphase separed binary liquids confined in mcm-41. *The Journal of Physical Chemistry C*, 120(20):11049–11053, 2016.

[51] R. Mhanna, A. Abdel Hamid, S. Dutta, R. Lefort, L. Noirez, B. Frick, and D. Morineau. More room for microphase separation: An extended study on binary liquids confined in sba-15 cylindrical pores. *The Journal of Chemical Physics*, 146(2):024501, 2017.

[52] Sujeet Dutta, Ronan Lefort, Denis Morineau, Ramona Mhanna, Odile Merdrignac-Conanec, Arnaud Saint-Jalmes, and Theo Leclercq. Thermodynamics of binary gas adsorption in nanopores. *Phys. Chem. Chem. Phys.*, 18(35):24361–24369, 2016.

[53] C. T. Kresge, M. E. Leonowicz, W. J. Roth, J. C. Vartuli, and J. S. Beck. Ordered mesoporous molecular sieves synthesized by a liquid-crystal template mechanism. *Nature*, 359(6397):710–712, 1992.

[54] Xiu S. Zhao, G. Q. (Max) Lu, and Graeme J. Millar. Advances in mesoporous molecular sieve mcm-41. *Industrial & Engineering Chemistry Research*, 35(7):2075–2090, 1996.

[55] Sumio Iijima and Toshinari Ichihashi. Single-shell carbon nanotubes of 1-nm diameter. *Nature*, 363(6430):603–605, 1993.

Chapter 2

Molecular dynamics simulation

Contents

2.1 Introduction

The Molecular Dynamics (MD) simulation is a powerful tool for the understanding of physical phenomena at the microscopic level. It allows us the study of the interactions between two molecules and to an ensemble of molecules representing a liquid in terms of microscopic (or molecular) details. This computational method is among the strongest tool existing for exploring structural and dynamical properties of complex systems and condensed phases. The concept of MD method is to simulate the motion of a set of particles, atoms or molecules over time by numerically integrating classical equation of motion. Although, we might ask why do we use classical mechanics rather than quantum mechanics to describe the motion of the atoms? The Schrödinger equation is so complex that it can only be solved analytically for a few simple cases. Indeed, a direct numerical solution on computers is limited to systems that have small numbers of atoms due to the large size of the space in which the Schrödinger equation is placed. Fortunately, Born-Oppenheimer approximation are used to simplify the problem. This approximation are based on the fact that the mass of electrons is much smaller than the mass of nuclei. The effect of electrons on the interaction between nuclei is then described by an effective potential. As another simplification, the nuclei are moved according to Newton's classical equations using either effective potentials resulting from quantum mechanics calculations, which include electron effects, known as *ab-initio* molecular dynamics simulation or empirical potentials that have been adjusted to the results of quantum mechanics calculations or experimental results defined as *classical* molecular dynamics simulations.

These numerical simulation methods for studying physical properties were developed in the 1960s [1]. The first concrete example of a numerical simulation was conducted at the Los Alamos National Laboratories held in 1953 [2]. In this work, Metropolis and al. used a stochastic technique for sampling points, based simply on a predetermined probability distribution defined on a multidimensional space. The simulation of MC was elaborated from this initial work. It followed that another simulation of MC used a potential of Lennard Jones examined by Wood and Parker in 1957 [3]. Their work has allowed the comparison of information collected from computer-generated and model-derived thermodynamic data experiments. These MC simulation methods remain useful to date as they allow us to make quantitative predictions on the compo-

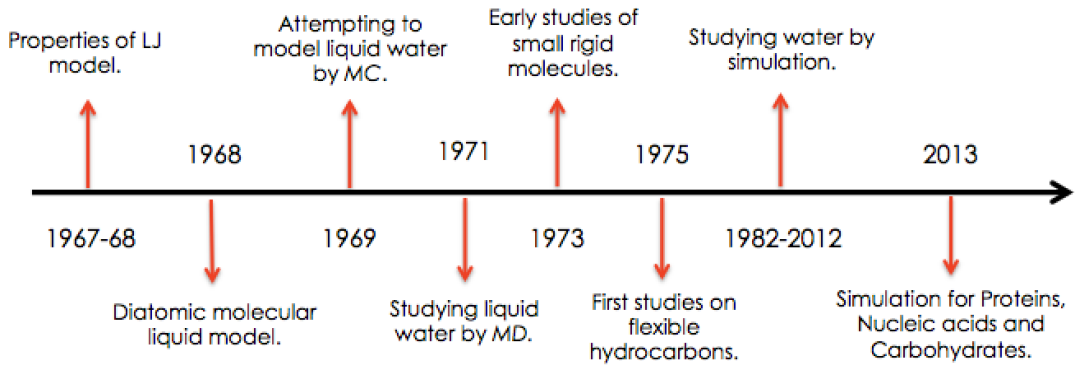

Figure 2.1: Timeline of numerical studies conducted between 1967 and 2013.

sition, structure and thermodynamic properties of several physical systems at different levels of complexity. However, it can not provide direct dynamic information despite the overwhelming evidence that MC has survived as an indispensable molecular simulation instrument.

Almost at the same period, Alder and Wainwright conducted the first technique that could provided the dynamic properties, referred as MD simulations in 1957 [4], they discussed the collision of an assembly of hard spheres. Interestingly, they highlighted a solid-phase transition that was not observed by the so-called MC simulations. MD simulation method is based on a fundamental dynamic equation (Newton's Law) to simulate the temporal evolution of a molecular system. It was in 1964 that Rahman and al. solved the equation of motion for a set of Lennard Jones particles [5]. A series of research presented in Figure 2.1 followed these numerical studies, using numerical and computational methods to comprehend distinct phenomena related to microscopic scale [6–17].

2.2 Statistical Mechanics

As molecular dynamics are used mainly for simulating behaviors at molecular or atomic level, the macroscopic physical property needs statistical mechanics to be used. Thermodynamics and statistical mechanics enable us to create a connection between the experimental macroscopic observations and the microscopic behavior of the simulated system. Both of these are strongly connected and we have to rely on both in order to perform and obtain informations from MD

simulations. MD requires, as an input, a description of the interparticle interactions to provide a picture of a system's microscopic behavior from the laws of classical mechanics. In order to well introduce MD simulation, we need to detail some concepts that are essential to understand the statistical physics that provides a basis for associating the microscopic properties of molecules with the macroscopic ones. Thus, it describes physical properties as the result of the statistical approach at the microscopic level. Herein we focus on classical liquids, meaning that the behavior of a liquid state can be described using laws of classical mechanics.

2.2.1 Classical description of liquids

In *Classical mechanics* the dynamical state of a system composed of N atoms at any particular time is determined completely by the *3N* coordinates $r^N = \{r_1,...,r_N\}$, where r^N represents the *3N* Cartesian components of position, and *3N* momenta of the atoms $p^N = \{p_1,...,p_N\}$ at the same time, with $p^N = mv^N$ and v^N represents the *3N* Cartesian components of atomic velocity. These 6N coordinates (*3N* positions and *3N* momenta) constitute the phase space and each phase space is connected to a microstate. We define a state of a system by a set of positions and momenta of N atoms by (r^{3N},p^{3N}), which is called a *phase space* denoted as $\Gamma = (r^{3N}, p^{3N})$. So, the time evolution of a system in classical description is governed by Newton's equations expressed as :

$$\sum_{i=1}^{N} F_i = m_i a_i = \frac{dp_i}{dt} \tag{2.1}$$

with F_i is the force acting on atom i, m_i and a_i is the mass and the acceleration of atom i respectively and t is the time. The equation (2.1) can be rewritten in cartesian coordinates as:

$$\sum_{i=1}^{N} F_{ix}(x,y,z) = m_i \frac{d^2x_i(t)}{dt^2}; \sum_{i=1}^{N} F_{iy}(x,y,z) = m_i \frac{d^2y_i(t)}{dt^2}; \sum_{i=1}^{N} F_{iz}(x,y,z) = m_i \frac{d^2z_i(t)}{dt^2} \tag{2.2}$$

where (F_{ix}, F_{iy}, F_{iz}) are the three component of the force $F(x,y,z)$ acting on atom i. From Equation (2.2), the $x_i(t)$, $y_i(t)$ and $z_i(t)$ can be derived. The atom's trajectory is calculated by this three-dimensional path.

2.2.2 Ergodic hypothesis: time average and ensemble average

By using Newton's equations coupled with the forces involved, we can deduce the whole history and predict the future behavior of the atoms. Then, a trajectory obtained by molecular dynamics provides such a set of configurations. Each configuration is defined by phase space trajectory as $\Gamma[r^N(t), p^N(t)]$. Therefore, a measurement of a physical quantity A by simulation is simply obtained as an arithmetic average of the various instantaneous values assumed by that quantity during the MD run. For each point of this trajectory, it is possible to calculate the value of A(t) as well as the experimentally measurable quantity A_{obs} that can be regarded as the ***time average*** of A(t) expressed as:

$$A_{obs} =< A(t) >= \lim_{\tau\to\infty} \frac{1}{\tau} \int_0^\tau A(\Gamma(t))dt \tag{2.3}$$

with τ is the observation time of the measurement and the brackets indicate an average value. The idea here is that MD simulation methods provide microscopic information in terms of 3N positions and 3N momenta of atoms as a function of time. While the statistical mechanics translate these 6N coordinates into macroscopic properties by using ergodic hypothesis and laws of thermodynamics. Interestingly, statistical mechanics calculate all macroscopic observable as averages over phase trajectories or as averages over an ensemble of systems. As a result, a macroscopic quantity A can be determined by averaging its values over a set of micro-state characteristics. Statistical mechanics makes it possible to replace a system that evolves over time with a representative set of simultaneous replicas of this system prepared in the same microscopic state. If these replicas show different values from the quantity to be measured A_{obs} at a given time t, their average is called ***ensemble average*** denoted as $< A >_{ensemble}$" and given by:

$$< A >_{ensemble}= \frac{1}{Z} \int A(r,p) \exp(-\beta E(r,p))drdp \tag{2.4}$$

with Z is the partition function which is a measure of the volume occupied by the system in the phase space. Basically, it gave us an information on how many microstates are accessible to our system in a given ensemble. This concept will be details later. $\beta = 1/\mathrm{kT}$ is the inverse temperature (k is the Boltzmann constant) and (r,p) represents the coordinates and the momenta of

atoms in the microstate. E is the energy of the microstate. Recall that a microscopic state is a point in the phase space. The equation (2.5) leads to the average value measured over time for a good number of replicas. This is the ergodic hypothesis, one of the fundamental axioms of statistical mechanics, which translates into the relationship (2.5) by considering an infinite number of configurations and an infinite sampling time [18, 19].

$$A_{obs} =< A(t) >=< A >_{ensemble} \tag{2.5}$$

2.2.3 Thermodynamic ensembles

In molecular dynamics simulation, various thermodynamic ensembles can be used. These ensembles are characterized by the thermodynamic parameters that are imposed: the number of particles (N), the volume (V), the total energy of the system (E), the temperature (T), the pressure (P), etc. In this section, we present the two NVT and NpT ensembles explored in this thesis.

Canonical ensemble: NVT

The canonical ensemble is the statistical ensemble where the number of particles N, the volume V and the temperature T are fixed. NVT ensemble represents a closed system with no exchange of matter or work with the external medium and in thermal contact with an energy reservoir. The partition function of the canonical ensemble is expressed:

$$Q(N, V, T) = \sum_{i:} \exp(-\beta E_i) \tag{2.6}$$

where the sum is expressed on all possible states i of the system, $\beta = 1/\mathrm{kT}$ is the inverse temperature (k is the Boltzmann constant) and E_i is the eneregy of state i.
Within the classical limit of statistical mechanics, any discrete summation on the accessible states is replaced by an integral on the phase space:

$$\sum_i \Rightarrow \frac{1}{h^3} \int d\Gamma \tag{2.7}$$

with $d\Gamma = dxdydzdp_xdp_ydp_z$ is the infinitesimal volume in the phase space.
In the classical limit this partition function for indistinguishable particles is:

$$Q(N,V,T) \equiv \frac{1}{N!h^{3N}} \int\int dr^{3N}dp^{3N} \exp[-\beta\mathscr{H}(r^{3N},p^{3N})] \tag{2.8}$$

with $\mathscr{H}(r^{3N},p^{3N})$ represents the Hamiltonian that characterizes these N particles, which is expressed in terms of the total potential energy U and the total kinetic energy K ($\mathscr{H}(r,p) = K(p) + U(r)$).
Following the definition of the ensemble average, a physical quantity A(r^{3N},p^{3N}) is determined according to the following Eq. (2.9) given by:

$$< A >_{NVT} \equiv \frac{\int\int dr^{3N}dp^{3N} \exp[-\beta\mathscr{H}(r^{3N},p^{3N})]A(r^{3N},p^{3N})}{\int\int dr^{3N}dp^{3N} \exp[-\beta\mathscr{H}(r^{3N},p^{3N})]} \tag{2.9}$$

Isothermal-isobaric ensemble: NpT

This ensemble is well suited for experimental observations based on normal laboratory conditions. In the NpT ensemble, the quantities N, P and T are conserved during the simulation. The volume varies isotropically (same variation in all directions of space) or anisotropically, and in this case, it is possible to choose the direction on which to apply the volume variation. The volume is therefore fluctuating. The volume should instead add to the list of phase-space microscopic quantities. In other words, the phase space of this system in this ensemble is specified by $<$ V, r_{3N}, p_{3N} $>$. Thus, the isothermal-isobaric partition function in the semi-classical form is :

$$Q_{NPT} = \frac{1}{N!h^{3N}V_0} \int dV \int dr^{3N}dp^{3N} \exp(-\beta[H(r^{3N},p^{3N};V) + PV]) \tag{2.10}$$

while V_0 is the unit volume.

2.3 Molecular dynamics simulation method

2.3.1 Definition

Molecular dynamics is a numerical simulation technique used to model the movement of a system of particles (nuclei of atoms, electrons, ions) over time in a particular or specific environment (temperature, pressure). In Newtonian mechanics (section 2.3.2), the particle (assimilated to a point mass) is subjected to a force (derived from an energy potential) that produces an acceleration on it [20, 21]. The equations are numerically integrated using an infinitesimal time step (section 2.3.3), guaranteeing the conservation of the system's energy, typically from one to two femtoseconds. The simulation will then consist in calculating at each moment the position, velocity and acceleration of each of the particles, as well as the forces between particles, using the results obtained at the previous time. It should be noted that the size and time-scale accessible by molecular dynamics are in the order of a few tens of nanometers, and a few picoseconds.

Molecular dynamics applies both to the structural study of molecules and to large interacting systems. However, since computing capacities are limited, thus the number of particles in a simulation is also limited. For example, to simulate an infinite material in one, two or three dimensions, the particles will be placed in a periodic space: this is referred as a simulation box (section 2.3.4). When calculating the forces, this periodicity of the space must be taken into account. In practice, a distinction will be made in the interaction strength (section 2.3.5) between short-range terms, which will not be affected by periodicity, i.e. only the closest particles will be taken into account, and a long-range term, which will need to take this into account. The long-range term is generally of the Coulomb type and will be calculated by the Ewald sum.

2.3.2 Equation of motion

As previously defined the MD method is a computer instrument that provides access to the time-dependent properties of a physical system. For this, it considers the atoms as a classical moving masses and has a velocity resulting from the forces applied on each atom. In Classical MD simulations atoms move according to the Newtonian equations of motion given by

$$F_i = m_i \vec{a}_i(t) = m_i \frac{dv_i(t)}{dt} = m_i \frac{d^2 r_i(t)}{dt^2}; F_i = -\frac{\partial}{\partial r_i} U \tag{2.11}$$

with F_i is the force acting on atom i, t is the time, v_i, m_i and r_i is the velocity, the mass and the position of atom i and U is the potential energy.

2.3.3 Integration algorithm

The solution of the differential equation (2.11) describing the motion of each of the N atoms of a system requires, because of its complexity, the use of numerical resolution methods.The most commonly used algorithms in molecular dynamics are the Beeman algorithm, the Gear method, the Leapfrog algorithm and finally the Verlet algorithm presented in this thesis.

Velocity verlet algorithm: The integration algorithms are based on finite difference methods. the concept of this method is to discretize the first or second order differential equations. Consequently, an algorithm that requires minimal computational effort is considered a good integrator. However, it also needs to be stable and accurate as a function of time and to respect the physical invariant such as the energy and the total momentum of the system. In general, a good integrator is a compromise between accuracy and computational time. There are also different integration algorithms (*Verlet simple* [6], *Verlet Leap-frog* [22], *Verlet velocity* [23] , etc...) that can be used and which differ in the way Taylor's development is implemented. To this argument, we used the *Verlet-velocity* algorithm, which is presented below.

We suppose that our system of interests is composed of N atoms, each atom i is distinguished in space by its position $\vec{r_i}$, and we note $\vec{r}$ = {$\vec{r_1}$, $\vec{r_2}$, ... $\vec{r_N}$ } the space vector that conveys all the positions of the atoms. Similarly, $\vec{v}$ = {$\vec{v_1}$, $\vec{v_2}$, ... $\vec{v_N}$ } is the space vector that contains all the velocities. We note $\vec{F_i}$ the total force exerted on the atom i (previously noted (F_i)). Verlet Velocity algorithm is based on a Taylor development to obtain the positions $\vec{r_i}$ of each atom at time t + δt such that

$$\vec{r_i}(t+\delta t) = \vec{r_i}(t) + \vec{v_i}(t)\delta t + \frac{\vec{F_i}(t)}{2m_i}\delta t^2 + O(\delta t^3) \tag{2.12}$$

In Eq. (2.12), δt is the time step which must be smaller than half of the collision time between the atoms. On the other hand, in order to calculate the velocities at t+δt, we need to define the forces $\vec{F_i}$ (t + δt) acting on each atom, i.e. $\vec{F_i}$(t + δt)=$-\nabla U_i$ [$\vec{r_1}$(t+δt) ,$\vec{r_2}$ (t + δt) ,...,$\vec{r_N}$(t+δt)]

and the positions is calculated as

$$\vec{r_i}(t) = \vec{r_i}(t+\delta t) - \vec{v_i}(t+\delta t)\delta t + \frac{\vec{F_i(t+\delta t)}}{2m_i}\delta t^2 + O(\delta t^3) \tag{2.13}$$

If we sum up Taylor's two developments, we get the following expression

$$\begin{aligned} \vec{r_i}(t) + \vec{r_i}(t+\delta t) = \vec{r_i}(t) + \vec{r_i}(t+\delta t) + \vec{v_i}(t)\delta t - \vec{v_i}(t+\delta t)\delta t \\ + \frac{\vec{F_i}(t)}{2m_i}\delta t^2 + \frac{\vec{F_i(t+\delta t}}{2m_i}\delta t^2 + O(\delta t^3) \end{aligned} \tag{2.14}$$

That is :

$$\vec{v_i}(t+\delta t) = \vec{v_i}(t) + \frac{\vec{F_i(t)} + \vec{F_i}(t+\delta t)}{2m_i}\delta t + O(\delta t^3) \tag{2.15}$$

The equations (2.12) and (2.15) represent the *Verlet Velocity* algorithm. This algorithm is simple to use, accurate and stable, which explains its success in molecular dynamics simulation codes. However, it is also slightly more expensive than other algorithms, since the forces have to be calculated at t + δt.

2.3.4 Periodic boundary conditions

The simulation box is in general a closed space. During the integration of motion equation the atoms close to the coin eventually leave outside. We must thus impose constraints on the surfaces to prevent this loss, and use a method to treat the leaving atoms, by reintegrating them into the box. As illustrated in Figure 2.2 the periodic boundary conditions (PBC) are applied [24] to avoid these boundary effects. That consists in replicating the finite set of atoms distributed according to the three dimensions. Indeed, the aim of the periodic boundary is to generate a surfaceless system.

As shown in Figure2.2, when an atom or molecule moves in the central box, its images move in the same way in the replicated boxes. The number of atoms in the central box is then conserved. There is no need to store the coordinates of all the images, only those of the atoms in the central box (that corresponds to the Cell 1 in Fig. 2.2). A given atom interacts with all other atoms in this infinite periodic system. This means that with the periodic boundary conditions the surface effect are removed and and infinite volume is created to represent a macroscopic system. In the

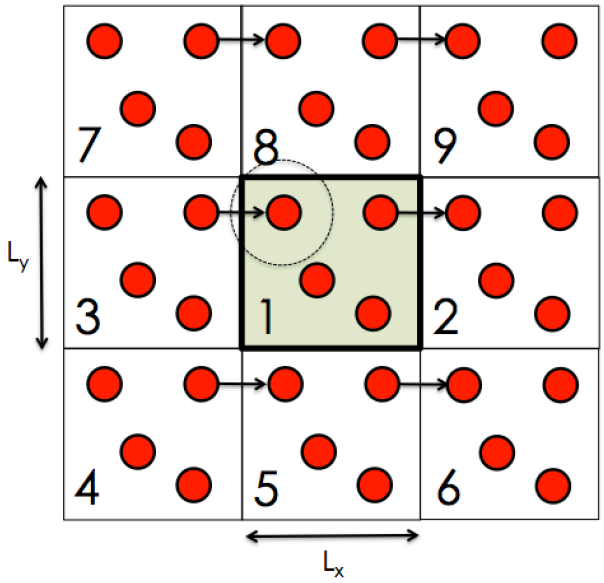

Figure 2.2: Two dimensional Periodic Boundary Conditions scheme for a cubic box. The simulation box is indexed 1 while the image boxes are indexed 2, 3, 4, 5, 6, 7, 8 and 9. When an atom leaves the boundaries of the cell ($1 \rightarrow 2$) its image in the opposite image cell enters the cell ($3 \rightarrow 1$).

case of an atom i at the $\vec{r_i}$ position, there is a set of image atoms at the ($\vec{r_i}$+nL) positions, $\vec{n}$ is arbitrary vector of three numbers. Given the PBC the potential energy can be written as

$$U(\vec{r}_1, ..., \vec{r}_n) = \sum_{i<j} U(r_{ij}) + \sum_{n} \sum_{i<j} U(|\vec{r_i} - \vec{r_j} + \vec{n}L|) \tag{2.16}$$

As the system is pseudo-infinite, an effect is generated that requires to make approximations to calculate the potential pairwise interactions. To do so, a convention about how distances are calculated is made.

Minimum image convention

Through the so-called "minimal image" approximation, each atom i of the central cell interacts with the nearest image of all the other atoms j. The distance between particle i at $\vec{r_i}$ and particle j at $\vec{r_j}$ is $\vec{r_{ij}}$=min($|\vec{r_i}$-$\vec{r_j}$+$\vec{n}$L|) on all $\vec{n}$. The circled atom in the primary cell (Cell 1 in Fig. 2.2) interacts only with each of the other N-1 particles in the secondary cell or their closest images such that the interactions are limited to the cutoff radius, equation(2.17), where L is the box

length.

$$r_c < \frac{L}{2} \tag{2.17}$$

It would be more realistic to include the interaction of each particle with all its image. Since we assumed that there is an infinite system, we need to choose a cut-off to perform calculations, which introduces truncation in potential, short range interaction (LJ) and long range electrostatic interaction. A procedure to treat the electrostatic interaction have been established by *EWALD* [25] that divide the problem into two parts.

2.3.5 Molecular interactions

The first step of a molecular dynamics simulation is to determine how to simulate a physical system composed of N molecules. Knowing that each molecule of this system is made of atoms, and each atom interacts with its neighbor. Then, the atoms close to each other involve electrons, and this leads to an interaction. The main point here is to discover how this interaction between atoms can be modeled and simulated.

As mentioned previously (Eq. (2.11)), forces are derived as the gradients of the potential in terms of atomic displacements. The aim of molecular dynamics simulation is to choose the interaction potential: a function U(r_1,...r_N) of the atomic positions, representing the potential energy of the system. This function is generally constructed from the relative positions of atoms relative to each other. The most basic choice for U is to write it as a sum of interactions in pairs. This function characterizes the most relevant ingredient that contains physics in MD simulation.

The potential energy U basically has two contributions: intramolecular and intermolecular interactions. The "intramolecular" component represents the flexibility of the molecules and the "intermolecular" component describes the interactions between "unbound" atoms, i.e the atoms are separated by more than three bonds; that can be divided in two terms taking into account of the long and short range interactions, i.e Van der Waals and electrostatic interactions respectively.

Non-bonded interactions

The intermolecular interactions are expressed as a sum of Lennard-Jones and Coulomb potentials:

$$U_{ij}(r) = \sum_{ia,jb} 4\epsilon_{ia,jb} \left[\left(\frac{\sigma_{ia,jb)}}{r_{ia,jb}} \right)^{12} - \left(\frac{\sigma_{ia,jb)}}{r_{ia,jb}} \right)^{6} \right] + \sum_{ia,jb} \frac{1}{4\pi\epsilon_0} \frac{q_{ia} q_{jb}}{r_{ia,jb}} \tag{2.18}$$

Thus the potential between two molecules i and j is defined as the sum of interactions between the sites a and b, on molecules i and j, respectively, with partial charges q_{ia} and q_{jb}, and the diameter Lennard-Jones $\sigma_{ia,jb}$, energy $\epsilon_{ia,jb}$ and relative distances $r_{ia,jb}$.

a) The Lennard-Jones potential.

The first term of Eq. (2.18) is the Lennard-Jones potential (LJ), which characterizes van der Waals interactions and its behavior is presented in Figure 2.3. This potential represents the interaction energy between two non-bonded atoms according to their separation distance. The LJ potential has an attractive part in term of $(\frac{1}{r})^6$ at long distances and strong repulsion in term of $(\frac{1}{r})^{12}$ at short distances. The Lennard-Jones intermolecular parameters were derived using the Lorentz-Berthelot rules for mixing $\sigma_{ab} = \sqrt{\epsilon_{aa}\epsilon_{bb}}$ and $\sigma_{ab} = (\sigma_{aa} + \sigma_{bb})/2$. The potential of

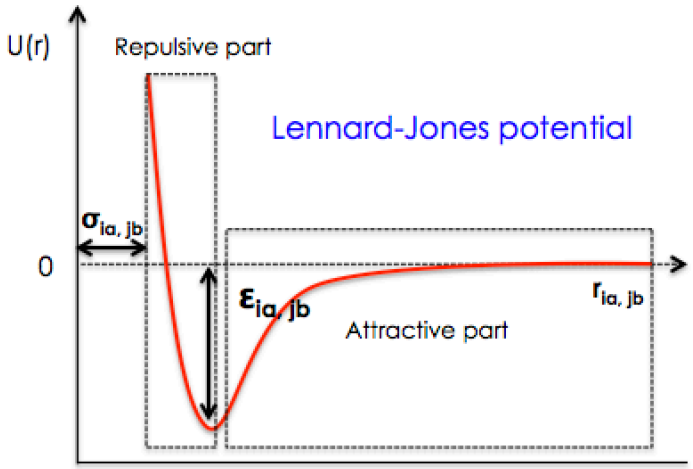

Figure 2.3: Profile of the Lennard-Jones potential.

Lennard-Jones (LJ) includes the attractive interaction of Van der Waals, which is prevalent at

long distances, and the electronic repulsion of Pauli, which is predominant at short distances, and which prevents the mutual interpenetration of electronic clouds of two atoms.

As illustrated in Figure 2.2 beyond r_c the LJ potential is close to zero and the potential can be then truncated such that $U(r_c)$=0. With the use of r_c in the case of Lennard-Jones potential (LJ), this truncation introduces a break in the calculation of the potential between two atoms, since it has a finite value for $r_{ia,jb} \leq r_c$ and is zero for $r_{ia,jb} > r_c$. To avoid this problem, the potential is often shifted in order to vanish at the cut-off radius:

$$U(r) = \begin{cases} U_{LJ}(r) - U_{LJ}(r_c) & \text{if r} \leq r_c \\ 0 & \text{if r} > r_c \end{cases} \tag{2.19}$$

b) Electrostatic interactions from the Ewald sum.

Unlike short Van der Waals interactions, the long range electrostatic interaction cannot be ignored at long distances. We suppose that our system is composed of N atoms placed in a cubic box. These atoms are subjected to periodic boundary conditions as shown previously. This means that we need to consider all interactions of the atoms with its periodic images. Ewald formalism is addressed in this calculation which it was developed by Ewald [25]. It is based on the following principle: if we consider a molecule placed in a central box, it will not only interact with neighbouring molecules but also with all its images located in the periodically reproduced cells. To calculate the position of an image box, a simple translation of a vector whose components represent an integer multiple of the dimensions of the central box can be used. This formalism is applied to the calculation of the interactions of the Colombians forces, and is the most used for the simulation of molecular dynamics.

The coulomb interaction energy of N atoms at locations $r_1, r_2, r_3, ..., r_N$ and possessing point charges $q_1, q_2, q_3, ..q_N$ respectively, is written as,

$$U_{elec} = \frac{1}{4\pi\epsilon_0} \sum_{i,j} \frac{q_i q_j}{|r_{ij}|} \tag{2.20}$$

where $r_{ij} = r_j - r_i$, ϵ_0 is vacuum permittivity and the sum is over all atomic pairs (i, j). These atoms are subjected to periodic boundary conditions (PBC) as shown previously, which are

described by three repeat vectors L_x, L_y and L_z (forming a box). To simplify our notation, we will write L_x, L_y and L_z, as L, where L represents the characteristic length of the simulation box. This means that whenever there is an atom q_i at location r_i, there are also atoms with charge q_i at $r_i + n_xL + n_yL + n_zL$, where n_x, n_y, n_z are arbitrary integers. In this case, we can choose $L = |L_x| = |L_y| = |L_z|$ and vectors n form a simple cubic lattice (n_x, n_y, n_z).
Then the total coulomb interaction energy for these atoms under PBC has to include the interactions between periodic images,

$$U_{elec} = \frac{1}{4\pi\epsilon_0} \sum_{n} \sum_{i,j} \frac{q_i q_j}{|r_{ij} + nL|} \tag{2.21}$$

The sum over all pairs can be rewritten into sums over all atoms, with a factor $\frac{1}{2}$ to cancel the double-counting.

$$U_{elec} = \frac{1}{4\pi\epsilon_0} \frac{1}{2} \sum_{n}{}' \sum_{i=1}^{N} \sum_{j=1}^{N} \frac{q_i q_j}{|\vec{r_{ij}} + nL|} \tag{2.22}$$

where the $'$ symbol is introduced to exclude the term $j = i$, if and only if n = 0. The infinite sum in equation 2.22 not only converges very slowly but also is conditionally convergent meaning that the result depends on the order of the summation. For this reason, there are several ways of proceeding in numerical simulation with truncation methods (spherical truncation, generalized reaction field, Wolf's sum, etc.), which in some cases provide simulation artifacts, or, in a more rigorous way, the Ewald's sum. In this thesis, we use the latter method, which is the most commonly used in numerical simulation research.

As shown in Fig. 2.4 the Ewald's sum transforms long-range interactions by summing the interaction energies of each charge of the first cell with all the periodic images and to improve the convergence by converting the function $\frac{1}{r}$ into two series, each converging more quickly according to the following principle:

$$\frac{1}{r} = \frac{\phi(r)}{r} + \frac{1 - \phi(r)}{r} \tag{2.23}$$

So the aim is to define a function $\phi(r)$ that is in line with i) the rapid variations from 1 to

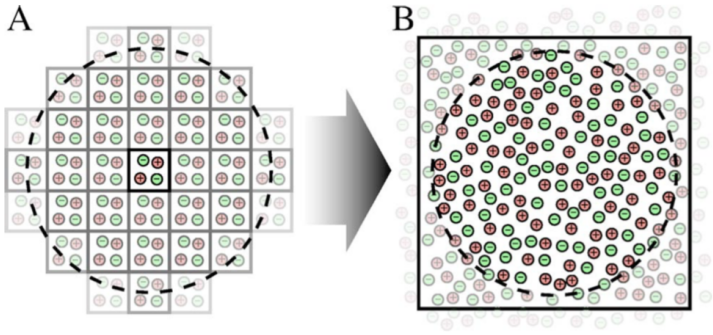

Figure 2.4: Schematic representation of the Ewald method of constructing the periodic cell network, [26]. A) Ewald sum replicated the simulation box to convergence, B)Radial cutoff methods to reach convergence for the larger systems.

small r and *ii*) the long slow decay at distant r. In practical terms, this is expressed in the Ewald sum as a series in real space to consider the interactions inside and near the cell-unity and a series in reciprocal space for interactions with the other cells. The approach of the Ewald summation method is based on the expression (2.21). This equation is rewritten by introducing around each charge center a of each molecule i a charge distribution term (diffusive charge) of the same quantity as the point charge q_i and of the opposite sign. In this way, by adding the total cloud charge, the q_i charge is completely nullified (Figure 2.4). As a result, the most commonly used form and, at the same time, the one originally used by Ewald formalism is a Gaussian distribution:

$$\rho_{Gauss}(r) = \frac{z_{ia}\alpha^3}{\pi^{\frac{3}{2}}} \exp(-\alpha^2 r^2) \tag{2.24}$$

where α is the gaussian distribution width. α is chosen according to the system under study. To filter the interaction between neighbouring charges, this distribution acts as an ionic atmosphere. The screened interactions are now short-ranged, and the total screened potential is calculated by summing over all the molecules in the central cube and all their images in the real space lattice of image boxes. For our case we followed the empirical relationship given in the *DL_POLY* manual [27] which is: α=3.2/(l_{min}/2) with l_{min} the length of the smallest side of the considered cubic box.

The electrostatic potential created by the site a of molecule i is the result of the non-screen q_i charge. Eventually, the total electrostatic potential form in the Ewald's sum is expressed as ,

$$
\begin{aligned}
U_{Elec}^{Total} &= U^S + U^L - U^{self} \\
&= \frac{1}{4\pi\epsilon_0}\frac{1}{2}\sum_n{}'\sum_{i=1}^{N}\sum_{j=1}^{N}\frac{q_i q_j}{|r_i - r_j + nL|} erfc\left(\frac{|r_i - r_j + nL|}{\sqrt{2}\sigma}\right) \\
&+ \frac{1}{2\epsilon_0}\sum_{k\neq 0}\frac{e^{-\sigma^2 k^2/2}}{k^2}|S(k)|^2 - \frac{1}{4\pi\epsilon_0}\frac{1}{\sqrt{2\pi}\sigma}\sum_{i=1}^{N} q_i^2
\end{aligned}
\tag{2.25}
$$

where $erfc$(x) is a complementary error function ($erfc$(x)=$[2/\sqrt{\pi}]\int \exp[-t^2]dt$) that falls to zero with an increase of x. This sum physically translates into:

1. Replicating the atomic charges of the studied system in the three dimensions of the real space.

2. Considering each point charge of the real space as a Gaussian distribution of charges of opposite sign from the point charge (Figure 2.5, "Sum in the real space").

3. The representation of the Gaussian distribution of charges of real space in reciprocal space. This last distribution of the opposite sign therefore serves to cancel out the Gaussian distributions (Figure 2.5, "Sum in reciprocal space").

In this way, as shown in Figure 2.5, the sum of the charges is converted into a sum of interactions between charges and Gaussian distributions.

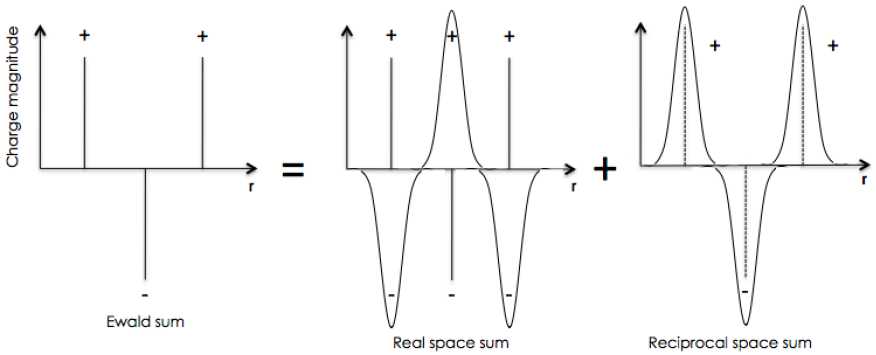

Figure 2.5: The elements of Ewald's summation of a one-dimensional system. The Gaussian is normalized by unit.

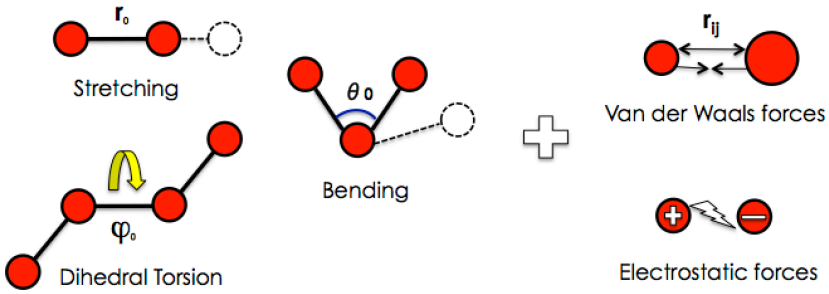

Figure 2.6: *Description of intra and inter-atomic interactions in a force field.*

Bonded interactions

Intramolecular interactions are described by several potentials, representing interactions between atoms linked by covalent bonds. The mathematical function forms used to describe these interactions are given by,

$$\begin{aligned} U^{Total} = & \sum_{bonds} K_r(r-r_0)^2 + \sum_{angles} K_\theta(\theta-\theta_0)^2 \\ & + \sum_{torsion} (\frac{V_1}{2}[1+cos(\phi)] + \frac{V_2}{2}[1-cos(2\phi)] + \frac{V_3}{2}[1+cos(3\phi)] + \frac{V_4}{2}[1-cos(4\phi)]) \end{aligned} \tag{2.26}$$

In this potential, these two atoms are coupled by the force that derives from a harmonic potential. As depicted in Figure 2.6, the harmonic potential is provided by the first term in Equation (2.26). In this expression, r is the interatomic distance between two atoms (Å), r_0 is is the equilibrium bond length (Å) and K_r is the strength of the bonds (kcal/mol^2). The second term describes the flexibility of the considered triplet of atoms, with θ is the valence angle between the three atoms (in degrees), θ_0 is the equilibrium angle (in degrees) and K_θ s the strength of valence angle (kcal/mol). The last term is the dihedral deformation energy term which refers to three bonds and therefore four consecutive atoms. In this equation, V_1, V_2, V_3 and V_4 are Fourrier constants and ϕ (in degrees) is the dihedral angle between the planes constructed by the four atoms.

2.3.6 Molecular parameters

A force field is a set of empirical parameters that describes the interactions between each atom. Accuracy of computer simulations depends critically on these models parameters, which are mainly the force fields between the components. These force fields are expressed in terms of bond lengths, angles, torsion angles, Lennard-Jones potential, and partial atomic charges. These parameters are derived from spectroscopic and diffraction experiments, quantum chemical calculations or empirical parameterizations used to reproduce liquid properties, such as density. The validity of a force field consists in reproducing other quantities that have not been used in the parameter adjustment process, for example, the thermodynamic properties of the mixing systems, the diffusion constants or the dynamic properties such as relaxation times. Currently, the most popular force fields are: CHARMM [28], AMBER [29], GROMOS [30], OPLS [31], GAFF [32] and COMPASS [33].

Through these force fields, small organic molecules, polymers, proteins or membranes can be simulated. In this thesis study, we chose to use OPLS-AA [31] (Optimized potentials for liquid simulations-all atoms) developed by William L. Jorgensen, which has proven to be relevant for describing many structural, thermodynamic and dynamic properties of molecular solids and liquids.

2.4 Confined systems

Silica cylindrical nanopore with a hydrophilic surface was managed by applying the procedure proposed by Brodka and Zerda [34]. We generated a cylindrical cavity along the z axis of the cubic silica cell of (35.7 and 71.3) Å by removing the atoms within a cylinder of diameter (D) (24 and 42) Å. From their coordination numbers, we distinguished bridging oxygen (O_b) bonded to two silicon atoms from non bridging oxygens (O_{nb}) bonded to only one silicon and bonded to one hydrogen atom (H_{nb}). An iterative procedure of atom (O and Si) removal was applied until only tetra-coordinated silicon atoms, bonded to a maximum of two O_{nbs}, were present in the structure. Finally, non-bridging oxygens were saturated with hydrogen atoms to form surface hydroxyl groups. This procedure leads to a realistic description of the irregular inner surface of the porous silicate and of the interfacial interactions between the fluid and the matrix (see

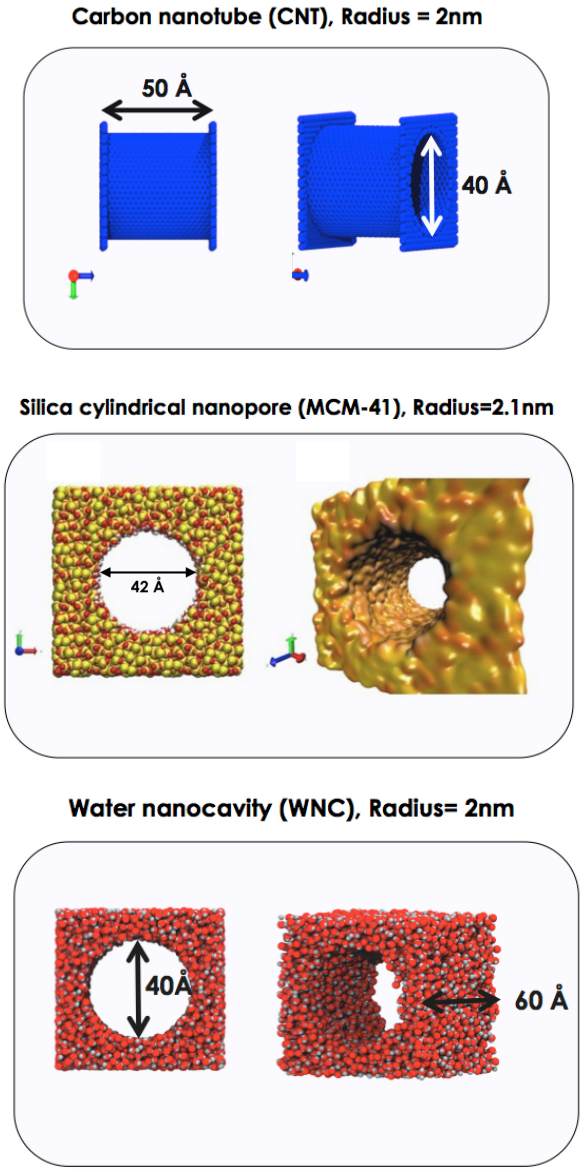

Figure 2.7: Schematic representation of carbon nanotube (CNT), the silica cylinrical nanopore (MCM-41) and the water nanocavity (WNC) used in this work.

Fig. 2.7). The inner surface coverage of silanol groups was about 7.5 nm^{-2}, which corresponds to highly hydrated protonated silica pore. Armchair CNT of radius (12 and 20) Å with a pore length of 50 Å was modeled by considering the uncharged force field developed by Werder et al. Water nanotube was built by carving a cylindrical nanopore of radius (10, 12 and 20) Å into an equilibrated cubic water box with a length box of 60 Å. Water molecules were modeled by considering the TIP4P/2005 model and were considered as frozen [35].

Bibliography

[1] Nicholas Metropolis and S. Ulam. The monte carlo method. *Journal of the American Statistical Association*, 44(247):335–341, 1949.

[2] Nicholas Metropolis, Arianna W. Rosenbluth, Marshall N. Rosenbluth, Augusta H. Teller, and Edward Teller. Equation of state calculations by fast computing machines. *The Journal of Chemical Physics*, 21(6):1087–1092, 1953.

[3] W. W. Wood and F. R. Parker. Monte carlo equation of state of molecules interacting with the lennard Äêjones potential. i. a supercritical isotherm at about twice the critical temperature. *The Journal of Chemical Physics*, 27(3):720–733, 1957.

[4] B. J. Alder and T. E. Wainwright. Phase transition for a hard sphere system. *The Journal of Chemical Physics*, 27(5):1208–1209, 1957.

[5] A. Rahman. Correlations in the motion of atoms in liquid argon. *Phys. Rev.*, 136:A405–A411, 1964.

[6] Loup Verlet. Computer "experiments" on classical fluids. i. thermodynamical properties of lennard-jones molecules. *Phys. Rev.*, 159:98–103, 1967.

[7] LOUP VERLET. Computer "experiments" on classical fluids. ii. equilibrium correlation functions. *Phys. Rev.*, 165:201–214, 1968.

[8] G. D. Harp and Bruce J. Berne. Linear and angular momentum autocorrelation functions in diatomic liquids. *The Journal of Chemical Physics*, 49(3):1249–1254, 1968.

[9] J.A. Barker and R.O. Watts. Structure of water; a monte carlo calculation. *Chemical Physics Letters*, 3(3):144 – 145, 1969.

[10] Aneesur Rahman and Frank H. Stillinger. Molecular dynamics study of liquid water. *The Journal of Chemical Physics*, 55(7):3336–3359, 1971.

[11] J. Barojas, D. Levesque, and B. Quentrec. Simulation of diatomic homonuclear liquids. *Phys. Rev. A*, 7(3):1092–1105, 1973.

[12] J.-P. Ryckaert and A. Bellemans. Molecular dynamics of liquid n-butane near its boiling point. *Chemical Physics Letters*, 30(1):123–125, 1975.

[13] Michael D. Morse and Stuart A. Rice. Tests of effective pair potentials for water: Predicted ice structures. *The Journal of Chemical Physics*, 76(1):650–660, 1982.

[14] *Water: From Interfaces to the Bulk*. Faraday Discussions. The Royal Society of Chemistry, 2009.

[15] R M Lynden-Bell. Towards understanding water: simulation of modified water models. *Journal of Physics: Condensed Matter*, 22(28):284107, 2010.

[16] I-Chun Lin, Ari P. Seitsonen, Ivano Tavernelli, and Ursula Rothlisberger. Structure and dynamics of liquid water from ab initio molecular dynamics Äîcomparison of blyp, pbe, and revpbe density functionals with and without van der waals corrections. *Journal of Chemical Theory and Computation*, 8(10):3902–3910, 2012.

[17] Luca Monticelli and Emppu Salonen. *Biomolecular Simulations: Methods and Protocols*, volume 924. Humana Press, 2013.

[18] Daan Frenkel and Berend Smit, editors. *Understanding Molecular Simulation: From Algorithms to Applications*. Academic Press, Inc., Orlando, FL, USA, 1st edition, 1996.

[19] Donald A. McQuarrie. *Statistical mechanics*. Harper, Row New York, 1975.

[20] M.P. Allen, M.P. Allen, D.J. Tildesley, T. ALLEN, and D.J. Tildesley. *Computer Simulation of Liquids*. Oxford Science Publ. Clarendon Press, 1989.

[21] D. C. Rapaport. *The Art of Molecular Dynamics Simulation*. Cambridge University Press, 2 edition, 2004.

[22] R.W. Hockney. Potential calculation and some applications. *Methods Comput. Phys.*, 1970.

[23] William C. Swope, Hans C. Andersen, Peter H. Berens, and Kent R. Wilson. A computer simulation method for the calculation of equilibrium constants for the formation of physical clusters of molecules: Application to small water clusters. *The Journal of Chemical Physics*, 76(1):637–649, 1982.

[24] M. Born and T. von Karman. Uber schwingungen im raumgittern. *Physikalishe Zeitschrift*, 13:297–309, 1912.

[25] P. P. Ewald. Die berechnung optischer und elektrostatischer gitterpotentiale. *Annalen der Physik*, 369(3):253–287, 1921.

[26] Christopher J. Fennell and J. Daniel Gezelter. Is the ewald summation still necessary? pairwise alternatives to the accepted standard for long-range electrostatics. *The Journal of Chemical Physics*, 124(23):234104, 2006.

[27] W. Smith and T. R. Forester. Dlpoly2.0: A general purpose parallel molecular dynamics simulation package. *Journal of Molecular Graphics*, 14(3):136 – 141, 1996.

[28] Frank A. Momany and Rebecca Rone. Validation of the general purpose quanta 3.2/charmm force field. *Journal of Computational Chemistry*, 13(7):888–900, 1992.

[29] S.R. Brozell D.S. Cerutti T.E. Cheatham III V.W.D. Cruzeiro T.A. Darden R.E. Duke D. Ghoreishi M.K. Gilson H. Gohlke A.W. Goetz D. Greene R Harris N. Homeyer S. Izadi A. Kovalenko T. Kurtzman T.S. Lee S. LeGrand P. Li C. Lin J. Liu T. Luchko R. Luo D.J. Mermelstein K.M. Merz Y. Miao G. Monard C. Nguyen H. Nguyen I. Omelyan A. Onufriev F. Pan R. Qi D.R. Roe A. Roitberg C. Sagui S. Schott-Verdugo J. Shen C.L. Simmerling J. Smith R. Salomon-Ferrer J. Swails R.C. Walker J. Wang H. Wei R.M. Wolf X. Wu L. Xiao D.M. York D.A. Case, I.Y. Ben-Shalom and P.A. Kollman. Amber 2018. *University of California, San Francisco*, 2018.

[30] W. F. van Gunsteren and H. J. C. Berendsen. Algorithms for macromolecular dynamics and constraint dynamics. *Molecular Physics*, 34(5):1311–1327, 1977.

[31] William L. Jorgensen, David S. Maxwell, and Julian Tirado-Rives. Development and testing of the opls all-atom force field on conformational energetics and properties of organic liquids. *Journal of the American Chemical Society*, 118(45):11225–11236, 1996.

[32] Junmei Wang, Romain M. Wolf, James W. Caldwell, Peter A. Kollman, and David A. Case. Development and testing of a general amber force field. *Journal of Computational Chemistry*, 25(9):1157–1174, 2004.

[33] H. Sun. Compass:Äâ an ab initio force-field optimized for condensed-phase applicationsoverview with details on alkane and benzene compounds. *The Journal of Physical Chemistry B*, 102(38):7338–7364, 1998.

[34] Brodka A. Properties of liquid acetone in silica pores: molecular dynamics simulation. *J Chem Phys*, 104:6319, 1996.

[35] Abascal JLF. A general purpose model for the condensed phases of water: Tip4p/2005. *J Chem Phys*, 123:234505, 2005.

Chapter 3

Micro-structure, micro-heterogeneity and non-ideality of associated liquids

Contents

3.1 Introduction and objectives

The hydrogen bond (HB), which is ubiquitous in self-assembly sciences including chemistry, biology, and physics, has been the subject of extensive investigation in the last 100 years. Among the HB former liquids, many works have been devoted on water to connect the structure with the macroscopic properties [6,9] and more especially its physical anomalies [10]. Alcohols are a class of HB liquids such that the molecules form the HB from their hydroxyl group (OH), whereas their hydrophobic moiety provides them an amphiphilic character [1–3]. Regarding the primary alcohols, HB leads to a chainlike structure which is less cohesive than the three-dimensional HB network of water, whereas the hydrophobic group is at the origin of the micellar structure (the molecular emulsion). This amphiphilic behavior leads to the structural heterogeneities at the nanoscale although the homogeneity and the full mixing are at the macroscopic scale. To microscopically characterize this heterogeneity and this microstructure, extensive experiments and simulations have been performed. The most studied alcohols are probably methanol and ethanol given their fascinating aqueous microscopic structure and their numerous applications. Usually, the heterogeneity of these two alcohols was examined by progressively diluting the HB network by using water and to a lesser extent from an aprotic or organic solvent [4, 5]. Indeed, the amphiphilic nature of the alcohols thereby solubilizes a large range of organic solvents that increases the heterogeneity and involves a strong deviation of thermodynamic properties from the ideal mixture behavior [5]. From the hexane-ethanol binary liquid mixture, Perera et al. have recently shown that the hydrogen-bonded structure persisted and induced a subsequent local segregation of ethanol [4] which allowed them to investigate the differences between clustering and heterogeneity [4] and structurally evidenced the heterogeneity from a prepeak in the structure factor. The presence of clusters then will be disconnected to the prepeak and to the heterogeneity. More recently the concept of "simple disorder" was defined if the excess quantities are always smoothly varying functions of molar fraction, whereas the notion of "complex disorder" was connected to the local heterogeneity or molecular emulsion evidenced by sharp changes occurring in the excess quantities with change of sign. Actually, these recent concepts could be used to microscopically understand the nonideality of binary mixtures.

Alcohols are amongst the simplest of all organic molecules that undergo a conventional hydro-

gen bond [6]. They are known as self-associated liquids [7]. In mixture with hydrocarbons, they exhibit physical changes which is strongly attributed to their bifunctional nature [8–11]. Undoubtedly, the alcohol-hydrocarbon mixtures are extremely affected by the HB network created by the alcohol molecules [12]. Predicting the physical properties of entire binary mixture from the one of pure liquids is impossible due to the non-ideality. This is owing to the complicated ordering of liquids in the presence of polar and non polar media.

The determination of the correlation between structural characteristics of binary organic mixtures and the excess thermodynamic properties were the focus of many theoretical and experimental works. Furthermore, several authors attempted to relate experimentally the local micro-structure of various organic binary liquids to the intensity of the intermolecular interactions [13–15]. Well, despite advances in experimental techniques, it remains difficult to provide more information on these micro-structures inducing local inhomogeneities in the atomic level. This local heterogeneity creates deviations from the ideal behavior of binary mixtures. If these micro-structures are evidenced by experimental measurements, their originalities are not well explained and it remains evident that improvements can still be made on the understanding of the structure of these liquids. This thesis helps to understand self-assemblies of associated liquids and their effects on the macroscopic properties. We consider then alcohols, given their identity covering a wide range of applications and their ability to self-organize. Notably, these systems are characterized by their highly directional interactions which tend to strongly associate the molecules. In our case, the non ideality behavior and local structure were explored from two types of mixtures. The first one is the TOL-alcohol system. This choice is mainly based on the ability of toluene molecules to create strong interactions with alcohol molecules as showed in our recent paper [16]. So, it so important to investigate our earlier findings for more alcohols liquids. The second system is composed of CHX-alcohol. Interestingly, CHX molecules can create weak interactions, as dispersion forces, with alcohols and it also miscible at whole range concentrations as TOL liquid.

In this context, this thesis aims to investigate these two perspectives by studying various liquids from molecular simulation. We performed equilibrium molecular dynamics simulations of Ethanol (EtOH), Propanol (PrOH), Butanol (BuOH), Pentanol (PeOH), Toluene, Cyclohexane

and their mixtures visiting the all-regions concentrations. Fundamentally these systems were studied in order to explore the effect of the dilution of the hydrogen bonding network by an apolar solvent. To achieve this goal, toluene (TOL) and cyclohexane (CHX) were used given their apolar character. Furthermore, these two apolar solvents were mixed with five types of alcohols in order to examine the carbon chain length effect on the hydrogen bond network of these alcohols.

3.2 Simulation validation

3.2.1 Methanol mixtures

We report in Figure 3.1 (a) the density of the liquid phase as a function of x_{MeOH} for both mixtures. In two cases the so-calculated densities are found in fair agreement with the experiments [11, 17] that validates the so-used models to describe MeOH, CHX and TOL molecules and their combining interactions. Experimentally, CHX/MeOH mixture is well known to demix between x_{MeOH}=0.2 and x_{MeOH} =0.8. This tendency to segregate is highlighted in Figure 3.1 (c) where snapshots of CHX/MeOH at x_{MeOH}=0.1, 0.5 and 0.9 are reported. As shown in Figure 3.1 (c) the phase separation is well recovered at x_{MeOH}=0.5 whereas at x_{MeOH}=0.1 and 0.9 the systems are miscible. This result is in good agreement with the experimental immiscible region (Figure 3.1 a) that allows us to make confident to the so-used OPLS force field. Moreover, as evidenced in Figure 3.1 (a) the so-calculated densities with higher systems (4000 molecules) are found in good concordance with simulations of 500 molecules that involves a small impact of size effects what bears out our computational procedure. The mechanical equilibrium of MD simulations of 500 molecules was checked by calculating the profile of the total pressure according to z direction. Given the isotropy of our system, the profiles according to three x, y and z directions were found similar.

We report in Figure 3.2 (a) the profile of the total microscopic pressure along the z direction for the CHX/MeOH for three methanol molar fractions, x_{MeOH}=0.1, 0.5 and 0.9. Let us mention that the so-calculated microscopic pressure was averaged on all configurations. Macroscopic pressure fluctuations that are on an order of hundreds of bar are typical. From the local pressure

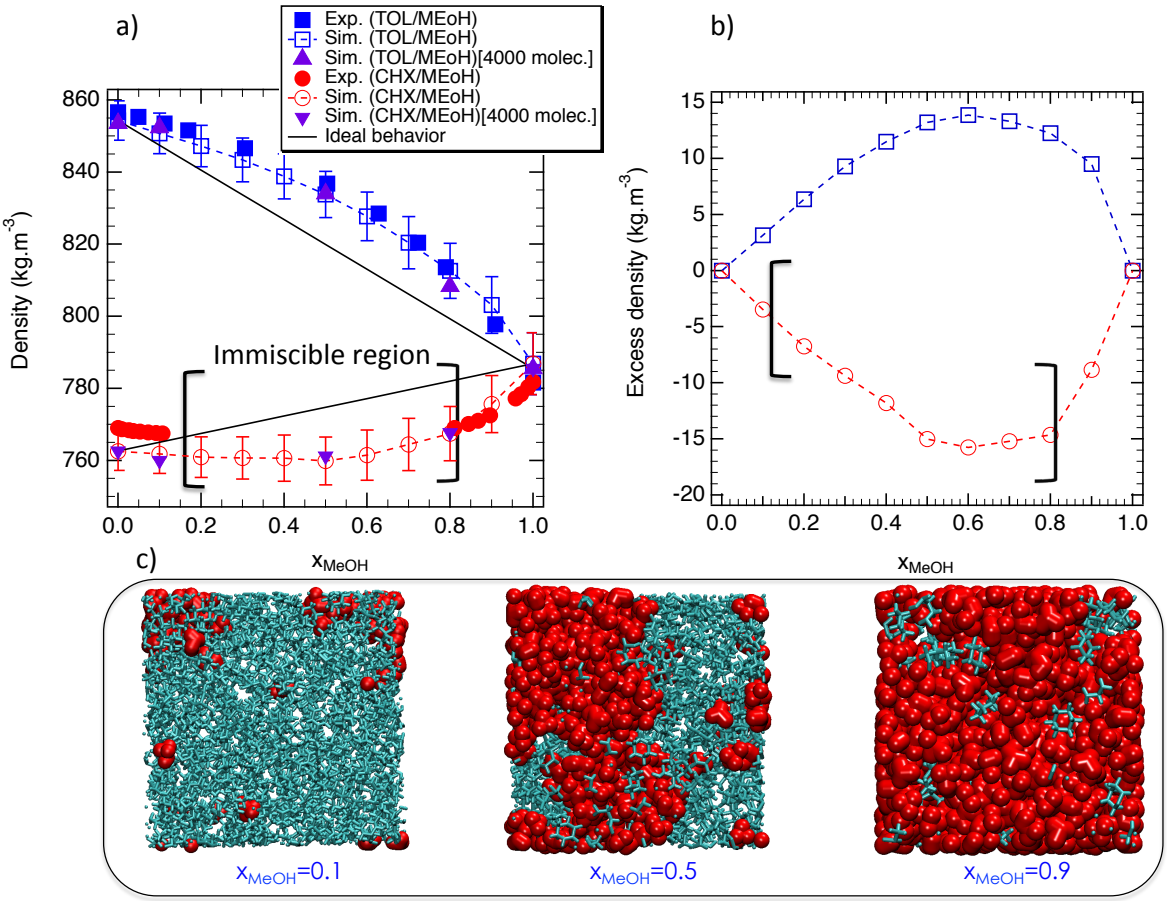

Figure 3.1: Simulated and experimental density (a) and the excess density (b) of the CHX-MeOH and TOL-MeOH mixtures as a function of x_{MeOH} at 300 K and 1 bar. The uncertainties about the density are too small to be represented. (c) Snapshots of binary mixture at x_{MeOH} = 0.1, 0.5, and 0.9 such that methanol is represented in red, and CHX is represented in cyan.

calculation, a deviation of 30-50 bar was obtained that is considered as correct in MD simulations. Indeed, the pressure is a macroscopic property and can be measured properly only as a time average. As shown in Fig. 3.2 (a) the pressure is constant along the z direction, highlighting that the mechanical equilibrium is well reached. As exhibited in Fig. 3.2 (a) the pressure oscillations are the same order of magnitude as that for the calculated pressure for the water reference system and that for the profile pressures reported in the literature [18]. The pressure profile was also calculated for x_{MeOH} = 0.5 for a system of 4000 molecules. As highlighted in Fig. 3.2 (a) the pressure profile is in good concordance with the calculated pressure for the system of 500 molecules, which suggests that the studied systems of 500 molecules are physically relevant

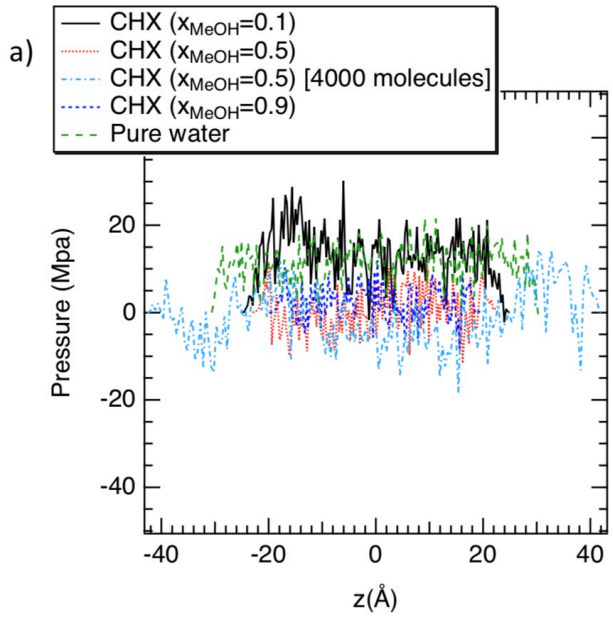

Figure 3.2: a) Profiles of the total pressure along the z direction for three methanol concentrations of CHX/MeOH mixtures and for water at 1bar and 300K.

to capture the microscopic insights into both binary mixtures. Interestingly, Fig. 3.2 (a) shows that at $x_{MeOH} = 0.5$, i.e., for the demixing system, the pressure profile is constant, highlighting the mechanical pressure [18–21] through the interface between methanol and cyclohexane.

3.2.2 Ethanol to pentanol mixtures

Unlike the mixture of methanol with CHX, the EtOH PrOH, BuOH and PeOH are fully miscible in CHX and in TOL [10, 11, 22, 23]. Figure 3.3 shows us the evolution of the simulated densities as a function of the alcohol concentrations. The uncertainties about the density are too small to be represented. Figures 3.3 a-d) shows a good agreement with experimental results for all mixtures [10, 11, 22, 23]. The so-used OPLS-AA force field is then validated also for Ethanol, Propanol, Butanol and Pentanol molecules. It means that our numerical results it produce the real behavior of these liquids and conclusion can be drawn correctly.

3.2.3 *Tert*-butanol mixtures

The variation in density mixture of TOL/TBA and CHX/TBA binary liquids as a function of x_{TBA} that is obtained at 300K and 1 bar was plotted in Fig. 3.4. The TOL and CHX molecules

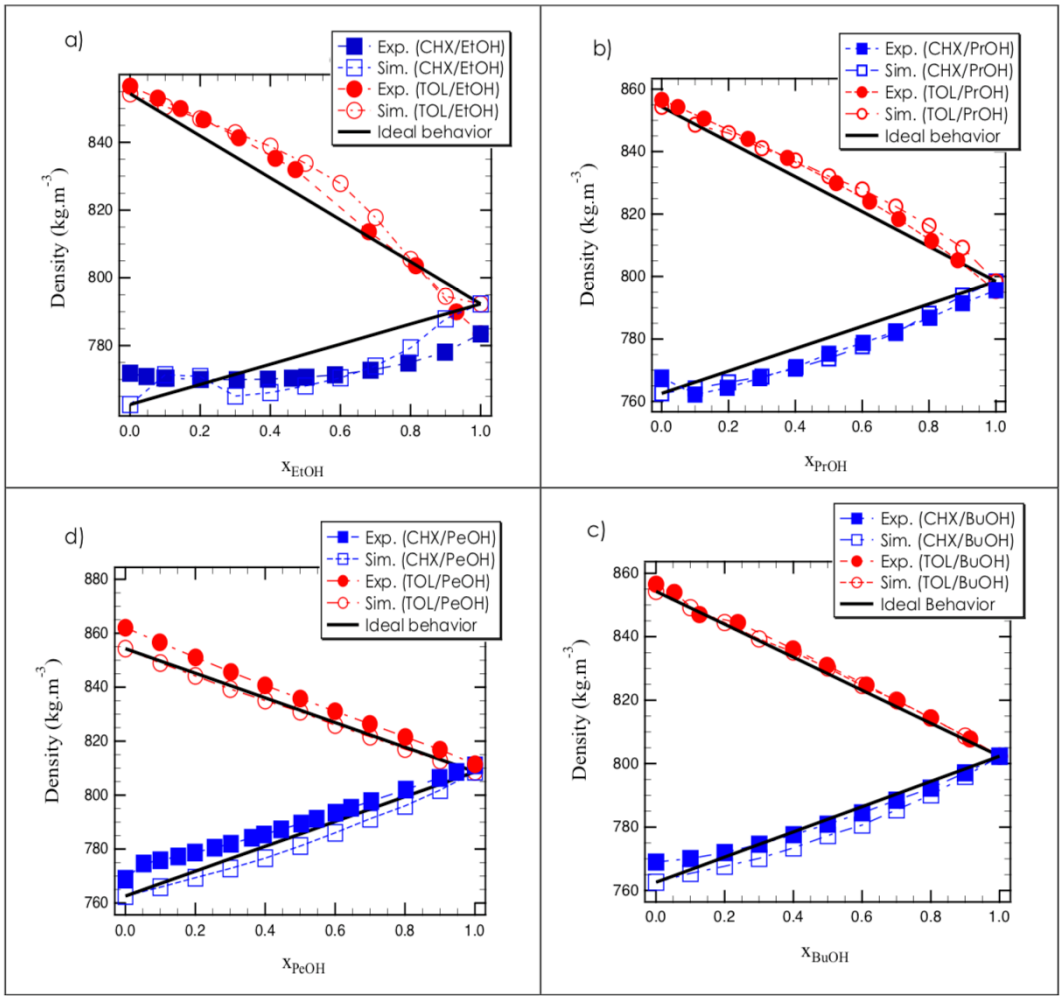

Figure 3.3: Simulated and experimental densities of a) TOL/EtOH + CHX/EtOH, b) TOL/PrOH + CHX/PrOH and c) TOL/BuOH + CHX/BuOH and d) TOL/PeOH + CHX/PeOH as a function of $x_{Alcohol}$ at 300K and 1 bar.

are miscible with TBA at each concentration. The miscibility trend observed in Fig. 3.4 is in good agreement with experimental observations [11, 24]. The so-use force field provides thus miscibility in fair agreement with experiments. Indeed, the simulated density is larger than the experimental value in both systems with a maximum difference of 9% which is considered as correct.

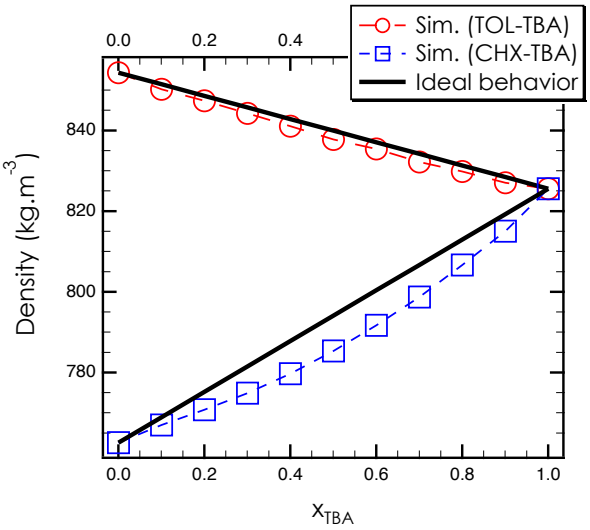

Figure 3.4: Simulated density of TOL/TBA and CHX/TBA as a function of x_{TBA} at 300K and 1 bar.

3.3 Non-ideality and structural heterogeneity

3.3.1 Non-ideality

1) Methanol-cyclohexane and methanol-toluene

As exhibited in Figure 3.1 (a), the density of the TOL/MeOH mixture presents a monotonic evolution as a function of x_{MeOH} whereas the CHX/MeOH mixture shows a minimum around x_{MeOH}=0.5. Additionally, both mixtures present a deviation of same order of magnitude in relation to the ideal density. Very interestingly, the CHX/MeOH mixture also presents a non-ideal behavior in the miscible regions (x_{MeOH}=0.1; 0.9). To quantify this non-ideality, we report in Figure 3.1 (b) the excess density of the mixtures as a function of x_{MeOH}. The excess density was evaluated as the difference between the simulated and the ideal densities. As exhibited in Figure 3.1 (b) the CHX/MeOH and the TOL/MeOH mixtures display a negative and a positive excess density, respectively. Moreover, Figure 3.1 (b) shows that both TOL/MeOH and CHX/MeOH mixtures present a change in monotony of the excess density. Furthermore, in the two miscible and immiscible zones the non-ideality of CHX/MeOH mixture (absolute value of the excess density) is higher than the TOL/MeOH one. These behaviors could be imputed to a change in the structural topology [25, 26] leading to a structural heterogeneity or a difference in

the interactions between both components of the binary liquid mixture [27]. Actually, contrary to the miscible zone, in the immiscible region of the CHX/MeOH mixture the difference is due to the phase separation.

2) Ethanol to pentanol-cyclohexane and ethanol to pentanol-toluene

As shown in Fig. 3.3 (a), the calculated density of TOL/EtOH binary mixture exceeds the value of the ideal density. For concentrations from 0.1 to 0.8 and when the ethanol concentration reached 0.9, a decrease in density is observed in comparison with the ideal density. interestingly, an increase in density is observed when $x_{EtOH} < 0.6$ while from x_{EtOH}=0.6 the density reaches its maximum and begins to decrease gradually. However, the density of CHX/EtOH mixture exceeds the ideal density at x_{EtOH}=[0.1,0.2] and from x_{EtOH}=0.3 the density begins to decrease. As observed from Fig. 3.3 (a), the TOL/EtOH and CHX/EtOH mixtures are presenting strong deviation from ideality behavior.

In Figure 3.3 (b) we report the density behavior of TOL/PrOH and CHX/PrOH binary systems as a function of x_{PrOH}. Both mixtures present a non-ideality behavior at the whole range concentrations, although the intensity of the observed deviation differs from one mixture to the other. For TOL/PrOH mixtures, there is a small increase in density relative to ideality by varying the propanol concentration from 0.1 to 0.5. Beyond x_{PrOH}=0.5, the density begins to decrease slightly. For CHX-PrOH system, a monotonic deviation is observed. From Figure 3.3 (c), the simulated densities of TOL/BuOH and CHX/BuOH mixtures are close to the ideality. Both of these two systems are weakly non-ideal. In Figure 3.3 (d), the variation of the density in TOL-PeOH mixture is practically ideal with a slight decrease compared to the ideal density at x_{PeOH}=[0.2, 0.4]. The so-calculated densities in CHX/PeOH systems are not very far from the ideal behavior. The same trend is also observed for the simulated densities with a parabolic shape around ideality.

In order to measure the magnitude deviation of binary mixtures, we represent in Figures 3.5 the excess densities of TOL/EtOH and CHX/EtOH, TOL/PrOH and CHX/PrOH, TOL/BuOH and CHX/BuOH and TOL/PeOH and CHX/PeOH. Figs. 3.5 (a) to (d) show that the excess densities are positive on all range composition for TOL/EtOH (with the exception of x_{EtOH}=0.9,

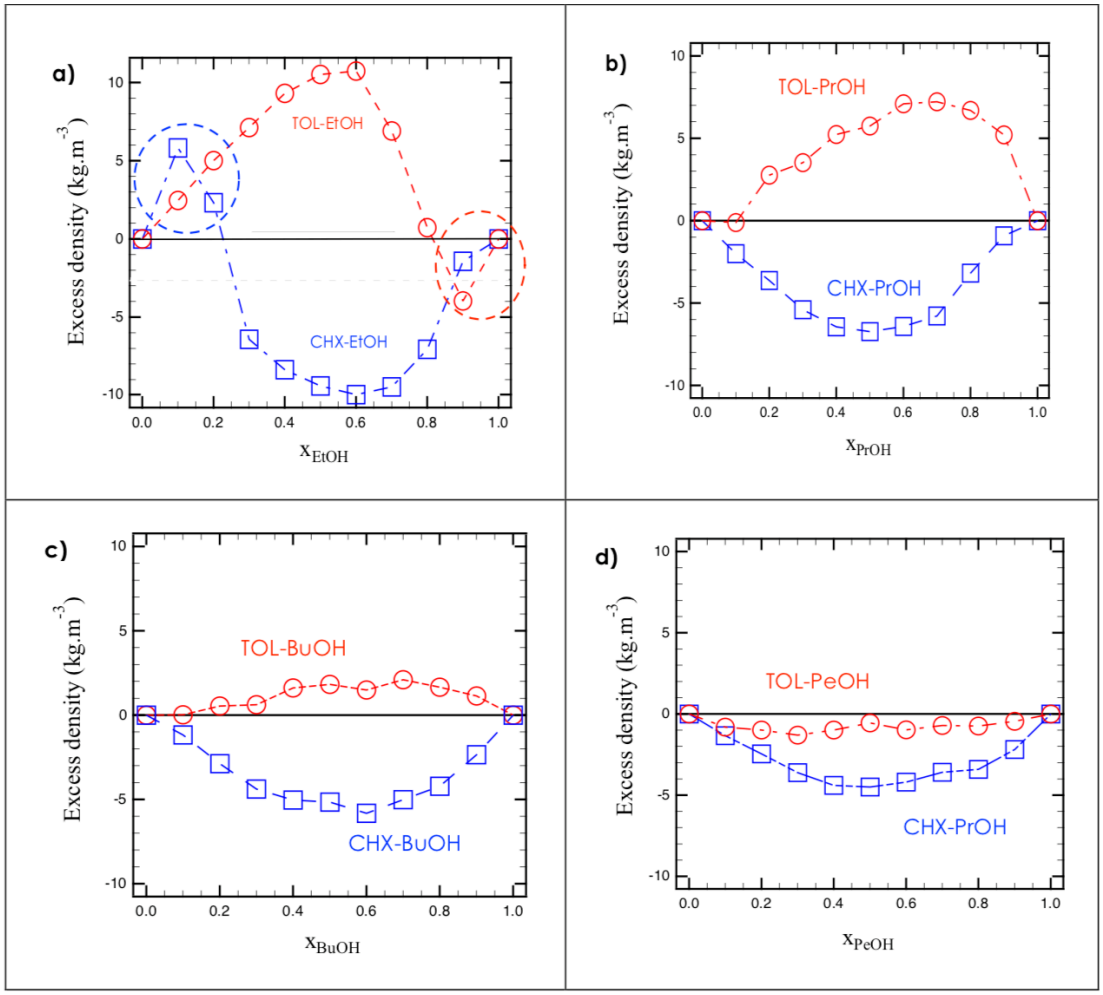

Figure 3.5: The excess densities of a) TOL/EtOH + CHX/EtOH, b) TOL/PrOH + CHX/PrOH and c) TOL/BuOH + CHX/BuOH and d) TOL/PeOH + CHX/PeOH as a function of $x_{Alcohol}$ at 300K and 1 bar.

where a negative deviation is evidenced), for TOL/PrOH and TOL/BuOH are positive. While in Figs. 3.5 (b) to (d), CHX/PrOH, CHX/BuOH and CHX/PeOH mixtures, negative values are shown. The CHX/EtOH excess densities are shown in Fig. 3.5 (a). Interestingly, below x_{EtOH}=0.3, the excess density are positive, while above x_{EtOH}=0.3, the excess density begins to exhibit negative deviations. The minima and maxima observed in Figures 3.5 (a)-(d) will be discussed later.

For solutions with toluene, such behavior suggests that alcohols form complexes with toluene, i.e toluene molecules probably create strong interactions with alcohol ones, leading to breaking of structuring HB framework created by alcohols molecules. Contrary to positive deviation,

a negative excess density can be attributed to the predominance of the dispersion forces and dipolar dissociation over the specific interactions on CHX-Alcohols mixtures [28, 29]. From thereon, In this case, the mixture will probably produce segregation in the local organisation of hydrophobic sites and hydrogen bonds. This means that the deviations are probably ascribable to the inefficient packing in the mixtures of these components as a result of their incompatible structures.

3) TBA-CHX and TBA-TOL

As mentioned previously, the evolution of TOL/TBA and CHX/TBA density as a function of the concentration (x_{TBA}) is given by Fig 3.4. The density mixture of TOL/TBA is close to the ideal behavior while the density of CHX/TBA is not (see Fig. 3.4). The difference between ideal density and real density behavior of CHX/TBA and TOL/TBA are reported in Figure 3.6. These excess densities are in close agreement with experimental data which confirms our OPLS-AA force field used to describe the molecular systems [11, 24]. Fig. 3.6 shows that excess density is negative at whole range concentrations. It is interesting to note that the absolute value of the excess density differs in the two mixtures (|Excess density| (CHX/TBA) > |Excess density| (TOL/TBA)). This significant deviation from ideality could be attributed to the topological structure of TOL molecules and CHX molecules. As previously mentioned

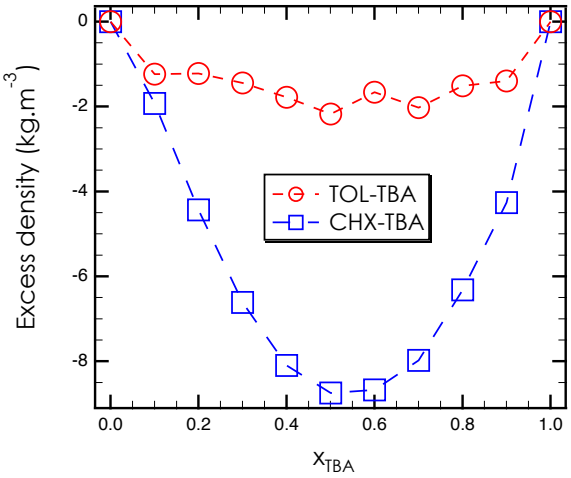

Figure 3.6: Excess density of TOL/TBA and CHX/TBA mixtures as a function of x_{TBA} at 300K and 1 bar.

toluene molecule allow π interaction from delocalized electrons contrary to the cyclohexane. Probably, the combination effect between π interaction and the structure of TBA molecules (auto-aggregator) may be responsible for these variations in non-ideality. It is interesting to mention that TBA molecules are known as auto-aggregating molecules. According to the study of Dixit et al. [30], TBA/Water mixture at a small concentration in TBA exhibits structural agglomeration, which causes anomalous behavior of physical properties. In our study, water is replaced by non polar solvents, leading to the absence of TBA-water hydrogen bonds. The differences in deviation highlighted from the negative excess density is may be caused by the specific microstructure due to the presence of clusters (i.e. self-assembly of molecules in finite groups).

4) Discussion

The non-ideality for both systems TOL/alcohols and CHX/alcohols was already found to be a result of a micro-structuring (Evans and Franck 1945 and Dixit et al. 2002; Guo et al 2003 [30–32]). It is now well established that the thermodynamics anomalous behavior of aqueous alcohol solutions are resulted from structural changes [30–32]. Indeed, Franck and Evans attempt to relate the non ideality behavior to the existence of structured water molecules surrounding non polar solutes, while Dixit et al. and Guo et al. explained the incomplete mixing behavior as a result of demixing of water and non polar moieties. Additionally, Soper et al. suggested a clustering model to explain non ideality deviation of water-alcohol solutions [33]. This clustering model is based in the molecular segregation. According to earlier study by Ness and Fletcher, for mixtures of alcohols with non-polar solvents, the anomalous behavior in the thermodynamic properties are typically related to two structural effects [34, 35]. First one is the association of alcohol molecules through their hydrogen bonds and the second one is about the formation of complexes between alcohol and solvent non polar molecules.

In order to explore the structure of the so-studied binary liquids, we examined the microscopic structure of each component in the mixture and investigated the local heterogeneities between the different molecules that can be caused by clustering mechanisms. Indeed, the non-ideality is correlated with the microscopic local structure of the liquids constituting a mixture likely leading

to spatial heterogeneities that are probably responsible for such macroscopic behavior.

3.3.2 Structural heterogeneity

1) Methanol-cyclohexane and methanol-toluene

Interestingly, as illustrated in Figure 3.7 for CHX/MeOH mixture, it seems that the immiscibility at low methanol concentration is due to the formation of the methanol pocket assimilated to a nucleation process leading to the formation of nanophases rich in methanol molecules such that the OH groups will be hidden from the organic solvent given of the lack of favorable interactions. The progressive formation of nanophases as a function of x_{MeOH} could then generate a structural heterogeneity. At high concentration in methanol of CHX/MeOH mixture (x_{MeOH}=0.8) the miscibility is recovered due to the percolating of the methanol nanophases. Actually, in the miscible region, the progressive formation of these nanophases increases the heterogeneity and could explain the non-ideality of CHX/MeOH mixture. To quantify this spatial heterogeneity, the heterogeneity order parameter (HOP) [36,37] was calculated. The HOP value increases with

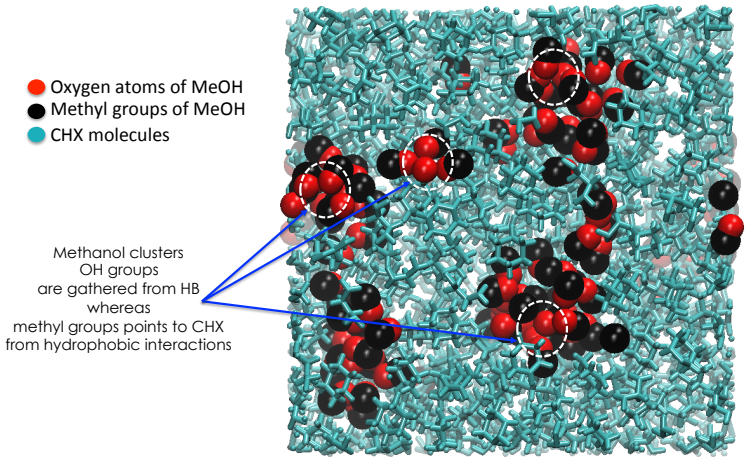

Figure 3.7: Snapshot of the CHX-MeOH mixture at x_{MeOH} = 0.2.

the expansion of the spatial heterogeneity because a tighter packing of sites results in a smaller r_{ij} , which leads to a larger HOP. Calculations were performed for both binary liquid mixtures. According to the study of Wang et al., the HOP of ideal particles homogeneously distributed is lower than 15.74, and a heterogeneous system exhibits a HOP greater than 15.74 [36]. We report in Fig. 3.8 the HOP value of each component as a function of the molar fraction in MeOH. First,

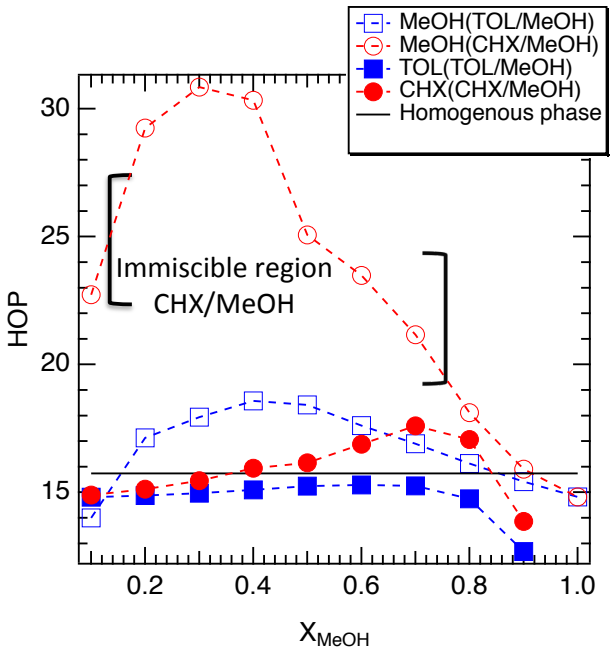

Figure 3.8: HOP as a function of the molar fraction in MeOH for both CHX-MeOH and TOL-MeOH mixtures.

in the pure MeOH liquid, the HOP is smaller than 15.74 highlighting the absence of spatial heterogeneity. Furthermore, as shown in Fig. 3.8, the addition of TOL or CHX molecules in the MeOH liquid generates spatial heterogeneity. In the miscible zone of the CHX-MeOH mixture, the HOP of methanol is higher than that in the TOL-MeOH mixture. As underlined in Fig. 3.7, that is the result of the formation of nanophases of methanol preceding the phase separation. The nonideality behavior of the CHX-MeOH mixture therefore can be then imputed to the strong heterogeneity in the miscible phase. That is probably the result of a lack of favorable interactions between CHX and MeOH. Contrary to the CHX-MeOH mixture, MeOH in TOL-MeOH shows a smaller HOP. Indeed, at $x_{MeOH} = 0.1$ HOP of MeOH is around 14 and 23 in TOL-MeOH and CHX-MeOH mixtures, respectively. In the case of the TOL-MeOH mixture, the HOP increases as a function of x_{MeOH} and is greater than 15.74 highlighting a microstructure. Let us mention that the microstructure is assimilated to the presence of the heterogeneities, and both terms will be subsequently used interchangeably. Whereas the spatial heterogeneity in the CHX-MeOH mixtures is the result of the local segregation and its propagation to strive for a total demixing, the molecular origin of the microstructure in the TOL-MeOH mixtures is then

yet to be determined. Interestingly, Fig. 3.8 highlights that the HOP of CHX and TOL (close to 15) is lower than the HOP of MeOH, which suggests a more homogenous distribution of the aprotic component in the mixtures.

2) Ethanol to Pentanol-Cyclohexane and Ethanol to Pentanol-Toluene

i) Instantaneous configuration observation

Figure 3.9 and 3.10 describe the molecular arrangement of CHX/alcohols and TOL/alcohols binary mixtures at $x_{alcohol}$=[0.1,0.3,0.5]. From Figure 3.10, strong local arrangement was observed for CHX molecules in presence of Ethanol. The local arrangement is defined as the agglomeration of the same type of molecule in the mixture. In the CHX/EtOH mixtures, the high excess density showed in Fig. 3.5 (a) could be explained from these specific agglomerations. Figures 3.9 depicts that CHX and EtOH molecules do not mix very well and the presence of irregular organization in the mixture was captured. Concerning the TOL/EtOH (Figure 3.9) mixture a homogeneous mixture was evidenced with less irregularities as a function of concentration. As shown in Figure 3.9 EtOH and TOL form nanophases which are smaller than those of the CHX/EtOH system. Indeed, the resulting microstructure of both mixtures are different and could be responsible of the non-ideality behavior as we discussed previously. PrOH mixtures (Figures 3.9 and 3.10) show less structural inhomogeneities in comparison with EtOH ones (this is viewed by the way that (TOL,CHX) and (EtOH, PrOH) molecules are packed together). The associated tendency of PrOH molecules are favored in presence of CHX molecules rather than TOL which leads to a formation of largest cluster in CHX/PrOH mixture. This suggests that in the case of TOL/PrOH, more molecules highlighted the creation of small clusters. These differences in clustering behavior of both components could be relevant to understand the density deviations observed (Figures 3.3 (b) and 3.5 (b)). The structural arrangement of CHX/BuOH and TOL/BuOH binary mixtures is also provided. In these mixtures, we start to observe the influence of the increase of the alkyl chain on the local structure. Indeed, a specific micro-structure is less observed and small clusters are formed in both mixtures in comparison with EtOH and PrOH ones. Regarding to the BuOH mixture, a good distribution of alcohol molecules in the mixture is observed. In CHX/BuOH mixtures, rich regions of CHX molecules are evidenced, while butanol crosses these

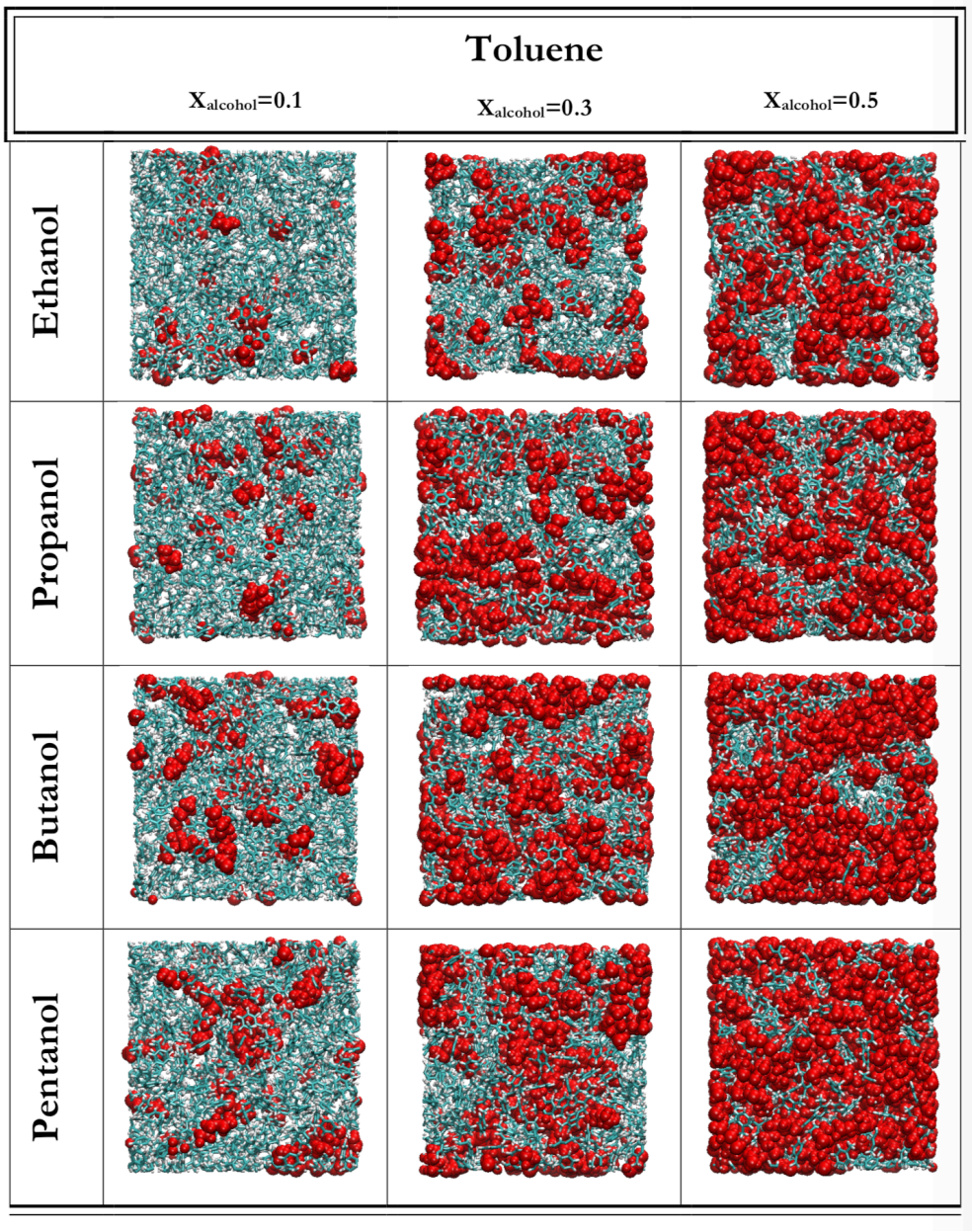

Figure 3.9: Snapshot structure of Ethanol, Propanol, Butanol and Pentanol with Toluene at $x_{Alcohol}$=[0.1,0.3,0.5]. Red and cyan colours describe alcohols and Toluene molecules, respectively.

regions through linear patterns. These regions are not present in TOL/BuOH mixture. Furthermore, the final snapshot configuration of two binary liquids composed of CHX/PeOH and

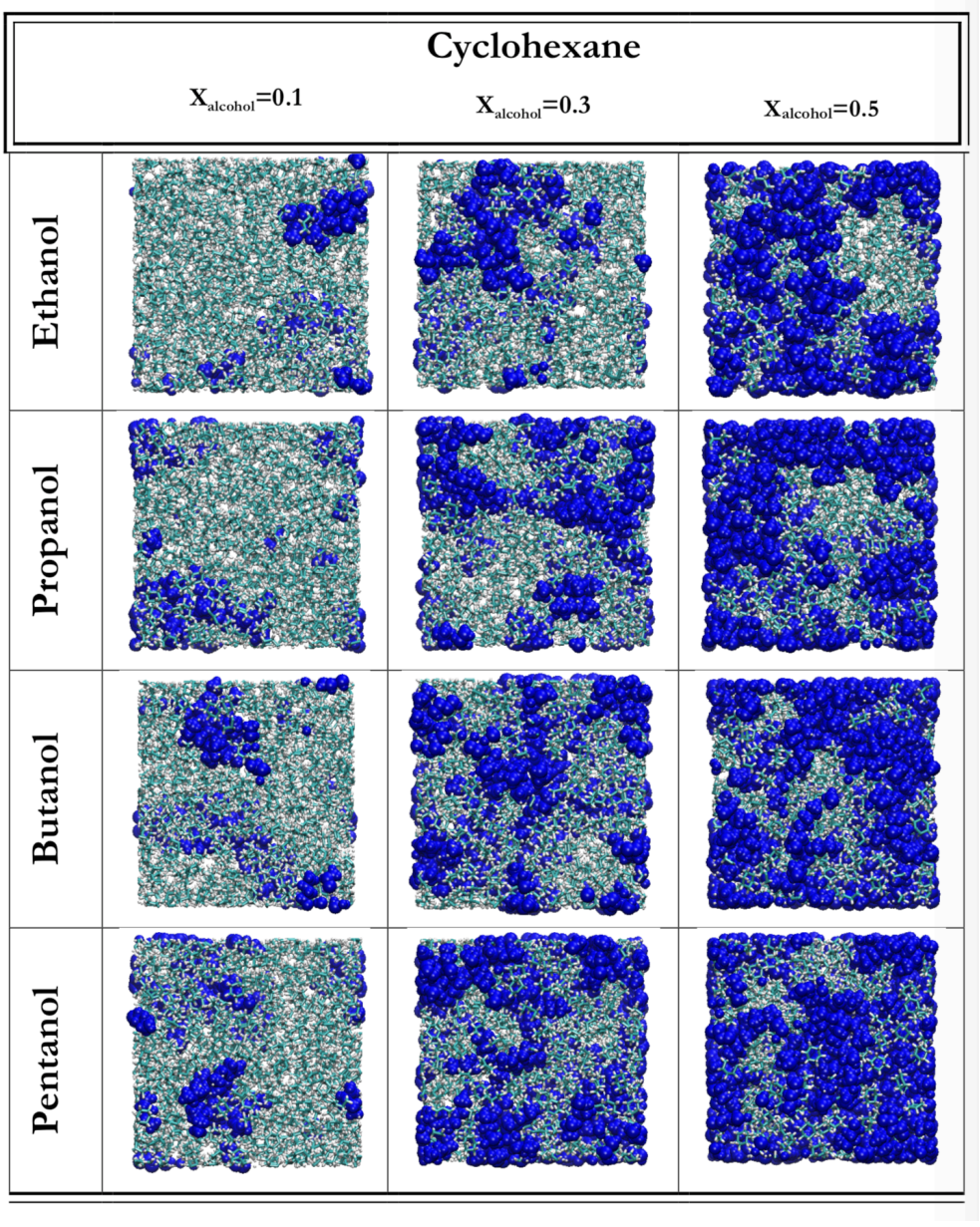

Figure 3.10: Snapshot structure of Ethanol, Propanol, Butanol and Pentanol with Cyclohexane at $x_{Alcohol}$=[0.1,0.3,0.5]. Blue and cyan colours describe alcohols and Cyclohexane molecules, respectively.

TOL/PeOH systems are provided. The resulting structures in both mixtures are similar and present the creation of small agglomerations. As expected, these groups are more extended in

CHX/PeOH mixtures. An interesting order which CHX mixture revealed local agglomeration in comparison with TOL is constantly observed, specific microstructure$_{(CHX/Alcohols)}$ > specific microstructure$_{(TOL/Alcohols)}$. To investigate these observations, we calculated the heterogeneity order parameter (HOP).

ii) Structural heterogeneity characterization

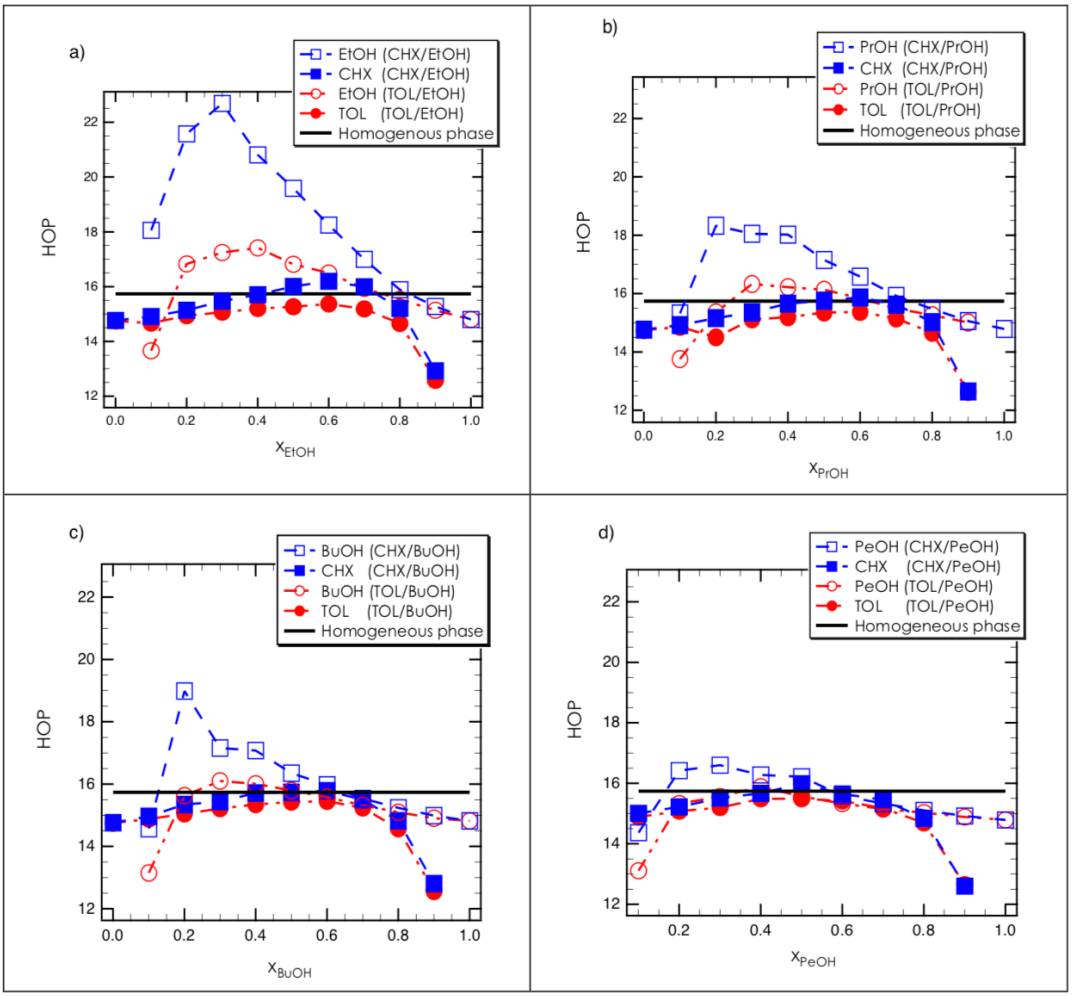

Figure 3.11: Heterogeneity order parameter of binary mixture with toluene and cyclohexane as a function of alcohol concentration: a) for TOL/EtOH + CHX/EtOH, b) for TOL/PrOH + CHX/PrOH, c) for TOL/BuOH + CHX/BuOH and d) for TOL/PEOH + CHX/PeOH.

In order to evaluate these microstructures, the heterogeneity order parameter (HOP) was calculated. We represent in Figure 3.11 (a)-(d) the HOP of all binary mixtures at whole range concentration. First, as it depicted in Fig. 3.11 (a), the HOP of pure EtOH is 14.8 that indicates a

homogeneous liquid; when we add CHX, the EtOH molecules begin to show local inhomogeneities, growing as a function of concentration. These heterogeneities disappear when we approach the ethanol rich-region ($x_{EtOH} = 0.9$), the system begins to structure homogeneously. The maxima of the excess density showed in Figure 3.5 (a) corresponds to a strong heterogeneity (HOP= 18 $>$ 15.74). This result validates our first hypothesis at the origin of the non-ideality behavior. Furthermore, a minimum of the excess density around $x_{EtOH} = 0.$ was previously highlighted. At x_{EtOH}=0.6, both components in the mixture exhibit local heterogeneity because HOP (CHX) = 16.75 and HOP (EtOH) = 18.75 seem to be responsible for the strong deviation from the ideal mixing density. It can be concluded that heterogeneity could conduct such behavior. Second, the addition of TOL to EtOH molecules generates less heterogeneities regardless CHX/EtOH binary liquids. Interestingly, EtOH in TOL is homogeneous at low EtOH concentration (x_{EtOH}=0.1) and in ethanol rich region (for $x_{EtOH} = 0.8$ and 0.9). The HOP of both (CHX ; TOL) molecules are homogeneous in pure and in mixtures with EtOH, except for CHX at $x_{EtOH} = 0.6$ it exhibits small local inhomogeneity as we've mentioned before.

In Figure 3.11 (b), the HOP of pure PrOH is 15 that corresponds to a homogeneous phase. The addition of CHX leads to spatial heterogeneity in PrOH for $0.2 < x_{PrOH} < 0.7$. At these concentrations, the excess density of CHX/PrOH mixture presents such that strong deviation. At low and high alcohol concentrations (x_{PrOH}=0.1 ; 0.8-0.9), the CHX/PrOH mixture approach the ideality behavior, that is in line with the homogeneous organization of PrOH molecules. The heterogeneity leads to then the negative deviation from ideality. Unlike CHX, TOL doesn't affect the homogeneity of PrOH molecules. Indeed, between x_{PrOH} =0.3 and 0.5, PrOH molecules are locally heterogeneous because HOP at $x_{PrOH} = 0.3$ is 16.5 greater than 15.74. On the contrary TOL molecules are homogeneously distributed in the mixture as the same as CHX (except for $x_{PrOH} = 0.6$ where the HOP(CHX)=15.85 $>$ 15.74). The HOP of each molecule in CHX/BuOH and TOL/BuOH mixtures are provided in Figure 3.11 (c). One important point is that BuOH in both mixtures present a heterogeneous at x_{BuOH}=$0.2 - 0.6$. A strong spatial heterogeneity (HOP= 19 $>$ 15.74) is also evidenced for BuOH in mixture with CHX at x_{BuOH}=0.2. It is necessary to remember that the HOP value increases when more sites are closer to each other, resulting in a higher value for more aggregated or clustered organization. Then, the resulting

heterogeneity could then explain the difference in non-ideality behavior of CHX/BuOH and TOL/BuOH mixtures. Negative deviation are attributed to these heterogeneities. Moreover, the both aprotic solvents in the two mixtures are homogeneous.

Figure 3.11 (d) shows the HOP of CHX/PeOH and TOL/PeOH binary mixtures as a function of x_{PeOH}. In the case of pure PeOH, the HOP has a small value of HOP = 14.76 < 15.74 which corresponds to a homogeneous liquid. The HOP of PeOH doesn't change in TOL/PeOH mixture, except at $x_{PeOH} = 0.4$, it becomes heterogeneous. That corroborates the quasi-ideality behavior of the TOL/PeOH mixture at whole range concentration with a minimum excess density at $x_{PeOH} = 0.4$. This minimum could be attributed to this spatial microstructure. On the other hand, the PeOH in PeOH/CHX mixtures shows a strong heterogeneity with the increase of PeOH quantity in the mixture ($x_{PeOH} < 0.6$). Indeed, one may argue that CHX favor the persistence of aggregated PeOH molecules at low alcohol concentrations. These organizations in CHX/PeOH could be responsible for the strong deviations showed in the excess density compared to the TOL/PeOH deviations.

3) TBA-CHX and TBA-TOL

We show in Figure 3.12 the structure of TOL/TBA and CHX/TBA mixtures as a function of three TBA concentrations (x_{TBA}=0.2, x_{TBA}=0.5, x_{TBA}=0.8). At x_{TBA}=0.2, TBA in TOL/TBA mixture show small pockets regularly distributed in the mixture. Figure 3.12 (a) showed the morphology of CHX/TBA molecules at x_{TBA}=0.2. On the contrary, less distributed clusters are found through the CHX/TBA mixture. It seems that there are regions rich in clusters and regions without any pocket of TBA molecules. Fig. 3.12 (b) shows that both mixtures exhibit nanophases of small sizes which they are more extensive in CHX-TBA mixture. Furthermore, the microstructure in TBA rich-region is depicted in Fig. 3.12 (c). These configurations allow us to make difference between large and small nanophases formed in CHX-TBA and TOL-TBA mixtures, respectively. It is interesting to mention that TBA is more aggregated in CHX than in TOL. Then, the formation of these aggregations could explain the ideality behavior showed in Fig 3.6. In order to investigate these structural organization, the HOP parameter was calculated. The Figure 3.13 reports the HOP of CHX-TBA and TOL-TBA binary mixtures. Molecules in

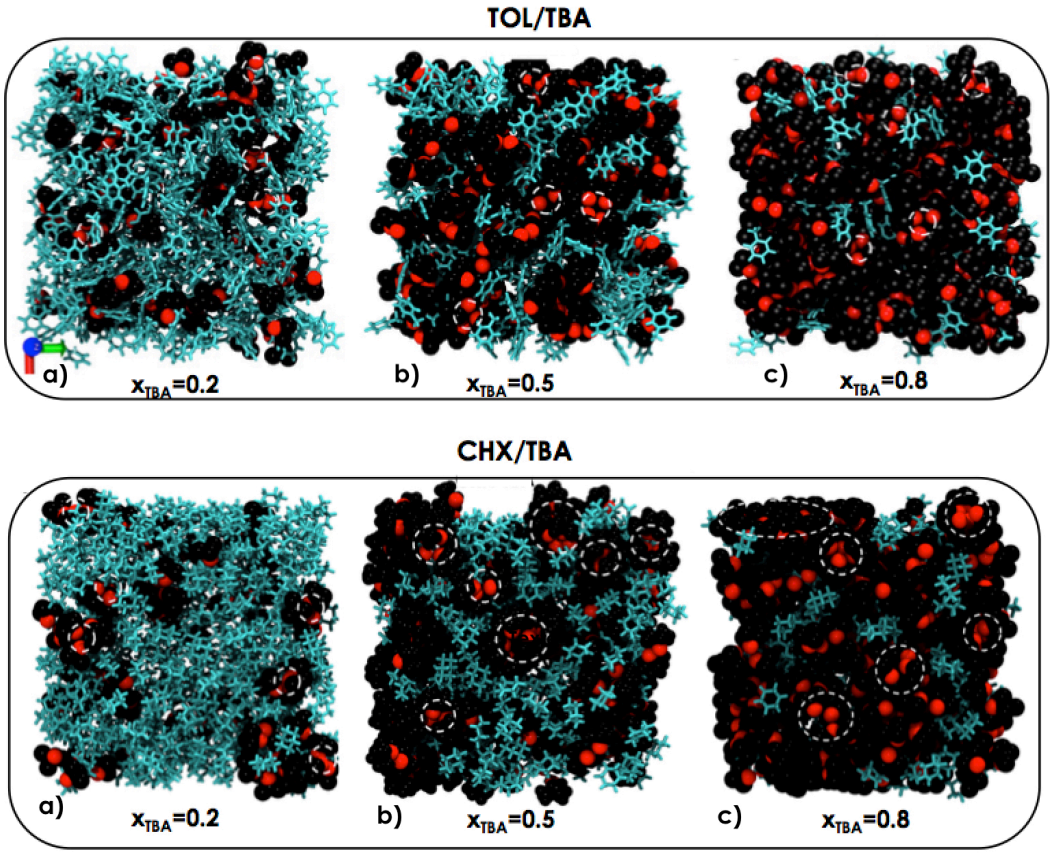

Figure 3.12: Snapshot of the TOL-TBA mixture at a) x_{TBA}=0.2, b) x_{TBA}=0.5 and c) x_{TBA}=0.8 and CHX-TBA mixture at a) x_{TBA}=0.2, b) x_{TBA}=0.5 and c) x_{TBA}=0.8. The same notation of Figure 3.7 is used.

both mixtures are locally distributed homogeneously except for TBA molecules in mixture with TOL at x_{TBA} = 0.3. That is highlighted by the value of the HOP which exceeds the estimated value for homogeneous distributed sites. In this mixture, one can conclude that the non-ideality behavior depicted in Fig. 3.6 is strongly correlated to the formation of these aggregations.

3.4 Molecular interactions

3.4.1 Local structure

1) Methanol mixtures

To unveil the microscopic insights ruling the miscibility and the non-ideal behavior of TOL/MeOH mixture. The radial distribution functions (RDF) between the centres of mass of the aprotic com-

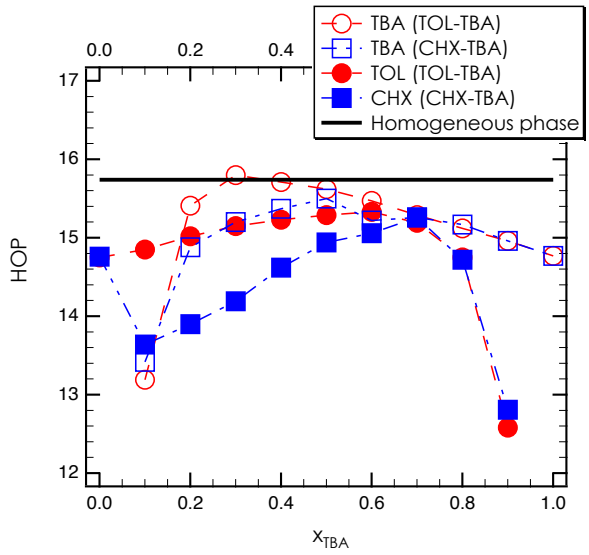

Figure 3.13: HOP as a function of the molar fraction in TBA for both CHX-TBA and TOL-TBA mixtures

ponent (TOL/TOL and CHX/CHX) are reported in Figure 3.14 . As shown in Figure 3.14 (a)

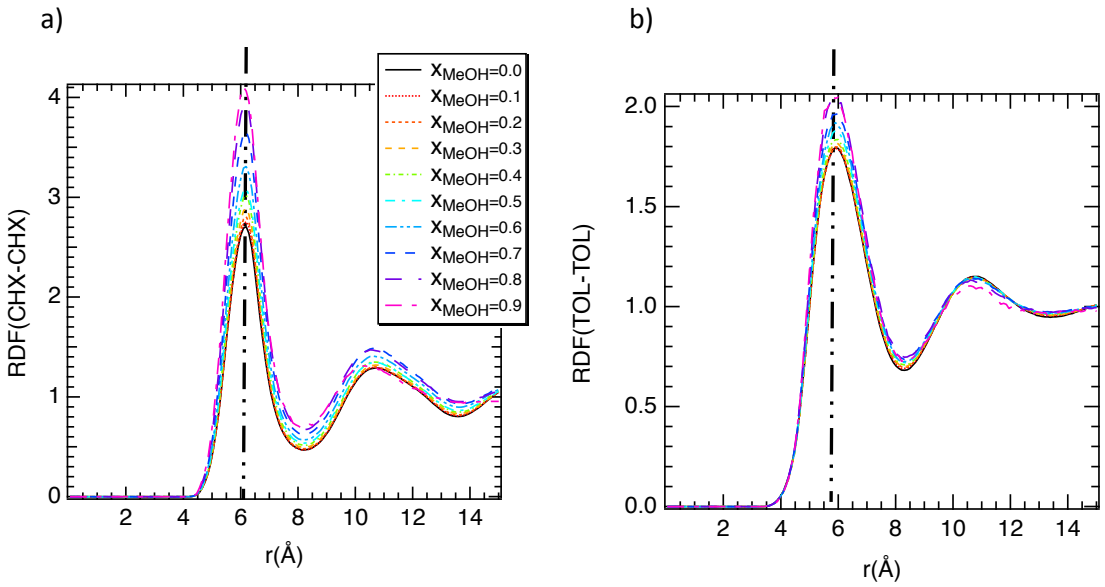

Figure 3.14: Radial distribution functions between centers of mass of the aprotic component for both CHX-MeOH (a) and (b) TOL-MeOH mixtures. The vertical dashed line represents the position of the first peak.

and Figure 3.14 (b) the first peak of RDF(CHX/CHX) and RDF(TOL/TOL) are respectively located at 6.1 Å and 5.9 Å that underlines a stronger interactions between toluene molecules due to the interactions between the aromatic cycles (this point will be discussed later on). Fur-

thermore, as highlighted in Figure 3.14 (a) and Figure 3.14 (b) the amplitudes of the first and second peak in both mixtures increase for the concentrated methanol solutions whereas the shape and the position of the peaks are less sensitive to the dilution. The increase of the peaks intensity involves then a higher local concentration in TOL (or CHX), which stands for that the probability of finding TOL (or CHX) molecule at a distance r from another molecule does not scale with the decrease of the TOL (or CHX) number density, but it actually decays to a smaller extent [2]. That is an obvious evidence of the microstructure and the partial mixing at the molecular scale [2]. In case of the CHX/MeOH mixture, this effect is higher because the increase in RDF intensity as a function of the decrease in x_{MeOH} is more pronounced, suggesting an increase in the spatial heterogeneity in line with the HOP calculations and the miscible regions. Interestingly, this increase in intensity is similar to that observed in nano-confined media where the excluded volume involves an increase in the interfacial concentration of confined fluids [1,38–40] and bears out the presence of nanophases.

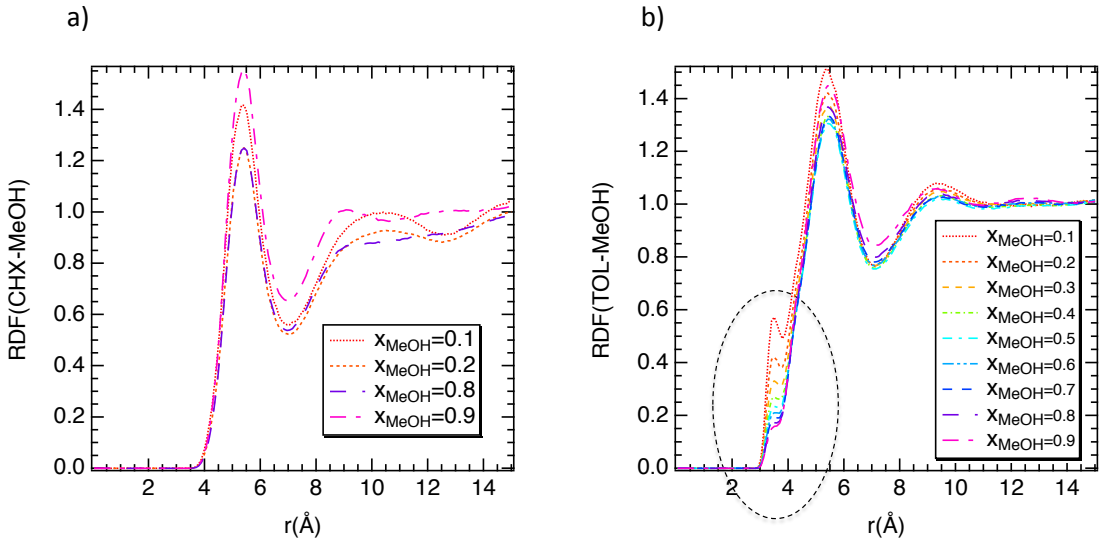

Figure 3.15: Radial distribution functions between centers of mass of aprotic component and methanol for both CHX-MeOH (a) and TOL- MeOH (b) mixtures in the miscible regions. The dashed circles highlights the peaks located around 3.5 Å.

Let us mention that the similar behavior is also observed with the second peak but in a lesser extent. To investigate the interactions between MeOH and TOL(CHX), the radial distribution functions between the centres of mass were calculated in the miscible regions and reported in Figure 3.15. As shown in Figure 3.15 (a) the location of the first peak is found around 6 Å

highlighting a hydrophobic character of the CHX-MeOH interactions and the absence of specific interactions. Additionally, as stated earlier the increase in intensity with the decrease in x_{MeOH} is the result of the heterogeneity and the formation of nanophases. Interestingly, Figure 3.15 (a) reveals a second peak at low concentrations (x_{MeOH} = 0.1 and 0.2) synonymous with favorable interactions which disappears between x_{MeOH} = 0.2 and x_{MeOH} = 0.8 to reappear at x_{MeOH} = 0.9 that is in fair agreement with the gap of miscibility observed in Figure 3.1. Regarding to the TOL/MeOH mixture, Figure 3.15 (b) displays a first peak around 3.5 Å underlining a strong interaction between toluene and methanol molecules. This result sheds light on a preferential interaction between methanol and toluene. To identify it, we report in Figure 3.16 the RDF be-

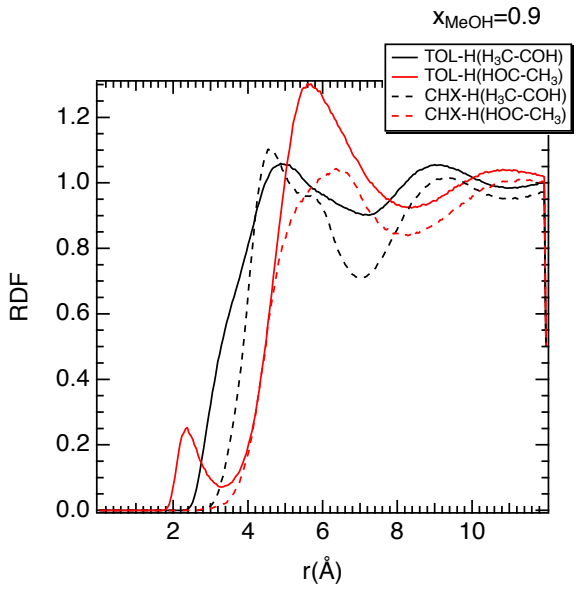

Figure 3.16: Radial distribution functions between the center of mass of the aprotic molecules and the hydrogen atoms of OH (HOC) and CH_3 (H_3C) groups of methanol for x_{MeOH} = 0.9.

tween the centres of mass of the aprotic component and hydrogen atoms of hydroxyl and methyl groups of methanol. Let us mention that the centre of mass of both TOL and CHX molecule is close to the centre of the cycle. Figure 3.16 highlights a strong interactions between OH groups and toluene molecules because distance of 2.5 Å was found that is the same order of magnitude that a hydrogen bond. This result suggests then a hydrogen bond like interaction probably induced by the aromatic cycles. Actually, this strong interaction is probably at the origin of the toluene miscibility in methanol and the positive excess density [27]. In the CHX/MeOH mixtures the CHX molecules self-organize to form hydrophobic nanophases.

2) Ethanol to pentanol mixtures

The most likely reason at the origin of the mismatch between the density of the mixture and the ideal behavior is probably the formation of HB-induced aggregates. To verify this hypothesis, the radial distribution functions (RDFs) of the EtOH, PROH, BuOH, PeOH, TOL and CHX mass centers have been managed. Figure 3.17 presents the RDFs of CHX-CHX and TOL-TOL distances for CHX-EtOH, CHX-PrOH, CHX-BuOH and CHX-PeOH, and TOL-EtOH, TOL-PrOH, TOL-BuOH and TOL-PeOH mixtures at whole range concentrations. For the pure liquids, the RDFs are in good agreement with RDF measured from Neutron scattering [41]. In Fig. 3.17, the CHX-CHX RDF is reported for four binary mixtures. As shown in Fig. 3.17 RDF exhibits a first and a second peak located at a distance of 6.1 Å and 10.8 Å, respectively. The first peak intensity changes from 2.67 to 3.52 for CHX-EtOH, 2.67 to 3.45 for CHX-PrOH, 2.67 to 3.33 for CHX-BuOH and 2.67 to 3.07 for CHX-PeOH, however the peak position remains nearly unaltered. All CHX-CHX RDF peaks are sharps and well-defined. From the concentration dependence of the (CHX-CHX) RDFs, a slight increase in the value of the first peak is reported, which is probably an indication of the space filling of the CHX molecules with the addition of alcohols in the mixture. The second peak that is located at 10.8 Å with a smaller dependence in concentration. The alkyl chain effects of alcohols on cyclohexane are shown by a decrease in the intensity of the first peak value from 3.52 to 3.03, from CHX-EtOH to CHX-PeOH mixtures. That involves the possibility of space filling decreases with an increase in the alkyl chain length of alcohol molecules. For toluene mixtures, the TOL-TOL RDFs displayed in Figure 3.17 show two large peaks. The first and second peak are located at distance of 5.9 Å and at 11.5 Å, respectively. The intensity of the first peak increases very slowly with the addition of alcohols molecules. The alkyl chain effect of alcohols is less marked compared to CHX/CHX mixtures. As previously discussed the location of the first peak of TOL and CHX molecules are indicating a strong interaction of TOL molecules at 5.9 Å rather than that of cyclohexane at 6.1 Å. Figure 3.18 presents the RDFs plots of centre of mass of CHX-Alcohols and TOL-alcohols molecules in all mixtures as a function of alcohol concentration. The Figure 3.18 presents RDFs for CHX-EtOH,

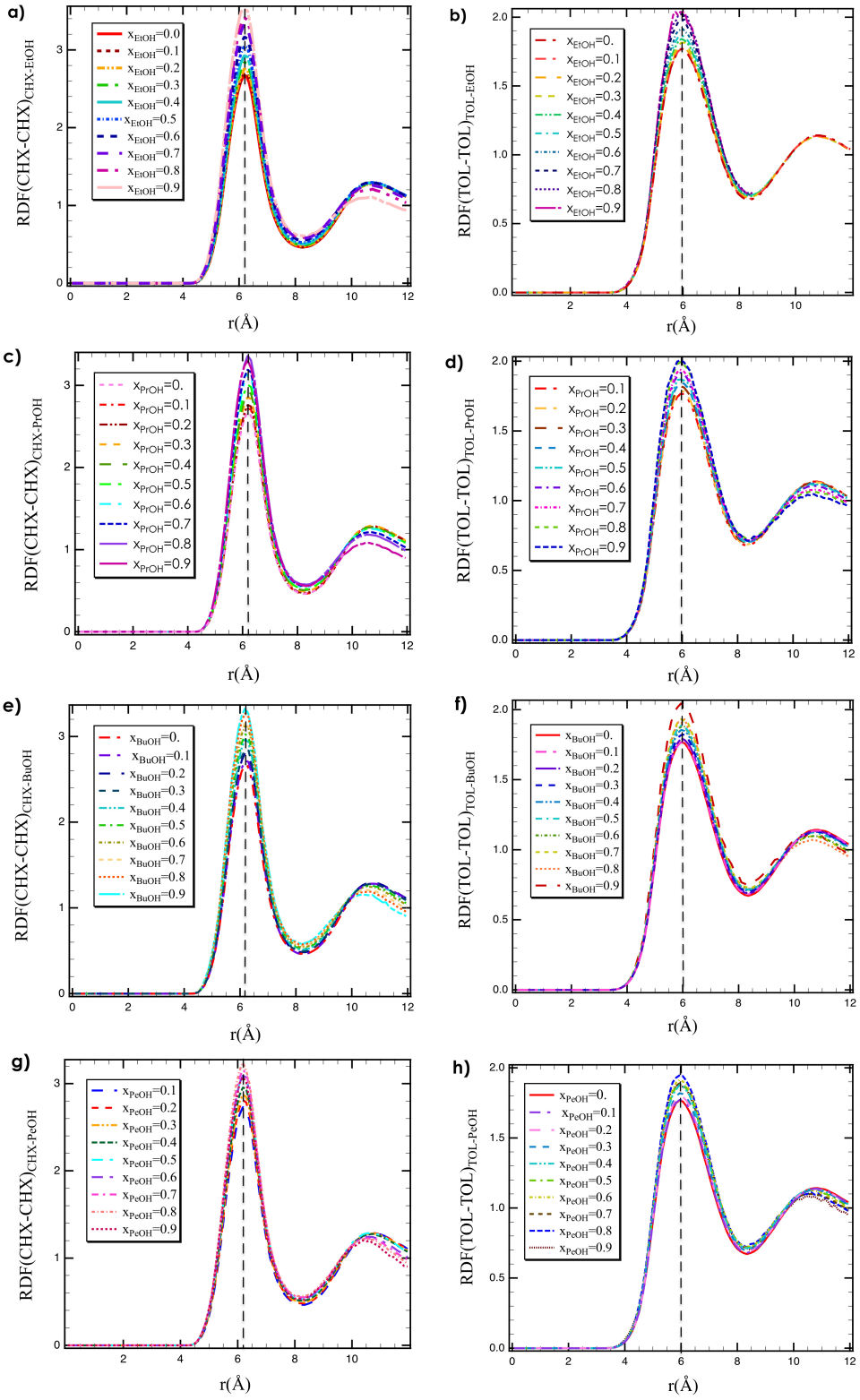

Figure 3.17: Radial distribution functions between centers of mass of the aprotic component for both (a) CHX-EtOH and (b) TOL-EtOH mixtures, (c) CHX-PrOH and (d) TOL-PrOH mixtures, (e) CHX-BuOH and (f) TOL-BuOH mixtures and (a) CHX-PeOH and (b) TOL-PeOH mixtures. The vertical dashed line represents the position of the first peak.

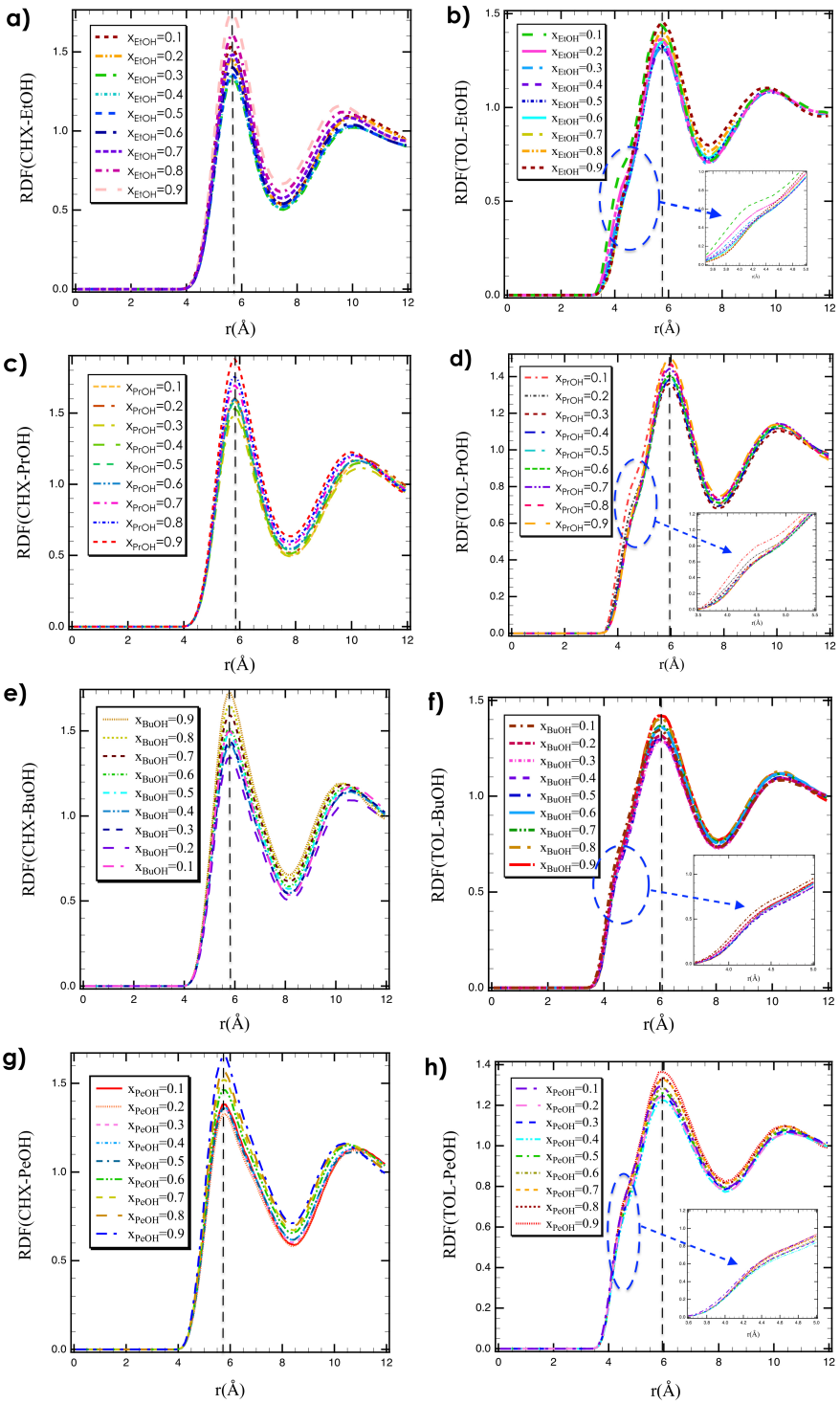

Figure 3.18: Radial distribution functions between centers of mass of the aprotic component and alcohols for (a) CHX-EtOH and (b) TOL-EtOH mixtures, (c) CHX-PrOH and (d) TOL-PrOH mixtures, (e) CHX-BuOH and (f) TOL-BuOH mixtures and (a) CHX-PeOH and (b) TOL-PeOH mixtures. The vertical dashed line represents the position of the first peak and the dashed circles highlights the shoulder position.

CHX-PrOH, CHX-BuOH and CHX-PeOH mixtures, respectively. The first and the second peak are located at a distance of 5.7 Å and at 9.6 Å. The intensity of the first peak increases with the increase of alcohol molecules. Figure 3.18 reports the RDFs of TOL-EtOH, TOL-PrOH, TOL-BuOH and TOL-PeOH as a alcohol mole fraction. Very interestingly, the RDFs between alcohol and TOL revealed two peaks with an evident shoulder in the first peak at short distances about 3.9 Å . This is characteristic of a strong interaction of TOL molecules with alcohol ones. This interaction is absent with CHX, which highlights a difference in the local structure of these two types of mixtures (CHX-alcohols and TOL-alcohols). That is an evidence of the solvation of toluene from alcohol molecules. Eventually, the long range interactions seem to be similar for both mixtures. That could explain the positive deviation in excess densities for TOL/alcohols mixtures while the negative excess density could be attributed to the strong cluster domains created by both molecules (CHX and alcohols).

3) TBA mixtures

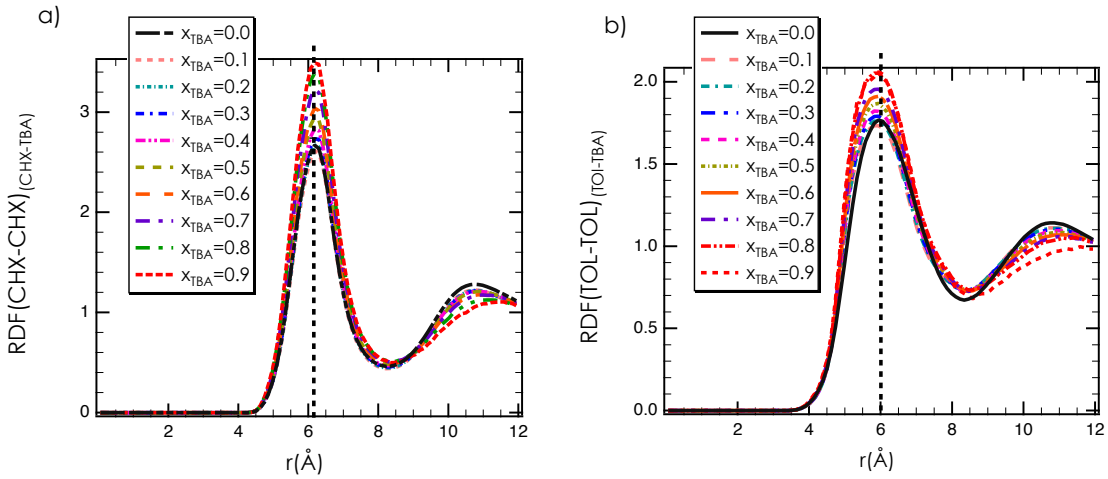

Figure 3.19: Radial distribution functions between centers of mass of the aprotic component for both CHX-TBA (a) and (b) TOL-TBA mixtures. The vertical dashed line represents the position of the first peak.

The structure analysis has been also conducted for TBA-TOL and TBA-CHX mixtures. Figure 3.19 reports the RDFs between TOL and CHX molecules as a function of TBA molecules. The CHX-CHX RDFs showed two peaks, one located at 6.1 Å and second located at 10.8 Å. The change in TBA concentration does not affect the peaks positions. For the TOL-TOL RDFs there

are two broad peaks located at 5.9 Å and at 10.8 Å, respectively. Concentration effect of TBA on the local structure of TOL are observed by the variation of peaks intensity with unchanged position peaks. Both structures indicates thus a similar behavior compared to local environment of RDFs in MeOH, EtOH, PrOH, BuOH and PeOH. Otherwise, Figure 3.20 underlines the RDFs

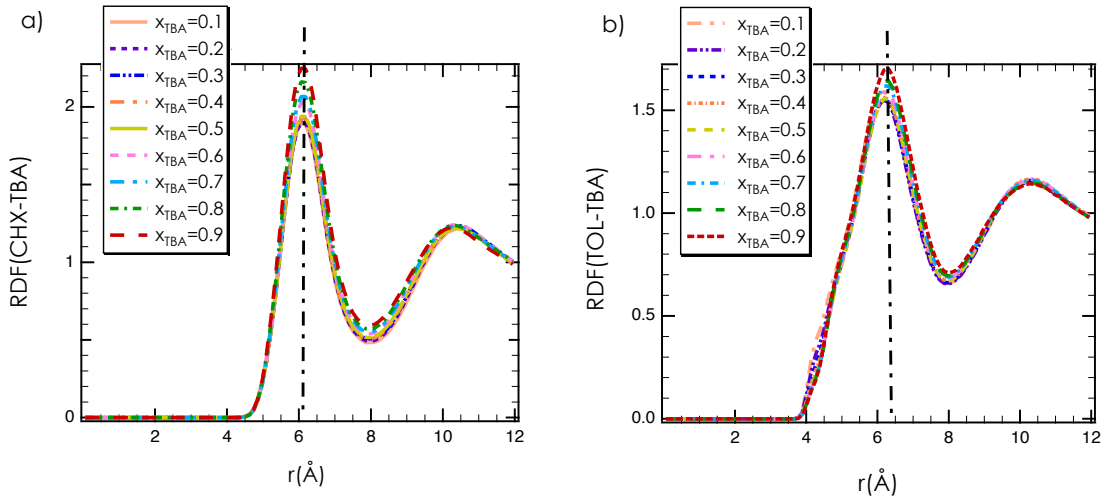

Figure 3.20: Radial distribution functions between centers of mass of aprotic component and tert-btanol (TBA) for both CHX-TBA (a) and TOL- TBA (b) mixtures. The vertical dashed line represents the position of the first peak.

of CHX-TBA and TOL-TBA as a function of TBA concentration. As shown in Fig. 3.20 (a), two sharp peaks were observed at 6.1 Å and at 10.8 Å in the RDF for CHX-TBA mixtures. The concentration dependence shows stronger effect on the first peak. This means that the addition of CHX changes the number of surrounding molecules in the first shell. Fig. 3.20 (b) reports the RDFs of TOL-TBA as a function of TBA concentration. As depicted in Fig. 3.20 (b) two broad peaks are observed with a slight shoulder. This shouldering are more important for MeOH > EtOH > PrOH > BuOH > PeOH > TBA which reflect an important task on the alkyl chain length for linear and branched alcohols. This increase of the alcohol hydrophobic part ($CH_3 - CH_2$...) affects the strength of the HB interaction (Hydroxyl part; $-OH$) of the molecules, while the interaction with the aromatic part of TOL would prefer short linear chains over large and branched ones. In this context, TBA creates less interactions with aromatic ring than other alcohols.

3.4.2 Dilution effect on hydrogen bonds network

Methanol mixtures

To characterize the microstructure in both mixtures the hydrogen bonds number per methanol molecule (nHB) was calculated. Hydrogen bonds were evaluated by considering the geometric criterion developed by Luzar and Chandler [42] such that the distance between hydrogen atom of one MeOH molecule and the oxygen atom of another one has to be smaller to 2.5 Å whereas the distance between two oxygen atoms of two MeOH molecules has to be smaller to 3.5 Å. We report in Figure 4.14 (a) nHB as a function of x_{MeOH} for both mixtures. Concerning the CHX/MeOH mixture, Figure 4.14 (a) shows a slight monotonic decrease in nHB because we move from 1.8 to 1.6 whereas a strong diminution is observed in case of the TOL/MeOH mixture that loses 1 hydrogen bond by moving from 1.8 to 0.8. Concerning the CHX/MeOH mixtures, the progressive formation of nanophases allows to conserve the hydrogen bonds number constant during the diluting. Indeed, the MeOH molecules are gathered in clusters, such that the OH groups are hidden from the CHX. In case of the TOL/MeOH mixture, the hydrogen bonding network is broken in favor of the interactions between TOL and MeOH molecules. That could suggest an increase in the dispersed MeOH molecules. This organization could be in line with an increase of small MeOH clusters (monomers and dimers) contrary to the CHX mixture where larger clusters could be favored. The increase in number of monomers and dimers in the TOL/MeOH mixture will be in accordance with the decrease of nHB. To be thorough, the analysis of the molecular interactions through Kirkwood-Buff integrals (KBIs) was carried out for both TOL-MeOH and CHX-MeOH mixtures. KBIs were calculated from corrected RDF calculations by considering the recent development purposed by Kruger and coworkers improving the KBIs' convergence [43, 44]. Details of calculations can be found in Refs. [43, 44]. We report in Fig. 4.14 (b) G_{ij} for all ij contributions in both TOL-MeOH and CHX-MeOH mixtures. In the case of the TOL-MeOH mixture, the predicted KBIs values are found in fair agreement with the experiment [5], suggesting that the calculation developed by Kruger and coworkers is well suitable to explore the binary liquid mixtures with microstructure. As exhibited in Fig. 4.14 (b) G_{ij} of MeOH-MeOH interactions is positive in both mixtures, indicating the favorable interactions. Furthermore a maximum is found at very low concentration in methanol ($x_{MeOH} = 0.2$) could

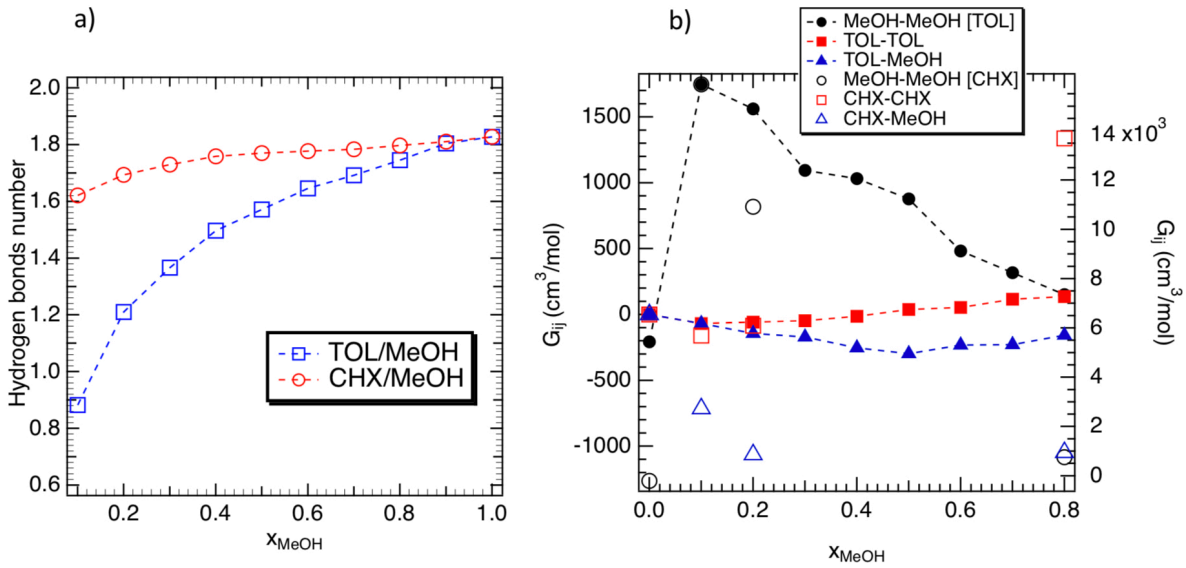

Figure 3.21: (a) nHB per methanol molecule as a function of the methanol concentration. (b) KBIs as a function of the methanol concentration for both TOL-MeOH and CHX-MeOH mixtures. In panel (b) the right axis corresponds to the MeOH-MeOH KBI for the CHX-MeOH mixture.

corresponds to the formation of the methanol cluster. The decrease in G_{ij} from $x_{MeOH} = 0.2$ could be probably due to the percolation of the hydrogen-bonding network where the interactions between methanol molecules are averaged. Cluster analysis and percolation of the hydrogen-bonding network will be analyzed in the following section. Interestingly, Fig. 4.14 (b) shows that the KBIs of MeOH-MeOH interactions in the CHX mixtures are higher than in TOL ones. That is the result of unfavorable interactions between CHX and MeOH molecules increasing the formation of methanol clusters and then their interactions. TOL-TOL and CHX-CHX KBIs are strongly smaller than MeOH-MeOH ones, which suggests weaker interactions given their hydrophobicity and their weak polarity. Let us mention that the crossed interactions are negative is evidence of the unfavorable interactions in comparison with self-interactions. Eventually, we observe that $G_{CHX-MeOH}$ are more negative than $G_{TOL-MeOH}$, which is in line with the observed immiscibility between CHX and MeOH.

Ethanol to pentanol mixtures

From TOL/TOL and CHX/CHX RDFs, we observe that CHX promotes the self-associating behavior of alcohol molecules, whereas TOL presents strong interaction with alcohols. Figure

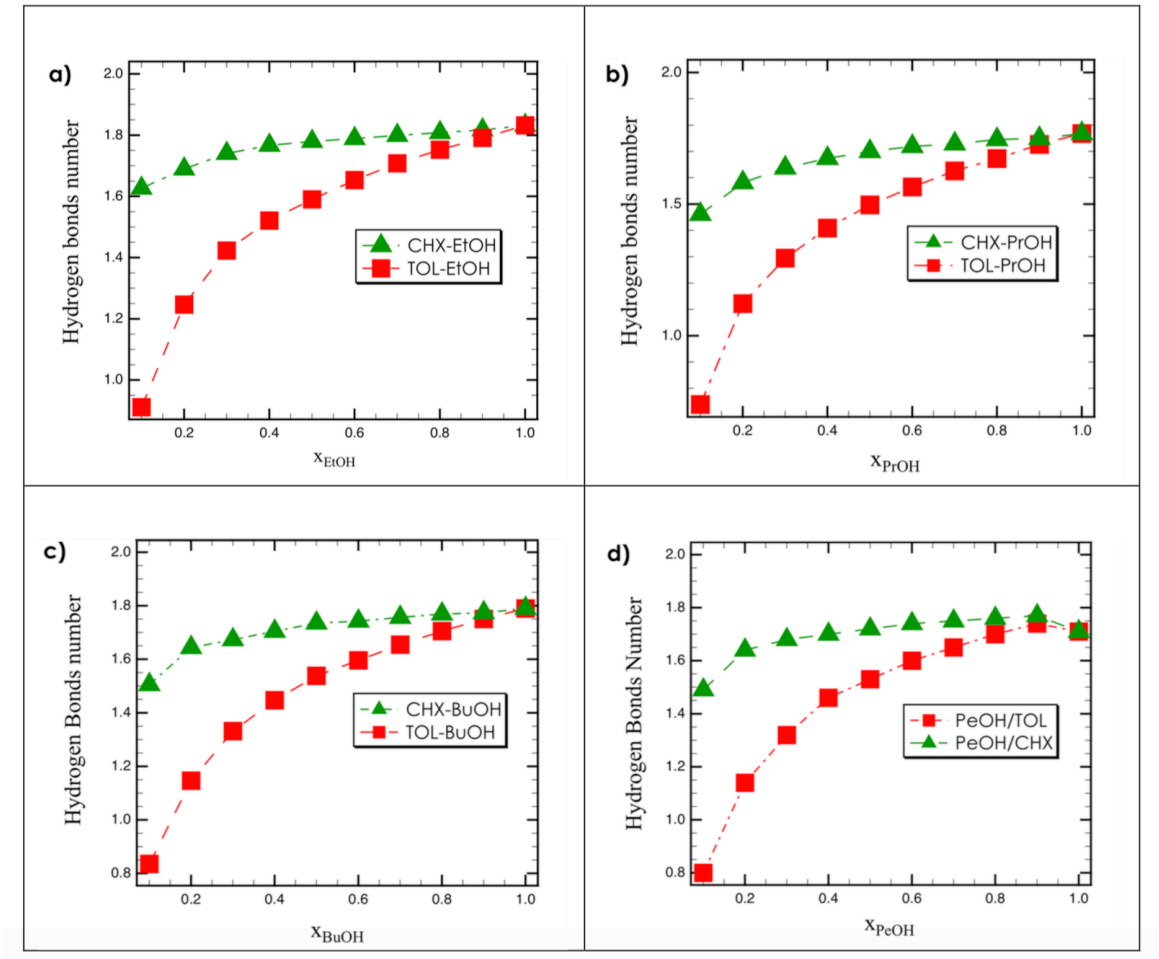

Figure 3.22: Number of the hydrogen bonds per alcohol molecule in a) EtOH/TOL, EtOH/CHX, b) PrOH/TOL, PrOH/CHX, c) BuOH/TOL, BuOH/CHX and d) PeOH/TOL, PeOH/CHX as a function of alcohol concentration..

4.15 (a), (b), (c) and (d) reports nHB of EtOH, PrOH, BuOH and PeOH, respectively in mixtures with CHX and TOL. Figure 4.15 (a) indicates a gradual decrease in the NHB of EtOH molecules with the addition of CHX molecules, ranging from 1.8 to 1.6, and interestingly a small reduction in HB number is observed. EtOH in TOL solution exhibits a strong dilution of the hydrogen bonds number that is highlighted by a significant decrease in nHB of EtOH from 1.8 to 0.8. In Figure 4.15 (a) indicates a loss of a strong hydrogen bond donor $-$OH of EtOH molecules.

This concerns the hydrogen atoms of EtOH molecules, where the HB donor of EtOH molecules is probably in interaction with the π-electrons of the aromatic ring of toluene. Then, it can be expected that the addition of TOL could generates more unassociated molecules (unbounded HB of EtOH molecules), involving more monomers and dimers than larger clusters. On the contrary, one may expect that the addition of CHX enhances the association between EtOH molecules leading to more larger clusters could be created. The nHB of PrOH molecules is shown in Figure 4.15 (b) in both mixtures. The nHB in CHX-PrOH mixtures decreases from 1.8 to 1.45 while in TOL-PrOH it decreases from 1.8 to 0.7 which highlights a strong dilution of the HB network. The PrOH molecules as EtOH ones depict a strong affinity with TOL molecules rather than CHX molecules. Additionally, the evolution of nHB of BuOH molecules in CHX and TOL was also investigated and reported in Figure 4.15 (c). Very interestingly, the addition of TOL molecules decreases the nHB of BuOH molecules. The nHB of BuOH varies very slowly with the addition of CHX to the mixture, which is illustrated by the fact that there is no disturbance of the HB network of BuOH molecules over the entire concentration range (it varies from 1.8 to 1.5). Figure 4.15 (d) presents the nHB of PeOH molecules in both mixtures as a function of PeOH concentration. We observe from Figure 4.15 (d) that nHB of PeOH decreased from 1.7 to 1.46 in CHX mixture and from 1.7 to 0.8 in TOL mixture which highlights a strong HB dilution by TOL molecules. The decrease in nHB of PeOH molecules in mixture with TOL are attributed to the high solvation degree in TOL molecules.

3.4.3 TBA mixtures

Figure 3.23 shows the evolution of TBA HB number in CHX and TOL mixtures.. As showed in Figure 3.23 HB number of TBA in CHX varied from 1.7 to 1.45 and in TOL changed from 1.7 to 0.8. This highlights a strong dilution of HB network by TOL rather than CHX. The breaking in HB generates more free hydroxyl groups in the mixture whereas in CHX a strong connection between TBA molecules is observed. As it evidenced from snapshots, a clustering phenomena are also observed with TOL. We can relate this dilution of nHB of TBA in TOL by the attracting forces between TOL and TBA. For CHX, large nano-domains of different cluster sizes are formed.

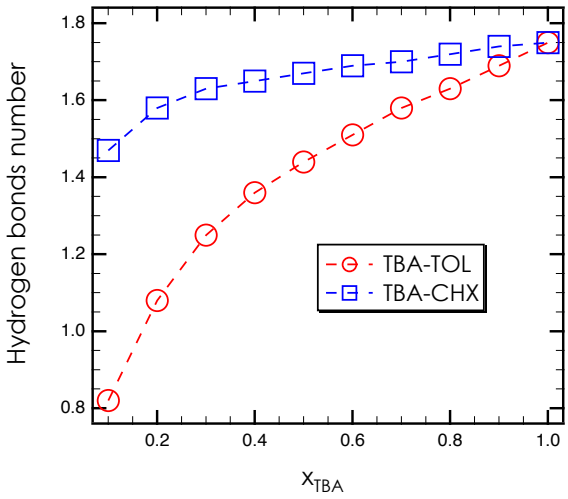

Figure 3.23: nHB per TBA molecule as a function of the TBA concentration.

a) Discussion

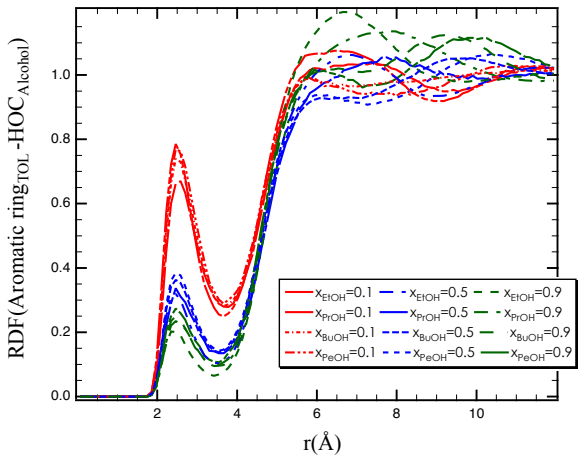

Figure 3.24: Radial distribution function of center of mass of the Aromatic part of Toluene molecules and the hydroxyl part of the alcohol (HOC): EtOH, PrOH, BuOH and PeOH as a function of alcohol concentration.

The presence of π electrons in toluene molecules leads to the formation of weak intermolecular complexes [45–50]. The RDFs between toluene on alcohols showed a shoulder close to the first peak involving a favorable interaction. To evidence the alcohols affinity for TOL molecules, we report in Figure 3.24 the local surroundings of the aromatic ring of toluene molecules in the presence of different alcohols made by calculating RDFs between the hydroxyl group (HOC) of the alcohol and the aromatic ring of TOL. As shown in Fig. 3.24, the RDFs reveal a favorable

interaction between HOP and aromatic rings at very small distance of 2.46 Å that is in line with the loss of the hydrogen bonds of alcohols molecules evidenced in Figure 4.15. Interestingly, there is a very strong dilution of the hydrogen bonding network. While in CHX-alcohol systems, it is preserved with a very small loss in the connected HB pattern.

3.5 Cluster analysis

1) Methanol mixtures

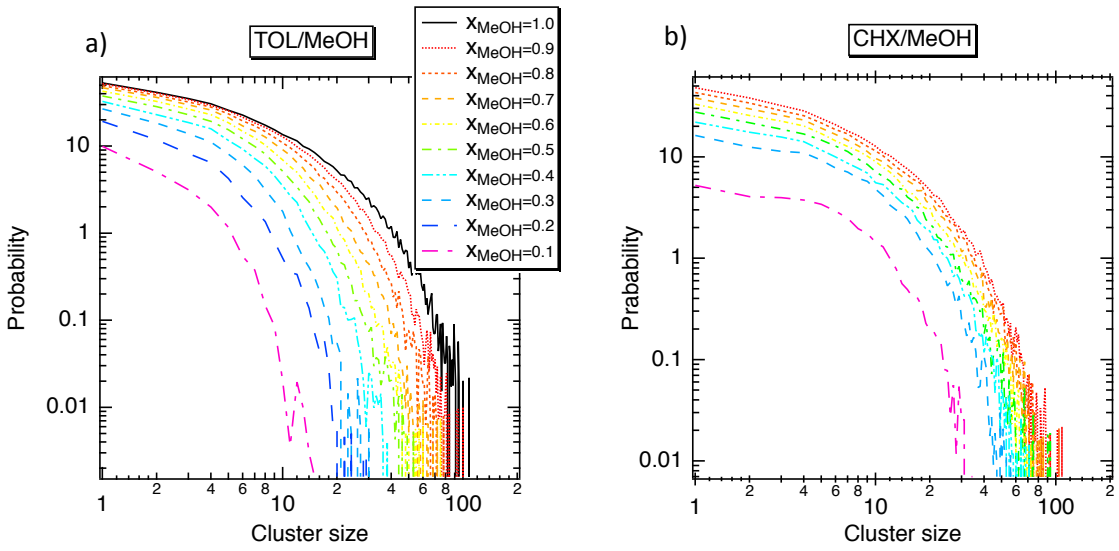

Figure 3.25: Cluster size probability as a function of the MeOH concentration in logarithmic scale in both TOL-MeOH (a) and CHX-MeOH (b).

We report in Fig. 3.25 the cluster size distribution of MeOH for both TOL-MeOH and CHX-MeOH mixtures. In both cases and in all range of concentrations the system does not percolate to form only one interconnected network [51] even if the cluster size increases as a function of the MeOH concentration. That could suggest the formation of methanol clusters of different sizes leading to a microstructure. From $x_{MeOH} = 0.2$ to $x_{MeOH} = 0.8$ (i.e., in the immiscible region) a broader size distribution of clusters is observed in the CHX-MeOH mixtures involving a wider size range of clusters. Additionally, we strive for a faster size distribution of the pure MeOH in the CHX/MeOH mixtures than in the TOL/MeOH ones. Actually, these two facts suggest an increase in the heterogeneity and the development of the segregation process. Moreover,

a faster decrease of the size distribution as the MeOH concentration increases is observed in the TOL/MeOH mixture. As shown in Figure 3.25 small clusters are rather favored in case of TOL/MeOH mixture, highlighting a better dispersion of toluene molecules in the mixture that in good accordance with the miscibility of toluene in MeOH. The rate of the linear (opened structure) and cyclic (closed structure) clusters were also evaluated. In both cases and in full range of MeOH concentration, high proportion of linear structures ($>$ 96 %) was found. We report in Figure 3.26 examples of opened and closed structures. We report in Figures 3.27 (a) and 3.27 (b) the clusters number from dimers to pentamers in both mixtures. Strikingly, at low concentrations the number of short clusters is four times higher in the TOL/MeOH mixtures in comparison with the CHX/MeOH mixtures. Additionally, Figure 3.27 exhibits a rapid decrease of the number of dimers and trimers as a function of the methanol concentration whereas the number of larger clusters increases. This result highlights the presence of clusters of different sizes leading to a spatial heterogeneity and then the microstructure. On the other hand, in the CHX/MeOH mixtures, a slight increase of the number of dimers and trimers is highlighted while a linear progression is observed for the number of tetramers and pentamers. This result exhibits the presence of nano-domains of different sizes related to a spatial heterogeneity in both mixtures ruled by different type of interactions. The linear increase in clusters number into the CHX/MeOH mixtures could be connected to the growth of the MeOH domains during the

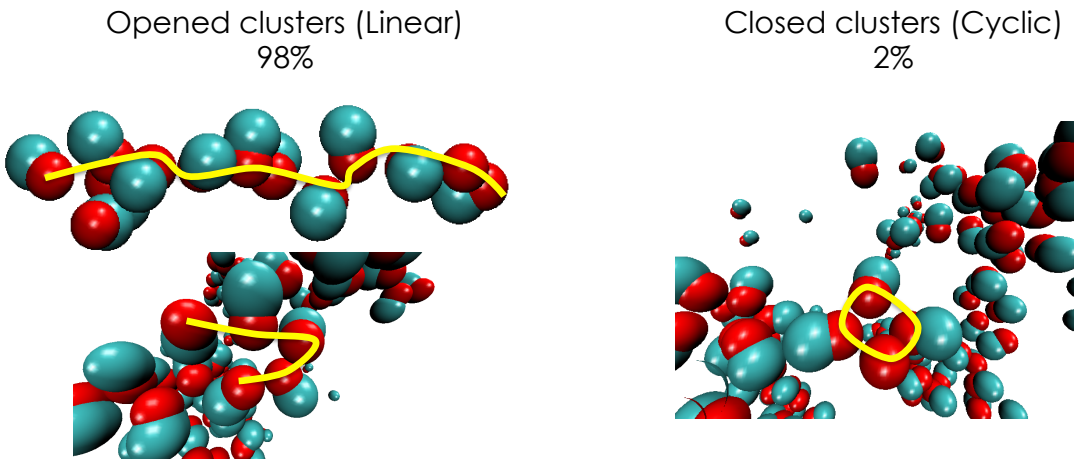

Figure 3.26: Illustrations of opened and closed clusters highlighted with the yellow solid lines. Red and cyan correspond to the oxygen atoms and methyl groups, respectively.

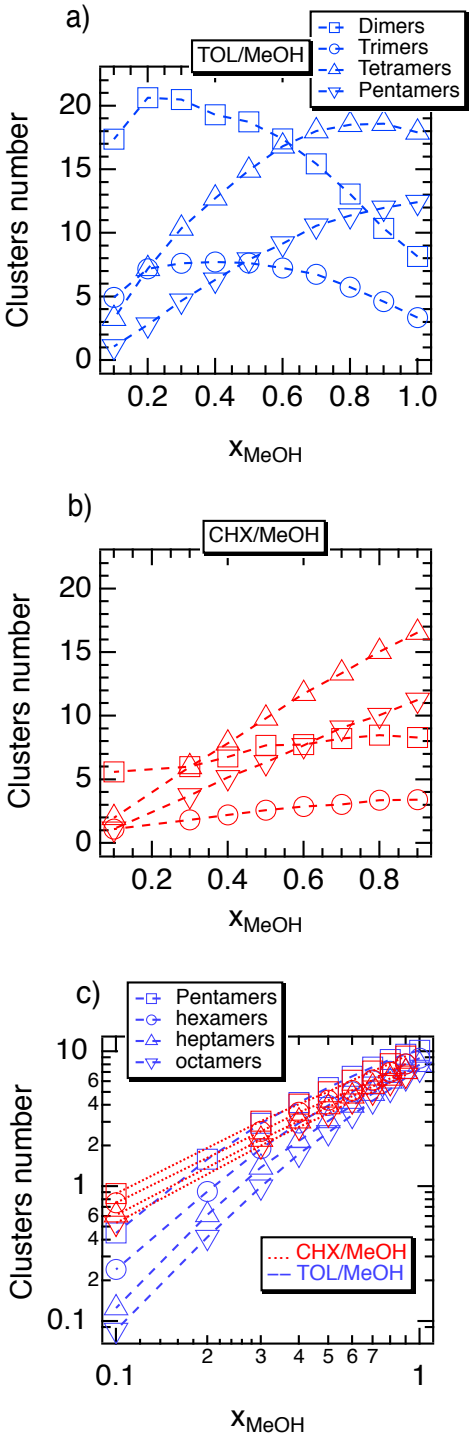

Figure 3.27: Cluster number as a function of the MeOH concentration for the dimers, trimers, tetramers, and pentamers in both TOL-MeOH (a) and CHX-MeOH (b). (c) Number of higher clusters for both TOL-MeOH and CHX-MeOH mixtures.

phase separation. Eventually, Figure 3.27 (c) depicts a greater number of higher clusters in the CHX/MeOH mixture bearing out thus the growth of the MeOH phase. Therefore, the difference in miscibility and in heterogeneity could be understood in terms of clusters size and distribution.

2) Ethanol to pentanol mixtures

Figure 3.28 compares the cluster number of ETOH (a), PrOH (b), BuOH (c) and PeOH (d) in TOL with those obtained in CHX as a function of alcohol concentration. The main results obtained in the CHX/EtOH and TOL/EtOH mixtures are reported as the change in monotony of deviations, the presence of higher heterogeneity in the CHX/EtOH systems compared to TOL/EtOH and the high dilution effect of TOL instead of CHX with notable interactions between the TOL aromatic group and the hydroxyl moieties in the alcohol molecules. All of these outcomes covered the fact that clusters can formed in both mixtures with more or less separated nanophases inducing spatial heterogeneities. Figure 3.28 reports the evolution of clusters number of EtOH in both mixtures as a function of EtOH concentration. EtOH in TOL produces more monomers than other cluster sizes while EtOH in CHX promotes the formation of larger clusters. This is corroborated by the presence of different cluster size in CHX involving spatial heterogeneities as it observed in Figure 3.11. On the other hand, cluster analysis for TOL/PrOH and CHX/PrOH systems were reported in Figure 3.28 (b). PrOH in TOL showed small clusters (dimers and trimers) with a larger number in monomers, whereas PrOH in CHX exhibits less monomers but the same size of dimers, trimers, tetramers and pentamers. Cluster number of BuOH in CHX and TOL is managed in Figure 3.28 (c). Figure 3.28 (c) highlights the formation of the same number of monomers in both mixtures. However their largest cluster is different. Indeed, the BuOH in CHX shows nanodomains of different sizes with the same proportion. In contrast, TOL shows more monomers and dimers than CHX. As mentioned previously, TOL is a HBs breaker. Alcohol molecules are then grouped into small clusters while monomers (Free HB) create connections with TOL molecules. CHX forces alcohol molecules to form nanophases. Concerning PeOH, cluster number in both media is depicted in Figure 3.28 (d) as a function of x_{PeOH}. In comparison to the CHX, we can observe an increase in monomers in TOL. There is no difference between CHX and TOL for other clusters. This could be due to the large alkyl tail

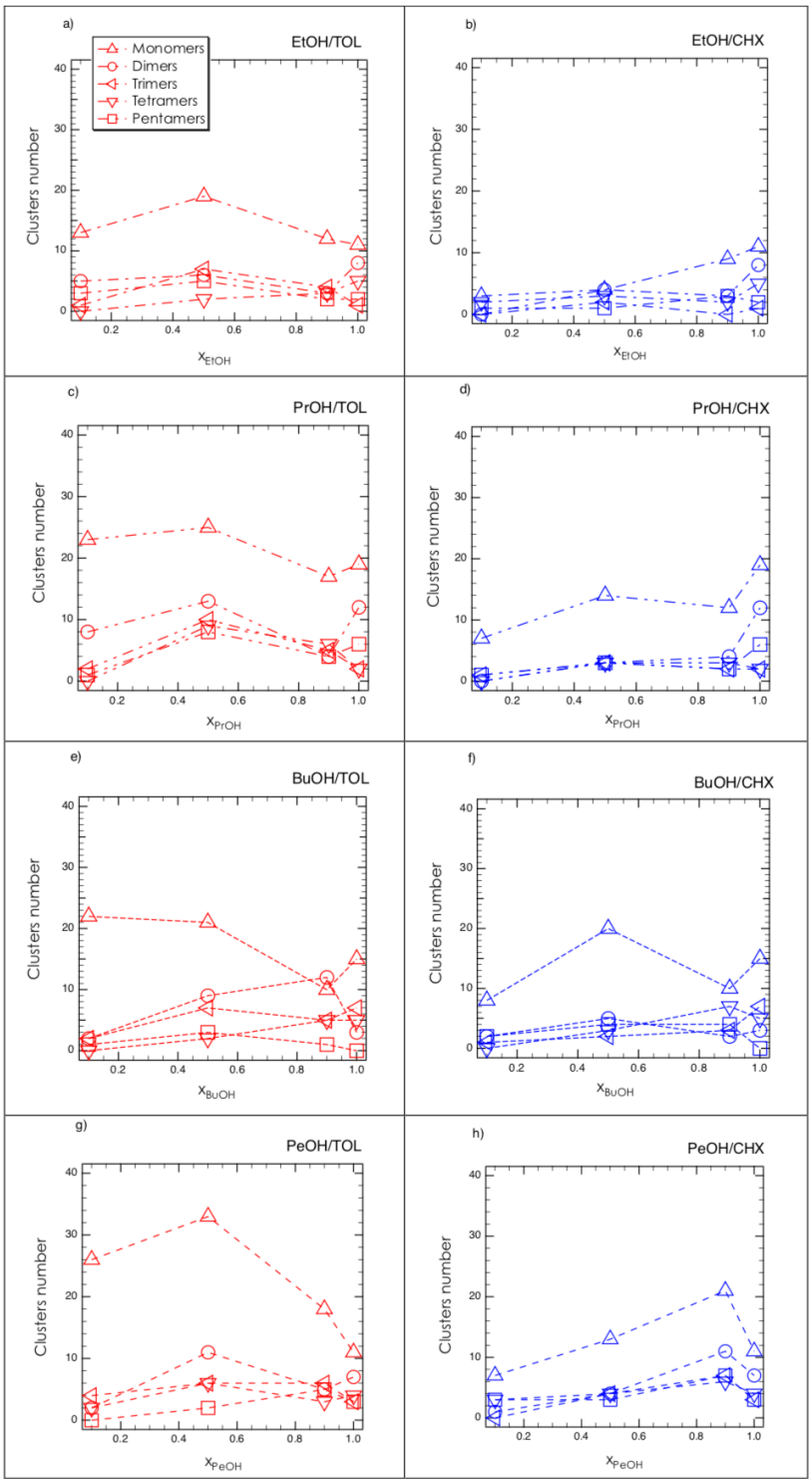

Figure 3.28: Cluster number as a function of the EtOH concentration for monomers, dimers, trimers, tetramers, and pentamers in (a) TOL/EtOH and CHX/EtOH, (b) TOL/PrOH and CHX/PrOH, (c) TOL/BuOH and CHX/BuOH and (d) TOL/PeOH and CHX-PeOH.

of PeOH molecules that occupied more space in both mixtures. Non ideality behavior can ben then attributed to these micro-heterogeneities created by molecular clusters formed by alcohols which generated micro-strucutres of all systems at the molecular level.

3) TBA mixtures

Figure 3.30 (e) presents the evolution of TBA cluster number in both mixtures as a function of TBA. A representative cluster from the mixture is shown in Fig. 3.29. TBA molecules in solutions with TOL are presenting more monomers than more large clusters. A notable amount of Tetramers are highlighted in this mixture at whole range concentration. TBA clusters in $x_{TBA} < 0.6$ are showing more monomers than tetramers, for example at x_{TBA}=0.3 there are 38 monomers, 10 tetramers 9 dimers. In comparison with CHX/TBA mixture, we conclude that the majority part of TBA molecules are grouped in clusters, i.e. assembling in tetramers clusters. This corroborates with our first results depicted in MeOH mixture at the first part of this Chapter. Interestingly, in CHX-TBA mixture, a progressive increase in the number of cluster were captured as a function of TBA concentration.

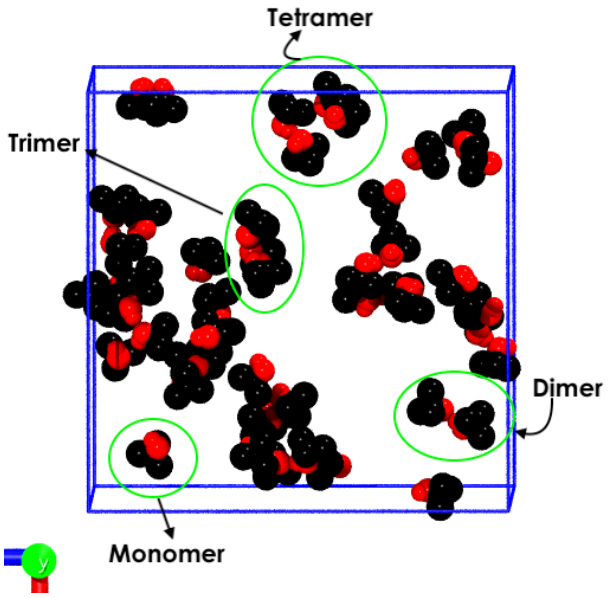

Figure 3.29: Representative cluster of TBA

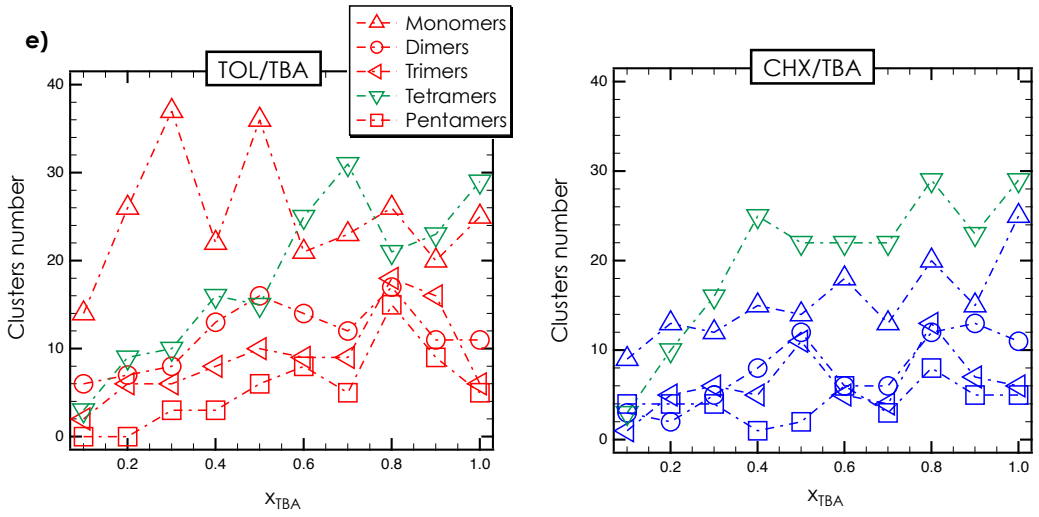

Figure 3.30: Cluster number as a function of the TBA concentration for the monomers, dimers, trimers, tetramers, and pentamers in both TOL-TBA (a) and CHX-TBA (b).

3.6 Clusters versus heterogeneity

Recently, Perera et al. have suggested that the structural signature of the heterogeneity and then the microstructure of ethanol mixture were related to the observation of a pre-peak in the structure factor around 0.8 $Å^{-1}$ [4]. More recently, Hureau et al., by studying *tert*-butanol, have established that the pre-peak was rather the structural signature of the presence of the closed clusters [3, 39]. The structure factor [S(Q) such that Q is the momentum transfer vector] was calculated in both mixtures to structurally highlight the microstructure. All details of the structure factor calculation can be found elsewhere [3]. Let us mention that the value of S(Q = 0) was not evaluated because at Q = 0 $Å^{-1}$ the system is poorly sampled, which explains that S(Q) begins from Q = 0.19 $Å^{-1}$. Indeed, Q = 0 $Å^{-1}$ corresponds to the very high distance in the real space that was slightly sampled in our finite MD simulations.

We report in Figs. 3.31 (a) and 3.31 (b) the total structure factor of both TOL-MeOH and CHX-MeOH mixtures, respectively, as a function of the methanol concentration. The total structure factor corresponds to the case where all atoms were considered. In both mixtures, Fig. 3.31 exhibits the absence of a pre-peak that is contradicts the fact that the pre-peak could be the structural signature of the heterogeneity.

However, this result is in line with the fact that the pre-peak is connected to the closed clus-

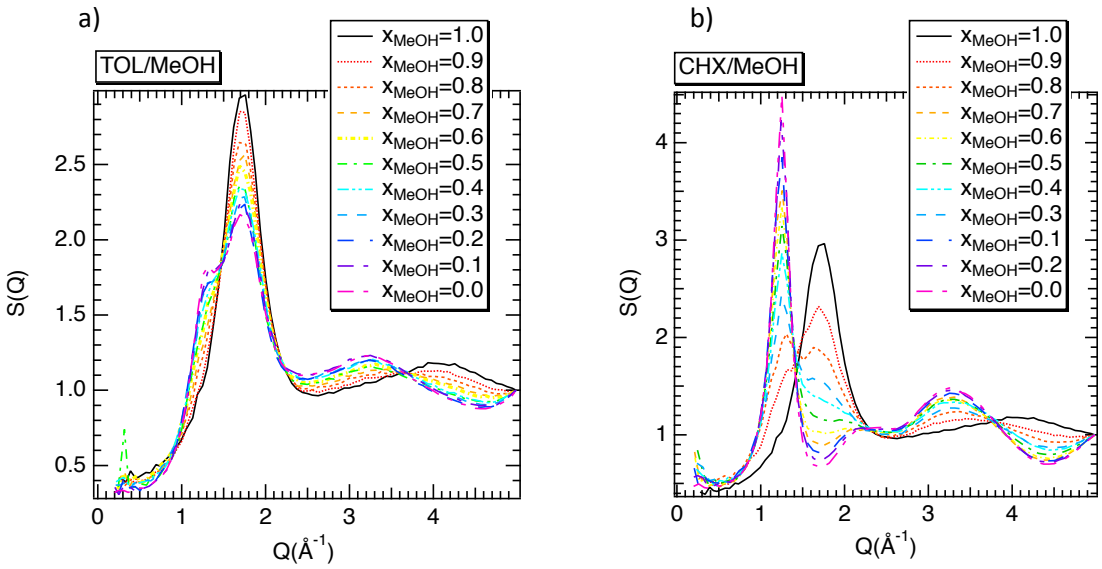

Figure 3.31: Total structure factor of the TOL-MeOH (a) and CHX-MeOH (b) mixtures as a function of methanol concentration.

ters (5% of cyclic clusters in both mixtures). Indeed, physically, the pre-peak at low Q can be assigned to the mesoscale spatial correlations between the hydrophilic parts surrounded by a hydrophobic shell. This situation occurs from molecules with a large hydrophobic moiety such as *tert*-butanol [3] (TBA) or ethanol [51] (ETOH).

By using the previous data obtained from molecular simulation of TBA [3] and ETOH [51], we

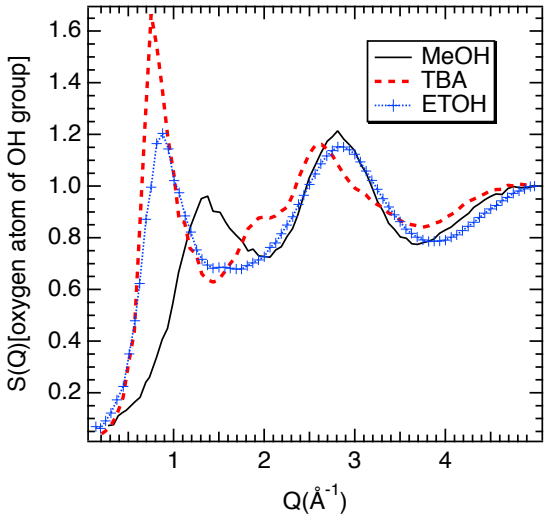

Figure 3.32: Partial structure factor of the oxygen atom of the OH group of methanol, ethanol, and *tert*-butanol liquids at 1 bar and 300 K.

report in Fig. 3.32 the partial structure factor of the hydroxide groups. A partial structure factor allowed us to highlight the pre-peak of the total structure factor that becomes the main one [3]. Details of the calculation of thee partial structure factor can be found in Ref. [3]. As shown in Fig. 3.32, TBA and ETOH present a first peak at 0.8 $Å^{-1}$, contrary to MeOH, which presents a first peak located at 1.4 $Å^{-1}$ The decrease of amplitude is the result of the decrease in the number of cyclic clusters. Indeed, in the TBA and ETOH liquids 95% and 15% of cyclic clusters were calculated, respectively, whereas in the pure methanol liquid, the rate of cyclic clusters is close to 5%. The shift from 0.8 to 1.4 $Å^{-1}$ sheds light on range of mesoscopic correlations and on the size of clusters. Indeed, methanol has smaller cyclic clusters involving an increase in the range of the interactions. Additionally, in three pure TBA, ETOH, and MeOH liquids, the HOP was found e qual to 14.9, 7.1, and 15.0, i.e., below 15.74, involving an absence of heterogeneity. In the pure liquids, this result indicates that the presence of clusters could be uncorrelated from the notion of heterogeneity, which is in line with the conclusion drawn by Perera et al. [4]. However, this result also suggests that the pre-peak will be a structural signature of the mesoscopic correlations between cyclic clusters, which is evidence of the heterogeneity of the microscopic scale.

The spatial heterogeneity of miscible liquid mixtures then would be the result of the local structural disruption of the homogenous structure in the pure liquid. Indeed, as observed in Fig. 4.14, by progressively increasing the toluene concentration, the initial hydrogen-bonding network corresponding to a homogenous structure is then locally broken due to the favorable toluene-methanol interactions leading to the spatial heterogeneity. As the toluene concentration increases, the heterogeneity increases to reach a maximum around $x_{MeOH} = 0.5$ (see Fig. 3.8). From $x_{MeOH} = 0.5$ to $x_{MeOH} = 0.0$ the HOP decreases, highlighting a loss of heterogeneity because the local disruption is then spatially propagated to recover an apparently homogenous structure. As shown in Figs. 3.7 and in 3.8 the non-ideality of the toluene-methanol mixture is quasi correlated to the HOP evolution and then to its structural heterogeneity.

3.7 Dynamical properties

In this part, the rotational and translational motion have been investigated. Translational dynamics has been studied by calculating the mean square displacement (MSD). We aim to investigate the so-observed structural anomalous from a dynamical standpoint. The rotational motion will be studied from the auto-correlation function of dipole moment C(t) and the relaxation times τ will be calculated.

3.7.1 Self-diffusion coefficient

1) Ethanol to pentanol mixtures

Table 3.1 reports the self-diffusion coefficients of pure components. A fair agreement with experimental results is observed for alcohols and for TOL and CHX molecules is showed with an error of about 13 % which is reasonable. In Table 3.1, a decrease in diffusion of large alcohols is

Pure liquids	$D_t^{Simulated.}$	$D_t^{Experimental.}$
Ethanol	1.07	1.08 [52]
		1.01 [53]
		1.16 [54]
1-Propanol	0.684	0.646 [53]
		0.627 [52]
		0.590 [54]
1-Butanol	0.400	0.426 [55]
		0.456 [52]
		0.504 [53]
1-Pentanol	0.302	0.296 [56]
		0.286 [57]

Table 3.1: Simulated and experimental self-diffusion coefficient of pure liquids in $10^{-9}m^2$ /s at T=300K and P=1 Bar

observed. The self-diffusion coefficients of each component as a function of alcohol concentration is reported in Figure 3.33. Three concentrations are chosen in order to explore the non-ideality observed in Figure 3.3 from the density and the excess density. Furthermore, 0.1 and 0.9 are the mole fractions of alcohols are also studied to evaluate the poor and rich alcohols regions.
In Figure 3.33, the self-diffusion coefficients of TOL/EtOH and CHX/EtOH, TOL/PrOH and CHX/PrOH, TOL/BuOH and CHX/BuOH, TOL/PeOH and CHX/PeOH are reported as a

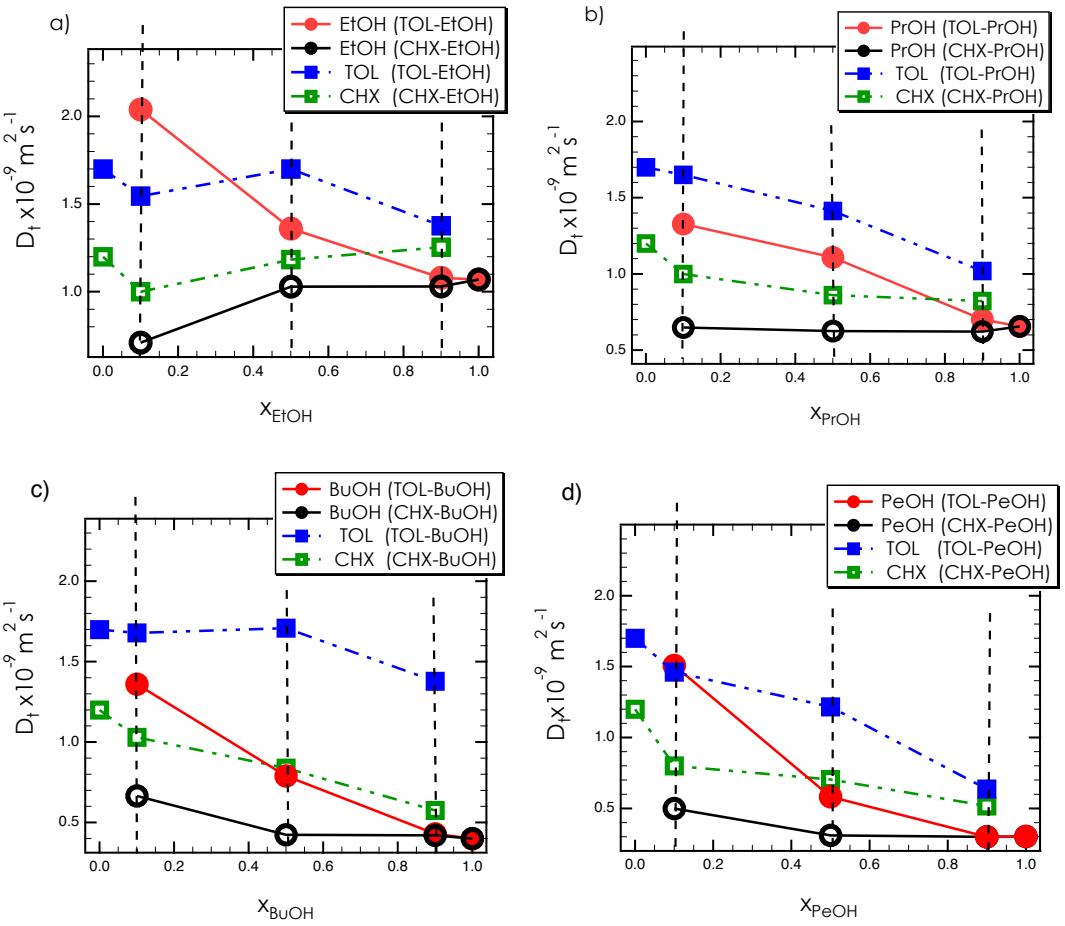

Figure 3.33: Self-diffusion coefficients for a) TOL,CHX) +EtOH, b) TOL,CHX) +PrOH, c) TOL,CHX) +BuOH and d) TOL,CHX) +PeOH.

function of alcohol concentration. Figure 3.33 (a) represents the D_t of EtOH molecules in both mixtures (TOL and CHX). EtOH in TOL at x_{EtOH}=0.1 showed a fast dynamics in the mixture (two times faster than its pure value), while EtOH in CHX shows a slowing in dynamics. Both aprotic molecules show a slight decrease in their diffusion tin relation to their pure value at low EtOH concentration. Interestingly, at x_{EtOH}=0.5, we observe an increase in D_t of EtOH in CHX as a function of x_{EtOH} whereas a slight decrease in the motion of EtOH in TOL is evidenced. At x_{EtOH}=0.5, we show a proportion of 7.6 % of EtOH monomers in TOL whereas 1.6 % of monomers in CHX is evidenced. That could be at the origin of the slow motion of EtOH molecules in EtOH with CHX. In EtOH rich-regions (x_{EtOH}=0.9) the motion of EtOH are similar to that in both aprotic solvent that is expected because there are the same rate of monomers

in both components (about 2.6 % of EtOH in TOL and 2% of EtOH in CHX). As previously reported, TOL breaks the HB networking of EtOH molecules. The dynamics is then impacted by the EtOH monomers and dimers. However, CHX doesn't break the nHB even a slight decrease of nHB is observed in Figure 3.23. The slow dynamics is probably governed by the molecular clustering phenomenon of different EtOH largest clusters such that tetramers and pentamers. TOL diffuses more faster than CHX at low and medium alcohol concentrations (x_{EtOH}=0.1 and 0.5) while at x_{EtOH}=0.9 a similar value is observed.

Figure 3.33 (b) shows the diffusion coefficients of different components in TOL/PrOH and CHX/PrOH mixture as a function of x_{PrOH} and we observe a faster diffusion of PrOH as EtOH in TOL in comparison with CHX. That corroborates, that our assumption about the preferential formation of monomers in PrOH/TOL binary mixture rather than PrOH/CHX one. Furthermore, TOL mostly interacts with PrOH molecules that allows us to observe an increase of dynamics, while CHX shows similar diffusion behavior as pure value.

In Figure 3.33 (c), a fast diffusion of BuOH in both mixtures are observed such that $D_{TOL}^{(PrOH)} > D_{CHX}^{(PrOH)}$. TOL in BuOH shows no significant concentration dependence of its self-mobility while the D_t of CHX decreases with increasing BuOH concentration. Concentration dependence of the self-diffusion coefficients in TOL, CHX and PeOH are provided by Figure 3.33 (d). PeOH shows faster diffusion in presence of TOL than in CHX (x_{PeOH}=0.1 and 0.5) that is in line with the presence of TOL. While at rich PeOH-regions similar dynamics is observed with similar microstructure (see Figure 3.28). Self-diffusion coefficient of TOL decreases as a function of PeOH addition while a slight decrease is also observed for CHX.

At low concentration, alcohols in TOL diffuse two times faster than their pure behavior. On the contrary, alcohols molecules in CHX at a similar concentration diffuse two times slower than alcohols molecules in their pure state. This is due to the new environment offered by TOL and CHX in each case separately. This is means that the polarity (π interaction) of apolar molecules mixed with alcohols impacts the self-diffusion. At $x_{Alcohol}$=0.5, EtOH in (EtOH/TOL) mixture diffuses even more than EtOH molecules in CHX; At x_{EtOH}=0.9, the molecules auto-diffuse similarly in both mixtures. Effectively, we have two close values to the pure self-diffusion coefficient. The study of the dynamics recorded in all these mixtures indicates that alcohols mixed with toluene

have a rapid motion when compared to alcohols in cyclohexane. Indeed, this observation points out that toluene creates strong molecular interactions and promotes the translational movement of molecular alcohols rather than cyclohexane.

2) TBA mixtures

Figure 3.34 reports the self-diffusion coefficients of TOL/TBA and CHX/TBA mixtures as a functions of concentration. Experimental self-diffusion coefficients were plotted for TOL/TBA which they are higher than those observed in this work and may be due to the fact that our measurements are carried out at a higher temperature than that used in their experiments. The agreement with experimental results was satisfactory. From Figure 3.34, TBA in TOL shows

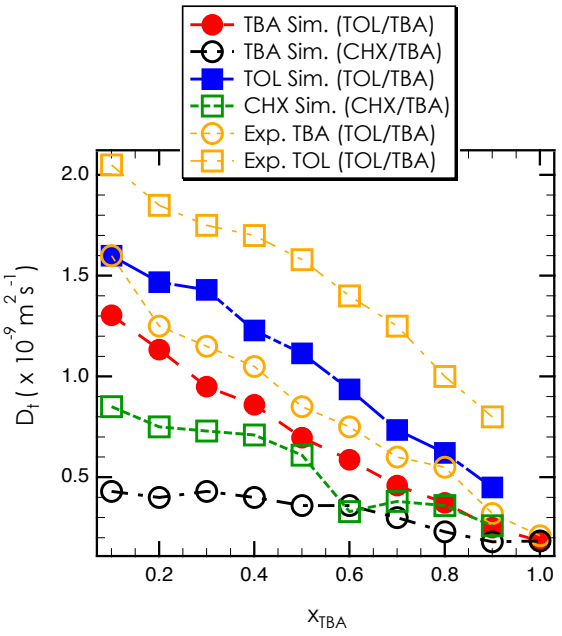

Figure 3.34: Self-diffusion coefficients for TOL/TBA and CHX/TBA mixtures.

and increase on D_t as a function of the x_{TBA} while D_t of TBA molecules in CHX are slightly increase. This could be related to the existence of a large number of free alcohol molecules in TOL (monomers and dimers) and to the lowest amount of free TBA molecules in the CHX/TBA mixture. In previous section Figure 3.30 has been shown different degree of aggregation of TBA molecules in both mixtures. The tendency of TBA molecules to self-aggregate in largest clusters

with CHX are probably at the origin of the slow motion observed in Figure 3.34. The TBA clustering has then an effect on the dynamics of the aprotic solvents.

3.7.2 Rotational diffusion

i) Dipole moment autocorrelation function C(t)

Ethanol to pentanol mixtures

We report in Fig. 3.35 the dipole moment autocorrelation function of EtOH, PrOH, BuOH and PeOH in mixtures in presence with TOL and CHX respectively. Figure 3.35 shows that molecules rotationally are disrupting in presence of TOL and CHX. the rotational motion of total dipole moment of alcohols increases when they are diluted with TOL rather than CHX. That is illustrated by a fast decay of the autocorrelation functions of EtOH, PrOH, BuOH and PeOH with the addition of TOL. A lesser effect on the rotational behavior were observed in CHX mixtures. These observations underpin our results suggesting a fast dynamics of alcohol molecules in presence of TOL in comparison with slow dynamics observed in CHX. The dynamics could be attributed to the microscopic aggregation of molecules leading to a strong micro-heterogeneity in the system showed by Figure 3.11. It is interesting to mention that the high dilution of the hydrogen bonding network of alcohols in the mixture with TOL are somehow the first factor that was impacted the resulting structures.

TBA mixtures

For the TBA/TOL and CHX/TBA mixtures, the evolution of the autocorrelation function of TBA dipole moment were reported as a function of time in Figure 3.36. The decay of the autocorrelation function of TBA molecules in TOLis found faster than CHX. As previously shown, CHX breaks the structure but does not break the nHB, rather it causes complexes formation. We think that the formation of large aggregates is at the origin of this slow rotational and translational motion showed. For the TBA/TOL binary mixture, the fact that there are more monomers could be an explanation of differences observed in both cases.

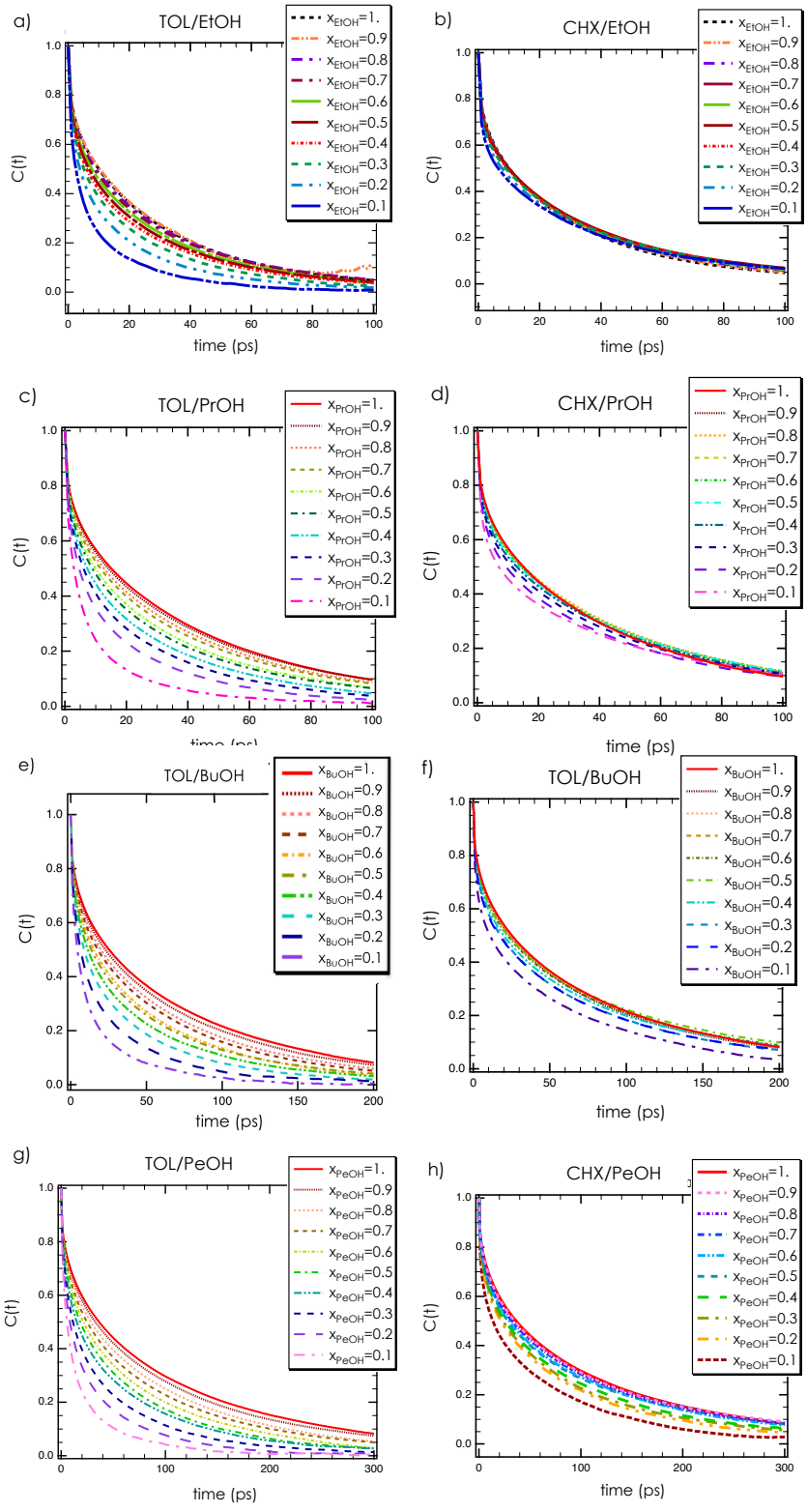

Figure 3.35: Evolution of the dipole moment autocorrelation function with composition in a) EtOH/TOL, b) EtOH/CHX, c) PrOH/TOL, d) PrOH/CHX, e) BuOH/TOL, f) BuOH/CHX, g) PeOH/TOL and h) PeOH/CHX.

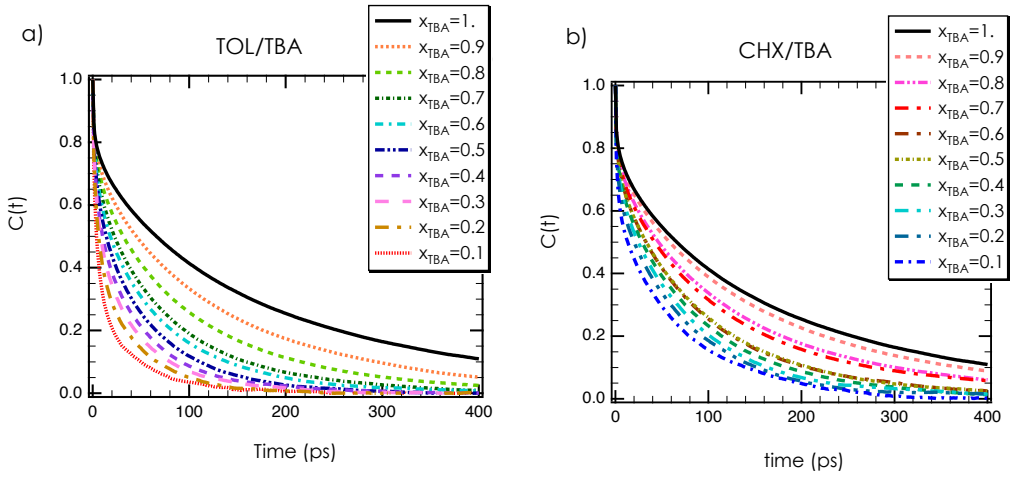

Figure 3.36: Evolution of the dipole moment autocorrelation function with composition in a) TBA/TOL, b) TBA/CHX.

ii) Dipolar relaxation time τ(ps)

By fitting the autocorrelation function of dipole moment of alcohols from the Debye model, the relaxation times τ have been calculated. Figure 3.37 (a), (b), (c) and (d) shows that alcohols in TOL are rapidly oriented compared to the same alcohols in CHX. Alcohols in TOL showed a short relaxation times and a long relaxation times were demonstrated by alcohols in CHX. This could be attributed to the evolution of the hydrogen bonding interactions in both mixtures. It has appeared to be an important factor influencing the rotational motion of the total dipole moment of alcohols and their relaxation times [58]. As a result, a wait-and-switch [58] model has been developed to describe the rotational dynamics of liquids [58]. Through this model, a "*waiting*" time is necessary for the hydrogen bonding network to reorganize itself and find the next available site to "*switch*" from one hydrogen bond to another.

The "wait-and-switch" model [58] can be used to correlate the observations of the dilution of the hydrogen bonding network to the total dipole reorientation dynamics of alcohol-TOL and alcohol-CHX mixtures. The nHB of alcohols in all mixtures are given in sec. 3.4.3. As shown previously, it was reported that the hydrogen bonding network of EtOH, PrOH, BuOH and PeOH is more extensive in CHX than in TOL. With TOL, the HB network seems to undergo a progressive dilution. For alcohols mixtures with CHX, the lower availability to make HBs at high CHX concentrations decreases the probability of dipole reorientation invoking a decrease

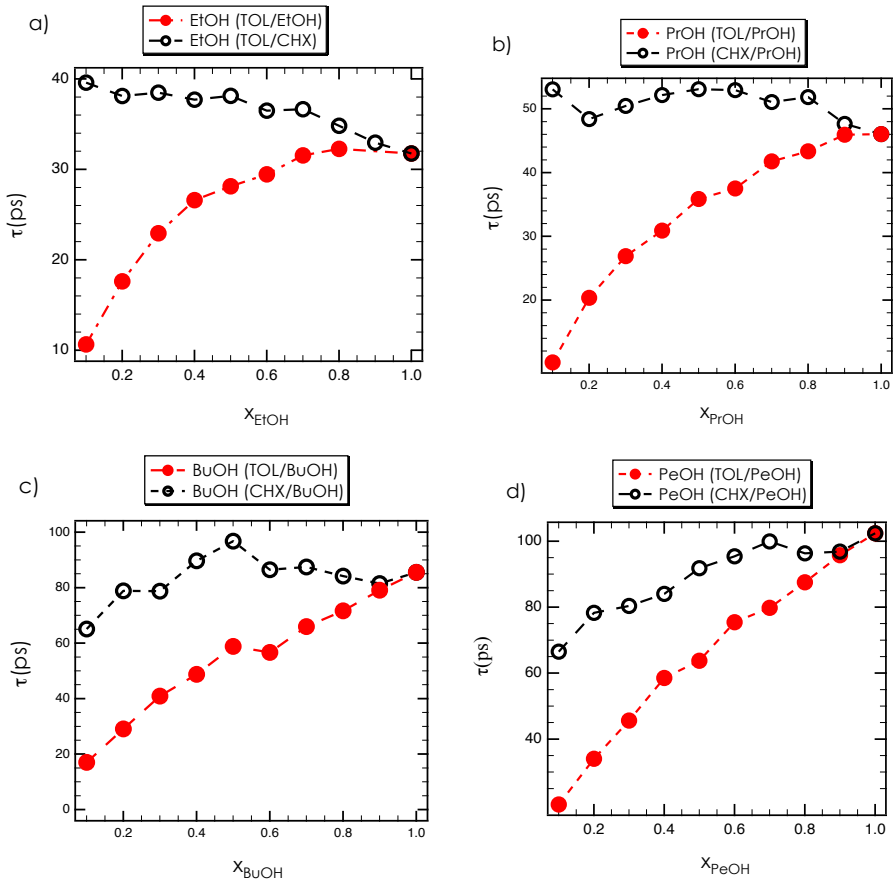

Figure 3.37: Variation of relaxation times in a) EtOH/TOL + EtOH+CHX, b) PrOH/TOL + PrOH/CHX, c) BuOH/TOL + BuOH/CHX and d) PeOH/TOL + PeOH/CHX as a function of alcohol concentration.

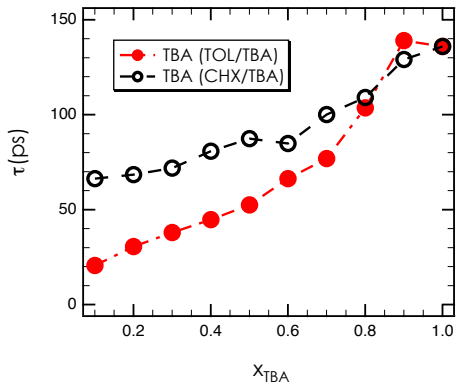

Figure 3.38: Variation of relaxation times in TBA/TOL + TBA/CHX as a function of TBA concentration.

in the dipolar relaxation. For Alcohols in TOL the HB sites increase as a function of $x_{alcohols}$. That generates a frequent "switch" of the liquid structure and, therefore, a faster relaxation response at higher TOL concentrations. The relaxation time of TBA molecules in CHX/TBA and in TOL/TBA is reported in Figure 3.38. As previously, slow relaxation time is observed for CHX/TBA systems while a rapid one evidenced in case of the TOL/TBA mixtures.

3.8 Conclusion

This work has focused on the exploration at the nanoscale of the non-ideality of methanol, ethanol, propanol, butanol, pentanol and tert-butanol in mixtures with toluene and cyclohexane by means of molecular dynamics simulations. Simulations fairly reproduced the experimental densities of all binary mixtures even at the miscibility region of methanol-cyclohexane binary mixtures. In all mixtures, the deviation from the ideal mixture behavior was observed and different intensities were recorded. In the case of toluene this non-ideality have been ascribed with the specific interactions between toluene and alcohol leading to a breaking in the hydrogen-bonding network involving clusters of different sizes and the spatial heterogeneity. Particularly, the immiscibility and the non-ideality (negative excess density) of the CHX-MeOH mixtures were the result of the unfavorable interactions between CHX and MeOH leading to a self-organizing of CHX molecules to form hydrophobic nano-phases at the origin of the structural heterogeneity in the miscible region. However, the non-ideality showed by ethanol, propanol, butanol, pentanol and tert-butanol (negative excess density except for low EtOH concentration) have been attributed to the hydrophobic character of CHX molecules with alcohols ones and the creation of largest clusters in comparison with alcohols in TOL. A strong dilution of the hydrogen bonding network by toluene molecules as well as cyclohexane molecules has been shown. Nanophases have been characterized in terms of pockets of linear clusters such that the difference in miscibility and in heterogeneity were understood in terms of cluster size and distribution for methanol-toluene and methanol-cyclohexane mixtures. Moreover, we have shown that the presence of clusters had to be uncorrelated from the notion of heterogeneity. Eventually, we have highlighted that the prepeak observed in the structure factor is independent of the degree of heterogeneity but is rather connected to the presence of cyclic clusters. Additionally, the dynamics of these liquids

were in line with the structural results given that a fast motion with a rapid relaxation times were shown by alcohol molecules in mixture with TOL whereas a slow motion with a long relaxation times of alcohols in CHX were captured. The results of this part allow us to differentiate between the intensity of the self-organization of liquids at their hydrogen bonding networks while distinguishing between ideal and non-ideal mixture in terms of microscopic local structuring.

Bibliography

[1] S. Dixit, J. Crain, W. C. K. Poon, J. L. Finney, and A. K. Soper. Molecular segregation observed in a concentrated alcohol?water solution. *Nature*, 416(6883):829–832, 2002.

[2] L. Dougan, S. P. Bates, R. Hargreaves, J. P. Fox, J. Crain, J. L. Finney, V. Reat, and A. K. Soper. Methanol-water solutions: A bi-percolating liquid mixture. *The Journal of Chemical Physics*, 121(13):6456–6462, 2004.

[3] Aziz Ghoufi, Ivanne Hureau, Ronan Lefort, and Denis Morineau. Hydrogen-bond-induced supermolecular assemblies in a nanoconfined tertiary alcohol. *The Journal of Physical Chemistry C*, 115(36):17761–17767, 2011.

[4] Martina Pozar, Bernarda Lovrincevicá, Larisa Zoranicá, Tomislav Primoracá, Franjo Sokolicá, and Aurelien Perera. Micro-heterogeneity versus clustering in binary mixtures of ethanol with water or alkanes. *Phys. Chem. Chem. Phys.*, 18:23971–23979, 2016.

[5] R. Mhanna, R. Lefort, L. Noirez, and D. Morineau. Microstructure and concentration fluctuations in alcohol,Ä-toluene and alcohol-cyclohexane binary liquids: A small angle neutron scattering study. *Journal of Molecular Liquids*, 218:198 – 207, 2016.

[6] Lester P. Kuhn. The hydrogen bond. i. intra- and intermolecular hydrogen bonds in alcohols1. *Journal of the American Chemical Society*, 74(10):2492–2499, 1952.

[7] Lorna Dougan, Jason Crain, John L. Finney, and Alan K. Soper. Molecular self-assembly in a model amphiphile system. *Phys. Chem. Chem. Phys.*, 12:10221–10229, 2010.

[8] Carl B. Kretschmer and Richard Wiebe. Thermodynamics of alcohol-Äêhydrocarbon mixtures. *The Journal of Chemical Physics*, 22(10):1697–1701, 1954.

[9] Goolla Narayana Swamy, Golla Dharmaraju, and Gurajala Kodanda Raman. Excess volumes of toluene mixtures with some alcohols at 303.15,ÄÇk. *Canadian Journal of Chemistry*, 58(3):229–230, 1980.

[10] R Thiyagarajan and L Palaniappan. Molecular interaction study of two aliphatic alcohols with cyclohexane. *CSIR*, pages 852–856, 2008.

[11] Pandharinath S. Nikam, Bapu S. Jagdale, Arun B. Sawant, and Mehdi Hasan. Densities and viscosities of binary mixtures of toluene with methanol, ethanol, propan-1-ol, butan-1-ol, pentan-1-ol, and 2-methylpropan-2-ol at (303.15, 308.15, 313.15) k. *Journal of Chemical & Engineering Data*, 45(4):559–563, 2000.

[12] Lucie Wilson, R. Bicca de Alencastro, and C. Sandorfy. Hydrogen bonding of n-alcohols of different chain lengths. *Canadian Journal of Chemistry*, 63(1):40–45, 1985.

[13] J. Turner and A. K. . The effect of apolar solutes on water structure: Alcohols and tetraalkylammonium ions. *The Journal of Chemical Physics*, 101(7):6116–6125, 1994.

[14] Christian Petersen, Artem A. Bakulin, Vlad G. Pavelyev, Maxim S. Pshenichnikov, and Huib J. Bakker. Femtosecond midinfrared study of aggregation behavior in aqueous solutions of amphiphilic molecules. *The Journal of Chemical Physics*, 133(16):164514, 2010.

[15] Guillaume Stirnemann, James T. Hynes, and Damien Laage. Water hydrogen bond dynamics in aqueous solutions of amphiphiles. *The Journal of Physical Chemistry B*, 114(8):3052–3059, 2010.

[16] I. Essafri and A. Ghoufi. Microstructure of nonideal methanol binary liquid mixtures. *Phys. Rev. E*, 99:062607, Jun 2019.

[17] Yoshimori Miyano and Walter Hayduk. Solubilities of butane, vapor pressures, and densities for benzene + cyclohexane, benzene + methanol, and methanol + cyclohexane solutions at 298 k. *Journal of Chemical & Engineering Data*, 38(2):277–281, 1993.

[18] A. Ghoufi, F. Goujon, V. Lachet, and P. Malfreyt. Surface tension of water and acid gases from monte carlo simulations. *The Journal of Chemical Physics*, 128(15):154716, 2008.

[19] F. Biscay, A. Ghoufi, and P. Malfreyt. Surface tension of water,Äìalcohol mixtures from monte carlo simulations. *The Journal of Chemical Physics*, 134(4):044709, 2011.

[20] F. Biscay, A. Ghoufi, V. Lachet, and P. Malfreyt. Prediction of the surface tension of the liquid-àívapor interface of alcohols from monte carlo simulations. *The Journal of Physical Chemistry C*, 115(17):8670–8683, 2011.

[21] A. Ghoufi and P. Malfreyt. Local description of surface tension through thermodynamic and mechanical definitions. *Molecular Simulation*, 39(8):603–611, 2013.

[22] Geraldine A. Torin-Ollarves, M. Carmen Martin, Cesar R. Chamorro, and Jose J. Segovia. Densities, viscosities, and isobaric heat capacities of the system (1-butanol+cyclohexane) at high pressures. *The Journal of Chemical Thermodynamics*, 74:153 – 160, 2014.

[23] Ohji Hiroyuki. Excess volumes of (1-pentanol + cyclohexane or benzene) at temperatures between 283.15 k and 328.15 k. *The Journal of Chemical Thermodynamics*, 34(6):849 – 859, 2002.

[24] Kazimierz Jerie, A. Baranowski, and Jacek Glinski. Structure of cyclohexane + t-butanol mixtures from positron annihilation and ultrasonic velocity measurements. 1993.

[25] Sergei Yu. Noskov, Guillaume Lamoureux, and Benoit Roux. Molecular dynamics study of hydration in ethanol-water mixtures using a polarizable force field. *The Journal of Physical Chemistry B*, 109(14):6705–6713, 2005.

[26] Ming-Liang Tan, Benjamin T. Miller, Jerez Te, Joseph R. Cendagorta, Bernard R. Brooks, and Toshiko Ichiye. Hydrophobic hydration and the anomalous partial molar volumes in ethanol-water mixtures. *The Journal of Chemical Physics*, 142(6):064501, 2015.

[27] R. Baskaran and T.R. Russ. Kubendran. Density and excess molar volume in a binary mixture of o-anisaldehyde and chlorobenzene at 303.15, 313.15, and 323.15 k. *Russian Journal of Physical Chemistry*, 83(3):350?352, 2009.

[28] Tasneem Shadma Ali Anwar and Nabi Firdosa. Volumetric, viscometric, and ultrasonic properties of liquid mixtures of cyclohexane with alkanols at different temperatures. *Journal for Natural Research A*, 65:8–9, Jun 2014.

[29] Akl M. Awwad and Malyuba A. Abu-Daabes. Densities, viscosities, and excess properties of (n-methylmorpholine+cyclohexane, +benzene, and +toluene) at t=(298.15, 303.15, 313.15, 323.15)k. *The Journal of Chemical Thermodynamics*, 40(4):645 – 652, 2008.

[30] S. Dixit, J. Crain, W. Poon, J. Finney, and A. K. Soper. Molecular segregation observed in a concentrated alcohol-water solution. *Nature*, 416:829, 2002.

[31] Henry S. Frank and Marjorie W. Evans. Free volume and entropy in condensed systems iii. entropy in binary liquid mixtures; partial molal entropy in dilute solutions; structure and thermodynamics in aqueous electrolytes. *The Journal of Chemical Physics*, 13(11):507–532, 1945.

[32] J.-H. Guo, Y. Luo, A. Augustsson, S. Kashtanov, J.-E. Rubensson, D. K. Shuh, H. Ågren, and J. Nordgren. Molecular structure of alcohol-water mixtures. *Phys. Rev. Lett.*, 91:157401, Oct 2003.

[33] Alan. K. Soper, Lorna Dougan, Jason Crain, and John. L. Finney. Excess entropy in alcohol-àíwater solutions:Äâ a simple clustering explanation. *The Journal of Physical Chemistry B*, 110(8):3472–3476, 2006.

[34] Hendrick C. Van Ness, Jon Van Winkle, Herbert H. Richtol, and Henry B. Hollinger. Infrared spectra and the thermodynamics of alcohol-hydrocarbon systems. *The Journal of Physical Chemistry*, 71(5):1483–1494, 1967.

[35] Aaron N. Fletcher. Effect of carbon tetrachloride upon the self-association of 1-octanol. *The Journal of Physical Chemistry*, 73(7):2217–2225, 1969.

[36] Yanting Wang and Gregory A. Voth. Tail aggregation and domain diffusion in ionic liquids. *The Journal of Physical Chemistry B*, 110(37):18601–18608, 2006.

[37] Song Li, Jose Leobardo Banulos, Pengfei Zhang, Guang Feng, Sheng Dai, Gernot Rother, and Peter T. Cummings. Toward understanding the structural heterogeneity and ion pair stability in dicationic ionic liquids. *Soft Matter*, 10:9193–9200, 2014.

[38] Denis Morineau and Christiane Alba-Simionesco. Liquids in confined geometry: How to connect changes in the structure factor to modifications of local order. *The Journal of Chemical Physics*, 118(20):9389–9400, 2003.

[39] Aziz Ghoufi, Ivanne Hureau, Denis Morineau, Richard Renou, and Anthony Szymczyk. Confinement of tert-butanol nanoclusters in hydrophilic and hydrophobic silica nanopores. *The Journal of Physical Chemistry C*, 117(29):15203–15212, 2013.

[40] Richard Renou, Anthony Szymczyk, and Aziz Ghoufi. Water confinement in nanoporous silica materials. *The Journal of Chemical Physics*, 140(4):044704, 2014.

[41] Marta Falkowska, Daniel T. Bowron, Haresh G. Manyar, Christopher Hardacre, and Tristan G. A. Youngs. Neutron scattering of aromatic and aliphatic liquids. *ChemPhysChem*, 17(13):2043–2055, 2016.

[42] Alenka Luzar and David Chandler. Effect of environment on hydrogen bond dynamics in liquid water. *Phys. Rev. Lett.*, 76:928–931, Feb 1996.

[43] Peter Kruger, Sondre K. Schnell, Dick Bedeaux, Signe Kjelstrup, Thijs J. H. Vlugt, and Jean-Marc Simon. Kirkwood-Äìbuff integrals for finite volumes. *The Journal of Physical Chemistry Letters*, 4(2):235–238, 2013.

[44] Noura Dawass, Peter Kruger, Sondre K. Schnell, Jean-Marc Simon, and T.J.H. Vlugt. Kirkwood-buff integrals from molecular simulation. *Fluid Phase Equilibria*, 486:21 – 36, 2019.

[45] G. Ravishanker, P. K. Mehrotra, M. Mezei, and David L. Beveridge. Aqueous hydration of benzene. *Journal of the American Chemical Society*, 106(15):4102–4108, 1984.

[46] Hideaki Takahashi, Daiki Suzuoka, and Akihiro Morita. Why is benzene soluble in water? role of oh/π interaction in solvation. *Journal of Chemical Theory and Computation*, 11(3):1181–1194, 2015.

[47] Kamil P. Gierszal, Joel G. Davis, Michael D. Hands, David S. Wilcox, Lyudmila V. Slipchenko, and Dor Ben-Amotz. π-hydrogen bonding in liquid water. *The Journal of Physical Chemistry Letters*, 2(22):2930–2933, 2011.

[48] Michinori. [UNK]Oki and Hiizu. Iwamura. Steric effects on the o-h...œÄ interaction in 2-hydroxybiphenyl. *Journal of the American Chemical Society*, 89(3):576–579, 1967.

[49] Yan Zhao, Oksana Tishchenko, and Donald G. Truhlar. How well can density functional methods describe hydrogen bonds to œÄ acceptors? *The Journal of Physical Chemistry B*, 109(41):19046–19051, 2005.

[50] Sakae Suzuki, Peter G. Green, Roger E. Bumgarner, Siddharth Dasgupta, William A. Goddard, and Geoffrey A. Blake. Benzene forms hydrogen bonds with water. *Science*, 257(5072):942–945, 1992.

[51] A. Ghoufi, F. Artzner, and P. Malfreyt. Physical properties and hydrogen-bonding network of water,-ethanol mixtures from molecular dynamics simulations. *The Journal of Physical Chemistry B*, 120(4):793–802, 2016.

[52] P.S. Tofts, D. Lloyd, C.A. Clark, G.J. Barker, G.J.M. Parker, P. McConville, C. Baldock, and J.M. Pope. Test liquids for quantitative mri measurements of self-diffusion coefficient in vivo. *Magnetic Resonance in Medicine*, 43(3):368–374, 2000.

[53] J. R. PARTINGTON, R. F. HUDSON, and K. W. BAGNALL. Self-diffusion of aliphatic alcohols. *Nature*, 169(4301):583–584, 1952.

[54] Kerry C. Pratt and William A. Wakeham. Self-diffusion in water and monohydric alcohols. *J. Chem. Soc., Faraday Trans. 2*, 73:997–1002, 1977.

[55] David W. McCall and Dean C. Douglass. Self-diffusion in the primary alcohols. *The Journal of Chemical Physics*, 32(6):1876–1877, 1960.

[56] Makio Iwahashi, Yoko Ohbu, Tadashi Kato, Yumi Suzuki, Kazuhiro Yamauchi, Yoshimi Yamaguchi, and Mitsuo Muramatsu. The dynamical structure of normal alcohols in their liquids as determined by the viscosity and self-diffusion measurements. *Bulletin of the Chemical Society of Japan*, 59(12):3771–3774, 1986.

[57] Manfred Holz, Stefan R. Heil, and Antonio Sacco. Temperature-dependent self-diffusion coefficients of water and six selected molecular liquids for calibration in accurate 1h nmr pfg measurements. *Phys. Chem. Chem. Phys.*, 2:4740–4742, 2000.

[58] P. Petong, R. Pottel, and U. Kaatze. Dielectric relaxation of h-bonded liquids. mixtures of ethanol and n-hexanol at different compositions and temperatures. *The Journal of Physical Chemistry A*, 103(31):6114–6121, 1999.

Chapter 4

Microphase separation of binary liquids mixture under nanoscale confinements

Contents

4.1 Introduction

Liquids behavior in regions of several molecular diameters can change completely once confined. More precisely, significant attention has been devoted to the structure and dynamics of nano-confined water owing its crucial role in biosystems. Any confined fluid behaves differently with respect to volume due to the presence of wall surfaces and the finite size of the pore in one or more dimensions. In this work, we elucidates the impact of a hydrophobic and hydrophilic confinement on the hydrogen bonding (HB) network of polar liquids at the nanoscale. The understanding of such phenomena is of wide interest for the design of new materials that could be used for heterogeneous catalysis, membrane separation, lubrication, drug delivery and petroleum recovery with no energy cost.

According to knight [1] et al. the confinement effect on the physical properties of water is governed by the changes in the HB network of water that is impacted by the creation of liquid-silica surface HBs interactions. Kremer et al. [2] studied poly(propylene glycol) in bulk state and in confined media within a native (hydrophilic) and a silanized (hydrophobic) unidirectional silica nanopores with average diameters of 4, 6 and 8 nm. Astonishingly, they distinguished between the surface effect and the confinement effect. Molecules near the surface wall are subjected to the surface effect, and the molecules far from the surface wall are subject to confinement effect. These three decades the confinement effects on the physics of fluids have been been intensively studied [3–17]. Many new properties have been then discovered such as the giant diffusion of liquids [18–20], the apparition of new phases and new transitions [21–24], giant dielectric properties [13, 14, 25–27], the increase of optical properties [28], and the possible mixing of non-miscible mixtures [29]. These observations indicated that the classical understanding of the physics of liquids should be revisited in confined geometry. Whereas these effects have been largely investigated in the case of confined single components [3–16] and immiscible binary mixtures [30–32] less works have been devoted to the confinement of miscible liquid mixtures [17, 33, 34].

Recently, Muthulakshmi and coworkers reported an experimental evidence of a partial phase separation of an ethanol-water mixture confined in mesoporous silica using positron annihilation lifetime spectroscopy. They showed that a small fraction of the ethanol molecules seemed to be anchored at the silica surface [35]. A similar results was also established by Guo et al. who have

studied confinement of an ethanol-water mixture between two planar silica walls [16]. A partial and local separation between water and ethanol close to the silica surface were thus evidenced [16]. In the same time Schmitz et al. have exhibited that the glycol-water mixture could undergo an interfacial separation [36]. This phenomenon was also numerically observed by You et al. who exhibited a local demixing of binary hard-core Yukawa mixtures in a slitlike pore [37]. More recently, Krycka et al. displayed a separation between two confined apolar liquids [34]. Whereas these works only suggest a partial separation of two hydrogen bonds forming liquids or two apolar liquids near the solid surface. Morineau and coworkers have recently provided a direct experimental structural evidence of the microphase separation of macroscopically miscible liquids consisting of a hydrogen bonds forming liquid and an apolar one [17]. They showed that a mixture of toluene (TOL) and *tert*-butanol (TBA) with a TBA/TOL volume fraction composition of 56/44% can demix and form a core-shell organization in a confined medium, where this mixture is fully homogenous in the bulk phase [17]. Up to now, the physical mechanism ruling this phase separation at the nanometric scale stays unknown. In this context, we suggest that this structure is the result of a peculiar hydrogen bond network.

In this part, we deeply study the microscopic structure of pure and binary liquids and the possibility to control the micro-phase separation under nanoscale confinement. Additionally, we aim to explore the role of the hydrophobic/hydrophilic nanopore in the microphase separation. To do so, we studied *tert*-butanol (TBA), toluene (TOL) and cyclohexane (CHX) and their binary mixtures as previously studied in the bulk phase, into confined media. The hydrophilic matrix is a water nanotube (WNT) characterized by OH heads that promotes the creation of strong interactions with liquids that form hydrogen bonds, such as TBA. In fact, the hydrophobic matrix is a carbon nanotube (CNT) that is characterized by carbon on its surface and can provide only weak interactions: couloumbiennes. Silica Nanopore (MCM-41) were used as weakly hydrophilic matrix. We also studied the effect of the pore size through the comparison between 2 radius sizes (r = 1nm and r=2nm) for WNT and CNT.

4.2 Confinement versus heterogeneity

4.2.1 Confinement through the silica cylindrical nanopore

By combining contrast matching from neutron scattering and a core-shell model (CS), Hamid et al. showed that a mixture of toluene (TOL) and tert-butanol (TBA) with a TBA/TOL volume fraction composition of 56/44% confined in cylindrical silica (MCM-41) of radius of 24 Å can separate [17], whereas this mixture is fully homogeneous in the bulk phase. In this CS model, TBA and TOL are, respectively, located close to the silica surface and at the centre of the pore. This peculiar structure is ascribed to the HBs between the TBA molecules and the silanol (SiOH). In this part, we aim to capture this Core-Shell (CS) structure and clarify the microscopic driving force that governs it. MD simulations of pure TBA, pure TOL and TBA/TOL mixtures were thus conducted in confined phase. For consistency with the experiments, the confined medium corresponds to a cylindrical silica nanopore with a radius of 24 Å. Notably, a highly hydrophilic nanopore with a ratio of 7.5 OH/nm^2 was considered to intensify the hydrogen-bond interactions between TBA and the silica surface and to promote the CS organisation. Indeed, experimentally, a ratio of 2.5 - 3.0 OH/nm^2 was measured.

4.2.2 Numerical evidence of the absence of a core-shell structure

We report in Figure 4.1 (a), the S_{HO} of pure TBA and TBA/TOL mixture with a TBA/TOL molar fraction composition of 56/44% in the bulk and confined phases. This fraction was chosen for consistency with the concentration used in neutron diffraction experiments [17]. As shown in Figure 4.1 (a), in the bulk phase, the main peak that is located at approximately 0.8 $Å^{-1}$ for pure TBA is slightly shifted toward 0.7 $Å^{-1}$ for the mixture. The presence of this peak in both cases is related to the persistence of TBA clusters in the mixture. The lessening in intensity highlights a partial dilution of the aggregates i.e. a breaking of clusters. This situation was clarified by the calculation of cluster size, which shows a decrease in cluster size from 3.9 molecules per aggregate for the pure TBA to 2.9 in the TBA/TOL mixture. The calculation of cluster size is based on the hydrogen bond computation. The decrease in size of TBA aggregates in the mixture is then the result of dilution of the hydrogen bonding network (i.e. a rupture of the HB network) [38, 39]. As shown in Figure 4.1 (a) , the position of the main peak of S_{HO}

for both confined situations (pure component and mixture) is similar to the position in the bulk phases. A decrease in intensity caused by the excluded volume is also observed [40]. This result appears to indicate that the long-range correlations of the TBA molecules in both confined and bulk phases are similar. Indeed, the cluster size of TBA aggregates in pure confined TBA is approximately 3.3 molecules per aggregate, whereas this value is 2.3 for the confined mixture. This decrease in cluster size is the same order of magnitude in both confined and bulk phases. These results show an absence of a CS organization. Indeed, in the case of a total demixing, the cluster size of TBA in both confined situations (pure TBA and TBA/TOL mixture) should be similar.

To highlight the local structure, the density profiles of the methyl groups of TBA (C_{TBA}) and carbon atoms of TOL (C_{TOL}) along the radial direction of the cylindrical pore are reported in Figure 4.1 (b). Given the excluded volume effect caused by the confinement in the radial direction, a layering structure is observed for both TBA and TOL, with a maximum density near the silica surface located at 24 Å. For both TBA and TOL, four layers are observed; these layers are related to the size of the molecules. As shown in Figure 4.1(b), the TOL and TBA molecules sample all positions from r = 0 to r = 20 Å (r is the radial position extending into the

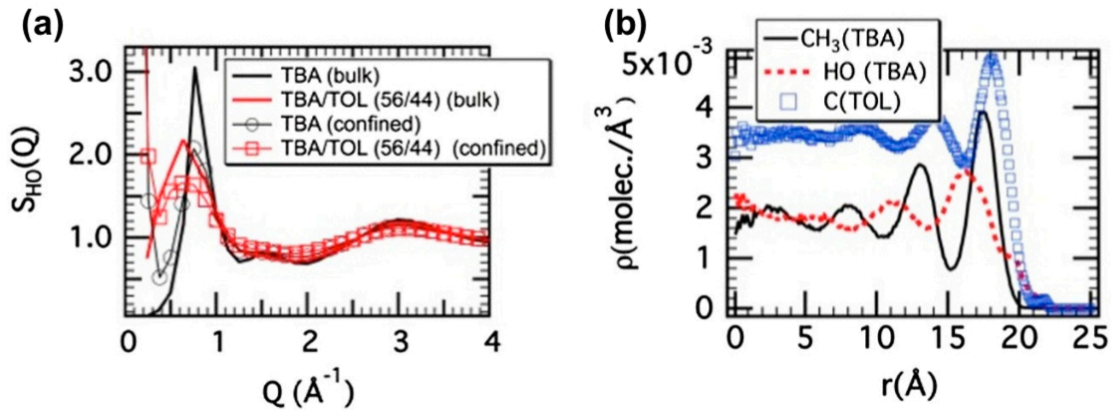

Figure 4.1: (a) Partial structure factors of hydrogen atoms of OH groups of TBA, SHO of pure liquids and of TBA/TOL mixture with a TBA/TOL molar fraction composition of 56/44% at 298 K and 1 bar in the confined and bulk phases. (b) Profiles of radial density of carbon atoms of TOL, hydrogen atoms of the OH group of TBA and carbon atoms of the methyl group of TBA in the TBA/TOL mixture with a TBA/TOL molar fraction composition of 56/44%

cylindrical nanopore), which emphases the absence of a CS organisation. Figure 4.1 (b) depicts a slight shoulder of HO density at r = 20 Å, whereas a large amount of TBA is located from the centre of the pore to 16 Å. In contrast, the carbon atoms of the methyl groups of TBA and the benzenic cycles of TOL are closer to the silica surface than the HO atoms, which suggests hydrophobic anchoring [41]. This structural behaviour is the result of the preferential hydrogen bonding of TBA between two TBA layers [41]. Using a CS model, Hamid et al. have shown that TBA preferentially adsorb on the silica surface. This discrepancy between both works shows that other models can be envisaged to fit the experimental data. Indeed, in their work, Hamid et al. used three models (TBA at the centre, TBA at the interface and homogenous case).

4.2.3 Validation of the force field and computational procedure

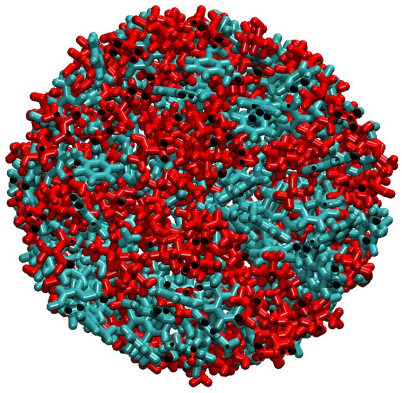

Figure 4.2: Illustration of confined TBA (red)/TOL(cyan) mixture into the cylindrical nanopore obtained from the force field developed by Brodka and Zerda [42]. For clarity, silica framework is removed. This Figure shows that TBA (red colour) and TOL (cyan colour) molecules sample as well the surface as centre of pore.

To verify our numerical result reflecting an absence of segregation, the silica force field developed by Brodka and Zerda [42] was also considered. Figure 4.2 obviously shows an absence of core-shell organisation that demonstrates that the so-obtained structure is independent of the force field. Additionally, MD simulation of a TBA/TOL mixture with a TBA/TOL molar fraction composition of 35/65% was also considered. We report thus in Figure 4.3 (a) and (b), the radial density of TBA and TOL for both 35/65% and 56/44% molar fraction composition. As shown in Figure 4.3 (a) and (b) for both molar compositions TOL and TBA molecules are located at the same position that highlights an absence of full demixing and a CS organisation.

To really highlight a possible micro phase separation, we report in 4.3 (c) and (d), the local molar fraction for both compositions. For both molar fractions, a homogenous mixture was observed at the centre of pore (from 0 to 5 Å). Into the layers, the increase in x_{TBA} is compensated by a decrease in x_{TOL} and reciprocally that involves a homogenous composition of TOL and TBA. Interestingly, close to the silica surface (around 20 Å) a slight interfacial segregation is observed because $x_{TBA} = 1.0$ in both cases. Although, a local demixing is highlighted close to the silica surface it does not propagate into the nanopore to form a CS structure. This is probably due to the weak hydrophilic interactions between the silica material and TBA. Interestingly, close to

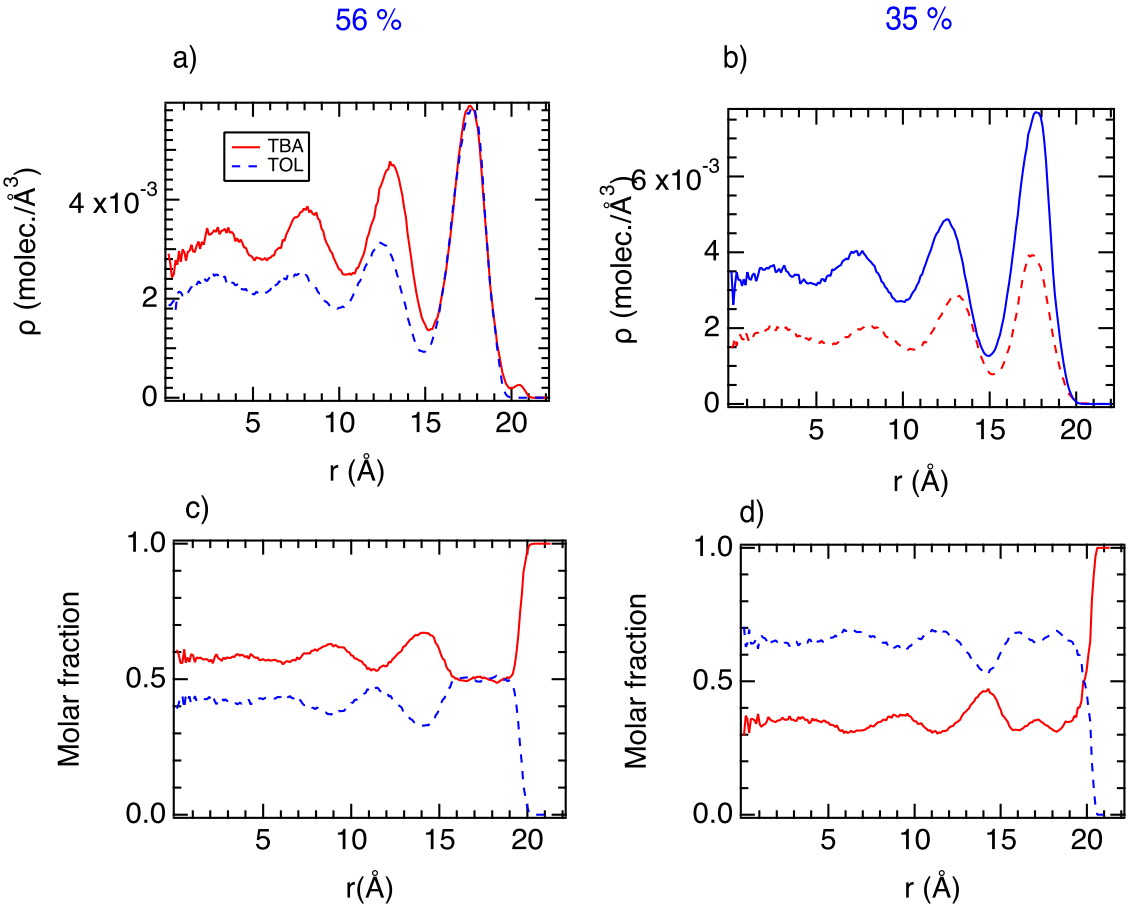

Figure 4.3: a) Profiles of radial density of centre of mass of TOL and TBA confined into the silica nanopore with a TBA/TOL molar fraction composition 56/44% such as the silica framework is described with the model of Brodka and Zerda [42]. (b) Profiles of radial density of centre of mass of TOL and TBA confined into the silica nanopore with a TBA/TOL molar fraction composition 35/65%.

the silica surface (around 20 Å) a slight interfacial segregation is observed because x_{TBA}=1.0 in

both cases. Although, a local demixing is highlighted close to the silica surface it does not propagate into the nanopore to form a CS structure. This is probably due to the weak hydrophilic interactions between the silica material and TBA. MD simulations combining hydrogenated and deuterated TBA and TOL have been conducted to exactly mimic the situation [17] (Figure 4.4). Furthermore, a long simulation (250 ns) of confined TBA/TOL with a TBA/TOL molar fraction composition 56/44% was also performed. In all cases, an absence of a CS structure is observed. Additionally, an initial CS configuration with TBA close to the silica surface and TOL at the centre of pore was considered. After 0.7 ns the initial CS organisation was broken to obtain an heterogeneous mixture. This result shows that the CS organisation is unstable and that the so-obtained results are not MD-time dependent while our MD simulations are well converged. Eventually, mean square displacement of TOL and TBA were also computed, both TBA and TOL molecules are moved of 24 and 15 Å along the axial and radial directions, respectively. This result shows that the simulation is ergodic and is long enough to allow the system to visit all of its energetically relevant states. How to thus explain the absence of the extinction of Bragg's peak (EBP) from neutron diffraction measurements [17] ? The CS organisation was highlighted by

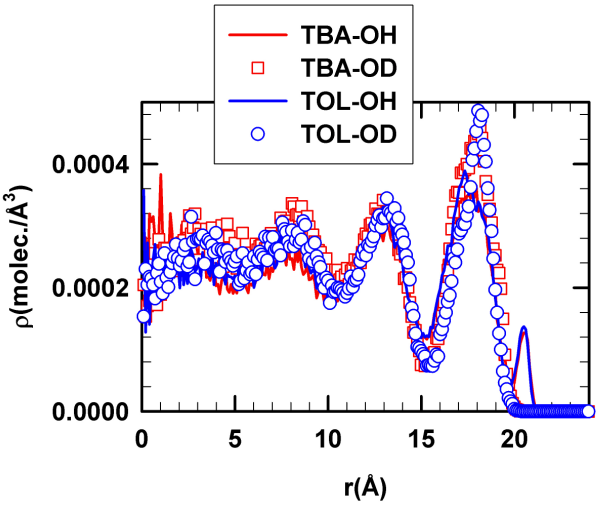

Figure 4.4: Profiles of radial density of centre of mass of hydrogenated (OH) and deuterated (OD) TOL and TBA confined into the silica nanopore with a TBA/TOL molar fraction composition 56/44% and with a deuterated/hydrogenated composition 50/50% for TOL and TBA.

adjusting the experimental data from a CS model but only two models were attempted, CS and the homogenous case. As the extinction of Bragg's peak is often associated to the heterogeneity

we explored it.

4.2.4 Molecular interpretation of neutron scattering measurements

We report in Figure 4.5 (a), a representation of the Connolly surface of TBA and TOL in the confined TBA/TOL mixture. As observed in Figure 4.5 (a), the confined TBA/TOL mixture appears to be heterogeneous given the presence of TBA and TOL nanophases. Indeed, Figure 4.5 (a) clearly depicts alternating TBA and TOL phases related to a local demixing, highlighting an absence of homogeneity. To quantify this spatial heterogeneity, the heterogeneity order parameter was calculated [43,44]. As it mentioned before, the value of HOP increases with increasing spatial heterogeneity because a tighter packing of sites results in a smaller r_{ij}, which leads to a larger HOP. Calculations were performed for both bulk and confined phases. For pure TBA and a TBA/TOL mixture in the bulk phase, HOP = 8.69 and HOP = 12.55, respectively. To verify that the so-calculated HOP is not affected by the layering organisation in the nanopore, the HOP was evaluated at the centre of the pore. For the confined TBA, a value of HOP = 16.93 was found, which indicates heterogeneity (>15.74), likely because of the confinement effect. For the confined TBA/TOL, HOP = 21.76. This strong increase with respect to the HOP of confined pure TBA clearly indicates the presence of strong heterogeneity, as previously observed in Figure 4.5 (a). These results shows that the absence of the extinction of Bragg's peak is in relation to the strong heterogeneity-inducing nanophases. This work allowed us to purpose another scenario that CS is one. MD simulations allowed us to clarify the confined structure by highlighting strong heterogeneity of the confined TBA/TOL mixture with respect to the bulk phase. This increase in heterogeneity with respect to the bulk phase is ascribed to the hydrophobic interactions of TOL and TBA with the silica surface. Indeed, as shown in Figure 4.1(a), the carbon atoms of both compounds preferentially adsorb onto the surface. A hydrophobic and hydrophilic network (related to HBs) can develop from the first adsorbed TOL and TBA molecules, driving local demixing, as shown in Figure 4.5 (a) contrary to the bulk phase where the mixture is homogeneous (see Figure 4.6). Therefore, this local demixing, which induces strong heterogeneity, is likely the physical process observed from neutron scattering measurements [17]. To understand the mechanism of formation of local demixing, grand-canonical Monte Carlo (GCMC) simulations

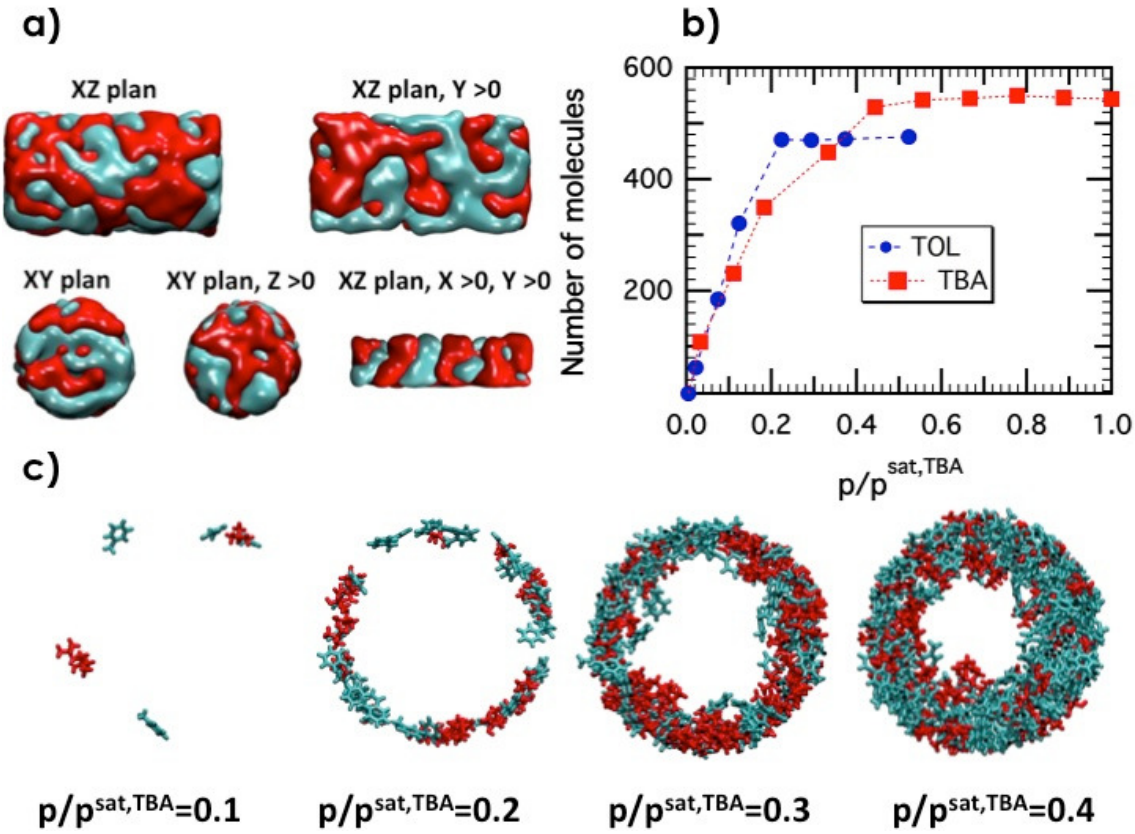

Figure 4.5: (a) Connolly's surface of confined TBA (red)/TOL(cyan) mixture in the cylindrical nanopore in different directions. (b) Isotherms of adsorption of pure TBA and TOL in the silica framework. (c) Illustration of confined TBA (red)/TOL(cyan) mixture in the cylindrical nanopore for four relative pressures. For clarity, the silica framework is omitted.

for different relative pressures were conducted. As shown in Figure 4.5 (b), the adsorbed amounts of pure TBA and TOL differ at low pressures, which suggests different affinities of TOL and TBA for the silica material.

To quantify the host-guest interactions, the isosteric heat of adsorption was computed for pure TBA and TOL at low loading. This result suggests a higher affinity of TOL with the silica surface, corroborating the hypothesis that the hydrophobic interactions rule the physisorption onto the silica nanopore, consistent with the so-observed structure. Figure 4.5 (c) shows snapshots of gradual nanopore filling by the TBA/TOL mixture with a TBA/TOL molar fraction composition of 56/44%. As shown in Figure 4.5 (c), no specific organisation is observed regardless of the pressure. However, local segregation and formation of nanophases are observed, and the sizes of the nanophases increase spatially with increasing pressure. Therefore, the heterogeneous

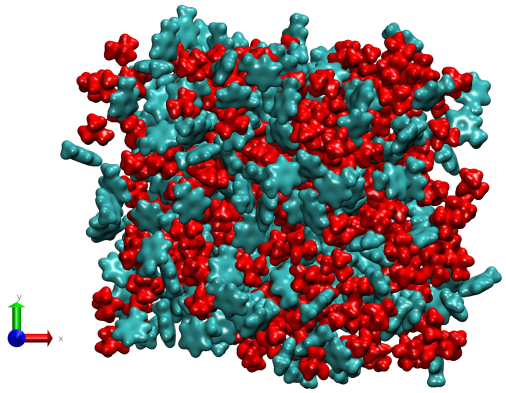

Figure 4.6: Illustration of TBA (red)/TOL(cyan) mixture in the bulk phase for a TBA/TOL molar fraction composition 56/44%.

anchoring that occurs at low pressures could act as a 'germ' of the heterogeneity. Additional TBA and TOL molecules are progressively adsorbed through HBs and hydrophobic interactions, respectively, leading to TBA and TOL nanophases. Eventually, the growth of these nanophases induces local demixing and heterogeneity. This interfacial heterogeneity seems to be ruled by (i) the difference in silica/fluids interactions between TOL and TBA as suggested from the calculation of Q_{st} and (ii) by the favourable hydrogen bonds between two TBA layers [38].

In this part, we showed that the nano-confinement induces strong heterogeneity, causing the absence of the extinction of Bragg's peak from neutron diffraction measurements. Our results illuminate another scenario based on the local segregation rather than a core-shell organisation of the confined TBA/TOL mixture. Ultimately, we show that the underlying mechanism is based on the formation and growth of a 'germ' of heterogeneity, leading to the formation of nanophases. Although this study highlights an absence of a CS structure of the confined TBA/TOL binary liquid into the hydrophilic nanopores, it would be worthwhile to study the behavior of other confined mixtures, size pore effect and the confinement through a hydrophobic medium as the carbon nanotubes.

4.3 Role of hydrophobicity and hydrophilicity

Now, to provide a full picture of the microphase separation, two different confining surfaces were used in this part. We have studied the behavior of TOL/TBA and we have compared it with

CHX/TBA mixture confined through a totally hydrophilic matrix and a totally hydrophobic matrix. Firstly, we study the microstructure of the so-mentioned mixtures in both nanopores of 2 nm pore size. In the second part, pore size effect on the microphase separation will be evaluated.

4.3.1 Strong and weak affinities impact

In Figure 4.7(a)-(b) the radial density profiles of confined pure TBA, TOL and CHX are reported. Figure 4.7(a)-(b) compares the radial density behavior of these three components within hydrophobic (Fig. 4.7 (a)) and hydrophilic (Fig. 4.7 (b)) nanopores. Interestingly, Figures 4.7 (a)-(b) indicate strong inhomogeneity in the density distribution of these liquids under both confinements. Furthermore, a formation of several layers around the wall surface are also observed. In the CNT (see Fig. 4.7 (a)) TOL in comparison with TBA and CHX is the closest molecule to the wall surface. This strong affinity with the CNT wall surface is attributed to the aromatic ring of TOL. This indeed promotes the interaction with the carbon atoms of the nanotube that could explain the strongest preferential layering of TOL near the wall surface. Interestingly, TOL pseudo-periodic modulation showed in the local density has been seen to propagate into the confined volume but it damped and gradually disappears. This means that TOL gradually loses memory of the wall and tends to assume again the bulk structure. However, the hydrophilic

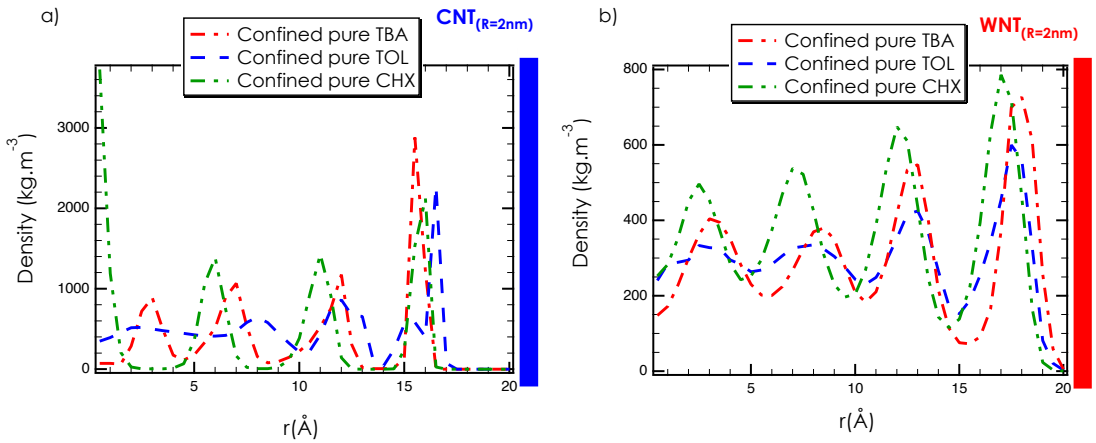

Figure 4.7: a) Radial density profile of pure confined TBA, TOL and CHX within a) Carbon nanotube (CNT) with r= 2nm and b) Water nanotube (CNT) with r= 2nm.

confinement effects on these pure liquids that is depicted in Figure 4.7 (b), points out a wave

like structure for all liquids with a period that remains constant as the radius increases. The distance between two concentration peaks is approximately 5 Å. Interestingly, TOL showed the same layering behavior which means that TOL can be restored to its bulk organization after 2 layers in both confinement. This may be due to the fact that Toluene has π-π interactions and a methyl group that makes it interact in both forms of environments in two ways. TBA molecules in the WNT are the closest molecules in comparison with TOL and CHX that could have resulted from the creation of a strong interaction with the confining surface. Snapshots observations are extracted from simulations and presented in Figure 4.8 (a) to (c) and (a') to (c'). We observe a layering-like structure of confined pure TBA, TOL and CHX in both types of confinement as it illustrated by the radial profile represented in Figure 4.7.

In order to have a good description of the local strong or weak affinity showed in both nanotubes, we present in Figure 4.9 the comparison of the radial atomic profile of TOL, CHX and TBA. Furthermore, we aim to zoom out on the preferential orientation of the molecules in the first layer. That could explain the affinity between TBA and the surface in the hydrophilic confinement. That allows us to check the affinity of TOL with the CNT wall. Figure 4.9 compares the local atomic density of pure TBA, TOL and CHX within the two confinements.
As shown in Figure 4.9 (a), under hydrophobic confinement, we can observe that TBA's methyl parts point toward the surface contrary to the hydroxyl tail. Indeed, the carbon atoms of the

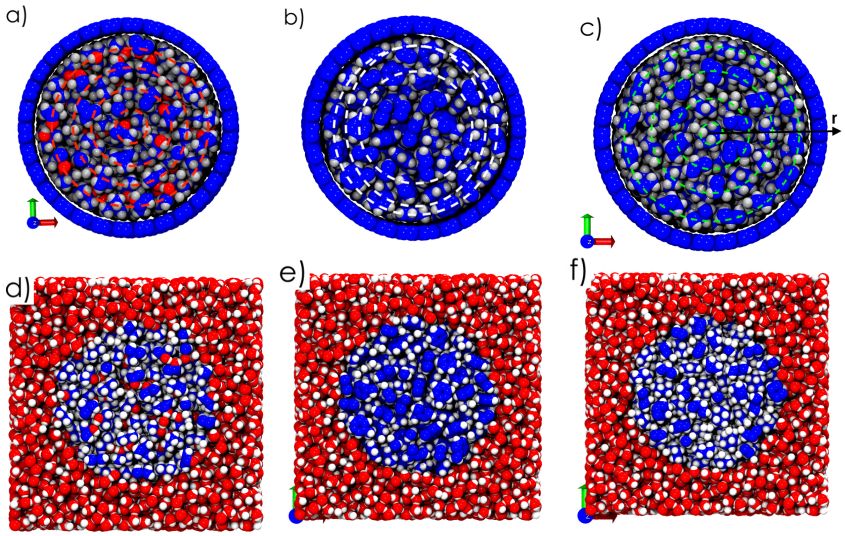

Figure 4.8: Illustrations of pure (a)-(d) TBA, (b)-(e) TOL and (c)-(f) CHX confined in CNT and in WNT, respectively.

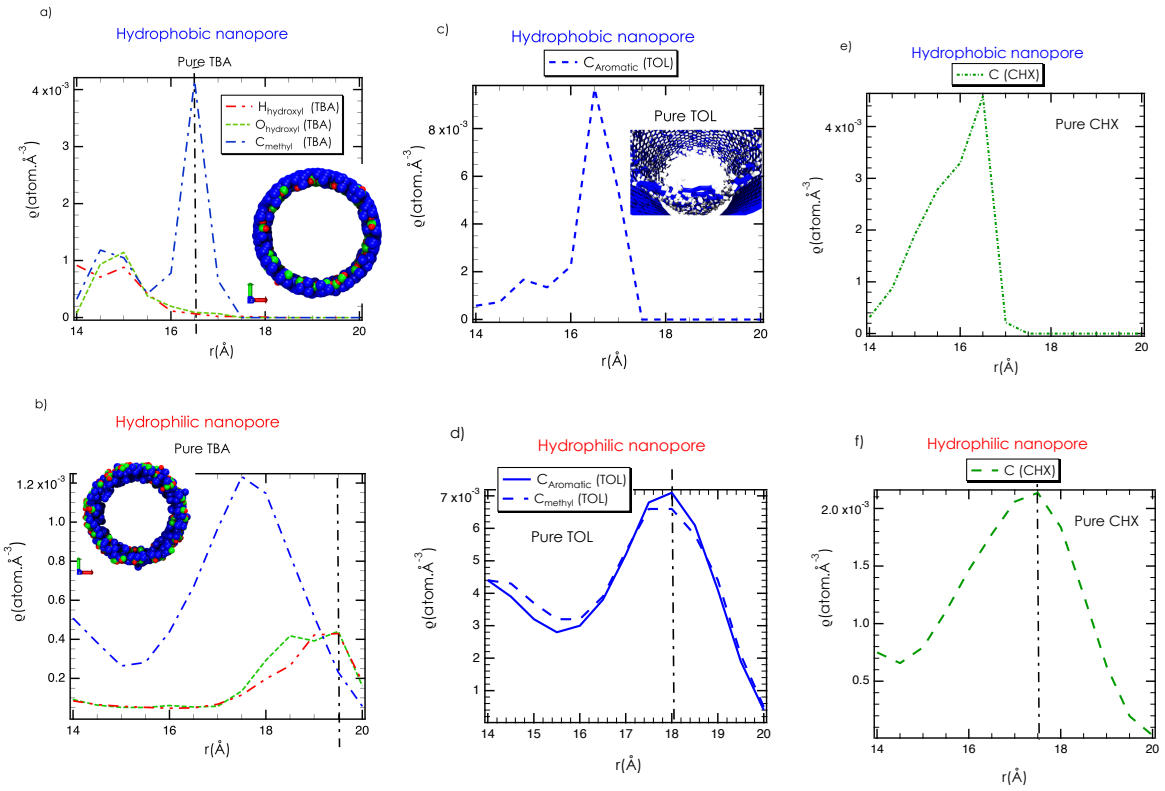

Figure 4.9: Atomic radial density profile of pure TBA (oxygen, hydrogen (HO part) and carbon of (CH_3) and TOL (carbon atoms of aromatic ring) and CHX (carbon atoms) confined within CNT (a,c,e) and within WNT (b,d,f), respectively.

methyl part of TBA are located around 16.5 Å while the oxygen and hydrogen atoms are located at 15 Å. This is evidenced by the structural snapshot in the same graph. As shown in Figure 4.9 (b), when we switch to the hydrophilic confinement in this case, we find an opposite behavior. A first peak is highlighted at 19.5 Å but the atoms of the hydroxyl part of TBA are closely anchored to the surface although the TBA methyl group's carbons are positioned at 17 Å. This means that the hydroxide groups are oriented towards the wall surface while the methyl groups are founded behind. This change in structural behavior can be explained by the presence of hydrophobic interactions between the methyl groups of TBA molecules and the carbon atoms of CNT. In the case of WNT, this affinity with the surface of TBA hydroxyl groups can be probably attributed to the creation of hydrogen bond type interactions with the surface.

The radial profile of the carbon atoms of the aromatic part and the carbon of TOL's methyl group is shown in Figures 4.9 (c) and 4.9 (d). Figure 4.9 (c) shows a preferred locations of the aromatic part of TOL with the hydrophobic wall surface. This figure shows a peak at 16.5 Å

and a second peak at 15 Å that depicts two different preferential locations close to the surface. However the molecules are rather adsorbed on the surface from stacking interactions between aromatic cycles. In the WNT, the two peaks of carbon atom profiles of the aromatic part and the methyl part of the TOL are found at a similar distance around 18 Å (see Fig. 4.9 (d)). This may be due to the creation of a strong interaction with the confining wall that requires a specific orientation. It is interesting to note that there is a broader peak observed in hydrophilic confinement that can be in favor of a specific structure close to the surface. Different preferred locations at the surface are illustrated by the presence of a large peak between 17 and 20 Å.
In the case of cyclohexane in hydrophobic confinement, we observe a very sharp peak around 16.8 Å with a shoulder at 15.5 Å which indicates that we have two preferred locations next to the confining surface. This can be explained by the creation of different hydrophobic interactions with the carbon nanotube (hydrophobic anchoring). In hydrophilic confinement the CHX has a broad peak ranging from 14.5 Å to 20 Å which emphasizes the fact that in hydrophilic confinement the CHX molecules do not have a preferential location near the surface. That's why we have a distance gap of 3 or 4 Å next to the surface.

4.3.2 Local demixing evidence of confined miscible mixtures

The behavior of binary mixtures of TOL/TBA and CHX/TBA confined in two frameworks is now studied and compared in this section. The local structure is described by the radial density profile showed in Figure 4.10. In Figure 4.10 (a)-(b), we provide the comparison in the radial density profile of TOL/TBA mixture in hydrophobic and hydrophilic confinement.
In a hydrophobic confinement, Fig. Figure 4.10 (a) shows a layering structure of TOL and TBA molecules along the nanopore radial direction. Obviously, near the wall surface between 17 Å and 15 Å, a local-demixing seems to be drawn inside the mixture. On the other hand, we provide the radial density profile of the same mixture confined within a water nanotube. As we can noticed from Figure 4.10 (b), we have a layering structure inside the water nanotube. In this case, the TBA molecules are located near the confining surface with a very weak percentage of TOL molecules. Moreover, Figure 4.10 (b) shows us a strong affinity near the wall surface between the TBA molecules and the water nanotube; this is evidenced by a peak at 18 Å and

the TOL shows a first main peak at 13 Å. There is microscopically a local demixing near the water surface. However, it should be noted that this mixture is fully miscible in the bulk phase. Probably, this local demixing may be due to two major factors: confinement effect and strong interaction effect. This point will be detailed later. For both confinements, we found that molecules are arranged into layers, but showed different affinities near the wall surfaces. TOL has showed a very strong affinity with the wall surface in CNT better than TBA molecules in the case of a hydrophobic confinement. However, in a hydrophilic confinement, we observed the reverse phenomenon. These results indicates that, the chemistry of the wall surface affect the

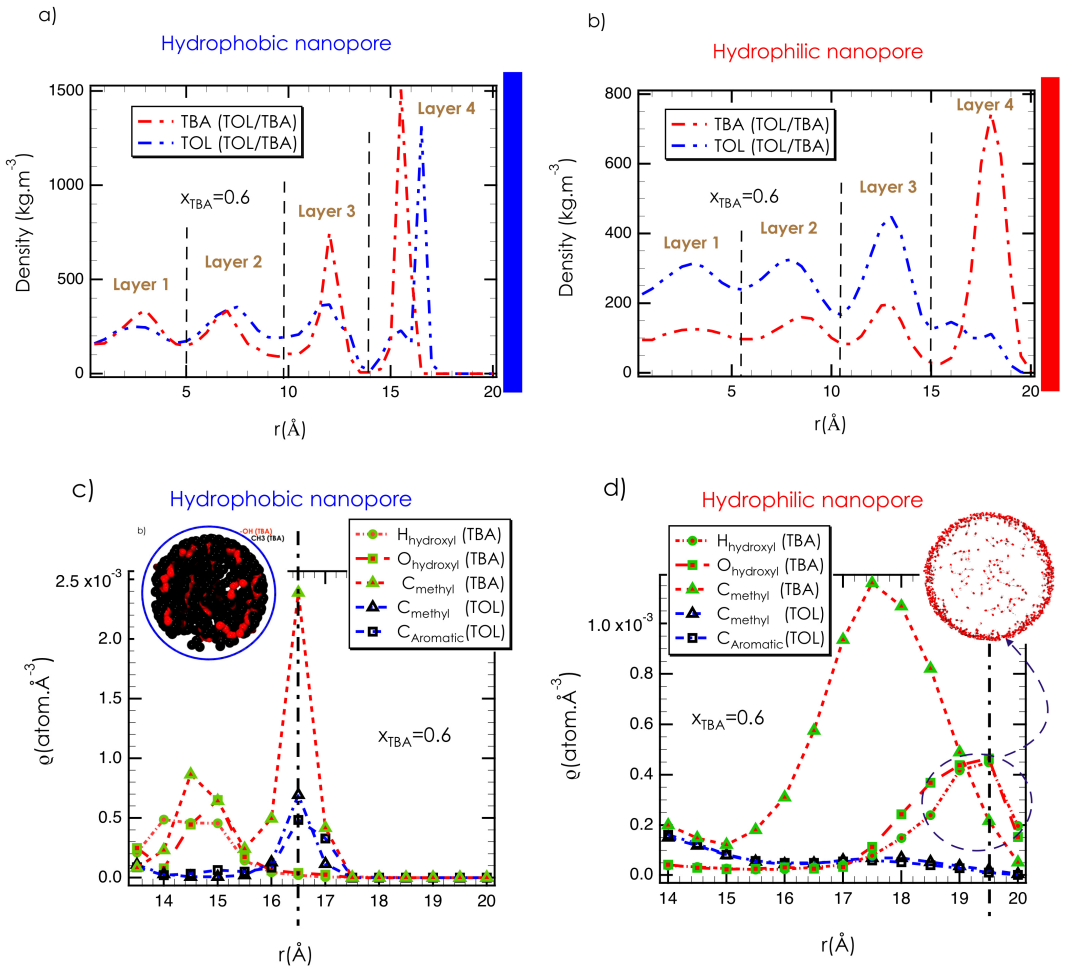

Figure 4.10: Radial density profile of TBA/TOL within a) carbon nanotube and b) water nanotube (r=20 Å). a-1) and b-1) are atomic radial profiles of TBA (oxygen, hydrogen (HO part) and carbon of $3CH_3$) and TOL (carbon atoms of aromatic ring and carbon atoms of methyl group) in hydrophobic and hydrophilic confinement, respectively.

preferential layered organization of these molecules near the surface.

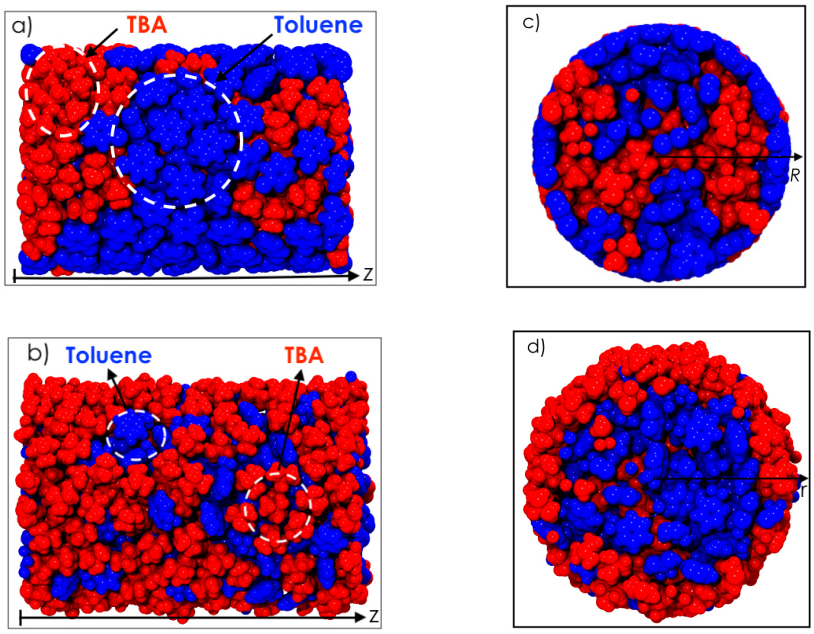

Figure 4.11: Snapshot illustration of TOL/TBA mixture within a) and c) CNT (r=2nm) in axial and radial directions, respectively and b) and d) WNT (r=2nm) in axial and radial directions, respectively.

Figure 4.11 presents the confined media snapshots obtained from both mixtures which corroborates our first observations. For TOL/TBA mixture confined in hydrophobic nanopore Figure 4.11 a,c) illustrates the formation of small nano-phases in TOL and TBA which highlights a non-mixing behavior inside the mixture. For TOL/TBA confined in the WNT, snapshots observations indicates the presence of local de-mixing behavior near the wall of the water nanotube which highlights a micro-phase separation near the wall surface (see Figure 4.11 b,d). In the axial direction Fig. 4.11 d), we observe more TBA molecules adsorbed on the surface with weak proportion of TOL molecules that is in line with the results evidenced from the radial profile.

The molecular preferential location of TOL/TBA mixture inside CNT and WNT were captured by the calculation of the atomic radial profile of TBA and TOL. In hydrophobic confinement, Figure 4.10 c) shows us that methyl groups of TBA, methyl group of TOL and aromatic groups are positioned at the same distance 16.5 Å. The carbon nanotube attracts the methyl groups of TBA, which seems to generate a local heterogeneities as it observed in Figure 4.11

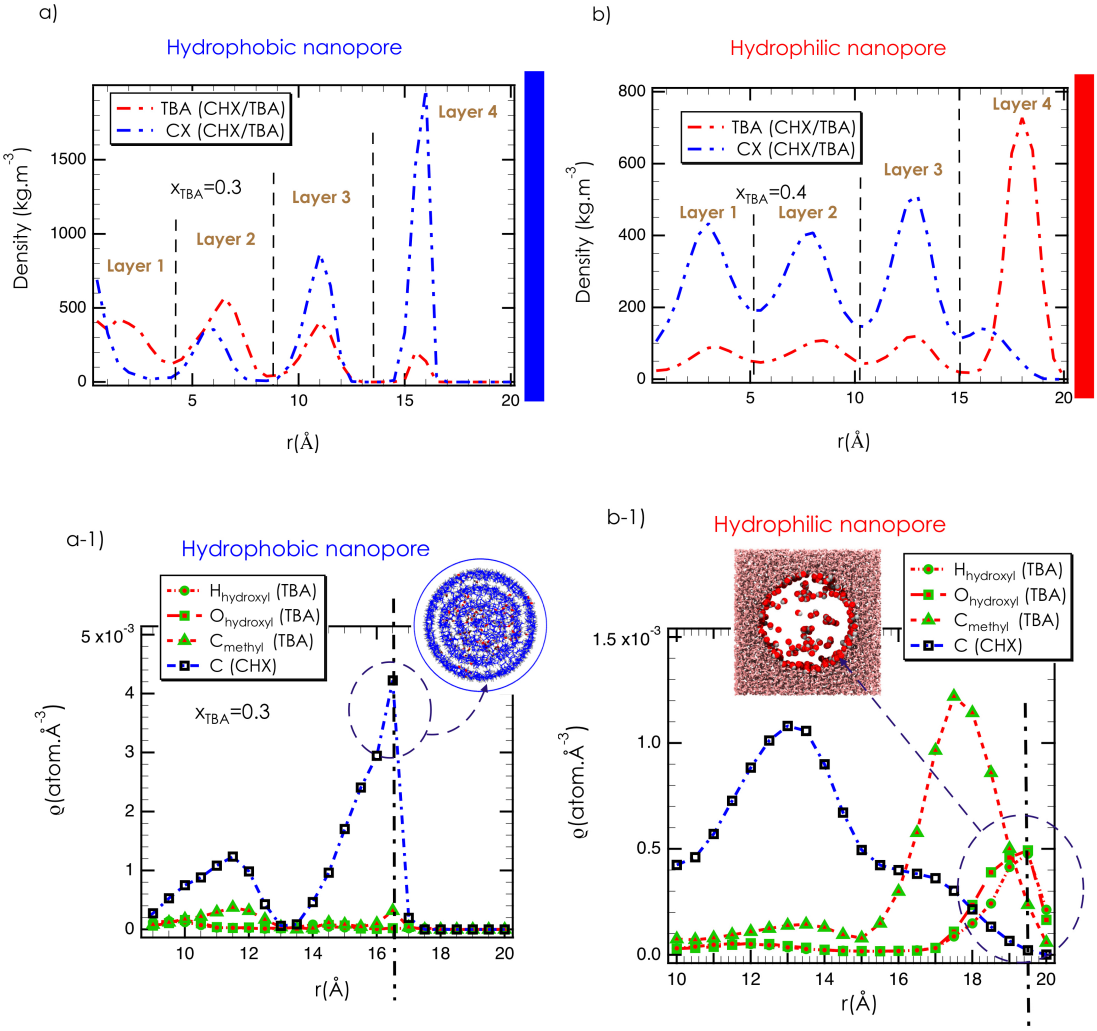

Figure 4.12: Radial density profile of CHX/TBA within a) carbon nanotube and b) water nanotube (r=20 Å). c) and d) are are atomic radial profiles of TBA (oxygen, hydrogen (HO part) and carbon of $3CH_3$) and CHX (carbon atoms) in hydrophobic and hydrophilic confinement, respectively.

a,c). Then, we can deduce that TBA molecules pointed the methyl part towards the surface while the hydroxyl part are found behind. However, TOL are adsorbed on the wall surface from $\pi - \pi$ stacking. In hydrophilic confinement, TBA atomic radial profile depicted in Figure 4.10 d) highlights a preferential anchoring of OH parts of TBA molecules towards the surface (19.5 Å), whereas the methyl group are located behind the OH group of TBA which shows a peak around 17.3 Å.

In addition, we examined the behavior of CHX/TBA inside CNT (hydrophobic) and WNT (hydrophilic). Figure 4.12 shows CHX/TBA mixture under a) hydrophobic and (b) hydrophilic

confinement. In both confinements, CHX and TBA molecules form 4 layers. The CHX and TBA are located near the wall surface in the hydrophobic confinement while an important proportion of CHX molecules is captured near the surface. The behavior of CHX/TBA inside the nanowater seems to be slightly different . Specifically, a local de-mixing behavior is observed near the wall surface. Indeed, a large concentration of TBA molecules is found at 19.5 Å near the wall surface whereas CHX molecules are located at 17 Å.

To this point, we have observed that the type of confinement affects the organization of liquids within these nanopores. In the case of hydrophilic confinement, alcohol molecules are more attracted to the confining surface, whereas hydrophobic confinement is the hydrocarbons that prefer to be present in large quantities beside the surface. In order to understand this preferential structuring in both confinements, the atomistic radial density profile of TBA, TOL and CHX atoms along the nanopore radial direction have been managed.

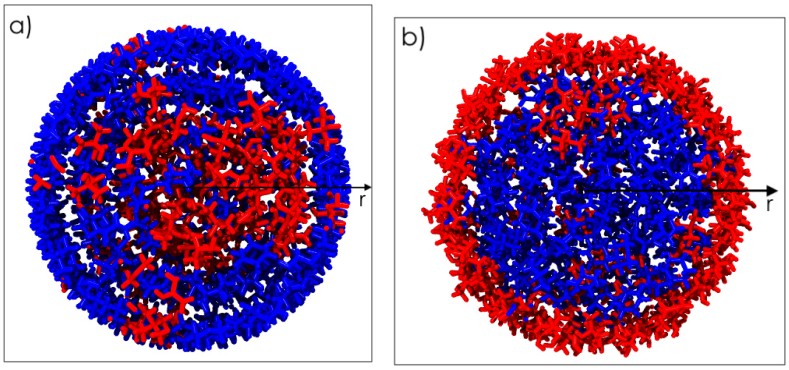

Figure 4.13: Snapshots of a) CHX/TBA within CNT and b) CHX/TBA within WNT.

From Fig. 4.13, we corroborate our previous conclusions obtained from the radial density profile highlighting a high density ratio in TOL close the wall surface while the TBA molecules are located in the center of the pore. The axial direction shows us a creation of small nanophases. Figure 4.13 highlights a microphase separation near the surface which confirms our conclusions drawn from the radial density profile (TBA peak at 18 Å and CHX peak at 16.5 Å). This suggest that the TBA molecules create strong interactions with the wall surface. However, this effective description does not fully address the microscopic origin of the local demixing behavior.

4.4 Molecular self-assemblies under nanoconfinements

4.4.1 Micro-heterogeneities

In order to investigate the presence of micro-heterogeneity in pure and binary mixtures, we calculate the heterogeneity order parameter (HOP) of confined pure CHX, TOL and TBA and their binary mixtures within CNT and WNT. According to the study of Wang et al., the HOP for homogeneously distributed ideal molecules is lower than 15.74 and a heterogeneous system exhibits a HOP greater than 15.74 [43].

a) Pure liquids

TBA, CHX and TOL showed a layer structure in both types of confinement. In hydrophobic confinement, the molecules of TOL, CHX that are close to the surface and TBA appears after. The TOL gives us a HOP value equal to 23.10 which indicates a local heterogeneity. Similarly, CHX's HOP is 22.66 which also shows spatial heterogeneity in the carbon nanotube. The TBA exhibits a high degree of heterogeneity compared to the two substances with an HOP of 24. Therefore, TBA in hydrophobic confinement is more inhomogeneous than TOL and CHX. In hydrophilic confinement, the HOP of CHX, TBA and TOL is 29.48, 29.29 and 29.11, respectively. This indicates a strong heterogeneous liquids under nanoscale confinement. Then, these heterogeneities could be explained by the confinement effect that induces by the surface-to-volume ratio.

b) TBA mixtures

The binary TOL/TBA mixture confined to the hydrophobic nanopore highlights a demixing behavior near the surface of the confinement. Snapshots show that the local formation of small nano-phases are present in both cases that is in line with heterogeneous mixtures. In hydrophobic confinement, the HOP of TBA and TOL are 25.15 and 25.18, respectively; these are significantly higher than 15.74 (homogeneous liquid) which highlights a strong heterogeneous distribution of TBA and TOL molecules in the mixture. Both components are heterogeneous in the mixture while at the same TBA concentration in bulk phase we showed that they are homogeneous. This is probably due to the confinement effect which tends to arrange molecules in layers from the confining surface and it keeps them away from their bulk behavior. In the hydrophilic confine-

ment, TOL is more heterogeneous than the TBA with a value of 29.66 while the TBA shows a value of 21.42. This may be due to the creation of strong interactions with the wall surface. However, TOL is less heterogeneous in comparison with TOL in hydrophobic confinement.
In the case of CHX/TBA binary mixture confined within hydrophilic confinement, it showed local demixing behavior near the wall surface. The TBAs at the interface separate from the CHX molecules (see Fig. 4.10 (d)) which may result from the creation of small nanophases leading to strong heterogeneities. This was attributed to the perturbation of the wall surface on interfacial TBAs. The HOP of CHX is 30.60 while TBA is 20.41 which points out a strong heterogeneity. The closeness of TBA to the confining surface leads to significant local heterogeneity in CHX molecules which is organized in three layers. In addition, the preferential orientation of TBA molecules near the wall surface causes a spatial heterogeneity recorded in the HOP. The preference of TBA to self-orientate near the confining surface is affected by strong interactions that occur. Although, the perturbation of its bulk identity produce a strong internal disturbance. In the case of the hydrophobic confinement, there are non-local demixing behavior showed. We have both components at the surface with the formation of small nanophases which could generates spatial heterogeneities in the mixture. For CHX, the HOP is equal to 19.77 while the TBA is 22.78. Indeed, we note that both CHX and TBA are heterogeneous under nanoscale hydrophobic confinement. TOL and CHX are non-polar, non H-bonding van der Waals molecules that present no specific interaction with the WNT, no special intermediate range order in the liquids state. While TBA is polar and provide hydrogen bonds type interaction which could interacts strongly with the surface. These two different interactions could be responsible for both mixtures showing high and low heterogeneity.

4.4.2 Hydrogen bonds number

The change in behavior of the TOL/TBA and CHX/TBA binary mixtures has been attributed to the chemistry of the wall surface. This elucidates the creation of hydrophobic type interactions with the CNT in TOL and in CHX liquids while a creation of hydrogen bond interaction between the WNT and TBAs were predicted. Figure 4.14 presents the hydrogen bond number of TBA molecules in pure and in mixture with TOL and CHX in CNT and in WNT. As depicted from

Figure 4.14 (a), the hydrogen bonds of TBA are not changing along the radial direction for pure TBA and for mixed TBA. Whereas a maximum of two bonds per TBA molecule are captured in the hydrophobic confinement. Interestingly, the CNT were extremely a good protector of the hydrogen bond number despite some failure near the surface. In WNT (see Figure 4.14 (b)), confined pure TBA shows approximately a value of 1.3 HBs per TBA molecule. This means a small decrease of the nHBs which is approximately equal to 1.7 in the bulk phase. This could probably results from the confinement effect on TBA topology structure. However, the profile of nHBs of TBA in mixture with CHX and with TOL indicates a high HB dilution which means that TBA loses the half of the HBs (nHB $\simeq$ 0.8). This is corroborated by the high dilution of the hydrogen bonding number of TBA molecules along the radial direction and near the wall surface.

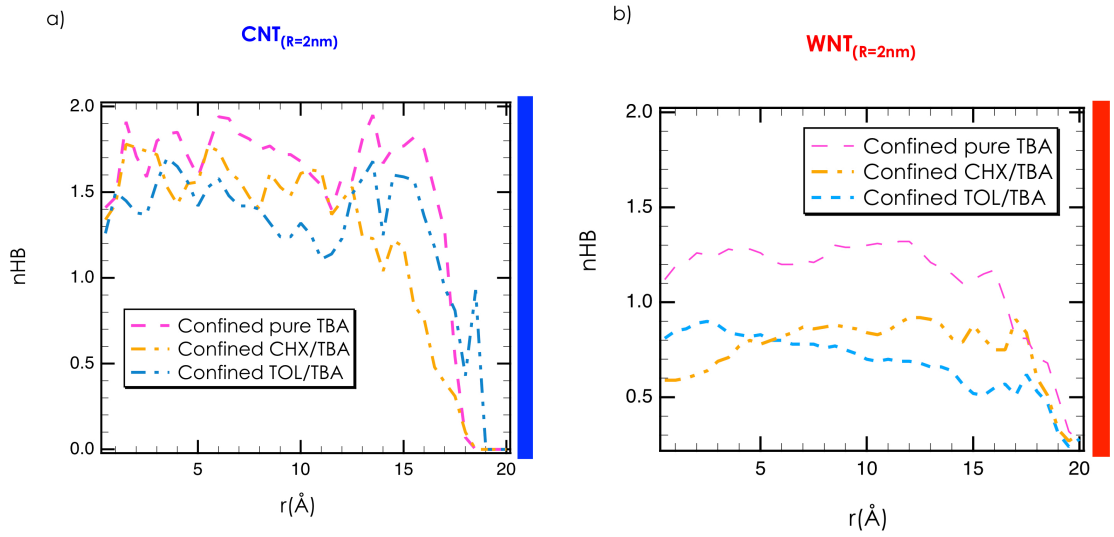

Figure 4.14: Radial hydrogen bond number (nHB) profile of pure and mixed TBA within a) CNT and b) WNT respectively.

As previously suggested for both confinements, the key difference may originates from the presence of TBA-water HBs interaction in the hydrophilic case, while TBA molecules form H-bonds between themselves in the hydrophobic case. This is shown by the distinct peak in the hydrogen distribution around 19.5 Å for CXH/TBA and TOL/TBA, a feature absent in the hydrophobic case. This is also reflected in the oxygen distributions which are displaced further from the surface in the hydrophobic pore, peaking at 15 Å for CHX/TBA and TOL/TBA

compared to 19.5 Å in the hydrophilic pore. In order to quantify the existence of the hydrogen bond interaction between TBA and Water nanotube, we calculate the hydrogen bond number based on geometrical criteria between the confining surface wall and TBA molecules. Figure 4.15 compares the radial profiles of the hydrogen bond of TBA-TBA and TBA-Water in (a) TOL/TBA and (b) CHX/TBA. From Figure 4.15 (a) we observe a strong dilution of TBA's hydrogen bonding network, which is basically made up of two hydrogen bonded neighbors. In TOL/TBA confined in the water nanotube at x_{TBA}=0.6, there is a significant decrease from nHB=1.51 to nHB=0.8. In the same figure, the average number of hydrogen bonds between the TBA and the nanopore surface is zero from 0 to 15 Å. From 15 Å (next to the confining surface), a hydrogen bond of TBA molecules is created near the surface, this is indicated by a peak that is located at 19.8 Å at a height corresponds to nHB=0.65. In the second figure, in the CHX/TBA mixture, the same behavior is observed. From these two Figures we observe a decrease of nHB within WNT as well as a creation of HB interaction with the surface. While in CNT, a very slow decrease of nHB is evidenced.

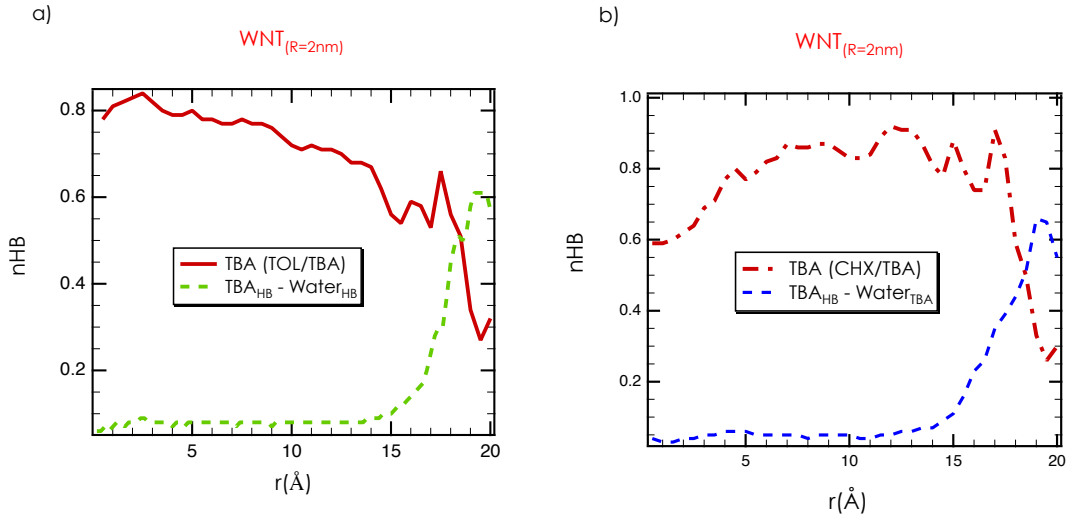

Figure 4.15: Radial hydrogen bond number (nHB) profile of TBA-TBA and TBA-Water in a) TOL/TBA mixture and b) CHX/TBA mixture.

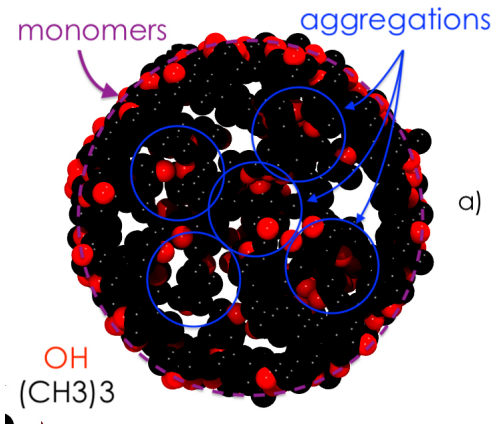

Figure 4.16: Presentation of molecular aggregates in TBA confined in a nanopore.

4.4.3 Confinement effect on clustering phenomenon

As discussed previously, cluster number size is calculated by the modified Stoddard algorithm based on HBs criteria. According to our results, there are strong HBs dilution of TBA molecules in the hydrophilic surface while in hydrophobic pore the HBs are preserved in average. Figure 4.17 reports the comparison of TBA cluster (see Fig. 4.16 (a)) number as pure liquid in bulk and in confined media: WNT and CNT. In this figure, we can see that in the water nanotube there are more monomers than other n-mers (dimers, trimers, etc.). In this figure the number of TBA clusters in the bulk phase is compared to those restricted to the hydrophilic or hydrophobic matrix. Hydrophilic confinement generates more monomer than dimers, trimers and tetramers or pentamers in binary mixtures as well as in the pure state. In comparison with hydrophobic confinement, the number of clusters reveals the creation of larger clusters around 22 molecules and there are less monomers. This corroborates our hypotheses. As expected, TBA loses its self-associating power through hydrogen bonding in the carbon nanotube as it loses half of its hydrogen bonds by forming a bond with the surface of the water nanotube (very strong interaction). Such interaction with the surface is the major factor in the phase separation created at the surface.

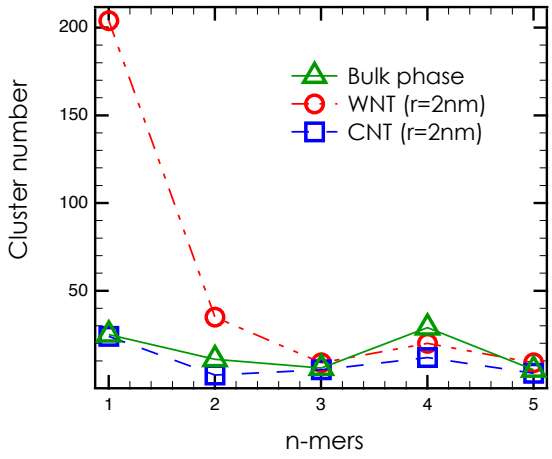

Figure 4.17: Comparison of the cluster number of pure TBA in Bulk and in confined media.

4.5 Pore size effect

By decreasing the pore size, we can evaluate the impact of confinement size on local demixing and determine whether microphase separation can be produced at the nanoscale. The binary mixtures of TOL/TBA and CHX/TBA and their pure states are confined in a water nanotube that has a radius of 1nm and a carbon nanotube that has a radius of 1.15nm.

4.5.1 Pure TBA, TOL and CHX

Figure 4.18 present the radial density profile of TOL, TBA and CHX liquids confined within a) CNT as hydrophobic nanopore and b) WNT as hydrophilic matrix. From Fig. 4.18 (b) we observe two distinct peaks for TBA, TOL and CHX which highlights a layered structure. Interestingly, first peak of TBA is located at 8 Å, peak of TOL is about 7.5 Å and peak of CHX is about 7 Å, this indicates a strong affinity with the surface of the water nanotube with TBA molecules as previously observed (Fig. 4.7 (b)). While in CNT, the local structure of these pure liquids differs from that of the hydrophilic confinement which is depicted in Figure 4.7 (a). Surprisingly, TOL shows a first significant peak at 8 Å and three other small peaks at 6.5, 4 and 3 Å respectively. This indicates a significant decrease in the production of distinct layered structures as observed earlier. Obviously, there is a fairly strong surface effect on TOL, which

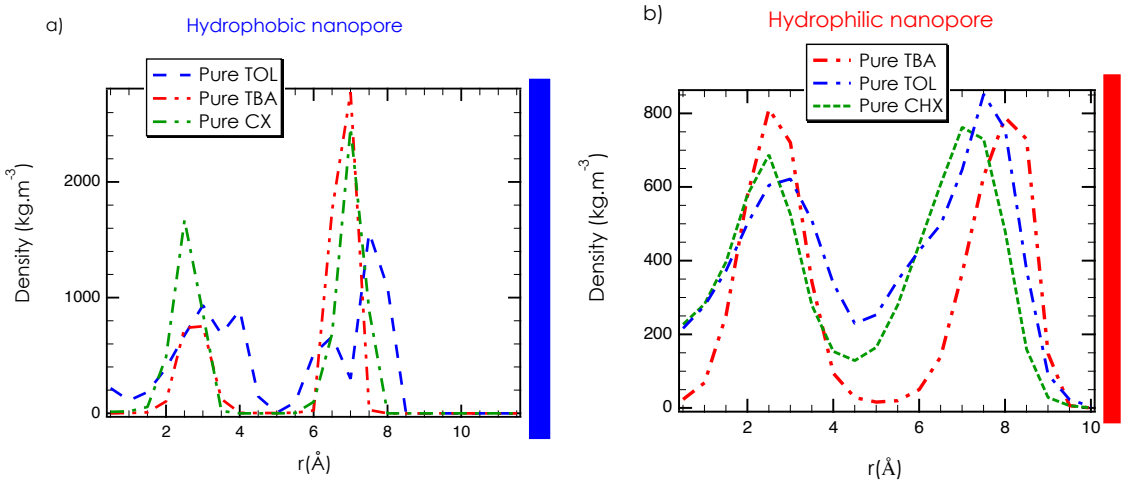

Figure 4.18: a) Radial density profile of pure confined TBA, TOL and CHX within a) Carbon nanotube (CNT) with r = 1.15 nm and b) Water nanotube (CNT) with r = 1nm

can be explained by the high affinity of TOLs with the surface wall of carbon nanotube. Whereas TBA and CHX first layer is located at 7 Å.

4.5.2 TOL/TBA and CHX/TBA binary mixtures

The local structure of the confined binary mixtures is described by the radial density profile. The observed behaviour of TOL/TBA and CHX/TBA confined in the hydrophobic matrix is displayed in Figure 4.19. Figure 4.19 presents the radial profile of the density of the TOL and TBA in the TOL/TBA mixture (c) and the density of the CHX and TBA in the CHX/TBA mixture (d) with a TBA concentration equal to 0.9. As illustrated in Figure 4.19 (c), there are two peaks of TBA and a single peak of TOL. An interesting fact is that the only peak of TOL is located at 7.8 Å while the central peak of TBA is located at 7 Å. This indicates that the TOL/TBA mixture separates nearby the confining surface. From our method of creating confined systems, it is evident that despite the poor affinity of TBA to the carbon nanotube, we have more TBA than TOL in the matrix. By observing the topology of this confined mixture, also shown in Figure 4.19 (c), we can see that all the molecules of TOL are at the end of the carbon nanotube. This allows us to conclude that at this concentration of TBA all the TOL molecules that have entered into confinement are captured by the surface while the TBA had no option except to fill the space and approach its behavior in a pure state. The high concentration

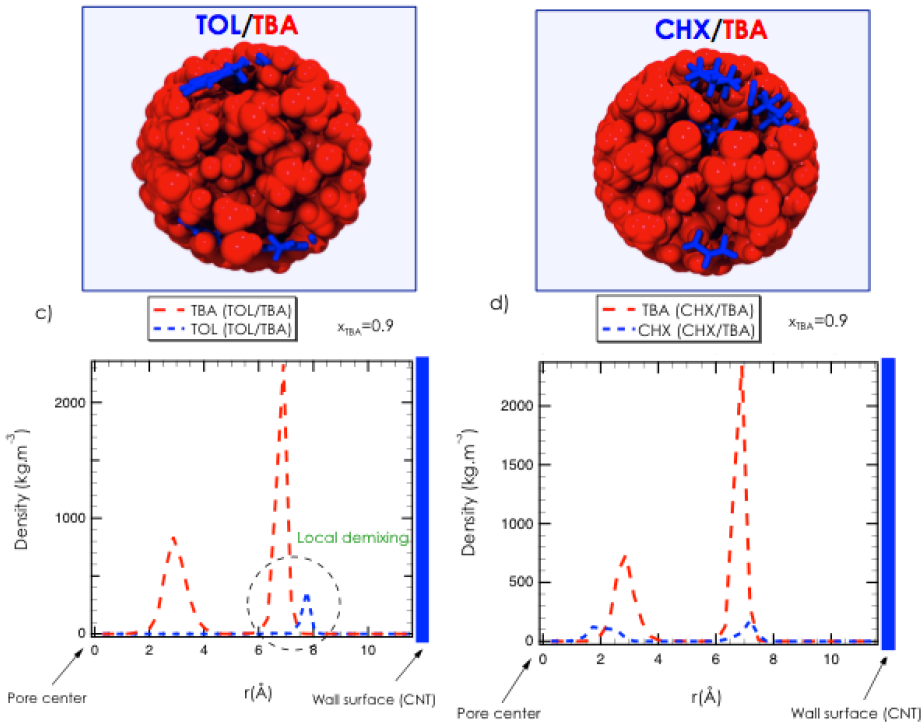

Figure 4.19: Snapshot observations and radial density profiles of a,b) TOL/TBA confined within carbon nanotube (CNT) with r= 11.5 Å and c,d) CHX/TBA confined within carbon nanotube (CNT) with r= 11.5 Å.

of TBA in the carbon nanotube can be explained by the self-association of TBA molecules which favors the entry of TBA than TOL. In the second Figure, we observe only two large peaks for the TBA and two small peaks for the CHX. In particular, the CHX/TBA confined in the carbon nanotube shows no phase separation, CHX is present on the surface as it is present in the center of the nanopore. This is corroborated by the structure topology given in the same Figure 4.19 (d).

In the case of hydrophilic confinement using the water nanotube, we represent both the radial profile of the density of TOL/TBA and CHX/TBA in Figure 4.20 with the structural results that we obtained from simulation trajectories. For the TOL/TBA mixture shown in Figure 4.20 b), there are 2 peaks (a large and a small one) that indicate a layered structure for both compounds. A local demixtion is observed near the surface. The large peak of TBA is located at 8 Å while the second small peak is observed at 2.5 Å, although the TOL shows a small peak next to the confined surface at 8 Å and a large peak at 3 Å. This indicates the high affinity of the water

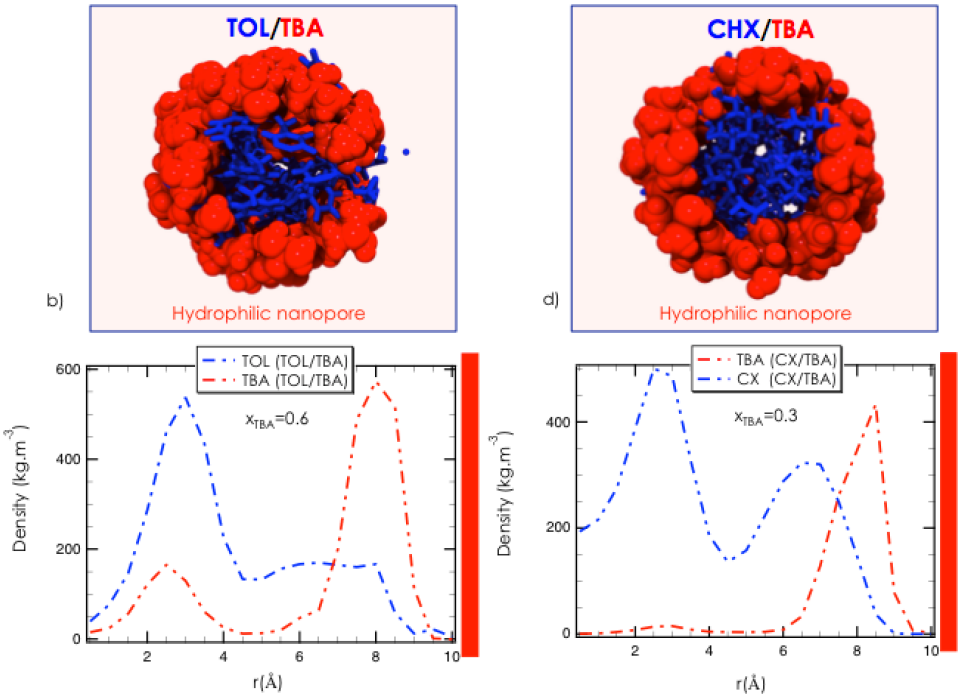

Figure 4.20: Snapshot observations and radial density profiles of a,b) TOL/TBA confined within water nanotube (WNT) with r= 10 Å and c,d) CHX/TBA confined within water nanotube (WNT) with r= 10 Å.

nanotube surface which attracts more TBA molecules than TOL. So one may wonder why there is not a higher concentration of TBA in the water nanotube such as the carbon nanotube since water attracts more TBA to the surface? The answer lies in TBA's identity.

As previously shown in the bulk phase, TBA at any concentration promotes the creation of molecular aggregates that are approximately 3.8 molecules in size on average per aggregate. This behavior is expected to coexist in carbon nanotubes, which may explain the high concentration of TBA. Under hydrophobic confinement, the TBA has only weak interaction with the surface and therefore the TBA preserves its molecular aggregates properly. In hydrophilic confinement, TBA interacts strongly with the surface (this is given by the high density of OH at a very short distance from the surface) which could affect its self-organizing powers within the water nanotube.

In Figure 4.20 (d), the radial profile of the CHX/TBA density reveals two layers of CHX and a single layer of TBA. The TBA peak is located at 8.5 Å and the two CHX peaks are located at 6.5 Å and 2.5 Å , this highlights a micro-phase separation near the surface. All the molecules of TBA

are at the surface while CHX is at the center of the pore. Interestingly, this micro-separation is also captured on the CHX/TBA topology image given in the same figure.

To understand the origin of these two nanostructures captured in the two binary mixtures in the hydrophilic confinement, the atomic density along the pore radius will be explored. The radial

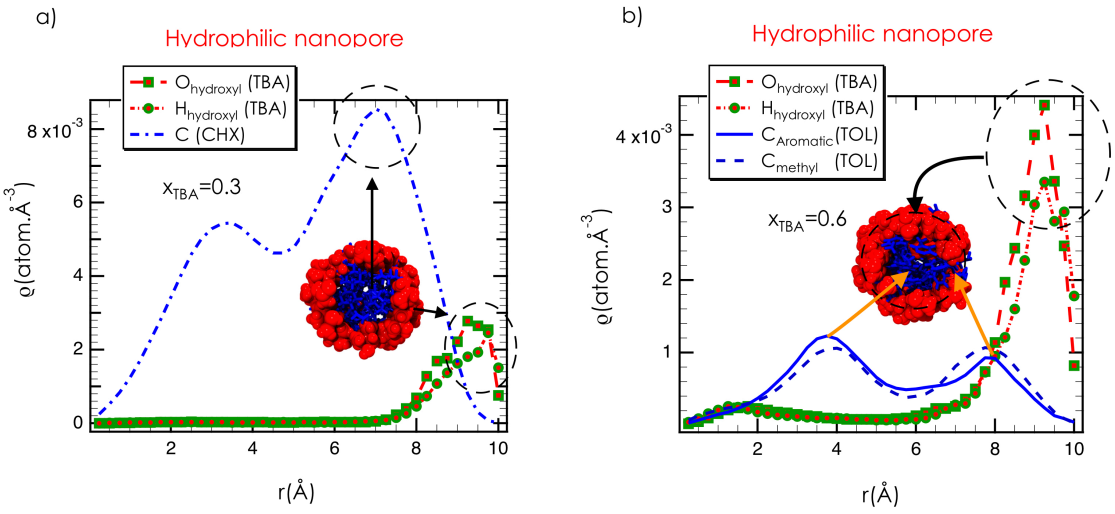

Figure 4.21: a) Profile of the radial density of hydrogen and oxygen atoms of hydroxide group (HO) of TBA, and carbon atoms of CHX. b) Profile of the radial density of hydrogen and oxygen atoms of hydroxide group (HO) of TBA, and carbon of benzenic cycle ($C_{aromatic}$) and methyl group (CH_3) of TOL.

density profile of the oxygen and hydrogen atoms of the hydroxyl part of TBA as well as the carbons of the aromatic and methyl part of TOL is shown in Figure 4.21 (b). The peak of the two atoms of the hydroxyl part of TBA is at the same distance at 9.3 Å while the first peak of the TOL carbons is at 8 Å which underlines the local demixing next to the surface and highlights the preferred orientation of the TBA hydroxyl group near the water nanotube. At this stage of the study, we understand that this preferred orientation of TBA molecules on the surface may be responsible for local demixing. Figure 4.21 (a) depicts the atomic radial density profile of oxygen and hydrogen atoms of the hydroxyl part of TBA molecules as well as the carbons atoms of CHX molecules. In CHX/TBA mixtures, where a micro-phase separation was captured, the atomic density profile highlights a strong anchoring of TBA molecules by their hydroxyl parts on the surface where a peak is recorded at 9.8 Å. On the other hand, the first peak of carbon atoms of CHX is captured at 7 Å which points out the micro-phase separation results showed

previously.

4.5.3 Hydrogen bond

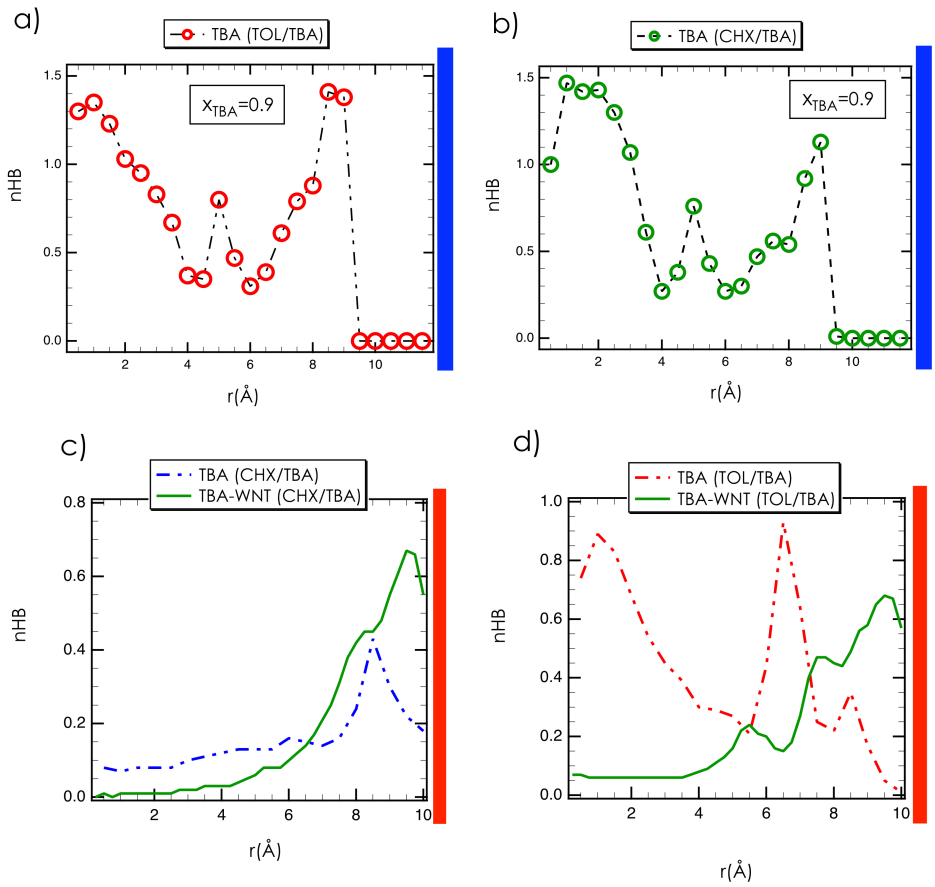

Figure 4.22: Hydrogen bond number profile of TBA in TOL/TBA a) in CHX/TBA b) within CNT and the Hydrogen bond number profile of TBA in CHX/TBA c) in TOL/TBA d) within WNT.

Figure 4.22 shows the profiles of the average number of TBA hydrogen bonds in the two binary mixtures in hydrophobic confinement (a) and (b), and in hydrophilic confinement (c) and (d). As previously reported, the TOL/TBA in CNT has showed a layering structure. From Figure 4.22 (a) a two broad peaks are captured at 8.5 Å and 1 Å which corresponds to 1.4 HBs per TBA molecule in average. This confirms that the observed layering structure correlates to the resulting nHB peaks that emphasize the predicted pattern between the TBA molecules in the hydrophobic confinement. Figure 4.22 (b) depicts the same behavior of CHX/TBA mixture in the hydrophobic confinement.

To characterize the interaction with the confining surface, the radial profile of the number of hydrogen bonds between TBA-Water molecules are shown in Figure 4.22 (c-d). Interestingly, between 15 and 20 Å for both mixtures a hydrogen bond interaction is captured between the TBA and the confining water surface. The CHX/TBA in hydrophilic confinement showed a microphase separation where TBA are adsorbed on the surface and the CHX is in the center of the nanopore as exhibited by the radial density profile. From Figure 4.22 (c), we observe no hydrogen bond in the center of the nanopore that confirms the absence of TBA molecules in the center of the nanopore, but near the surface, we have found that TBA creates two hydrogen bond interactions, one with the water surface and one between its molecules. Figure 4.22 (d) shows the profile of the nHB of TBA-TBA and TBA-water in the TOL/TBA mixture. In this figure, two peaks can be observed: the first is located at 1 Å and the second at 6.5 Å. This shows that the TBA molecules are connected to each other through the hydrogen bond within the nanopore. Interestingly, there is also a creation of a hydrogen bond with the confining surface at 9.5 Å.

All this shows that the microphase-separation is probably due to the creation of hydrogen bonding of TBA with the surface as shown previously. Size effect could be considered a key factor for the creation of microphase-separation at the nanoscale since it has not previously been observed with a larger pore size where one is only able to create local demixtion.

4.6 Tuning liquid-solid interactions

As previously reported recent experimental works suggested that the confinement into a cylindrical nanopore induced the microphase separation of a binary liquid, despite the miscible character of its bulk counterpart. A core-shell organization was evidenced such that one of the liquids was strongly anchored to the solid surface whereas the other one was confined at the center of the pore. At the same time, we showed in the previous sections a strong heterogeneity and the absence of core-shell organization. In this part, we refine the solid-liquid interactions to reproduce qualitatively the experimental adsorption isotherms of both single liquids as well as the microphase separation and capture the core-shell structure.

4.6.1 Force field refinement

To be in line with experiment, the confining medium corresponds to a cylindrical silica nanopore of radius of 24 Å. To reproduce the adsorption isotherms of the pure components the solid-liquid interactions were refined. The OPLS force field was used to model the TOL and TBA molecules as previous. Indeed, it was shown that the thermodynamic properties of TBA/TOL mixtures were closely reproduced from the OPLS model [45]. Whereas the intramolecular contributions (bonds, bending, and dihedral angles) were conserved as original, the partial charges were calculated using ab-initio calculations. Silica material was modeled by considering the ClayFF force field [46]. To refine the LJ parameters ruling the solid-liquid interactions, we began to predict the adsorption isotherm by considering the initial force fields.

Concerning the TBA adsorption through nanoporous silica, Fig. 4.23 shows a qualitative

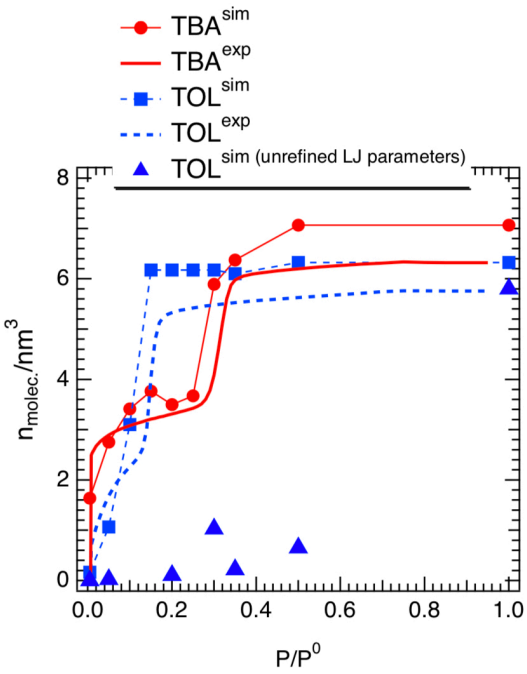

Figure 4.23: Adsorption isotherm of the TBA/TOL mixture confined in the silica nanopore as a function of the relative pressure such that P_0 is the saturation pressure vapor of TBA

agreement between simulation and experiment that highlights the quality of ClayFF and OPLS force fields and their combining using the Lorentz-Berthelot mixing rules. As shown in Figure 4.23 the predicted adsorption isotherm of toluene strongly differs with experiment. To improve the silica-TOL interactions we adapted the procedure discussed in Ref. [47] initially developed

to derive the coarse-grained parameters from atomistic simulations. The LJ parameters have been optimized by minimizing the value of the function $F = \frac{1}{n}\sum_{i=1}^{n}\frac{f_i^{sim}-f_i^{exp}}{s_i^2}$ according to a procedure detailed in Ref. [47]. In this relation, s_i is the estimated statistical uncertainty, f_i^{sim} and f_i^{exp} are the values of the ith properties on n. In this work n = 2 and corresponds to the enthalpy of adsorption and adsorbed amount at low partial pressure. The minimum condition of F is that every partial derivative must be zero [47]. Optimized LJ parameters are provided in Table 4.1. Figure 4.23 shows that the predicted adsorption isotherms are in fair agreement with those obtained from experiments [33]. Interestingly, Figure 4.23 exhibits that the capillary condensation pressure is qualitatively reproduced for both TOL and TBA components. These results allowed us to be confident in these refined interactions.

	σ(Å)	ϵ(K)
Si-CH3	3.6475	46.17061
Si-CH	3.6725	47.54915
Si-C	3.6725	47.54915

Table 4.1: Crossed Lennard-Jones parameters. CH3 is the carbon of the methyl groups of toluene, CH the carbon of the CH groups of toluene, and C the carbon without hydrogen atoms in toluene

4.6.2 Microscopic origin of microphase separation

We have studied 7 compositions of TOL/TBA (x_{TBA}=0, 0.24, 0.49, 0.51, 0.71, 0.83, 1.0). As shown in Figure 4.24 (b), for both pure components, a layering structure was observed due to the confinement effect at the nanometric scale [7]. Whereas three layers are observed for both cases, the interfacial TBA layer seems closer to the silica surface suggesting that the attractive interactions between the silica nanopore and TBA molecules are stronger. As shown in Figure 4.25 the hydroxide groups (OH) of the TBA molecules point towards the silica surface. The driving force of this interfacial anchoring is probably the result of the strong hydrogen bonding (HB) network between porous silica and TBA molecules. This point will be discussed later. Interestingly, as shown in Figure 4.25 this HB anchoring leads to a peculiar organization such that hydrophobic and hydrophilic (HB) domains are disposed in alternating succession. These results should probably impact the molecular structure of confined mixture. The density profile of the SiOH groups is also reported in Figure 4.25. As shown in Figure 4.25 the SiOH profile

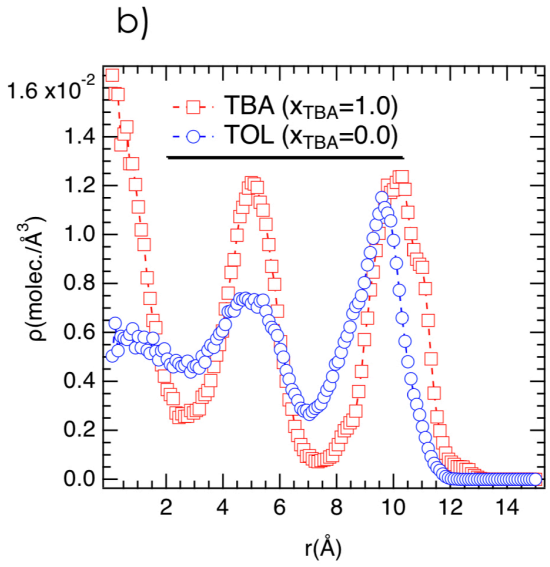

Figure 4.24: b) Density profiles of the center of mass of pure TBA and TOL confined into the nanoporous silica material obtained at 308 K and 1 bar.

begins from 11.5 Å and presents a peak around 14 Å highlighting the roughness of the surface. Calculation of the accessible volume by probing the porous volume by an atom of Argon allowed us to approximatively evaluate the pore radius at 12 Å.

From x_{TBA}=0.24 to 0.83, Figure 4.26 (from Figure 4.26 (a) to Figure 4.26 (d)) shows that TBA molecules were adsorbed close to the interface constituting a first layer whereas the toluene molecules are located right after. For x_{TBA}=0.83 the second and third layers correspond to a homogenous mixture phase reminiscent of the bulk medium. Very interestingly, Figure 4.26 highlights the progressive development of two phases as the TBA concentration decreases. Indeed, for x_{TBA}=0.71 the TBA molecules are almost only located close to the silica surface in the first adsorbed layer without TOL molecules. For x_{TBA}=0.49 that corresponds to the concentration where the core-shell organization was observed experimentally, the microphase separation is nearly complete. Interestingly, the distance between peaks of TOL and TBA seems to decrease as a function of the decrease in molar fraction in TBA. Indeed, whereas for panels (a) and (b) in Figure 4.26 the distance between the interfacial TOL and TBA density ($d_{TBA-TOL}$) is $\sim$ 4 Å, the distance is greatly reduced to just $\sim$ 1 Å for x_{TBA}=0.49 and x_{TBA}=0.24. The difference in the $d_{TBA-TOL}$ as a function of the TBA molar fraction is due to the progressive increase in TOL. Indeed, for the TBA fraction lower than 0.5 corresponding to an unsaturated

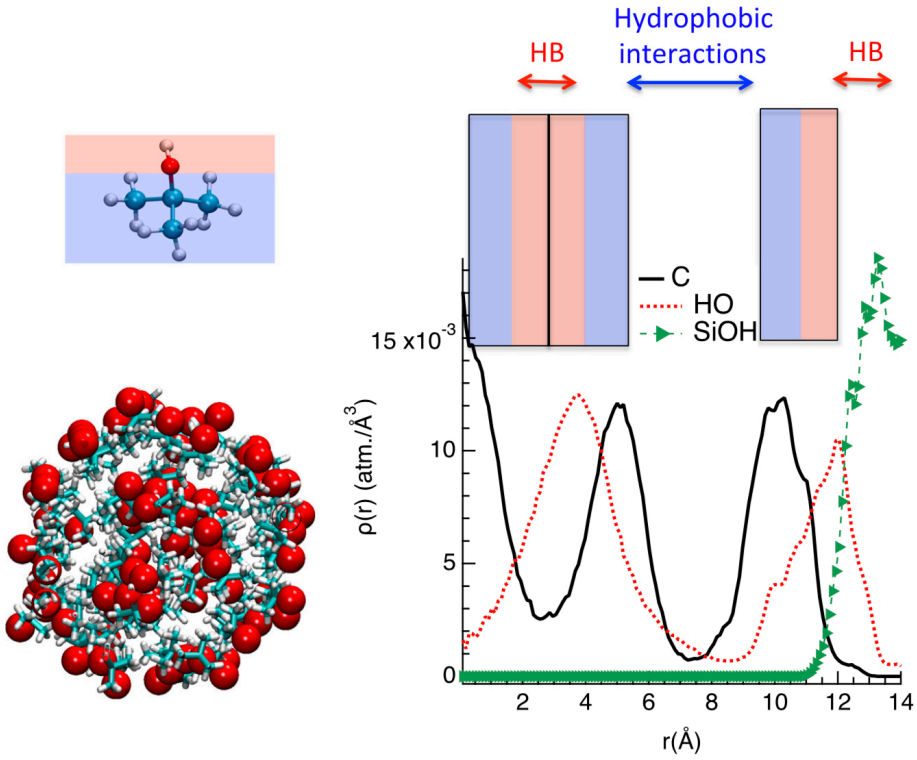

Figure 4.25: Density profiles of OH groups, carbon atoms of TBA molecules and SiOH groups in case of x_{TBA}=1.0.

solid interface in TBA molecules, the SiOH surface can then adsorb the TOL molecules. The progressive adsorption in TOL molecules at the silica surface is then at the origin of the decrease of $d_{TBA-TOL}$ with the increase in TOL fraction and then is at the origin of the interpenetration of TOL molecules. That can be observed from the atomic density in the Figure 4.27 where this progressive interpenetration as a function of x_{TBA} is well evidenced. Indeed, from Figure 4.27 (a) (x_{TBA}=0.24) to Figure 4.27 (d) (x_{TBA}=0.83) the decrease in $d_{TBA-TOL}$ and the increase in the interpenetration region (dashed circles in Figure 4.27) are well established.

The formation of a first TBA layer anchored at the silica surface is induced by the strong hydrogen bonds between the silanol groups SiOH of the silica material and the OH groups of the TBA molecules. Indeed, hydrogen bonds number were computed by considering a geometrical criterium based on the quantum consideration [48] where two molecules are chosen as being hydrogen bonded only if their inter-oxygen distance is less than 3.5 Å, and simultaneously the oxygen-hydrogen is less than 2.5 Å. The profile of the hydrogen bonds number (nHB) per

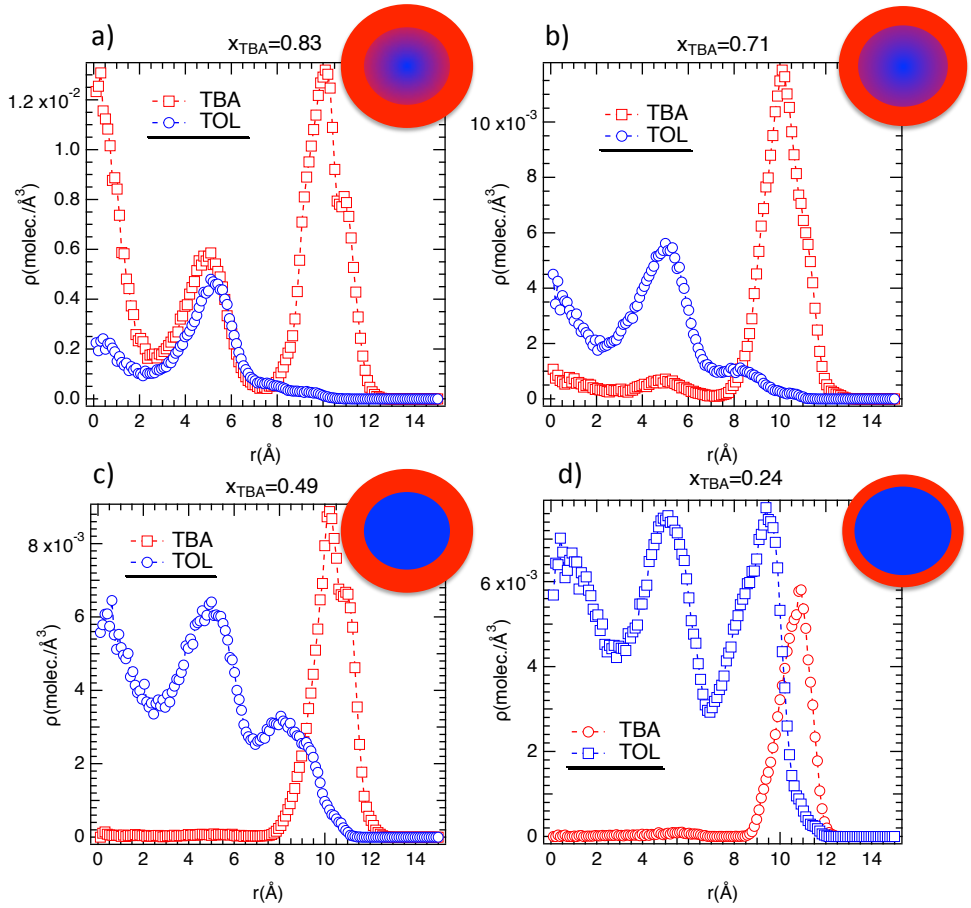

Figure 4.26: Profiles of radial density of the center of mass of TBA and TOL molecules for x_{TBA} = 0.83 (a), 0.71 (b), 0.49 (c), and 0.24 (d). The insets illustrate the core-shell organization, the TBA (red color) close to the surface and the TBA/TOL (TOL is blue colored) mixture at the center of pore; from 0.83 to 0.24 the width of the interfacial layer decreases, whereas the concentration in TBA decreases at the center of pore.

molecule was then reported in Figure 4.28 (b) for x_{TBA}=0.24. As shown in Figure 4.28 (b) a peak of nHB was observed close to the silica surface beyond the bulk value. As observed in Figure 4.28 (b) this peak is the result of two contributions, the hydrogen bonds (HB) between silica wall and the OH groups of TBA and HB between TBA molecules. That highlights a strong hydrogen bonding network between TBA and silica material that is at the origin of the core-shell organization.

To ensure this hypothesis, MD simulations through a weakly hydrophilic silica nanopore (WH) was carried out. Figure 4.29 (a) shows that the weak ability of WH to establish interfacial hydrogen bonds between the silanol groups and the TBA molecules explains the absence of microphase

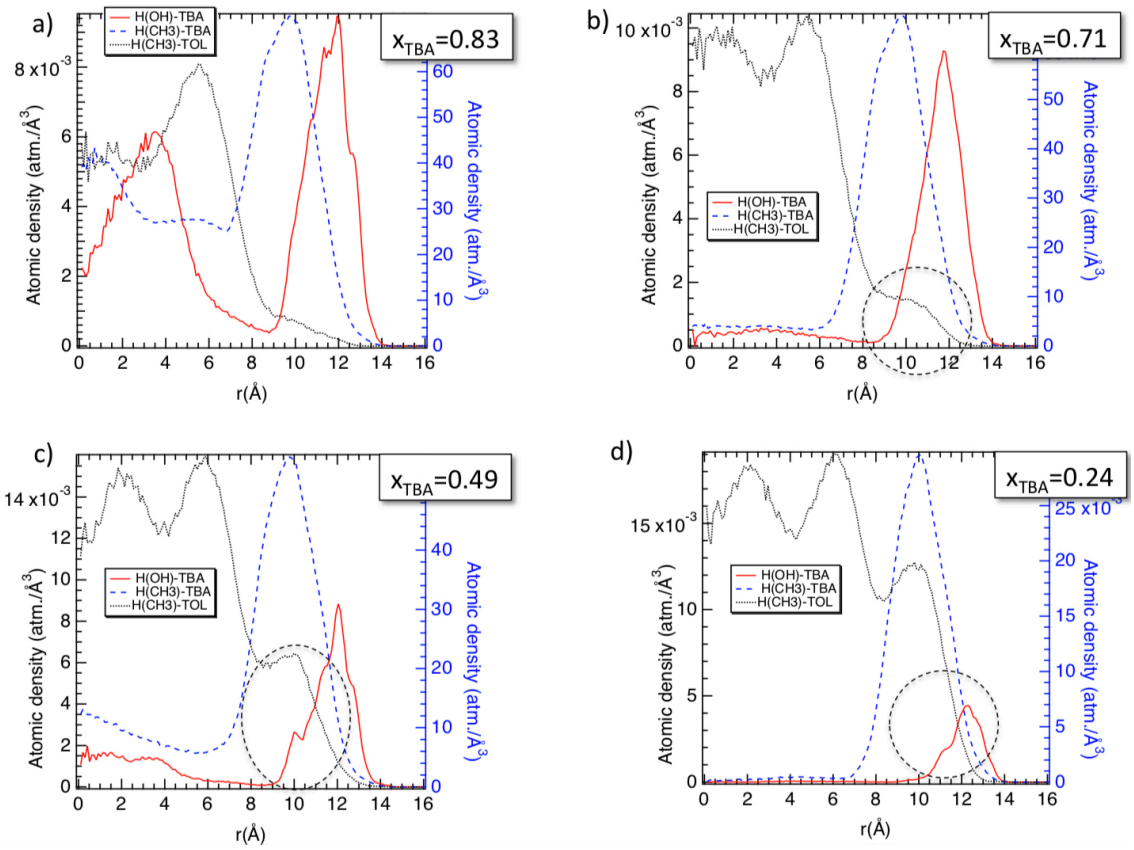

Figure 4.27: Profiles of radial density of the hydrogen atoms of the OH and CH3 groups of TBA and hydrogen atoms of CH_3 group of TOL for x_{TBA} = 0.83 (a), 0.71 (b), 0.49 (c), and 0.24 (d). The dashed circle represents the interpenetration region of TOL molecules in the interfacial layer.

separation. That bears out the fact that the interfacial anchoring from HB is the driving force to observe a microphase segregation. Interestingly, Figure 4.29 (b) exhibits that the carbon atoms of TBA and TOL are preferentially adsorbed in comparison with the hydroxide groups of TBA that underlines a hydrophobic anchoring related to the interactions between silicon and carbon atoms. It seems then that the strong interfacial hydrogen bonding network between TBA molecules and the silica material rules the preferential adsorption of TBA at the interface.

To strengthen this result, MD simulation of confined TBA/TOL mixture into a pure hydrophilic nanopore for a TBA concentration of x_{TBA}=0.24 was carried out. The ideal hydrophilic nanopore corresponds to a water nanotube (WNT) as previously showed. As shown in Figure 4.30 (c) TBA molecules are preferentially adsorbed at the water surface given the strong hydrogen bonds between TBA and water molecules leading to a core-shell structure with a homogeneous TBA/TOL

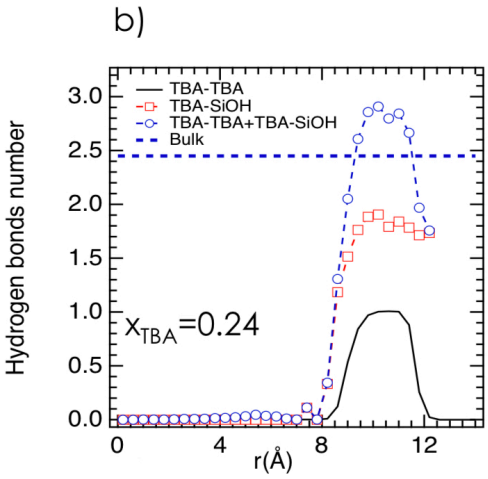

Figure 4.28: b) Profiles of the hydrogen bonds number per TBA molecules along the radial direction of the silica cylindrical nanopore.

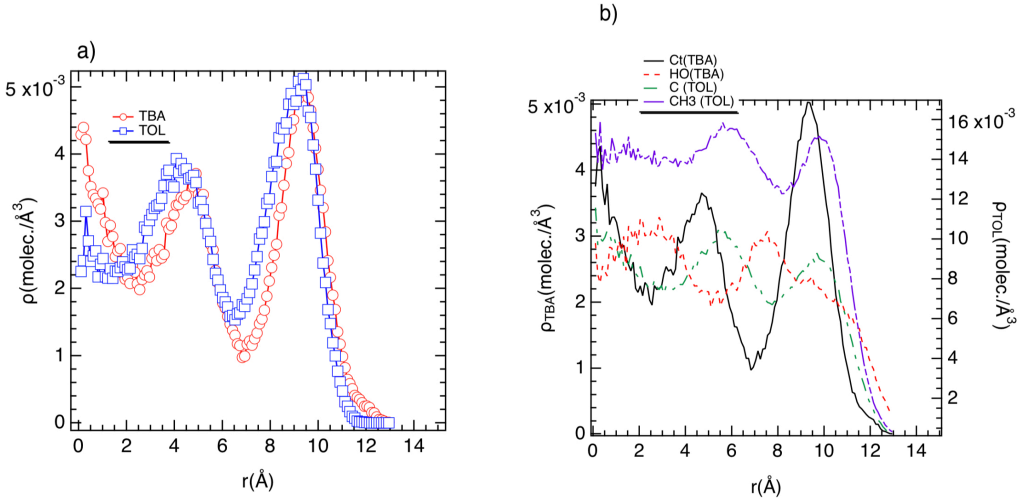

Figure 4.29: a) Profile of the radial density of center of mass of TBA and TOL molecules confined into the weakly hydrophilic silica nanopore. b) Profile of the radial density of tertiary carbon (C_t), hydrogen atom of hydroxide group (HO) of TBA, and carbon of benzenic cycle (C) and methyl group (CH_3) of TOL.

mixture at the centre of pore. These results indicate that the highly hydrophilic surface induces a microphase separation of TBA/TOL mixture and could also suggest that a hydrophobic surface is not able to discriminate TBA and TOL molecules because TOL is fully hydrophobic. However, Figure 4.30 (d) shows that a carbon nanotube (CNT) is also capable to separate TBA and TOL by forming a core-shell structure such that TOL and TBA molecules are respectively preferentially located at the CNT surface and at the centre of pore.

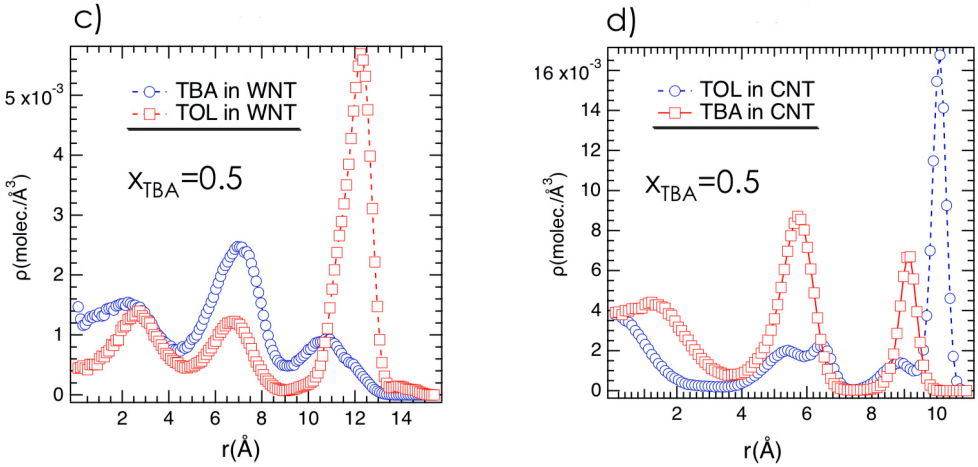

Figure 4.30: c) Profile of the radial density of TBA and TOL liquids confined into a water nanotube (WNT) with a pore radius of 12 Å. d) Profile of the radial density of TBA and TOL liquids confined into a carbon nanotube (CNT) with a pore radius of 12 Å.

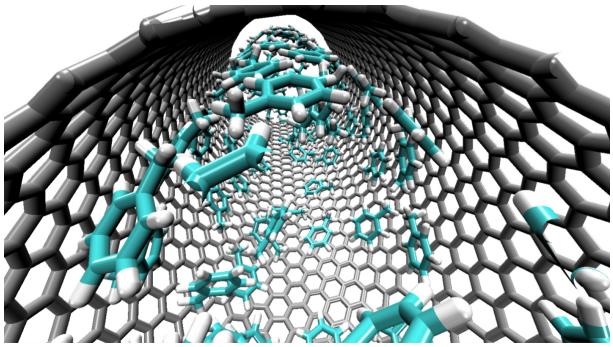

Figure 4.31: Snapshot illustrating the confinement of TOL molecules in the carbon nanotube of pore radius of 12 Å.

As shown in Figure 4.31 this separation is the result of a commensurate organization due to stacking interactions between benzenic cycles of CNT and TOL molecules. To go a little further, the curvature effect was also investigated. Indeed, as often shown the curvature induced by the cylindrical geometry can drastically impacted the physical properties in relation to the slitlike confinement [19, 20]. We carried out then MD simulation of a TBA/TOL mixture with a TBA concentration of x_{TBA}=0.5 confined through two silica slitlike pores such that the confinement in term of confined volume was conserved (two silica walls separated by a distance of 24 Å as illustrated in Figure 4.32 (a)).

As observed in Figure 4.32 (b) segregation between both liquids is observed highlighting that the separation is rather ruled by the interactions between the silica surface and TBA than the

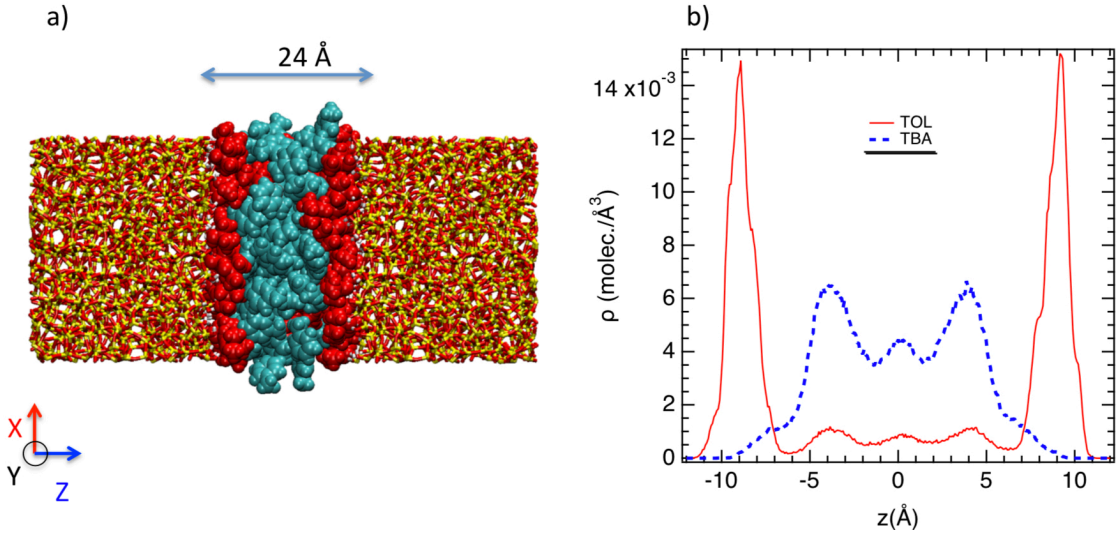

Figure 4.32: a) Illustration of the confined TOL (cyan color) and TBA (red color) for x_{TBA} = 0.5, between two silica walls separated by a distance of 24 Å. Red and yellow colors correpond to the oxygen and silicon atoms. b) Profile of the axial density of centers of mass of TBA and TOL molecules confined between two silica slabs separated by a distance of 24 Å.

pore geometry. Eventually, pore size effect was also investigated and MD simulations of confined TBA/TOL mixture with a TBA concentration of x_{TBA}=0.5 confined in a silica nanopore of radius of 6 Å and 18 Å were carried out. As shown in Figure 4.33, the microphase separation and the

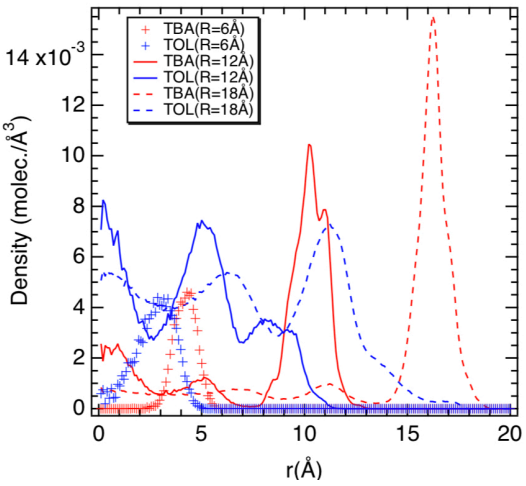

Figure 4.33: Profiles of radial density of the center of mass of TBA and TOL molecules for x_{TBA}= 0.50 for three pore radii (R = 6, 12, and 18 Å)

core-shell organization are still observed that corroborates that the driving force is connected to the interfacial anchoring by hydrogen bonds allowing that preferential adsorption of TBA

molecules. Additionally, Morineau et al. have recently shown, from Neutron scattering [49], that the core-shell organization was also observed with a pore radius of 43 Å. Therefore, the solid-liquid interactions and more especially the solid-liquid hydrogen bonds seem to overcome the bulk ones whatever the pore diameter leading to the microphase separation and the core-shell structure. Eventually, by comparing the structures obtained from the silica nanotube and from the CNT material (smoothness nanopore) we show that the core shell organization is independent of the surface roughness. Although, the core-shell structure is indirectly correlated to the capillary condensation the main mechanism is related to the wetting on the silica surface and then to the interfacial interactions between TBA/TOL and the SiOH. Therefore the microphase separation at the nanoscale cannot be related to any putative de-wetting phenomenon, nor could it be understood by considering solely the capillary condensation of the gas. Indeed, a vision of the intermolecular interactions and then the strength of wetting is needed to capture the origin of the microphase, what was performed in this work.

4.7 Conclusion

We have investigated the microscopic structure of TOL, TBA and CHX and their mixtures inside 2nm and 1nm pore size of CNT and WNT using MD simulations. We examined the confinement type dependency of these mixtures and their local properties. For both confinements, we found that molecules are arranged into layers, but showed different affinities near the wall surfaces. In the case of hydrophobic confinement, TOL displayed a very strong affinity to the wall surface in CNT better than TBA molecules. However, we observed the opposite in a completely hydrophilic confinement. TOL has showed a very strong affinity with the wall surface in CNT better than TBA molecules in the case of a hydrophobic confinement. However, in a totally hydrophilic confinement, we observed the inverse. These data suggest that the wall surface chemistry influences such molecules ' preferential layered organization near the surface. We also found at this stage that the form of confinement affects the fluid organization within these nanopores. In the case of hydrophilic confinement, alcohol molecules are more attracted to the confining surface, whereas hydrophobic confinement is the hydrocarbons that prefer to be present in large quantities beside the surface. By tuning the surface chemistry of the nanopore

to mimic hydrophilic and hydrophobic confinement, we show that it is possible to control the structural characteristics of the core-shell structure.The molecular origin of the microphase separation is then ascribed to the strong hydrogen bonds and a commensurate arrangement between the confining material and both liquids. In this work, the TOL/TBA mixture that is homogenous in the bulk liquid phase was confined at the nanoscale into cylindrical pores. We showed that the nano-confinement can induce, under a few conditions, microphase separation of binary mixture with a core-shell organization in line with Neutron scattering experiments. Phase separation was evidenced by highlighting both liquid-liquid and liquid-solid interfaces by means of the profiles of the density of centre of mass and the local surface tension. By computing the radial profile of the hydrogen bonds number and by tuning the hydrophilicity of the surface of the silica nanopore we established that the phase separation was ruled at the molecular scale by the strong hydrogen bonds between TBA molecules and the silica material that favors the HB anchoring. Confinement through a carbon nanotube showed an inverse core-shell structure with TOL anchored at the solid surface highlighting an hydrophobic anchoring due to a commensurate organization implying the benzenic cycles stacking. These results shed light on the possibility to control the nanostructure of multicomponent fluids under confinement at the nanoscale by tuning the surface chemistry of nanopore. The nanoconfined phase separation seems to be independent to the pore size and is essentially connected to the strength of pore-fluid interactions. As shown in Figure 4.29 (a) the microphase separation has not been established from a weakly hydrophilic pore whereas the core-shell structure was also recovered from a hydrophobic matrix (CNT) highlighting that the phase separation is unambiguously connected to the liquid-solid interactions. Determination of a theoretical model predicting the phase separation as a function of the strength of the solid-liquid interactions could be possible by tuning progressively (thermodynamic integration) the pore liquid interactions (Lennard-jones parameters and partial charges). However, it will be difficult to connect this model with the realistic materials where the interactions are too complexes. We think, that the so-developed strategy consisting in the refining of the pore-wall interactions by a comparison with experiment is probably the most relevant approach. Qualitatively, the microphase separation can be then predicted if one considers a mixture of an amphiphilic component and a hydrophobic one confined in pure hydrophilic

and hydrophobic pores. Although the development of a theoretical model to predict the phase separation in a nanoconfined pore seems to be difficult to connect with realistic materials it is possible to predict the optimal conditions to observe the core-shell organization that means the maximal number of TBA molecules anchored at the surface.

Indeed the pore volume can be calculated as $V_{pore}= \pi R_{pore}^2 L_z$ where R_{pore} is the pore radius of the nanopore while L_z is the height of the nanotube, the volume of the core region is $V_{core}= \pi R_{core}^2 L_z$ such that R_{core} is the radius of the core region. The volume of the interfacial zone, i.e., the shell can be then evaluated as $V_{pore}= \pi(R_{pore}^2 - R_{core}^2)L_z$ such that $R_{core} = R_{pore} - e_{shell}$ with e_{shell} corresponding to the thickness of the interfacial shell. e_{shell} is computed from the density profile. From the density profiles calculations, we found that e_{shell}=4 Å. If we consider the bulk density as the interfacial density the number of TBA molecules interfacially anchored can be calculated as $N_{TBA,s} = V_{shell} \cdot \rho_{TBA,bulk}$. With R_{pore}=12 Å and e_{shell}=4 Å an interfacial saturation of $N_{TBA,s} = 57$ was predicted. Therefore, for the TBA molar fraction corresponding to a number of TBA molecules less than $N_{TBA,s}$ the TBA will be fully anchored and a full core-shell organization will be observed (i.e., x_{TBA}=0.71, 0.49 and 0.24). Beyond $N_{TBA,s}$, TBA molecules will be also located in the centre of pore and in the intermediary layer. From simulations, we found that the solid interface is saturated for $N_{TBA,s}$=56 molecules that bears out our previous structural model. In Figure 4.26 (a), the molar fraction x_{TBA}=0.83 corresponds to 79 TBA and 16 toluene molecules. Therefore other TBA molecules (79-57) are distributed at the centre of pore and in the intermediate layer. As shown in Figure 4.24 (b) the first layer is located between 0 and 3 Å, the second between 3 and 7.5 Å while the last is located between 7.5 and 12 Å. As the layer size corresponds to the molecule size and that TOL molecule is higher than TBA one, 3.5 Å vs 3.0 Å it appears that TOL molecules have no place at the centre of pore contrary to the intermediate layer where the layer size is 4.5 Å.

Eventually, the microphase separation raises exiting questions about its impact on the molecular dynamics and the liquid flow in nanochannel, as suggested by the recent report on multiple glassy dynamics [50]. Further insight about this aspect could be attained from ongoing experimental spectroscopy and molecular simulation studies.

Bibliography

[1] Andrew W. Knight, Nikolai G. Kalugin, Eric Coker, and Anastasia G. Ilgen. Water properties under nano-scale confinement. *Scientific Reports*, 9:8246, 2019.

[2] Wycliffe K. Kipnusu, Mahdy M. Elmahdy, Mohamed Elsayed, Reinhard Krause-Rehberg, and Friedrich Kremer. Counterbalance between surface and confinement effects as studied for amino-terminated poly(propylene glycol) constraint in silica nanopores. *Macromolecules*, 52(4):1864–1873, 2019.

[3] STEVE GRANICK. Motions and relaxations of confined liquids. *Science*, 253(5026):1374–1379, 1991.

[4] Jacob Klein and Eugenia Kumacheva. Confinement-induced phase transitions in simple liquids. *Science*, 269(5225):816–819, 1995.

[5] Fabio Bruni, Maria Antonietta Ricci, and Alan K. Soper. Water confined in vycor glass. i. a neutron diffraction study. *The Journal of Chemical Physics*, 109(4):1478–1485, 1998.

[6] Alan K. Soper, Fabio Bruni, and Maria Antonietta Ricci. Water confined in vycor glass. ii. excluded volume effects on the radial distribution functions. *The Journal of Chemical Physics*, 109(4):1486–1494, 1998.

[7] Denis Morineau and Christiane Alba-Simionesco. Liquids in confined geometry: How to connect changes in the structure factor to modifications of local order. *The Journal of Chemical Physics*, 118(20):9389–9400, 2003.

[8] Mataz Alcoutlabi and Gregory B McKenna. Effects of confinement on material behaviour at the nanometre size scale. *Journal of Physics: Condensed Matter*, 17(15):R461–R524, apr 2005.

[9] B. Coasne, S. K. Jain, and K. E. Gubbins. Freezing of fluids confined in a disordered nanoporous structure. *Phys. Rev. Lett.*, 97:105702, Sep 2006.

[10] C Alba-Simionesco, B Coasne, G Dosseh, G Dudziak, K E Gubbins, R Radhakrishnan, and M Sliwinska-Bartkowiak. Effects of confinement on freezing and melting. *Journal of Physics: Condensed Matter*, 18(6):R15–R68, jan 2006.

[11] Ghoufi A. Molecular simulations of confined liquids: an alternative to the grand canonical monte carlo simulations. *J Chem Phys*, 134:074104–1, 2011.

[12] Aziz Ghoufi, Ivanne Hureau, Ronan Lefort, and Denis Morineau. Hydrogen-bond-induced supermolecular assemblies in a nanoconfined tertiary alcohol. *The Journal of Physical Chemistry C*, 115(36):17761–17767, 2011.

[13] A. Ghoufi, A. Szymczyk, R. Renou, and M. Ding. Calculation of local dielectric permittivity of confined liquids from spatial dipolar correlations. *EPL (Europhysics Letters)*, 99(3):37008, aug 2012.

[14] H. Zhu, A. Ghoufi, A. Szymczyk, B. Balannec, and D. Morineau. Anomalous dielectric behavior of nanoconfined electrolytic solutions. *Phys. Rev. Lett.*, 109:107801, Sep 2012.

[15] Aziz Ghoufi, Ivanne Hureau, Denis Morineau, Richard Renou, and Anthony Szymczyk. Confinement of tert-butanol nanoclusters in hydrophilic and hydrophobic silica nanopores. *The Journal of Physical Chemistry C*, 117(29):15203–15212, 2013.

[16] Xiang-Yang Guo, Tobias Watermann, and Daniel Sebastiani. Local microphase separation of a binary liquid under nanoscale confinement. *The Journal of Physical Chemistry B*, 118(34):10207–10213, 2014.

[17] Hamid ARA. Microphase separation of binary liquids confined in cylindrical pores. *J Phys Chem C*, 120:9245, 2016.

[18] G. Hummer, J. C. Rasaiah, and J. P. Noworyta. Water conduction through the hydrophobic channel of a carbon nanotube. *Nature*, 414(6860):188–190, 2001.

[19] Kerstin Falk, Felix Sedlmeier, Laurent Joly, Roland R. Netz, and Lyderic Bocquet. Molecular origin of fast water transport in carbon nanotube membranes: Superlubricity versus curvature dependent friction. *Nano Letters*, 10(10):4067–4073, 2010.

[20] Aziz Ghoufi, Anthony Szymczyk, and Patrice Malfreyt. Ultrafast diffusion of ionic liquids confined in carbon nanotubes. *Scientific Reports*, 6:28518, 2016.

[21] Andriy V. Kityk, Matthias Wolff, Klaus Knorr, Denis Morineau, Ronan Lefort, and Patrick Huber. Continuous paranematic-to-nematic ordering transitions of liquid crystals in tubular silica nanochannels. *Phys. Rev. Lett.*, 101:187801, Oct 2008.

[22] Simon Gruener and Patrick Huber. Spontaneous imbibition dynamics of an n-alkane in nanopores: Evidence of meniscus freezing and monolayer sticking. *Phys. Rev. Lett.*, 103:174501, Oct 2009.

[23] Christos Grigoriadis, Hatice Duran, Martin Steinhart, Michael Kappl, Hans-Jurgen Butt, and George Floudas. Suppression of phase transitions in a confined rodlike liquid crystal. *ACS Nano*, 5(11):9208–9215, 2011.

[24] V. Ballenegger and J.-P. Hansen. Dielectric permittivity profiles of confined polar fluids. *The Journal of Chemical Physics*, 122(11):114711, 2005.

[25] Douwe Jan Bonthuis, Stephan Gekle, and Roland R. Netz. Dielectric profile of interfacial water and its effect on double-layer capacitance. *Phys. Rev. Lett.*, 107:166102, Oct 2011.

[26] Douwe Jan Bonthuis, Stephan Gekle, and Roland R. Netz. Dielectric profile of interfacial water and its effect on double-layer capacitance. *Phys. Rev. Lett.*, 107:166102, Oct 2011.

[27] Cui Zhang, Francois Gygi, and Giulia Galli. Strongly anisotropic dielectric relaxation of water at the nanoscale. *The Journal of Physical Chemistry Letters*, 4(15):2477–2481, 2013.

[28] Olivier Emile, Janine Emile, and Aziz Ghoufi. Influence of the interface on the optical activity of confined glucose films. *Journal of Colloid and Interface Science*, 477:103 – 108, 2016.

[29] Juan-Pedro Palomares-Baez, Emanuele Panizon, and Riccardo Ferrando. Nanoscale effects on phase separation. *Nano Letters*, 17(9):5394–5401, 2017.

[30] Pawel Keblinski, Wen-Jong Ma, Amos Maritan, Joel Koplik, and Jayanth R. Banavar. Molecular dynamics of phase separation in narrow channels. *Phys. Rev. E*, 47:R2265–R2268, Apr 1993.

[31] Lev D. Gelb and K. E. Gubbins. Liquid-liquid phase separation in cylindrical pores: Quench molecular dynamics and monte carlo simulations. *Phys. Rev. E*, 56:3185–3196, Sep 1997.

[32] Lev D. Gelb and K.E. Gubbins. Studies of binary liquid mixtures in cylindrical pores: phase separation, wetting and finite-size effects from monte carlo simulations. *Physica A: Statistical Mechanics and its Applications*, 244(1):112 – 123, 1997.

[33] Sujeet Dutta, Ronan Lefort, Denis Morineau, Ramona Mhanna, Odile Merdrignac-Conanec, Arnaud Saint-Jalmes, and Theo Leclercq. Thermodynamics of binary gas adsorption in nanopores. *Phys. Chem. Chem. Phys.*, 18:24361–24369, 2016.

[34] Kathryn L. Krycka, Joseph A. Dura, Luther J. Langston, and Christopher M. Burba. Nanoconfinement-induced phase segregation of binary benzene-Äìcyclohexane solutions within a chemically inert matrix. *The Journal of Physical Chemistry C*, 122(14):7676–7684, 2018.

[35] Michael F. Harrach, Barbara Drossel, Wadim Winschel, Torsten Gutmann, and Gerd Buntkowsky. Mixtures of isobutyric acid and water confined in cylindrical silica nanopores revisited: A combined solid-state nmr and molecular dynamics simulation study. *The Journal of Physical Chemistry C*, 119(52):28961–28969, 2015.

[36] T Muthulakshmi, D Dutta, Priya Maheshwari, and P K Pujari. Evidence for confinement induced phase separation in ethanol–water mixture: a positron annihilation study. *Journal of Physics: Condensed Matter*, 30(2):025001, dec 2017.

[37] Rebecca Schmitz, Niels Muller, Svenja Ullmann, and Michael Vogel. A molecular dynamics simulations study on ethylene glycol-water mixtures in mesoporous silica. *The Journal of Chemical Physics*, 145(10):104703, 2016.

[38] Ghoufi A. Physical properties and hydrogen-bonding network of water-ethanol mixtures from molecular dynamics simulations. *J Phys Chem B*, 120:793, 2016.

[39] Wang Y. Tail aggregation and domain diffusion in ionic liquids. *J Phys Chem B*, 110:18601, 2006.

[40] Ghoufi A. Hydrogen-bond-induced supermolecular assemblies in a nanoconfined tertiary alcohol. *J Phys Chem C*, 115:17761, 2011.

[41] Ghoufi A. Confinement of tert-butanol nanoclusters in hydrophilic and hydrophobic silica nanopores. *J Phys Chem C*, 117:15203, 2013.

[42] Brodka A. Properties of liquid acetone in silica pores: molecular dynamics simulation. *J Chem Phys*, 104:6319, 1996.

[43] Li S. Toward understanding the structural heterogeneity and ion pair stability in dicationic ionic liquids. *Soft Matter*, 10:9193, 2014.

[44] Mhanna R. More room for microphase separation: an extended study on binary liquids confined in sba-15 cylindrical pores. *J Chem Phys*, 146:024501–1, 2017.

[45] I. Essafri, J. Courtin, and A. Ghoufi. Numerical evidence of heterogeneity and nanophases in a binary liquid confined at the nanoscale. *Molecular Simulation*, 44(9):728–735, 2018.

[46] Randall T. Cygan, Jian-Jie Liang, and Andrey G. Kalinichev. Molecular models of hydroxide, oxyhydroxide, and clay phases and the development of a general force field. *The Journal of Physical Chemistry B*, 108(4):1255–1266, 2004.

[47] A. Ghoufi, D. Morineau, R. Lefort, and P. Malfreyt. Toward a coarse graining/all atoms force field (cg/aa) from a multiscale optimization method: An application to the mcm-41 mesoporous silicates. *Journal of Chemical Theory and Computation*, 6(10):3212–3222, 2010.

[48] Alenka Luzar and David Chandler. Effect of environment on hydrogen bond dynamics in liquid water. *Phys. Rev. Lett.*, 76:928–931, Feb 1996.

[49] Ramona Mhanna, Abdel Razzak Abdel Hamid, Sujeet Dutta, Ronan Lefort, Laurence Noirez, Bernhard Frick, and Denis Morineau. More room for microphase separation: An extended study on binary liquids confined in sba-15 cylindrical pores. *The Journal of Chemical Physics*, 146(2):024501, 2017.

[50] Abdel Razzak Abdel Hamid, Ramona Mhanna, Pierre Catrou, Yann Bulteau, Ronan Lefort, and Denis Morineau. Multiple glass transitions of microphase separated binary liquids confined in mcm-41. *The Journal of Physical Chemistry C*, 120(20):11049–11053, 2016.

Chapter 5

Summary and future research

5.1 Summary of the current work

The investigations conducted in the present thesis were intended to provide insight into the hydrogen bonding (HB) network at the nanoscale. Liquid-forming hydrogen bonding, linear and branched chain alcohols were investigated and mixed with apolar molecules (toluene and cyclohexane) to study the dilution of the HB network. The structure and dynamics of these binary mixtures have been then studied.

This work has focused on the exploration at the nanoscale of the non-ideality of methanol, ethanol, propanol, butanol, pentanol and tert-butanol in mixtures with toluene and cyclohexane by means of molecular dynamics simulations. Simulations fairly reproduced the experimental densities of all binary mixtures even at the miscibility region of methanol-cyclohexane binary mixtures. In all mixtures, the deviation from the ideal mixture behavior was observed and different intensities were recorded. In the case of toluene this non-ideality have been ascribed with the specific interactions between toluene and alcohol leading to a breaking in the hydrogen-bonding network involving clusters of different sizes and the spatial heterogeneity. Particularly, the immiscibility and the non-ideality (negative excess density) of the CHX-MeOH mixtures were the result of the unfavorable interactions between CHX and MeOH leading to a self-organizing of CHX molecules to form hydrophobic nano-phases at the origin of the structural heterogeneity in the miscible region. However, the non-ideality showed by ethanol, propanol, butanol, pen-

tanol and tert-butanol (negative excess density except for low EtOH concentration) have been attributed to the hydrophobic character of CHX molecules with alcohols ones and the creation of largest clusters in comparison with alcohols in TOL. A strong dilution of the hydrogen bonding network by toluene molecules as well as cyclohexane molecules has been shown. Nanophases have been characterized in terms of pockets of linear clusters such that the difference in miscibility and in heterogeneity were understood in terms of cluster size and distribution for methanol-toluene and methanol-cyclohexane mixtures. Moreover, we have shown that the presence of clusters had to be uncorrelated from the notion of heterogeneity. Eventually, we have highlighted that the prepeak observed in the structure factor is independent of the degree of heterogeneity but is rather connected to the presence of cyclic clusters. Additionally, the dynamics of these liquids were in line with the structural results given that a fast motion with a rapid relaxation times were shown by alcohol molecules in mixture with TOL whereas a slow motion with a long relaxation times of alcohols in CHX were captured. The results of this part allow us to differentiate between the intensity of the self-organization of liquids at their hydrogen bonding networks while distinguishing between ideal and non-ideal mixture in terms of microscopic local structuring.

Toluene/*tert*-butanol and cyclohexane/*tert*-butanol were studied under nanoscale confinement. This systems choice is based on recent experimental observation where a micro-phase separation of toluene/*tert*-butanol miscible binary mixture were attributed to the hydrogen bonds interaction created between the alcohol molecules and the confining wall surface. Such binary liquids are miscible at any concentration and homogeneous on a microscopic scale. Confined toluene/*tert*-butanol mixture behavior within the MCM-41 silica cylindrical nanopore illustrated a clear spatial heterogeneity leading to the formation of nano-phases (segregation). While the confinement of the same mixture under a totally hydrophilic matrix as our nanopore prototype called a water nanotube, the behavior is different where local de-mixing behavior is captured near the wall surface. This was attributed to the creation of hydrogen bonds interactions between water molecules on the surface and *tert*-butanol molecules at the interface. However, toluene/*tert*-butanol has also been studied in the hydrophobic nanopore, the carbon nanotube. A hydrophobic local de-mixing was highlighted for toluene/*tert*-butanol near the wall surface that is attributed to the hydrophobic anchoring of toluene molecules on the confining surface.

Interestingly, no de-mixing behavior was observed for cyclohexane/*tert*-butanol mixture within the carbon nanotube, which is a barely predictable because there is no favorable interactions between the confining surface and cyclohexane molecules. In the hydrophilic water nanotube, cyclohexane/*tert*-butanol mixture for the first time showed a local hydrophilic de-mixing near the wall surface. That was attributed to the hydrogen bonds interactions with *tert*-butanol and water molecules at the interface. At this point, the pore size effect was also explored. The results mentioned previously were obtained for a radius(size pore)=2nm. In a carbon nanotube of 1.15 nm pore size, the toluene/*tert*-butanol mixture has again shown de-mixing behavior even if the pore size is decreased. However, cyclohexane/*tert*-butanol has always indicated that there is no hydrophobic de-mixing behavior. In the water nanotube, there are significant differences in behavior once the pore size is reduced. In the water nanotube at 1nm pore size, toluene/*tert*-butanol mixture showed a strong hydrophilic de-mixing behavior. While cyclohexane/*tert*-butanol revealed a micro-phase separation under the hydrophilic nanopore (water nanotube). So far, no core-shell organization has been observed for the two mixtures confined in the three types of confinement. At such a point, we decided to study the adsorption isotherms of toluene/*tert*-butanol liquid mixture in order to quantify the surface interactions with the silica cylindrical nanopore (MCM-41). Finally, by improving the solid-liquid interactions, we are able to qualitatively reproduce the experimental adsorption isotherms of both single liquids, the micro-phase separation and the core-shell structure. The tuning of the surface chemistry of the nanopore in order to model the hydrophilic and hydrophobic confinement has shown that it is possible to control the structural characteristics of the core shell structure. The molecular origin of the micro-phase separation is then ascribed to the strong hydrogen bonds and a commensurate arrangement between the confining material and both liquids.

5.2 Future research

As an extension of this research, it could be more complementary to study other binary miscible liquids within hydrophilic and hydrophobic nano-pores as well as their transport inside nano-channels. It is interesting to correlate the structure to the dynamics of liquids at this scale. In addition to that, the study of filling processes by imbibition in order to evaluate the impact of

filling on structuring could be an interesting vast area of research to enhance our understanding of the relation between structure-dynamics property inside the nano-porous materials.

Appendix A

Appendix structural and dynamical analysis

A.1 Total density

Density refers to how much matter is packed into a substance, and it's usually measured in grams per cubic centimeter (g/cm^3). Density is a measure that compares the amount of matter of an object to its volume. For example, an object with a lot of material in a certain volume has a high density. If an object is heavy and compact, it has a high density. Density is obtained by dividing the mass of an object by its volume. The structure of our molecular systems were first explored by density calculation. This is accomplished by a simple density calculation, applying this equation to our simulation trajectories:

$$\rho = \frac{n_a.M_a + n_b.M_b}{< V >} \tag{A.1}$$

Where <.> indicates the average value, the (n_a, M_a) and (n_b, M_b) are the number of molecules and the molar mass of the alcohol and the aprotic molecules respectively.

A.2 Radial distribution function:

The radial distribution function (RDF), (or pair correlation function) $g(r)$ in a system of particles (atoms, molecules, colloids, etc.), describes how density varies as a function of distance from a reference particle. Radial distribution function analysis is an important feature to explore matters local order. It gave us a statistical description of atomic positions. Atomic arrangement can be described from this function. It can be measured experimentally by scattering experiments. The RDF is usually determined by calculating the distance between all particle pairs and binning them into a histogram. The histogram is then normalized with respect to an ideal gas, where particle histograms are completely uncorrelated. For three dimensions, this normalization is the number density of the system multiplied by the volume of the spherical shell, which mathematically can be expressed as $g(r) = 4\pi r^2 \rho dr$, where ρ is the number density.
RDF was calculated from $\mathrm{RDF(i-j)} =< \mathrm{H(r_{ij})} >< \mathrm{V} > /4\pi \mathrm{r_{ij}^2} \delta \mathrm{N_i N_j}$ such that $\mathrm{H(r_{ij})}$ is the number of i-j pairwise interactions located at $\mathrm{r_ij}$, V is the volume, $\mathrm{r_ij}$ the distance between i and j particles, $\mathrm{N_i}$ and $\mathrm{N_j}$ the number of i and j particles and $< . >$ is the statistical average.

A.3 Heterogeneity order parameter

The local structural order was investigated through the use of the heterogeneity order parameter (HOP) [1]. The HOP is defined as

$$HOP = \frac{1}{N_S} \sum_{i=1}^{N_S} \sum_{j=1}^{N_S} \exp\left(-\frac{r_{ij}^2}{2\sigma^2}\right) \tag{A.2}$$

where $\mathrm{r_{ij}}$ is the distance between sites i and j and $\sigma = \mathrm{L/Ns^{1/3}}$, L is the simulation box length, and $\mathrm{N_s}$ is the number of sites for which the HOP is being computed. The HOP value increases when more sites are closer to each other, resulting in a higher value for more aggregated or clustered geometries.
The HOP is so defined that it is topologically invariant with the absolute distances between sites, thus independent of the simulation box size L. Because the weights of the sites far from the target site decrease quickly with distance, the HOP approaches a constant with increasing

number of sites. Some ideal systems with sites that is uniformly distributed in a cubic box were constructed, and the HOP was computed for these systems with periodic boundary conditions applied. The HOP takes a fixed number of 15.7496 when the number of sites is larger than 1000.

A.4 Hydrogen bond number

Hydrogen bonds are non-covalent interactions occurrisng between the H atom of a dipolar molecule such as water, and the unshared electron pair of another atom (i.e., O or N). The definition of the hydrogen bond used in this thesis is based on the geometric criteria developed by Luzar and Chandler [2]. That is, an intermolecular pair is hydrogen bonded if the following conditions are fully satisfied.

1. The distance between oxygen atoms is less than R_{O-O}=3.6 Å.

2. The distance between donor hydrogen atom and acceptor oxygen atom is less than R_{O-H}= 2.4 Å.

3. The angle between the vector that connects the two oxygen atoms and the vector that connects donor intramolecular oxygen and hydrogen atoms is less than 30°.

A.5 Hydrogen-bonded clusters

Calculation of cluster size based on the hydrogen bonds is performed by considering the modified algorithm of Stoddard [3].

A.6 Partial structure factor

The structure factor ($S^{Liq}(Q)$) was computed from eq.(A.3) where (Q) is the momentum transfer vector, N_L the number of molecules of liquid, n_L the number of atoms belonging of one liquid molecule, r_{km} is the vector position $r_{km}= r_m - r_k$ and b_i the coherent diffusion length of atom i. The brackets stand for time and isotropic average carried out over the angles of Q in spherical coordinates of a sum of the scattering intensity arising from every couples of atoms (θ, ϕ)

$$S^{Liq}(Q)) = \frac{(\sum_{j=1}^{N_L} \sum_{k=1}^{n_L} \sum_{m=1}^{n_L} b_k b_m \exp(-iQr_{km}))_{\theta,\phi}}{N_L(\sum_{i=1}^{n_L} b_i)^2} \tag{A.3}$$

. Thus, the structure factor is expressed by steradians corresponding to the cross section measured by neutron scattering. $S^{Liq}(Q)$ is normalised by the number of molecules (N_L) to compare the bulk and confined phases. Then the unit of eq.(A.3) is molecules by steradian.

A.7 Time correlation function of dipole moment

A.7.1 Definition

We define a time-correlation function as:

$$C(t) =< A(t_0) \cdot A(t) > \tag{A.4}$$

where the angle brackets represent an ensemble average and A is the dynamic variable of interest. If we compare the value of A(t) with its value at zero time, A(0) the two values will be correlated at sufficiently short times, but at longer times the value of A(t) will have no correlation with its value at t=0. Information on relevant dynamical processes is contained in the time decay of C(t). The starting time is arbitrary so we can also discuss the ensemble average starting at any time, t.

$$C(t) =< A(\tau) \cdot A(t+\tau) > \tag{A.5}$$

Normalization may also be applied by dividing by <A(0)A(0) >. The normalized function is a decay from a value of one to some lower value (not always zero). It represents the loss of correlation with the initial value. The short time value is proportional to $<A^2>$. The asymptotic long time value is proportional to $< A >^2$ as shown in the figure below.

A.7.2 The time-correlation function method

The decay shown in the figure is the average of a large number of trajectories. We can see that C(t) decays from $< A^2 >$ to $< A >^2$. This means that initially C(0) =< A(0)A(0) > which is clear from our definition. Note that this value is shown as 1.0 on the y-axis because of normalization. As time goes on the value of A(t) changes and becomes less correlated with

its value at time zero. At long enough times A(t) has no correlation and so its average value is <A(t)>. The average value of A at time zero is <A(0)>. These averages are both average values of A and should be the same. Thus, $< A(0) >< A(t) > =< A(0) >< A(0) > = < A(0) >^2$. The value of zero shown in the Figure above is arbitrary. The normalized long time value is $< A(0) >^2 / <A(0)A(0)>$ and is less than one, but is zero only if <A(0)> = 0.

A.7.3 Dipole moment

Even though the total charge on a molecule is zero, the nature of chemical bonds is such that the positive and negative charges do not completely overlap in most molecules. Such molecules are considered to be polar because they possessed a permanent dipole moment. The dipole moment is given by,

$$\boldsymbol{\mu} = \sum_{1}^{n} q_i(\mathbf{r_i} - \mathbf{r_{cm}}) \tag{A.6}$$

Then, the time correlation function of dipole moment is expressed as,

$$\Phi(t) = \frac{< \boldsymbol{\mu}(t + t_0) \cdot \boldsymbol{\mu}(t_0) >}{< \boldsymbol{\mu}(t_0)^2 >} \tag{A.7}$$

A.8 Relaxation time of dipole moment

The relaxation function $\Phi(t)$ is a linear function of a property of a system that evolves towards equilibrium after the sudden removal of a perturbation.

A.8.1 Debye model

$$\Phi(t) = \exp(-\frac{t}{\tau_D}) \tag{A.8}$$

A.8.2 Kohlrausch model

$$\Phi(t) = \exp\left(-(\frac{t}{\tau_K})^{\beta_K}\right) \tag{A.9}$$

where τ_D and τ_K is a parameter with the dimensions of time and β_K is $0 < \beta_K \leq 1$. In studies of the relaxation of complex systems, the Kohlrausch function is frequently used as a purely

empirical relaxation function, given that it allows gauging in a simple way deviations from the 'canonical' single exponential behavior by means of parameter β_{K}.

A.9 Mean square displacement (MSD)

A.9.1 Definition

The mean square displacement of atoms in a simulation can be easily computed by its definition:

$$MSD = \left\langle |r(t) - r(0)|^2 \right\rangle \tag{A.10}$$

where $\langle \cdots \rangle$ denotes here averaging over all the atoms (or all the atoms in a given subclass). Care must be taken to *avoid* considering the 'jumps' of particles to refold them into the box when using periodic boundary conditions as contributing to diffusion.

The MSD contains information on the atomic diffusivity. If the system is solid, MSD saturates to a finite value, while if the system is liquid, MSD grows linearly with time. In this case it is useful to characterize the system behavior in terms of the slope, which is the *diffusion coefficient* D:

$$D_s = \frac{1}{6} \lim \frac{\mathrm{dMSD}(t)}{dt}$$

Bibliography

[1] Li S. Toward understanding the structural heterogeneity and ion pair stability in dicationic ionic liquids. *Soft Matter*, 10:9193, 2014.

[2] Alenka Luzar and David Chandler. Effect of environment on hydrogen bond dynamics in liquid water. *Phys. Rev. Lett.*, 76(6):928–931, 1996.

[3] Stoddard S. Identifying clusters in computer experiments on sytems of particles. *J Comput Phys*, 27:291, 1978.

Bibliography

[1] Christopher J. Fennell and J. Daniel Gezelter. Is the ewald summation still necessary? pairwise alternatives to the accepted standard for long-range electrostatics. *The Journal of Chemical Physics*, 124(23):234104, 2006.

[2] Brodka A. Properties of liquid acetone in silica pores: molecular dynamics simulation. *J Chem Phys*, 104:6319, 1996.

[3] George A. Jeffrey and Wolfram Saenger. *The Importance of Hydrogen Bonds*, pages 3–14. Springer Berlin Heidelberg, 1991.

[4] J. Klein and E. Kumacheva. Confinement-induced phase transitions in simple liquids. *Science*, 269(5225):816–819, 1995.

[5] M. Alcoutlabi and Gregory B. McKenna. Effects of confinement on material behaviour at the nanometre size scale. *Journal of Physics: Condensed Matter*, 17(15):R461–R524, 2005.

[6] B. Coasne, S. K. Jain, and K. E. Gubbins. Freezing of fluids confined in a disordered nanoporous structure. *Phys. Rev. Lett.*, 97(10):105702, 2006.

[7] C. Alba-Simionesco, B. Coasne, G. Dosseh, G. Dudziak, K. E. Gubbins, R. Radhakrishnan, and M. Sliwinska-Bartkowiak. Effects of confinement on freezing and melting. *Journal of Physics: Condensed Matter*, 18(6):R15–R68, 2006.

[8] Steve Granick. Motions and relaxations of confined liquids. *Science*, 253(5026):1374–1379, 1991.

[9] A. Ghoufi, A. Szymczyk, R. Renou, and M. Ding. Calculation of local dielectric permittivity of confined liquids from spatial dipolar correlations. *EPL (Europhysics Letters)*, 99(3):37008, 2012.

[10] H. Zhu, A. Ghoufi, A. Szymczyk, B. Balannec, and D. Morineau. Anomalous dielectric behavior of nanoconfined electrolytic solutions. *Phys. Rev. Lett.*, 109(10):107801, 2012.

[11] A. Ghoufi and P. Malfreyt. Importance of the tail corrections on surface tension of curved liquid-vapor interfaces. *The Journal of Chemical Physics*, 146(8):084703, 2017.

[12] I. Essafri, J-C. Le breton, A. Saint-Jalmes, A. Soldera, A. Szymczyk, P. Malfreyt, and A. Ghoufi. Contact angle and surface tension of water on a hexagonal boron nitride monolayer: a methodological investigation. *Molecular Simulation*, 45(4-5):454–461, 2019.

[13] Kumar Varoon Agrawal, Steven Shimizu, Lee W. Drahushuk, Daniel Kilcoyne, and Michael S. Strano. Observation of extreme phase transition temperatures of water confined inside isolated carbon nanotubes. *Nature Nanotechnology*, 12:267, 2016.

[14] Song Hi Lee and Peter J. Rossky. A comparison of the structure and dynamics of liquid water at hydrophobic and hydrophilic surfaces: Äîa molecular dynamics simulation study. *The Journal of Chemical Physics*, 100(4):3334–3345, 1994.

[15] S. Han, M. Y. Choi, P. Kumar, and H. Eugene Stanley. Phase transitions in confined water nanofilms. *Nature Physics*, 6(9):685–689, 2010.

[16] Alexander I. Kolesnikov, Jean-Marc Zanotti, Chun-Keung Loong, Pappannan Thiyagarajan, Alexander P. Moravsky, Raouf O. Loutfy, and Christian J. Burnham. Anomalously soft dynamics of water in a nanotube: A revelation of nanoscale confinement. *Phys. Rev. Lett.*, 93(3):035503, 2004.

[17] W. Sparreboom, A. van den Berg, and J. C. T. Eijkel. Principles and applications of nanofluidic transport. *Nature Nanotechnology*, 4(11):713–720, 2009.

[18] Surya Singh. Nanomedicine nanoscale drugs and delivery systems. *Journal of Nanoscience and Nanotechnology*, 10(12):7906–7918, 2010.

[19] Vitaly V. Chaban, Timur I. Savchenko, Sergiy M. Kovalenko, and Oleg V. Prezhdo. Heat-driven release of a drug molecule from carbon nanotubes: A molecular dynamics study. *The Journal of Physical Chemistry B*, 114(42):13481–13486, 2010.

[20] Tamsyn A. Hilder and James M. Hill. Modeling the loading and unloading of drugs into nanotubes. *Small*, 5(3):300–308, 2009.

[21] Morineau D. Does molecular self-association survive in nanochannels? *J Phys Chem Lett*, 1:1155, 2010.

[22] Ghoufi A. Hydrogen-bond-induced supermolecular assemblies in a nanoconfined tertiary alcohol. *J Phys Chem C*, 115:17761, 2011.

[23] Chandler D. Interfaces and the driving force of hydrophobic assembly. *Nature*, 437:640, 2005.

[24] Niharendu Choudhury. Effect of surface hydrophobicity on the dynamics of water at the nanoscale confinement: A molecular dynamics simulation study. *Chemical Physics*, 421:68–76, 2013.

[25] Wolfram Saenger. Structure and dynamics of water surrounding biomolecules. *Annual Review of Biophysics and Biophysical Chemistry*, 16(1):93–114, 1987.

[26] Biman Bagchi. Water dynamics in the hydration layer around proteins and micelles. *Chemical Reviews*, 105(9):3197–3219, 2005.

[27] Jan Swenson, Helen Jansson, and Rikard Bergman. Relaxation processes in supercooled confined water and implications for protein dynamics. *Phys. Rev. Lett.*, 96:247802, 2006.

[28] G. Garberoglio, M. Sega, and R. Vallauri. Inhomogeneity effects on the structure and dynamics of water at the surface of a membrane: A computer simulation study. *The Journal of Chemical Physics*, 126(12):125103, 2007.

[29] Niharendu Choudhury. Orientational dynamics of water trapped between two nanoscopic hydrophobic solutes: A molecular dynamics simulation study. *The Journal of Chemical Physics*, 133(15):154515, 2010.

[30] Winarto, Eiji Yamamoto, and Kenji Yasuoka. Separation of water-alcohol mixtures using carbon nanotubes under an electric field. *Phys. Chem. Chem. Phys.*, 21(28):15431–15438, 2019.

[31] Shaoyi Jiang, Charles L. Rhykerd, and Keith E. Gubbins. Layering, freezing transitions, capillary condensation and diffusion of methane in slit carbon pores. *Molecular Physics*, 79(2):373–391, 1993.

[32] M. W. Maddox and K. E. Gubbins. Molecular simulation of fluid adsorption in buckytubes. *Langmuir*, 11(10):3988–3996, 1995.

[33] Erich A. Muller, Luis F. Rull, Lourdes F. Vega, and Keith E. Gubbins. Adsorption of water on activated carbons:,Äâ a molecular simulation study. *The Journal of Physical Chemistry*, 100(4):1189–1196, 1996.

[34] Alberto Striolo, Ariel A. Chialvo, Peter T. Cummings, and Keith E. Gubbins. Water adsorption in carbon-slit nanopores. *Langmuir*, 19(20):8583–8591, 2003.

[35] A. Striolo, A. A. Chialvo, K. E. Gubbins, and P. T. Cummings. Water in carbon nanotubes: Adsorption isotherms and thermodynamic properties from molecular simulation. *The Journal of Chemical Physics*, 122(23):234712, 2005.

[36] Abhijit V. Shevade, Shaoyi Jiang, and Keith E. Gubbins. Adsorption of water-Äîmethanol mixtures in carbon and aluminosilicate pores: a molecular simulation study. *Molecular Physics*, 97(10):1139–1148, 1999.

[37] Abhijit V. Shevade, Shaoyi Jiang, and Keith E. Gubbins. Molecular simulation study of water-Äìmethanol mixtures in activated carbon pores. *The Journal of Chemical Physics*, 113(16):6933–6942, 2000.

[38] Santiago Romero-Vargas Castrillon, Nicolas Giovambattista, Ilhan A. Aksay, and Pablo G. Debenedetti. Effect of surface polarity on the structure and dynamics of water in nanoscale confinement. *The Journal of Physical Chemistry B*, 113(5):1438–1446, 2009.

[39] G. Hummer, J. C. Rasaiah, and J. P. Noworyta. Water conduction through the hydrophobic channel of a carbon nanotube. *Nature*, 414(6860):188–190, 2001.

[40] L. D. Gelb, K. E. Gubbins, R. Radhakrishnan, and M. Sliwinska-Bartkowiak. Phase separation in confined systems. *Reports on Progress in Physics*, 63(4):727–727, 2000.

[41] Q. Zhang, Jie Zheng, A. Shevade, L. Zhang, Stevin H. Gehrke, Grant S. Heffelfinger, and Shaoyi Jiang. Transport diffusion of liquid water and methanol through membranes. *The Journal of Chemical Physics*, 117(2):808–818, 2002.

[42] T. Ohkubo, T. Iiyama, and K. Kaneko. Organized structures of methanol in carbon nanospaces at 303 k studies with in situ x-ray diffraction. *Chemical Physics Letters*, 312(2):191–195, 1999.

[43] T. Ohkubo, T. Iiyama, K. Nishikawa, T. Suzuki, and K. Kaneko. Pore-width-dependent ordering of c2h5oh molecules confined in graphitic slit nanospaces. *The Journal of Physical Chemistry B*, 103(11):1859–1863, 1999.

[44] T. Ohkubo and K. Kaneko. Oriented structures of alcohol hidden in carbon micropores with erdf analysis. *Colloids and Surfaces A: Physicochemical and Engineering Aspects*, 187-188:177–185, 2001.

[45] Regis Guegan, Denis Morineau, and Christiane Alba-Simionesco. Interfacial structure of an h-bonding liquid confined into silica nanopore with surface silanols. *Chemical Physics*, 317(2):236 – 244, 2005.

[46] Michael F. Harrach, B. Drossel, W. Winschel, T. Gutmann, and G. Buntkowsky. Mixtures of isobutyric acid and water confined in cylindrical silica nanopores revisited: A combined solid-state nmr and molecular dynamics simulation study. *The Journal of Physical Chemistry C*, 119(52):28961–28969, 2015.

[47] X-Y. Guo, T. Watermann, and D. Sebastiani. Local microphase separation of a binary liquid under nanoscale confinement. *The Journal of Physical Chemistry B*, 118(34):10207–10213, 2014.

[48] T. Muthulakshmi, D. Dutta, Priya Maheshwari, and P. K. Pujari. Evidence for confinement induced phase separation in ethanol–water mixture: a positron annihilation study. *Journal of Physics: Condensed Matter*, 30(2):025001, 2017.

[49] R. Schmitz, N. Muller, S. Ullmann, and M. Vogel. A molecular dynamics simulations study on ethylene glycol-water mixtures in mesoporous silica. *The Journal of Chemical Physics*, 145(10):104703, 2016.

[50] Kathryn L. Krycka, Joseph A. Dura, Luther J. Langston, and Christopher M. Burba. Nanoconfinement-induced phase segregation of binary benzene-Äìcyclohexane solutions within a chemically inert matrix. *The Journal of Physical Chemistry C*, 122(14):7676–7684, 2018.

[51] Hamid ARA. Microphase separation of binary liquids confined in cylindrical pores. *J Phys Chem C*, 120:9245, 2016.

[52] A. Abdel Hamid, R. Mhanna, P. Catrou, Y. Bulteau, R. Lefort, and D. Morineau. Multiple glass transitions of microphase separated binary liquids confined in mcm-41. *The Journal of Physical Chemistry C*, 120(20):11049–11053, 2016.

[53] R. Mhanna, A. Abdel Hamid, S. Dutta, R. Lefort, L. Noirez, B. Frick, and D. Morineau. More room for microphase separation: An extended study on binary liquids confined in sba-15 cylindrical pores. *The Journal of Chemical Physics*, 146(2):024501, 2017.

[54] Sujeet Dutta, Ronan Lefort, Denis Morineau, Ramona Mhanna, Odile Merdrignac-Conanec, Arnaud Saint-Jalmes, and Theo Leclercq. Thermodynamics of binary gas adsorption in nanopores. *Phys. Chem. Chem. Phys.*, 18(35):24361–24369, 2016.

[55] C. T. Kresge, M. E. Leonowicz, W. J. Roth, J. C. Vartuli, and J. S. Beck. Ordered mesoporous molecular sieves synthesized by a liquid-crystal template mechanism. *Nature*, 359(6397):710–712, 1992.

[56] Xiu S. Zhao, G. Q. (Max) Lu, and Graeme J. Millar. Advances in mesoporous molecular sieve mcm-41. *Industrial & Engineering Chemistry Research*, 35(7):2075–2090, 1996.

[57] Sumio Iijima and Toshinari Ichihashi. Single-shell carbon nanotubes of 1-nm diameter. *Nature*, 363(6430):603–605, 1993.

[58] Nicholas Metropolis and S. Ulam. The monte carlo method. *Journal of the American Statistical Association*, 44(247):335–341, 1949.

[59] Nicholas Metropolis, Arianna W. Rosenbluth, Marshall N. Rosenbluth, Augusta H. Teller, and Edward Teller. Equation of state calculations by fast computing machines. *The Journal of Chemical Physics*, 21(6):1087–1092, 1953.

[60] W. W. Wood and F. R. Parker. Monte carlo equation of state of molecules interacting with the lennard Äêjones potential. i. a supercritical isotherm at about twice the critical temperature. *The Journal of Chemical Physics*, 27(3):720–733, 1957.

[61] B. J. Alder and T. E. Wainwright. Phase transition for a hard sphere system. *The Journal of Chemical Physics*, 27(5):1208–1209, 1957.

[62] A. Rahman. Correlations in the motion of atoms in liquid argon. *Phys. Rev.*, 136:A405–A411, 1964.

[63] Loup Verlet. Computer "experiments" on classical fluids. i. thermodynamical properties of lennard-jones molecules. *Phys. Rev.*, 159:98–103, 1967.

[64] LOUP VERLET. Computer "experiments" on classical fluids. ii. equilibrium correlation functions. *Phys. Rev.*, 165:201–214, 1968.

[65] G. D. Harp and Bruce J. Berne. Linear and angular momentum autocorrelation functions in diatomic liquids. *The Journal of Chemical Physics*, 49(3):1249–1254, 1968.

[66] J.A. Barker and R.O. Watts. Structure of water; a monte carlo calculation. *Chemical Physics Letters*, 3(3):144 – 145, 1969.

[67] Aneesur Rahman and Frank H. Stillinger. Molecular dynamics study of liquid water. *The Journal of Chemical Physics*, 55(7):3336–3359, 1971.

[68] J. Barojas, D. Levesque, and B. Quentrec. Simulation of diatomic homonuclear liquids. *Phys. Rev. A*, 7(3):1092–1105, 1973.

[69] J.-P. Ryckaert and A. Bellemans. Molecular dynamics of liquid n-butane near its boiling point. *Chemical Physics Letters*, 30(1):123–125, 1975.

[70] Michael D. Morse and Stuart A. Rice. Tests of effective pair potentials for water: Predicted ice structures. *The Journal of Chemical Physics*, 76(1):650–660, 1982.

[71] *Water: From Interfaces to the Bulk*. Faraday Discussions. The Royal Society of Chemistry, 2009.

[72] R M Lynden-Bell. Towards understanding water: simulation of modified water models. *Journal of Physics: Condensed Matter*, 22(28):284107, 2010.

[73] I-Chun Lin, Ari P. Seitsonen, Ivano Tavernelli, and Ursula Rothlisberger. Structure and dynamics of liquid water from ab initio molecular dynamics Äîcomparison of blyp, pbe, and revpbe density functionals with and without van der waals corrections. *Journal of Chemical Theory and Computation*, 8(10):3902–3910, 2012.

[74] Luca Monticelli and Emppu Salonen. *Biomolecular Simulations: Methods and Protocols*, volume 924. Humana Press, 2013.

[75] Daan Frenkel and Berend Smit, editors. *Understanding Molecular Simulation: From Algorithms to Applications*. Academic Press, Inc., Orlando, FL, USA, 1st edition, 1996.

[76] Donald A. McQuarrie. *Statistical mechanics*. Harper, Row New York, 1975.

[77] M.P. Allen, M.P. Allen, D.J. Tildesley, T. ALLEN, and D.J. Tildesley. *Computer Simulation of Liquids*. Oxford Science Publ. Clarendon Press, 1989.

[78] D. C. Rapaport. *The Art of Molecular Dynamics Simulation*. Cambridge University Press, 2 edition, 2004.

[79] R.W. Hockney. Potential calculation and some applications. *Methods Comput. Phys.*, 1970.

[80] William C. Swope, Hans C. Andersen, Peter H. Berens, and Kent R. Wilson. A computer simulation method for the calculation of equilibrium constants for the formation of physical clusters of molecules: Application to small water clusters. *The Journal of Chemical Physics*, 76(1):637–649, 1982.

[81] M. Born and T. von Karman. Uber schwingungen im raumgittern. *Physikalishe Zeitschrift*, 13:297–309, 1912.

[82] P. P. Ewald. Die berechnung optischer und elektrostatischer gitterpotentiale. *Annalen der Physik*, 369(3):253–287, 1921.

[83] W. Smith and T. R. Forester. Dlpoly2.0: A general purpose parallel molecular dynamics simulation package. *Journal of Molecular Graphics*, 14(3):136 – 141, 1996.

[84] Frank A. Momany and Rebecca Rone. Validation of the general purpose quanta 3.2/charmm force field. *Journal of Computational Chemistry*, 13(7):888–900, 1992.

[85] S.R. Brozell D.S. Cerutti T.E. Cheatham III V.W.D. Cruzeiro T.A. Darden R.E. Duke D. Ghoreishi M.K. Gilson H. Gohlke A.W. Goetz D. Greene R Harris N. Homeyer S. Izadi A. Kovalenko T. Kurtzman T.S. Lee S. LeGrand P. Li C. Lin J. Liu T. Luchko R. Luo D.J. Mermelstein K.M. Merz Y. Miao G. Monard C. Nguyen H. Nguyen I. Omelyan A. Onufriev F. Pan R. Qi D.R. Roe A. Roitberg C. Sagui S. Schott-Verdugo J. Shen C.L. Simmerling J. Smith R. Salomon-Ferrer J. Swails R.C. Walker J. Wang H. Wei R.M. Wolf X. Wu L. Xiao D.M. York D.A. Case, I.Y. Ben-Shalom and P.A. Kollman. Amber 2018. *University of California, San Francisco*, 2018.

[86] W. F. van Gunsteren and H. J. C. Berendsen. Algorithms for macromolecular dynamics and constraint dynamics. *Molecular Physics*, 34(5):1311–1327, 1977.

[87] William L. Jorgensen, David S. Maxwell, and Julian Tirado-Rives. Development and testing of the opls all-atom force field on conformational energetics and properties of organic liquids. *Journal of the American Chemical Society*, 118(45):11225–11236, 1996.

[88] Junmei Wang, Romain M. Wolf, James W. Caldwell, Peter A. Kollman, and David A. Case. Development and testing of a general amber force field. *Journal of Computational Chemistry*, 25(9):1157–1174, 2004.

[89] H. Sun. Compass:Ää an ab initio force-field optimized for condensed-phase applicationsoverview with details on alkane and benzene compounds. *The Journal of Physical Chemistry B*, 102(38):7338–7364, 1998.

[90] Abascal JLF. A general purpose model for the condensed phases of water: Tip4p/2005. *J Chem Phys*, 123:234505, 2005.

[91] S. Dixit, J. Crain, W. C. K. Poon, J. L. Finney, and A. K. Soper. Molecular segregation observed in a concentrated alcohol?water solution. *Nature*, 416(6883):829–832, 2002.

[92] L. Dougan, S. P. Bates, R. Hargreaves, J. P. Fox, J. Crain, J. L. Finney, V. Reat, and A. K. Soper. Methanol-water solutions: A bi-percolating liquid mixture. *The Journal of Chemical Physics*, 121(13):6456–6462, 2004.

[93] A. Ghoufi, I. Hureau, R. Lefort, and D. Morineau. Hydrogen-bond-induced supermolecular assemblies in a nanoconfined tertiary alcohol. *The Journal of Physical Chemistry C*, 115(36):17761–17767, 2011.

[94] Martina Pozar, Bernarda Lovrincevicá, Larisa Zoranicá, Tomislav Primoracá, Franjo Sokolicá, and Aurelien Perera. Micro-heterogeneity versus clustering in binary mixtures of ethanol with water or alkanes. *Phys. Chem. Chem. Phys.*, 18(34):23971–23979, 2016.

[95] R. Mhanna, R. Lefort, L. Noirez, and D. Morineau. Microstructure and concentration fluctuations in alcohol-toluene and alcohol-cyclohexane binary liquids: A small angle neutron scattering study. *Journal of Molecular Liquids*, 218:198–207, 2016.

[96] Lester P. Kuhn. The hydrogen bond. i. intra- and intermolecular hydrogen bonds in alcohols1. *Journal of the American Chemical Society*, 74(10):2492–2499, 1952.

[97] Lorna Dougan, Jason Crain, John L. Finney, and Alan K. Soper. Molecular self-assembly in a model amphiphile system. *Phys. Chem. Chem. Phys.*, 12(35):10221–10229, 2010.

[98] Carl B. Kretschmer and Richard Wiebe. Thermodynamics of alcohol-hydrocarbon mixtures. *The Journal of Chemical Physics*, 22(10):1697–1701, 1954.

[99] Goolla Narayana Swamy, Golla Dharmaraju, and Gurajala Kodanda Raman. Excess volumes of toluene mixtures with some alcohols at 303.15,ÄÇk. *Canadian Journal of Chemistry*, 58(3):229–230, 1980.

[100] R Thiyagarajan and L Palaniappan. Molecular interaction study of two aliphatic alcohols with cyclohexane. *CSIR*, pages 852–856, 2008.

[101] Pandharinath S. Nikam, Bapu S. Jagdale, Arun B. Sawant, and Mehdi Hasan. Densities and viscosities of binary mixtures of toluene with methanol, ethanol, propan-1-ol, butan-1-ol, pentan-1-ol, and 2-methylpropan-2-ol at (303.15, 308.15, 313.15) k. *Journal of Chemical & Engineering Data*, 45(4):559–563, 2000.

[102] Lucie Wilson, R. Bicca de Alencastro, and C. Sandorfy. Hydrogen bonding of n-alcohols of different chain lengths. *Canadian Journal of Chemistry*, 63(1):40–45, 1985.

[103] A. K. Turner, J. and. The effect of apolar solutes on water structure: Alcohols and tetraalkylammonium ions. *The Journal of Chemical Physics*, 101(7):6116–6125, 1994.

[104] Christian Petersen, Artem A. Bakulin, Vlad G. Pavelyev, Maxim S. Pshenichnikov, and Huib J. Bakker. Femtosecond midinfrared study of aggregation behavior in aqueous solutions of amphiphilic molecules. *The Journal of Chemical Physics*, 133(16):164514, 2010.

[105] Guillaume Stirnemann, James T. Hynes, and Damien Laage. Water hydrogen bond dynamics in aqueous solutions of amphiphiles. *The Journal of Physical Chemistry B*, 114(8):3052–3059, 2010.

[106] I. Essafri and A. Ghoufi. Microstructure of nonideal methanol binary liquid mixtures. *Phys. Rev. E*, 99(6):062607, 2019.

[107] Yoshimori Miyano and Walter Hayduk. Solubilities of butane, vapor pressures, and densities for benzene + cyclohexane, benzene + methanol, and methanol + cyclohexane solutions at 298 k. *Journal of Chemical & Engineering Data*, 38(2):277–281, 1993.

[108] A. Ghoufi, F. Goujon, V. Lachet, and P. Malfreyt. Surface tension of water and acid gases from monte carlo simulations. *The Journal of Chemical Physics*, 128(15):154716, 2008.

[109] F. Biscay, A. Ghoufi, and P. Malfreyt. Surface tension of water,Äìalcohol mixtures from monte carlo simulations. *The Journal of Chemical Physics*, 134(4):044709, 2011.

[110] F. Biscay, A. Ghoufi, V. Lachet, and P. Malfreyt. Prediction of the surface tension of the liquid-àívapor interface of alcohols from monte carlo simulations. *The Journal of Physical Chemistry C*, 115(17):8670–8683, 2011.

[111] A. Ghoufi and P. Malfreyt. Local description of surface tension through thermodynamic and mechanical definitions. *Molecular Simulation*, 39(8):603–611, 2013.

[112] Geraldine A. Torin-Ollarves, M. Carmen Martin, Cesar R. Chamorro, and Jose J. Segovia. Densities, viscosities, and isobaric heat capacities of the system (1-butanol+cyclohexane) at high pressures. *The Journal of Chemical Thermodynamics*, 74:153–160, 2014.

[113] Ohji Hiroyuki. Excess volumes of (1-pentanol + cyclohexane or benzene) at temperatures between 283.15 k and 328.15 k. *The Journal of Chemical Thermodynamics*, 34(6):849 – 859, 2002.

[114] Kazimierz J., A. Baranowski, and Jacek G. Structure of cyclohexane + t-butanol mixtures from positron annihilation and ultrasonic velocity measurements. 1993.

[115] Sergei Yu. Noskov, Guillaume Lamoureux, and Benoit Roux. Molecular dynamics study of hydration in ethanol-water mixtures using a polarizable force field. *The Journal of Physical Chemistry B*, 109(14):6705–6713, 2005.

[116] Ming-Liang Tan, Benjamin T. Miller, Jerez Te, Joseph R. Cendagorta, Bernard R. Brooks, and Toshiko Ichiye. Hydrophobic hydration and the anomalous partial molar volumes in ethanol-water mixtures. *The Journal of Chemical Physics*, 142(6):064501, 2015.

[117] R. Baskaran and T.R. Russ. Kubendran. Density and excess molar volume in a binary mixture of o-anisaldehyde and chlorobenzene at 303.15, 313.15, and 323.15 k. *Russian Journal of Physical Chemistry*, 83(3):350?352, 2009.

[118] Tasneem Shadma Ali Anwar and Nabi Firdosa. Volumetric, viscometric, and ultrasonic properties of liquid mixtures of cyclohexane with alkanols at different temperatures. *Journal for Natural Research A*, 65:8–9, 2014.

[119] Akl M. Awwad and Malyuba A. Abu-Daabes. Densities, viscosities, and excess properties of (n-methylmorpholine+cyclohexane, +benzene, and +toluene) at t=(298.15, 303.15, 313.15, 323.15)k. *The Journal of Chemical Thermodynamics*, 40(4):645–652, 2008.

[120] S. Dixit, J. Crain, W. Poon, J. Finney, and A. K. Soper. Molecular segregation observed in a concentrated alcohol-water solution. *Nature*, 416:829, 2002.

[121] Henry S. Frank and Marjorie W. Evans. Free volume and entropy in condensed systems iii. entropy in binary liquid mixtures; partial molal entropy in dilute solutions; structure and thermodynamics in aqueous electrolytes. *The Journal of Chemical Physics*, 13(11):507–532, 1945.

[122] J.-H. Guo, Y. Luo, A. Augustsson, S. Kashtanov, J.-E. Rubensson, D. K. Shuh, H. gren, and J. Nordgren. Molecular structure of alcohol-water mixtures. *Phys. Rev. Lett.*, 91(15):157401, 2003.

[123] Alan. K. Soper, Lorna Dougan, Jason Crain, and John. L. Finney. Excess entropy in alcohol-àíwater solutions:Äâ a simple clustering explanation. *The Journal of Physical Chemistry B*, 110(8):3472–3476, 2006.

[124] Hendrick C. Van Ness, Jon Van Winkle, Herbert H. Richtol, and Henry B. Hollinger. Infrared spectra and the thermodynamics of alcohol-hydrocarbon systems. *The Journal of Physical Chemistry*, 71(5):1483–1494, 1967.

[125] Aaron N. Fletcher. Effect of carbon tetrachloride upon the self-association of 1-octanol. *The Journal of Physical Chemistry*, 73(7):2217–2225, 1969.

[126] Yanting Wang and Gregory A. Voth. Tail aggregation and domain diffusion in ionic liquids. *The Journal of Physical Chemistry B*, 110(37):18601–18608, 2006.

[127] Song Li, Jose Leobardo Banulos, Pengfei Zhang, Guang Feng, Sheng Dai, Gernot Rother, and Peter T. Cummings. Toward understanding the structural heterogeneity and ion pair stability in dicationic ionic liquids. *Soft Matter*, 10(45):9193–9200, 2014.

[128] Denis Morineau and Christiane Alba-Simionesco. Liquids in confined geometry: How to connect changes in the structure factor to modifications of local order. *The Journal of Chemical Physics*, 118(20):9389–9400, 2003.

[129] A. Ghoufi, I. Hureau, D. Morineau, R. Renou, and A. Szymczyk. Confinement of tert-butanol nanoclusters in hydrophilic and hydrophobic silica nanopores. *The Journal of Physical Chemistry C*, 117(29):15203–15212, 2013.

[130] R. Renou, A. Szymczyk, and A. Ghoufi. Water confinement in nanoporous silica materials. *The Journal of Chemical Physics*, 140(4):044704, 2014.

[131] Marta Falkowska, Daniel T. Bowron, Haresh G. Manyar, Christopher Hardacre, and Tristan G. A. Youngs. Neutron scattering of aromatic and aliphatic liquids. *Chem. Phys. Chem.*, 17(13):2043–2055, 2016.

[132] Alenka Luzar and David Chandler. Effect of environment on hydrogen bond dynamics in liquid water. *Phys. Rev. Lett.*, 76(6):928–931, 1996.

[133] Peter Kruger, Sondre K. Schnell, Dick Bedeaux, Signe Kjelstrup, Thijs J. H. Vlugt, and Jean-Marc Simon. Kirkwood-Äìbuff integrals for finite volumes. *The Journal of Physical Chemistry Letters*, 4(2):235–238, 2013.

[134] Noura Dawass, Peter Kruger, Sondre K. Schnell, Jean-Marc Simon, and T.J.H. Vlugt. Kirkwood-buff integrals from molecular simulation. *Fluid Phase Equilibria*, 486:21 – 36, 2019.

[135] G. Ravishanker, P. K. Mehrotra, M. Mezei, and David L. Beveridge. Aqueous hydration of benzene. *Journal of the American Chemical Society*, 106(15):4102–4108, 1984.

[136] Hideaki Takahashi, Daiki Suzuoka, and Akihiro Morita. Why is benzene soluble in water? role of oh/π interaction in solvation. *Journal of Chemical Theory and Computation*, 11(3):1181–1194, 2015.

[137] Kamil P. Gierszal, Joel G. Davis, Michael D. Hands, David S. Wilcox, Lyudmila V. Slipchenko, and Dor Ben-Amotz. π-hydrogen bonding in liquid water. *The Journal of Physical Chemistry Letters*, 2(22):2930–2933, 2011.

[138] Michinori. [UNK]Oki and Hiizu. Iwamura. Steric effects on the o-h...œÄ interaction in 2-hydroxybiphenyl. *Journal of the American Chemical Society*, 89(3):576–579, 1967.

[139] Yan Zhao, Oksana Tishchenko, and Donald G. Truhlar. How well can density functional methods describe hydrogen bonds to œÄ acceptors? *The Journal of Physical Chemistry B*, 109(41):19046–19051, 2005.

[140] Sakae Suzuki, Peter G. Green, Roger E. Bumgarner, Siddharth Dasgupta, William A. Goddard, and Geoffrey A. Blake. Benzene forms hydrogen bonds with water. *Science*, 257(5072):942–945, 1992.

[141] A. Ghoufi, F. Artzner, and P. Malfreyt. Physical properties and hydrogen-bonding network of water-ethanol mixtures from molecular dynamics simulations. *The Journal of Physical Chemistry B*, 120(4):793–802, 2016.

[142] P.S. Tofts, D. Lloyd, C.A. Clark, G.J. Barker, G.J.M. Parker, P. McConville, C. Baldock, and J.M. Pope. Test liquids for quantitative mri measurements of self-diffusion coefficient in vivo. *Magnetic Resonance in Medicine*, 43(3):368–374, 2000.

[143] J. R. PARTINGTON, R. F. HUDSON, and K. W. BAGNALL. Self-diffusion of aliphatic alcohols. *Nature*, 169(4301):583–584, 1952.

[144] Kerry C. Pratt and William A. Wakeham. Self-diffusion in water and monohydric alcohols. *J. Chem. Soc., Faraday Trans. 2*, 73(7):997–1002, 1977.

[145] David W. McCall and Dean C. Douglass. Self-diffusion in the primary alcohols. *The Journal of Chemical Physics*, 32(6):1876–1877, 1960.

[146] Makio Iwahashi, Yoko Ohbu, Tadashi Kato, Yumi Suzuki, Kazuhiro Yamauchi, Yoshimi Yamaguchi, and Mitsuo Muramatsu. The dynamical structure of normal alcohols in their

liquids as determined by the viscosity and self-diffusion measurements. *Bulletin of the Chemical Society of Japan*, 59(12):3771–3774, 1986.

[147] Manfred Holz, Stefan R. Heil, and Antonio Sacco. Temperature-dependent self-diffusion coefficients of water and six selected molecular liquids for calibration in accurate 1h nmr pfg measurements. *Phys. Chem. Chem. Phys.*, 2(20):4740–4742, 2000.

[148] P. Petong, R. Pottel, and U. Kaatze. Dielectric relaxation of h-bonded liquids. mixtures of ethanol and n-hexanol at different compositions and temperatures. *The Journal of Physical Chemistry A*, 103(31):6114–6121, 1999.

[149] Andrew W. Knight, Nikolai G. Kalugin, Eric Coker, and Anastasia G. Ilgen. Water properties under nano-scale confinement. *Scientific Reports*, 9:8246, 2019.

[150] Wycliffe K. Kipnusu, Mahdy M. Elmahdy, Mohamed Elsayed, Reinhard Krause-Rehberg, and Friedrich Kremer. Counterbalance between surface and confinement effects as studied for amino-terminated poly(propylene glycol) constraint in silica nanopores. *Macromolecules*, 52(4):1864–1873, 2019.

[151] F. Bruni, M. A. Ricci, and A. K. Soper. Water confined in vycor glass. i. a neutron diffraction study. *The Journal of Chemical Physics*, 109(4):1478–1485, 1998.

[152] A. K. Soper, F. Bruni, and M. A. Ricci. Water confined in vycor glass. ii. excluded volume effects on the radial distribution functions. *The Journal of Chemical Physics*, 109(4):1486–1494, 1998.

[153] Ghoufi A. Molecular simulations of confined liquids: an alternative to the grand canonical monte carlo simulations. *J Chem Phys*, 134:074104–1, 2011.

[154] G. Hummer, J. C. Rasaiah, and J. P. Noworyta. Water conduction through the hydrophobic channel of a carbon nanotube. *Nature*, 414(6860):188–190, 2001.

[155] Kerstin Falk, Felix Sedlmeier, Laurent Joly, Roland R. Netz, and Lyderic Bocquet. Molecular origin of fast water transport in carbon nanotube membranes: Superlubricity versus curvature dependent friction. *Nano Letters*, 10(10):4067–4073, 2010.

[156] A. Ghoufi, A. Szymczyk, and P. Malfreyt. Ultrafast diffusion of ionic liquids confined in carbon nanotubes. *Scientific Reports*, 6:28518, 2016.

[157] Andriy V. Kityk, M. Wolff, K. Knorr, D. Morineau, R. Lefort, and P. Huber. Continuous paranematic-to-nematic ordering transitions of liquid crystals in tubular silica nanochannels. *Phys. Rev. Lett.*, 101(18):187801, 2008.

[158] S. Gruener and P. Huber. Spontaneous imbibition dynamics of an n-alkane in nanopores: Evidence of meniscus freezing and monolayer sticking. *Phys. Rev. Lett.*, 103(17):174501, 2009.

[159] C. Grigoriadis, H. Duran, M. Steinhart, M. Kappl, H-J. Butt, and G. Floudas. Suppression of phase transitions in a confined rodlike liquid crystal. *ACS Nano*, 5(11):9208–9215, 2011.

[160] V. Ballenegger and J.-P. Hansen. Dielectric permittivity profiles of confined polar fluids. *The Journal of Chemical Physics*, 122(11):114711, 2005.

[161] Douwe J. Bonthuis, S. Gekle, and Roland R. Netz. Dielectric profile of interfacial water and its effect on double-layer capacitance. *Phys. Rev. Lett.*, 107(16):166102, 2011.

[162] Douwe J. Bonthuis, S. Gekle, and Roland R. Netz. Dielectric profile of interfacial water and its effect on double-layer capacitance. *Phys. Rev. Lett.*, 107(16):166102, 2011.

[163] C. Zhang, F. Gygi, and G. Galli. Strongly anisotropic dielectric relaxation of water at the nanoscale. *The Journal of Physical Chemistry Letters*, 4(15):2477–2481, 2013.

[164] Olivier E., J. Emile, and A. Ghoufi. Influence of the interface on the optical activity of confined glucose films. *Journal of Colloid and Interface Science*, 477:103–108, 2016.

[165] J-P. Palomares-Baez, E. Panizon, and R. Ferrando. Nanoscale effects on phase separation. *Nano Letters*, 17(9):5394–5401, 2017.

[166] P. Keblinski, W-J. Ma, A. Maritan, J. Koplik, and Jayanth R. Banavar. Molecular dynamics of phase separation in narrow channels. *Phys. Rev. E*, 47(4):R2265–R2268, 1993.

[167] Lev D. Gelb and K. E. Gubbins. Liquid-liquid phase separation in cylindrical pores: Quench molecular dynamics and monte carlo simulations. *Phys. Rev. E*, 56(3):3185–3196, 1997.

[168] Lev D. Gelb and K.E. Gubbins. Studies of binary liquid mixtures in cylindrical pores: phase separation, wetting and finite-size effects from monte carlo simulations. *Physica A: Statistical Mechanics and its Applications*, 244(1):112–123, 1997.

[169] Ghoufi A. Physical properties and hydrogen-bonding network of water-ethanol mixtures from molecular dynamics simulations. *J Phys Chem B*, 120:793, 2016.

[170] Wang Y. Tail aggregation and domain diffusion in ionic liquids. *J Phys Chem B*, 110:18601, 2006.

[171] Ghoufi A. Confinement of tert-butanol nanoclusters in hydrophilic and hydrophobic silica nanopores. *J Phys Chem C*, 117:15203, 2013.

[172] Li S. Toward understanding the structural heterogeneity and ion pair stability in dicationic ionic liquids. *Soft Matter*, 10:9193, 2014.

[173] Mhanna R. More room for microphase separation: an extended study on binary liquids confined in sba-15 cylindrical pores. *J Chem Phys*, 146:024501–1, 2017.

[174] I. Essafri, J. Courtin, and A. Ghoufi. Numerical evidence of heterogeneity and nanophases in a binary liquid confined at the nanoscale. *Molecular Simulation*, 44(9):728–735, 2018.

[175] Randall T. Cygan, Jian-Jie Liang, and Andrey G. Kalinichev. Molecular models of hydroxide, oxyhydroxide, and clay phases and the development of a general force field. *The Journal of Physical Chemistry B*, 108(4):1255–1266, 2004.

[176] A. Ghoufi, D. Morineau, R. Lefort, and P. Malfreyt. Toward a coarse graining/all atoms force field (cg/aa) from a multiscale optimization method: An application to the mcm-41 mesoporous silicates. *Journal of Chemical Theory and Computation*, 6(10):3212–3222, 2010.

[177] Stoddard S. Identifying clusters in computer experiments on sytems of particles. *J Comput Phys*, 27:291, 1978.

Etude de la microstructure des liquides binaires en phases Bulk et Nano-Confinées

Ilham Essafri

I. Introduction et objectifs

Ces dernières décennies, les nanosciences et les nanotechnologies ont connu un essor très important dans tous les domaines, qui demande dans un premier temps la bonne compréhension de certains phénomènes à l'échelle nanométrique. Particulièrement, Il a été montré que la plupart de ces phénomènes sont contrôlés par le réseau de la liaison hydrogène, par exemple l'auto-assemblage, la formation d'agrégats ou de microémulsion, le repliement des protéines ou l'assemblage des protéines jusqu'au relargages de médicaments. Intéressement, avec l'avancée des nanosciences et des nanotechnologies on manipule beaucoup de liquides à l'échelle du nanomètres alors qu'il est devenu intéressant d'une manière impérative est bien d'essayer de revisiter notre compréhension de ces réseaux de liaison hydrogène à ces échelles là.

L'objectif de ce travail est comprendre le rôle du réseau de liaison hydrogène des alcools à l'échelle nanométrique et est ce que ces réseaux de liaison hydrogène vont survivre sous confinement nanométrique ou ils vont transiter vers un autre type de réseau ou bien est ce que ces réseaux de liaison hydrogène vont être impacter par les effets de surface. Et essayer aussi de comprendre comment les propriétés de différents liquides formateurs de liaisons hydrogènes vont se modifier sous confinement nanométriques. Donc l'objectif principal de ma thèse était d'étudier la structure de différents liquides et leurs mélanges confinés à l'échelle nanométriques et essayer d'établir un lien entres les différentes propriétés de ces liquides avec leurs réseaux de liaison hydrogène. Donc le plan de ma thèse est composé de deux grandes parties :

- La première partie se concentre sur l'étude des liquides binaires en phase Bulk : l'objectif de cette partie est de décrire correctement la structure des mélanges liquides ainsi que leurs propriétés physiques et d'en établir un lien. De plus, cette partie permettra aussi de valider les champs de forces utilisé, donc l'idée c'est d'avoir une référence « *phase Bulk* » afin de mieux appréhender les modifications en « *phase confinée* ».

- La 2ème partie concerne l'étude des mélanges binaires en phase confinée: l'objectif est d'étudier la structuration de ces mélanges sous confinement nanométrique et de répondre à la question de l'auto-organisation de ces mélanges à l'échelle nanométrique.

II. Microstructure des mélanges liquides binaires de méthanol non idéal

1. Objectif :

La non-idéalité des mélanges binaires est souvent liée à la nature des interactions entre les deux liquides et à l'hétérogénéité à l'échelle nanométrique de la microstructure. Lorsque l'un des liquides est un formateur de liaisons hydrogène et le second est aprotique, la dilution progressive du réseau de liaisons hydrogène conduit à un regroupement et des nano-phases. En considérant deux mélanges, toluène-méthanol et cyclohexane-méthanol, la non-idéalité et sa connexion avec la structure à l'échelle nanométrique et les interactions intermoléculaires sont étudiées numériquement. Contrairement au toluène totalement miscible dans le méthanol, le cyclohexane présente une plage d'immiscibilité élevée qui en fait un système pertinent pour étudier la nucléation (ségrégation locale) et sa propagation.

2. Méthode : Phase BULK

Le méthanol, le toluène et le cyclohexane ont été modélisés par le champ de force de tous les atomes flexible non polarisable pour les simulations liquides (OPLS). En effet, il a été récemment montré que les modèles OPLS étaient quantitativement reproduits aux propriétés thermodynamiques et interfaciales. Les interactions intermoléculaires sont composées de la répulsion-dispersion et des contributions électrostatiques modélisées respectivement par les potentiels de Lennard-Jones (LJ) et coulombiens. Les interactions électrostatiques ont été tronquées à 12 Å et calculées en utilisant la somme d'Ewald avec une précision de 10^{-6}. Les interactions à courte distance ont été modélisées en utilisant le potentiel de Lennard-Jones en utilisant un seuil de 12 Å. Ici, les interactions entre des sites LJ différents de deux molécules ont été déterminées par la règle de combinaison de Lorentz-Berthelot. Les erreurs statistiques pour les propriétés calculées ont été estimées à l'aide de la méthode des moyennes de bloc. Des conditions aux limites périodiques ont été appliquées dans les trois directions. Des simulations MD ont été réalisées dans l'ensemble statistique NpT de telle sorte que N est le nombre de particules, T est la température, et p est la pression. Des simulations de dynamique moléculaire ont été effectuées à T = 300 K et p = 1bar en utilisant un pas de temps de 0,001 ps pour

échantillonner 10 ns (phases d'acquisition et d'équilibrage). Toutes les simulations MD ont été réalisées à partir du progiciel DL_POLY en utilisant une combinaison des algorithmes de thermostat et barostat Velocity-Verlet et Nosé-Hoover. La configuration initiale a été construite par une distribution aléatoire de molécules de méthanol (MeOH), de toluène (TOL) et de cyclohexane (CHX). Onze fractions molaires en MeOH (x_{MeOH}) ont été étudiées {0, 0,1, 0,2, 0,3, 0,4, 0,5, 0,6, 0,7, 0,8, 0,9, 1}.

3. Résultats de la Phase Bulk

Nous rapportons sur la figure 1 (a) la densité de la phase liquide en fonction de x_{MeOH} pour les deux mélanges. Dans deux cas, les densités ainsi calculées se trouvent en assez bon accord avec les expériences qui valident les modèles utilisés pour décrire les molécules MeOH, CHX et TOL et leurs interactions de combinaison. Expérimentalement, le mélange CHX/MeOH est bien connu pour se dissocier entre $x_{MeOH} = 0,2$ et $x_{MeOH} = 0,8$. Cette tendance à la ségrégation est mise en évidence sur la figure 1 (c) où des instantanés de CHX-MeOH à $x_{MeOH} = 0,1$, 0,5 et 0,9 sont indiqués. Comme le montre la figure 1 (c), la séparation de phase est bien récupérée à $x_{MeOH} = 0,5$, alors qu'à $x_{MeOH} = 0,1$ et 0.9 les systèmes sont miscibles.

Comme le montre la figure 1 (a), la densité du mélange TOL-MeOH présente une évolution monotone en fonction de X_{MeOH}, alors que le mélange CHX-MeOH montre un minimum autour $X_{MeOH} = 0,5$. De plus, les deux mélanges présentent un écart du même ordre de grandeur par rapport à la densité idéale calculée à partir de $\rho = X_{MeOH}\ \rho_{MeOH} + (1 - X_{MeOH})\ \rho_{CHX/TOL}$. De manière très intéressante, le mélange CHX-MeOH présente également un comportement non idéal dans les régions miscibles. Pour quantifier cette non-idéalité, nous rapportons sur la figure 1 (b) l'excès de densité des mélanges en fonction de X_{MeOH}. L'excès de densité a été évalué comme la différence entre les densités simulées et idéales. Comme le montre la figure 1 (b), les mélanges CHX- MeOH et TOL-MeOH présentent respectivement un excès de densité négatif et positif.

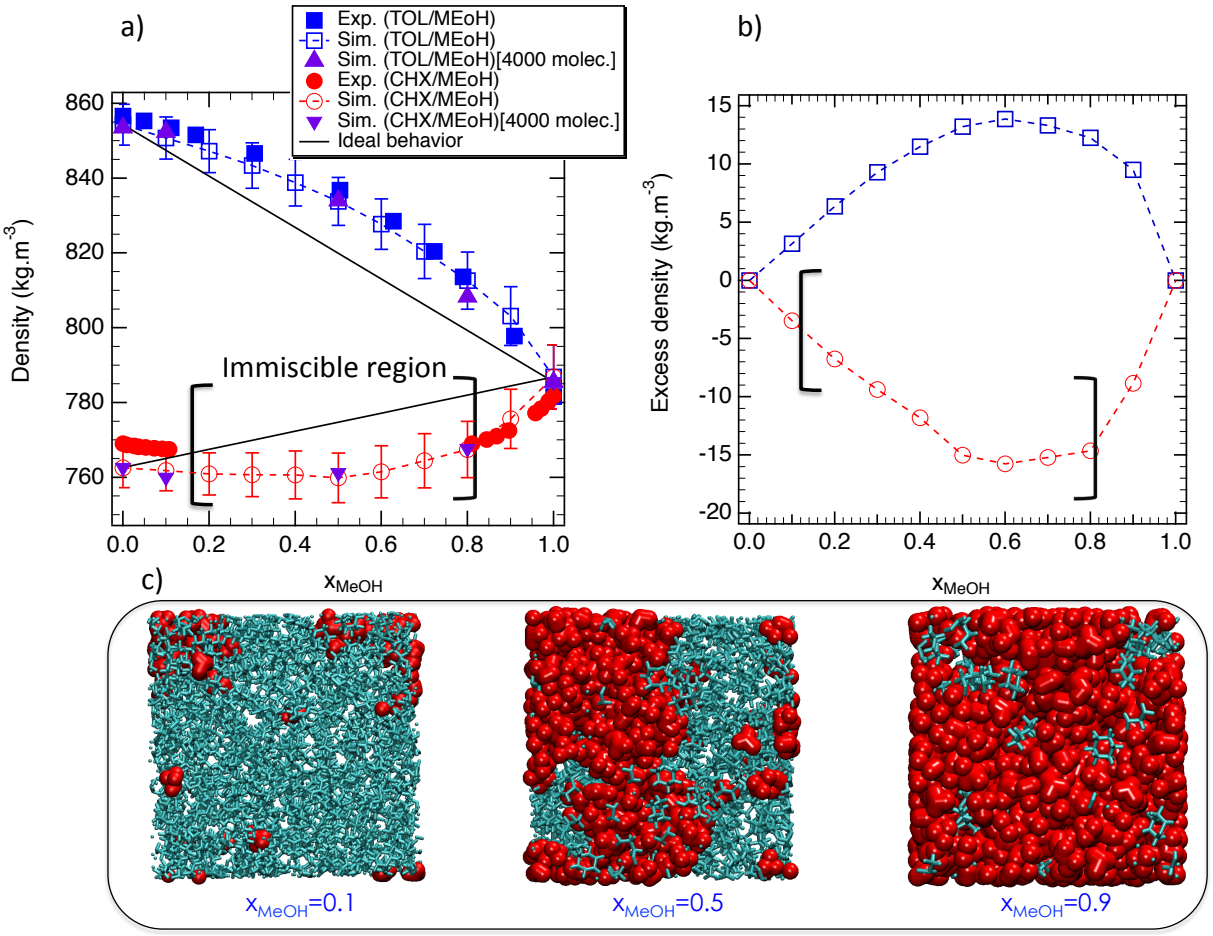

Figure 1: Densité simulée et expérimentale (a) et excès de densité (b) des mélanges CHX-MeOH et TOL-MeOH en fonction de X_{MeOH} à 300 K et 1 bar. Les incertitudes sur la densité sont trop faibles pour être représentées. (c) Images instantanées du mélange binaire à X_{MeOH} = 0,1, 0,5 et 0,9 de sorte que le méthanol est représenté en rouge, et CHX est représenté en bleu.

De plus, la figure 1 (b) montre que les mélanges TOL-MeOH et CHX-MeOH présentent un changement de monotonie de l'excès de densité. En outre, dans les deux zones miscibles et non miscibles, la non-idéalité du mélange CHX-MeOH (valeur absolue de l'excès de densité) est supérieure à celle du TOL-MeOH. Ces comportements pourraient être imputés à un changement de la topologie structurale conduisant à une hétérogénéité structurelle ou à une différence dans les interactions entre les deux composants du mélange liquide binaire. En effet, contrairement à la zone miscible, dans la zone non miscible du mélange CHX-MeOH la différence est due à la séparation de phase. Fait intéressant, il semble que l'immiscibilité à faible concentration de méthanol soit due à la formation de groupe en forme de poche de méthanol assimilée à un processus de nucléation conduisant à la formation de nanophases riches en molécules de méthanol telles que les groupes OH

sont cachés du solvant organique étant donné l'absence d'interactions favorables. La formation progressive de nanophases pourrait alors générer une hétérogénéité structurelle. A haute concentration en méthanol (X_{MeOH} = 0,8) la miscibilité est récupérée grâce à la percolation des nanophases de méthanol. En effet, dans la région miscible, la formation progressive de ces nanophases augmente l'hétérogénéité et pourrait expliquer la non-idéalité du mélange CHX-MeOH.

4. Discussion :

Ces travaux ont porté sur l'exploration à l'échelle nanométrique de la non-idéalité des mélanges liquides binaire méthanol/toluène et méthanol/cyclohexane au moyen de simulations de dynamique moléculaire. Les simulations reproduisaient assez bien la miscibilité totale du toluène dans le méthanol, et la gamme de miscibilité du cyclohexane a été établie quantitativement. Dans les deux mélanges, l'écart par rapport au comportement idéal du mélange a été observé.

Dans le cas du toluène, cette non-idéalité (excès de densité positive) et la miscibilité ont été attribuées aux interactions spécifiques entre le toluène et le méthanol conduisant à une rupture du réseau de liaisons hydrogène impliquant des grappes de tailles différentes et l'hétérogénéité spatiale. L'immiscibilité et la non-idéalité (excès de densité négatif) des mélanges CHX-MeOH étaient le résultat des interactions défavorables entre CHX et MeOH conduisant à une auto-organisation des molécules CHX pour former des nano-phases hydrophobes à l'origine de l'hétérogénéité structurelle dans la région de miscibilité.

Les nano-phases ont été caractérisées en termes de poches de grappes linéaires de sorte que la différence de miscibilité et d'hétérogénéité a été comprise en termes de taille et de distribution des grappes.

De plus, nous avons montré que la présence de clusters devait être dé-corrélée de la notion d'hétérogénéité. Finalement, nous avons mis en évidence que le pré-pic observé dans le facteur de structure est indépendant du degré d'hétérogénéité mais est plutôt lié à la présence d'amas cycliques.

III. Séparation micro-phase d'un mélange liquide binaire miscible sous confinement à l'échelle nanométrique

1. Contexte scientifique et problématique :

Des résultats récents ont fourni une preuve structurelle expérimentale directe de la séparation en micro-phase de liquides macroscopiquement miscibles constitués de liquide formateurs de liaisons hydrogène et de liquide apolaire. En effet, la structure d'un mélange comprenant du toluène (TOL) et du *tert*-butanol (TBA) confinées dans un nano-pore de silice cylindrique (MCM-41) de rayon 24 Å ont été explorées par diffusion neutronique et comparées à la phase miscible. A l'aide d'un modèle noyau-coquille (NC), les auteurs ont établi, pour la première fois, une structure tubulaire à phases séparées à l'échelle moléculaire avec les molécules TBA formant une couche à la surface des pores (coquille), entourant une phase riche en TOL au centre du pore (noyau). Bien que ces expériences aient révélé la présence d'une séparation en micro-phase, l'organisation locale et les processus microscopiques contrôlant la structure CS doivent être clarifiés. Dans un premier travail numérique on a montré que le nano-confinement du mélange TBA / TOL dans un nano-pore de silice n'induisait qu'une forte hétérogénéité (voir figure 2). Ce résultat met alors en évidence un scénario basé sur la ségrégation locale plutôt que sur une organisation noyau-coquille du mélange confiné TBA/TOL.

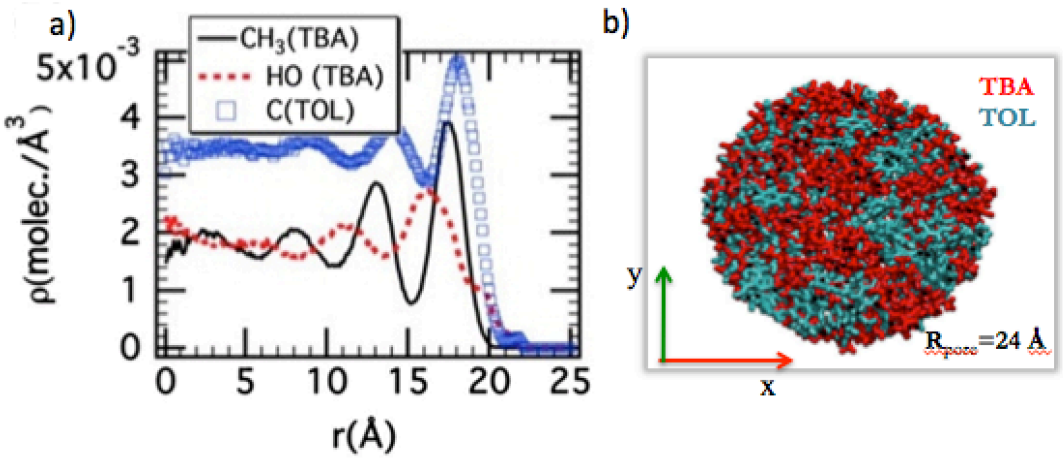

Figure 2: (a) Les profils de densité radiale des atomes de carbone de TOL, des atomes d'hydrogène du groupe OH de TBA et des atomes de carbone du groupe méthyle de TBA dans le mélange TBA/TOL avec une composition de fraction molaire de TBA/TOL de 56/44%, cette courbe montre une structure en couche et une absence d'une organisation en noyau-coquille. (b) Image instantanée de la structuration de liquides confinées, cette illustration montre un mélange TBA (rouge)/TOL (bleue) confiné dans le nanopore cylindrique. La structure du pore de silice est enlevée. Cette figure montre que les molécules de TBA (couleur rouge) et de TOL (couleur bleue) sont présentes à la surface et au centre du pore.

2. Objectif :

A l'aide de simulations atomistiques, nous visons à capturer la structure NC et à clarifier la force motrice microscopique qui la régit. Pour ce faire, les interactions solide-liquide ont été affinées pour reproduire qualitativement l'isotherme d'adsorption expérimental des composants purs TBA et TOL confinés à travers le nano-pore de silice. Ce raffinement nous a permis de fournir de nouvelles informations sur la compréhension moléculaire de la séparation en micro-phase. De plus, en ajustant la chimie de surface du nano-pore pour imiter les matériaux poreux hydrophiles et hydrophobes, nous avons étudié le rôle de la chimie de surface sur la démixtion. Des simulations de dynamique moléculaire (MD) ont ensuite été réalisées.

3. Méthode : Phase Confinée

1.1. Modèle

Le nano-pore cylindrique de silice à surface hydrophile a été généré en appliquant la procédure proposée par Bródka et Zerda. Nous avons généré une cavité cylindrique le long de l'axe z de la cellule de silice cubique de 35,7 Å en supprimant les atomes dans un cylindre de diamètre (D) 24 Å. De leurs nombres de coordination, nous avons distingué l'oxygène de pont (O_b) lié à deux atomes de silicium à partir d'oxygène non pontant (O_{nb}) liés à un seul silicium et liés à un atome d'hydrogène (H_{nb}). Une procédure itérative d'élimination des atomes (O et Si) a été appliquée jusqu'à ce que seuls des atomes de silicium tétra-coordonnés, liés à un maximum de deux O_{nbs}, soient présents dans la structure. Enfin, les oxygènes non-liants ont été saturés d'atomes d'hydrogène pour former des groupes hydroxyle en surface. Cette procédure conduit à une description réaliste de la surface interne irrégulière du silicate poreux et des interactions interfaciales entre le fluide et la matrice. La couverture de surface interne des groupes silanol était d'environ 7,5 nm^{-2}, ce qui correspond à un pore de silice protonée hautement hydratée. Bien que la matrice de silice ait été maintenue par la suite rigide, la rotation autour de la liaison Si-O des groupes hydroxyles a été autorisée à partir de l'algorithme de contraintes SHAKE, où la distance entre les atomes d'oxygène et d'hydrogène est maintenue fixée à 1,09 Å.

Les interactions intermoléculaires sont la somme des contributions de Lennard-Jones électrostatiques et dispersions-répulsions. L'ossature de silice a été modélisée en utilisant le champ de force ClayFF développé par Cygan et al. TBA et TOL ont été modélisés au moyen du champ de force OPLS flexible non polarisable tous atomes (AA). Alors que les paramètres de Lennard-Jones d'origine ont

été initialement conservés, les charges partielles ont été calculées à partir de calculs ab-initio. Le calcul des charges partielles a été effectué sur la base d'un ensemble de base de type gaussien 6-311G (d, p). Dans un premier temps, la géométrie a été optimisée, tandis que dans la deuxième étape, les charges partielles ont été calculées à partir de la méthode CHELPG (CHarges from ELectrostatic Potentials using a Grid-based). Ces calculs ont été effectués en utilisant le code gaussien.

Les interactions de van der Waals croisées entre TOL et TBA ont été calculées en utilisant les règles de mélange Lorentz-Berthelot. Les paramètres LJ entre le nano-pore de silice et TOL ont été optimisés pour reproduire qualitativement l'isotherme expérimentale. Le nanotube de carbone de rayon 12 Å avec une longueur de pore de 100 Å a été modélisé en considérant le champ de force non chargé développé par Werder et al. Le nanotube d'eau a été construit en découpant un nano-pore cylindrique de rayon 12 Å dans une boîte à eau cubique équilibrée avec une longueur de boîte de 59Å. Les molécules d'eau ont été modélisées en considérant le modèle TIP4P/2005 et ont été considérées comme congelées. Une membrane de silice faiblement hydrophile a également été modélisée en combinant le champ de force universel (UFF) pour décrire les atomes d'oxygène et d'hydrogène, tandis que les atomes de silicium ont été décrits en utilisant le champ de force DREIDING. Les paramètres de Lennard-Jones croisés ont été calculés en considérant les règles de mélange de Lorentz- Berthelot.

1.2. Simulation MD

Les simulations MD ont été effectuées en utilisant un pas de temps de 0,002 ps pour échantillonner 10 ns (phase d'acquisition). Le temps d'équilibrage correspond à 10 ns. Toutes les simulations MD ont été réalisées avec le package DL_POLY en utilisant la combinaison de l'algorithme Velocity-Verlet et du thermostat Nosé-Hoover. Les nombres de molécules confinées de TBA et TOL purs et de TBA / TOL binaire ont été calculés en utilisant la simulation GCMC à la pression de saturation de la vapeur et 308 K. Les compositions en TBA et TOL sont fournies dans le tableau 2.

1.3. Simulation de Monte Carlo

Des simulations de Monte Carlo ont été réalisées dans le grand ensemble statistique canonique. Des conditions aux limites périodiques ont été appliquées dans les trois directions. Le nano-pore de silice était considéré comme rigide et seul l'hydrogène du silanol peut tourner à partir d'un mouvement angulaire impliquant des groupes SiOH. Chaque cycle consistait en N coups choisis aléatoirement

avec des probabilités fixes: translation du centre de masse d'un mouvement choisi au hasard, rotation d'une sélection aléatoire autour de son centre de masse, changement de la conformation interne par le mouvement de repousse de biais configurationnel et mouvement d'essai d'insertion/suppression. Les fréquences de chaque type de mouvement sont de 0,20 pour la translation, 0,20 pour la rotation, 0,20 pour le changement de conformation et 0,4 pour l'insertion/suppression. Les simulations GCMC comprenaient 700 000 cycles.

2. Résultats de la Phase Confinée:

Comme le montre la figure, pour les deux composants purs, une structure en couches a été observée en raison de l'effet de confinement à l'échelle nanométrique. Considérant que trois couches sont observées pour les deux cas, la couche interfaciale de TBA semble plus proche de la surface de silice, ce qui suggère que les interactions attractives entre le nano-pore de silice et des molécules de TBA sont plus fortes. Comme représenté sur la figure, les groupes hydroxyde (OH) des molécules TBA pointent vers la surface de la silice. La force motrice de cet ancrage interfacial est probablement le résultat du réseau de liaisons hydrogène (LH) fort entre la silice poreuse et les molécules de TBA. De manière intéressante, comme le montre la figure 3, cet ancrage HB conduit à une organisation particulière telle que les domaines hydrophobe et hydrophile (HB) sont disposés en succession alternée. Ces résultats devraient probablement avoir un impact sur la structure moléculaire du mélange confiné. Le profil de densité des groupes SiOH est également indiqué sur la figure 3. Comme représenté sur la Fig. 3, le profil SiOH commence à 11,5 Å et présente un pic autour de 14 Å, mettant en évidence la rugosité de la surface. Le calcul du volume accessible en sondant le volume poreux par un atome d'Argon nous a permis d'évaluer approximativement le rayon des pores à 12 Å.

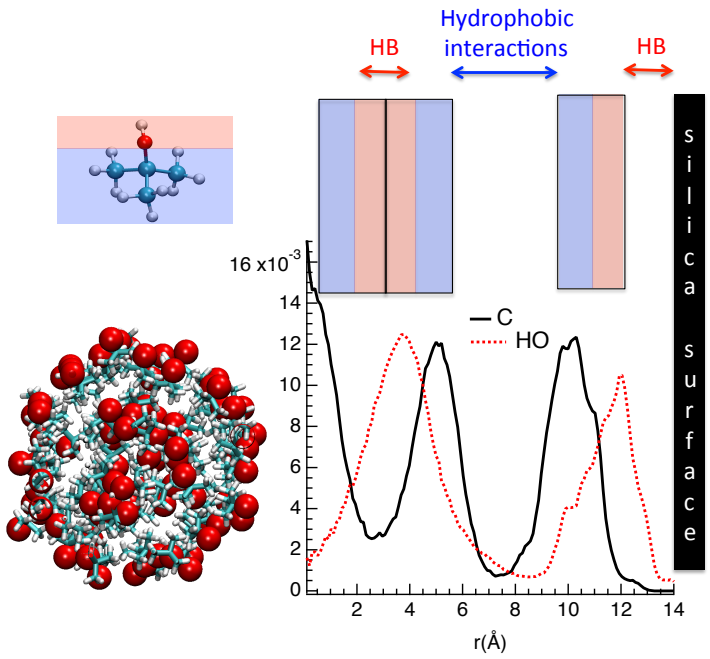

Figure 3: Profils de densité des groupes OH, des atomes de carbone des molécules de *tert*-butanol (TBA) et des groupes SiOH dans le cas où X_{TBA} = 1,0.

De x_{TBA} = 0,24 à 0,83, la figure 4 (de la figure 4a-d) montre que les molécules de TBA ont été adsorbées près de l'interface constituant une première couche, alors que les molécules de toluène sont situées juste après. Pour x_{TBA} = 0,83, les deuxième et troisième couches correspondent à une phase de mélange homogène rappelant le milieu en Bulk. De manière très intéressante, la figure 4 met en évidence le développement progressif de deux phases à mesure que la concentration de TBA diminue. En effet, pour x_{TBA} = 0,71, les molécules TBA sont presque uniquement localisées à proximité de la surface de la silice dans la première couche adsorbée sans molécules de TOL.

Pour x_{TBA} = 0,49 qui correspond à la concentration où l'organisation noyau-coquille a été observée expérimentalement, la séparation en micro-phase est presque complète. Il est intéressant de noter que la distance entre les pics de TOL et de TBA semble diminuer en fonction de la diminution de la fraction molaire de TBA. En effet, alors que sur la figure 4a, b la distance entre la densité interfaciale TOL et TBA ($d_{TBA-TOL}$) est d'environ 4 Å, la distance est fortement réduite à seulement ~ 1 Å pour x_{TBA} = 0,49 et x TBA = 0,24. La différence dans le $d_{TBA-TOL}$ en fonction de la fraction molaire TBA est due à l'augmentation progressive de TOL. En effet, pour la fraction TBA inférieure à 0,5 correspondant à une interface solide insaturée dans les molecules TBA, la surface SiOH peut alors

adsorber les molécules TOL. L'adsorption progressive en molécules TOL à la surface de la silice est alors à l'origine de la diminution de $d_{TBA-TOL}$ avec l'augmentation de la fraction TOL et est alors à l'origine de l'interpénétration des molécules TOL.

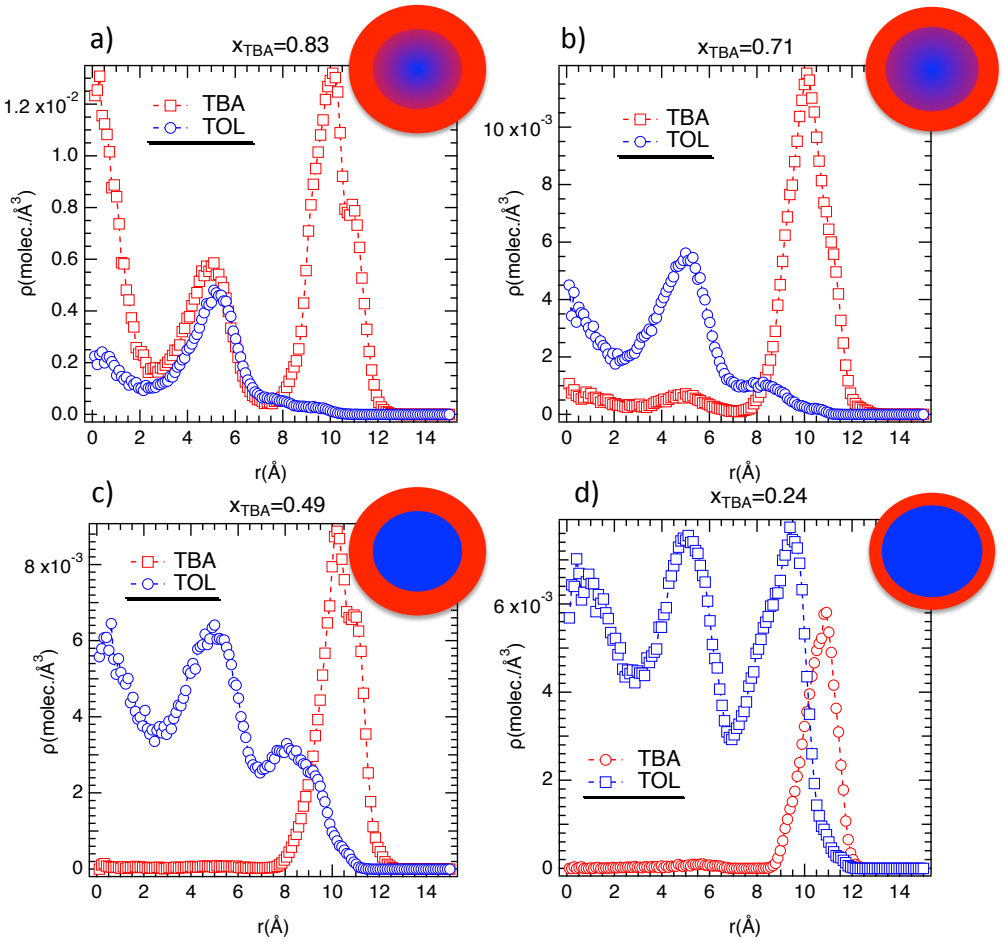

Figure 4: Profils de la densité radiale du centre de masse des molécules de *tert*-butanol (TBA) et de toluène (TOL) pour xTBA = 0,83 (a), 0,71 (b), 0,49 (c) et 0,24 (d). Les images encadrées illustrent l'organisation noyau-coquille, le TBA (couleur rouge) près de la surface et le mélange TBA/TOL (TOL est de couleur bleue) au centre des pores ; de 0,83 à 0,24, la largeur de la couche interfaciale diminue, tandis que la concentration en TBA diminue au centre des pores.

3. Discussion

Dans ce travail, nous avons montré que le nano-confinement peut induire, dans quelques conditions, une séparation en micro-phase du mélange binaire avec une organisation noyau-coquille conforme aux expériences de diffusion neutronique.

La séparation de phase a été soulignée par la mise en évidence des interfaces liquide-liquide et liquide-solide au moyen des profils de densité du centre de masse et de la tension superficielle locale. En calculant le profil radial du nombre de liaisons hydrogène et en ajustant l'hydrophilicité de la surface du nano-pore de silice, nous avons établi que la séparation de phase était régie, à l'échelle moléculaire, par les fortes liaisons hydrogène entre les molécules TBA et le matériau de silice qui favorise l'ancrage de la liaison hydrogène.

Le confinement à travers un nanotube de carbone a montré une structure noyau-coquille inverse avec TOL ancré à la surface solide mettant en évidence un ancrage hydrophobe dû à une organisation proportionnée impliquant l'empilement des cycles benzéniques. Ces résultats éclairent la possibilité de contrôler la nanostructure de fluides multi-composants sous confinement à l'échelle nanométrique en ajustant la chimie de surface du nano-pore.

La séparation en phase nano-confinée semble indépendante de la taille des pores et est essentiellement liée à la force des interactions pore-fluide. Ces résultats éclairent la possibilité de contrôler la nanostructure de fluides multi-composants sous confinement à l'échelle nanométrique en contrôlant la chimie de surface du nano-pore.

La séparation en micro-phase n'a pas été établie à partir d'un pore faiblement hydrophile, alors que la structure noyau-coquille a également été récupérée à partir d'une matrice hydrophobe (nanotube de carbone), soulignant que la séparation de phase est sans ambiguïté liée aux interactions liquide-solide.

UNIVERSITÉ DE RENNES 1

Titre : Etude de la microstructure des liquides binaires en phases Bulk et Nano-Confinées

Mots clés : Liquide binaire, simulation de dynamique moléculaire, séparation de phase, effet de confinement, liaison hydrogène

Résumé : L'étude des liquides formant des liaisons hydrogène sous confinement à l'échelle nanométrique ont fait l'objet de cette thèse. Nous avons étudié le comportement physique de liquides binaires en volume et en phases nano-confinées à l'aide de simulations de dynamique moléculaire. Nous montrons qu'il est possible de contrôler les caractéristiques structurelles de la structure noyau-coquille en affinant la chimie de surface du nano-pore pour recréer des confinements hydrophiles et hydrophobes. Par conséquent, on a mis en évidence une organisation noyau-coquille telle que l'un des liquides était fortement ancré à la surface solide tandis que l'autre était confiné au centre du pore.

Title : Microstructure of binary mixtures in bulk and nanoconfined phases

Keywords : Binary liquids, Molecular dynamics simulation, phase separation, confinement effect, hydrogen bond

Abstract : The study of the hydrogen bonded liquids under nanoscale confinement were the focus of this thesis. By molecular dynamics simulations, we've investigated the physical behavior of binary liquids in bulk and nanoconfined phases. By tuning the surface chemistry of the nanopore to mimic hydrophilic and hydrophobic confinement, we show that it is possible to control the structural characteristics of the core–shell structure. Thereon, a core–shell organization was evidenced such that one of the liquids was strongly anchored to the solid surface whereas the other was confined at the center of the pore.